

Oil & Natural Gas Technology

DOE Award No.: DE-FC26-06NT43067

Final Scientific/Technical Report

Mechanisms Leading to Co-Existence of Gas and Hydrate in Ocean Sediments

Submitted by:

Center for Petroleum and Geosystems Engineering
The University of Texas at Austin
Austin, Texas 78712

and

Department of Civil and Environmental Engineering
Massachusetts Institute of Technology
Cambridge, Massachusetts 02139

Prepared for:

United States Department of Energy
National Energy Technology Laboratory

April 11, 2012



Office of Fossil Energy

DE-FC26-06NT43067

**MECHANISMS LEADING TO CO-EXISTENCE OF
GAS HYDRATE IN OCEAN SEDIMENTS**

Final Report

1 October 2006 to 31 December 2011

by

Steven Bryant

and

Ruben Juanes

31 March 2012

Work Performed under Contract No. DE-FC26-06NT43067

Prepared for U.S. Department of Energy

Robert Vagnetti, Project Manager

U.S. Department of Energy

National Energy Technology Laboratory

P.O. Box 880

Morgantown, WV 26507-0880

Prepared by

Center for Petroleum and Geosystems Engineering

The University of Texas at Austin

Austin, Texas 78712

and

Department of Civil and Environmental Engineering

MIT

Cambridge, Massachusetts 02139

DISCLAIMER

This report was prepared as an account of work sponsored by an agency of the United States Government. Neither the United States Government nor any agency thereof, nor any of their employees, makes any warrantee, express or implied, or assumes any legal liability or responsibility for the accuracy, completeness, or usefulness of any information, apparatus, product, or process disclosed, or represents that its use would not infringe privately owned rights. Reference herein to any specific commercial product, process, or service by trade name, trademark, manufacturer, or otherwise does not necessarily constitute or imply its endorsement, recommendation, or favoring by the United States Government or any agency thereof. The views and opinions of authors expressed herein do not necessarily state or reflect those of the United States Government or any agency thereof.

ABSTRACT

In this project we have sought to explain the co-existence of gas and hydrate phases in sediments within the gas hydrate stability zone. We have focused on the gas/brine interface at the scale of individual grains in the sediment. The capillary forces associated with a gas/brine interface play a dominant role in many processes that occur in the pores of sediments and sedimentary rocks. The mechanical forces associated with the same interface can lead to fracture initiation and propagation in hydrate-bearing sediments. Thus the unifying theme of the research reported here is that *pore scale phenomena are key to understanding large scale phenomena in hydrate-bearing sediments whenever a free gas phase is present.*

Our analysis of pore-scale phenomena in this project has delineated three regimes that govern processes in which the gas phase pressure is increasing: fracturing, capillary fingering and viscous fingering. These regimes are characterized by different morphology of the region invaded by the gas. On the other hand when the gas phase pressure is decreasing, the corresponding regimes are capillary fingering and compaction. In this project, we studied all these regimes except compaction. Many processes of interest in hydrate-bearing sediments can be better understood when placed in the context of the appropriate regime. For example, hydrate formation in sub-permafrost sediments falls in the capillary fingering regime, whereas gas invasion into ocean sediments is likely to fall into the fracturing regime.

Our research provides insight into the mechanisms by which gas reservoirs are converted to hydrate as the base of the gas hydrate stability zone descends through the reservoir. If the reservoir was no longer being charged, then variation in grain size distribution within the reservoir explain hydrate saturation profiles such as that at Mt. Elbert, where sand-rich intervals containing little hydrate are interspersed between intervals containing large hydrate saturations. Large volumes (of order one pore volume) of gaseous and aqueous phases must be transported into the gas hydrate stability zone. The driver for this transport is the pressure sink induced by a reduction in occupied pore volume that accompanies the formation of hydrate from gas and water. Pore-scale imbibition models and bed-scale multiphase flow models indicate that the rate-limiting step in converting gas to hydrate is the supply of water to the hydrate stability zone. Moreover, the water supply rate is controlled by capillarity-driven flux for conditions typical of the Alaska North Slope. A meter-scale laboratory experiment confirms that significant volumes of fluid phases move into the hydrate stability zone and that capillarity is essential for the water flux. The model shows that without capillarity-driven flux, large saturations of hydrate cannot form. The observations of thick zones of large saturation at Mallik and Mt Elbert thus suggest that the primary control on these systems is the rate of transport of gaseous and aqueous phases, driven by the pressure sink at the base of the gas hydrate stability zone.

A key finding of our project is the elucidation of “capillary fracturing” as a dominant gas transport mechanism in low-permeability media. We initially investigate this phenomenon by means of grain-scale simulations in which we extended a discrete element mechanics code (PFC, by Itasca) to incorporate the dynamics of first single-phase and then multiphase flow. A reductionist model on a square lattice allows us to determine some of the fundamental dependencies of the mode of gas invasion (capillary

fingering, viscous fingering, and fracturing) on the parameters of the system. We then show that the morphology of the gas-invaded region exerts a fundamental control on the fabric of methane hydrate formation, and on the overpressures caused by methane hydrate dissociation. We demonstrate the existence of the different invasion regimes by means of controlled laboratory experiments in a radial cell. We collapse the behavior in the form of a phase diagram fully characterized by two dimensionless groups: a modified capillary number and a “fracturing number” that reflects the balance between the pressure forces that act to open conduits in the granular pack, and frictional forces that resist it. We use all this small-scale knowledge to propose simple mechanistic models of gas migration and hydrate formation at the geologic bed scale. We propose that methane transport in lake and oceanic sediments is controlled by dynamic conduits, which dilate and release gas as the falling hydrostatic pressure reduces the effective stress below the tensile strength of the sediments. We test our model against a four-month record of hydrostatic load and methane flux in Upper Mystic Lake, Mass., USA, and show that it captures the complex episodicity of methane ebullition. Our quantitative conceptualization opens the door to integrated modeling of methane transport to constrain global methane release from lakes and other methane-rich sediment systems, and to assess its climate feedbacks.

TABLE OF CONTENTS

	Page
DISCLAIMER	ii
ABSTRACT	iii
TABLE OF CONTENTS	iv
EXECUTIVE SUMMARY	1
Unifying Theme	1
Key Findings	2
Development and Application of Bed Scale Models	3
Capillarity Dominated Behavior	4
Geologic Context for Capillarity-Dominated Processes in Sub-Permafrost Hydrate-Bearing Sediments	4
Physical Phenomena Critical to the Proposed Model	7
Gas reservoir Conversion to Hydrate: Bed-Scale Volumetric Considerations	15
Gas Reservoir Conversion to Hydrate: Role of Pore-Scale Imbibition	28
Summary of Influence of Pore-Scale Imbibition on Hydrate Saturation Profiles	59
Gas Reservoir Conversion to Hydrate: Role of Pressure-Driven Fluid Phase Transport at Bed-Scale	60
Summary of Applicability of Pressure-Driven Transport Model for Conversion of Gas Reservoirs to Hydrate	77
Gas Reservoir Conversion to Hydrate: Role of Capillarity-Driven Fluid Phase Transport at Bed-Scale	78
Summary of Applicability of Capillarity-Driven Transport Model for Conversion of Gas Reservoirs to Hydrate	84
Gas Reservoir Conversion to Hydrate: Experimental Validation of Fluid Transport in Response to Hydrate Formation	84
References for Capillarity Dominated Behavior in Hydrate-Bearing Sediments	114
Fracturing Dominated Behavior	120
Preferential mode of gas invasion in sediments: Grain-scale mechanistic model of coupled multiphase fluid flow and sediment mechanics	126
Crossover from fingering to fracturing in deformable disordered media	158
Thermodynamic and hydrodynamic constraints on overpressure caused by hydrate dissociation: A pore-scale model	168
Capillary fracturing in granular media	177
A conduit dilation model of methane venting from lake sediments	184
Numerical modeling of hydrate formation and methane gas transport through dynamic conduits	193
References for Fracturing Dominated Behavior	208
Appendix – Description of Underlying Models	222
Model Sediments	222
Advanced Methods for Simulating Drainage and Imbibition	222

Coupled Capillarity-Controlled Fluid Displacement with Mechanics.....	223
Publications on Hydrate-Bearing Sediments	223
Theses and Dissertations.....	224
Progress Reports	224

EXECUTIVE SUMMARY

Unifying Theme

A remarkable feature of many naturally occurring gas hydrates is the presence of a free gas phase migrating through sediment that also contains stable hydrate. The long term persistence of these features defies expectations based on thermodynamics. In this project we have sought to explain the co-existence of gas and hydrate phases by focusing on the gas/brine interface. This interface is present when a gas phase occupies any part of a sediment, from the gas/water contact at the base of a free gas accumulation to the meniscus at the leading edge of a fracture induced by gas pressure. The capillary forces associated with a gas/brine interface play a dominant role in many processes that occur in the pores of sediments and sedimentary rocks. Thus the unifying theme of the research reported here is that *pore scale phenomena are key to understanding large scale phenomena in hydrate-bearing sediments whenever a free gas phase is present*. Pore scale phenomena of particular interest include drainage, imbibition, grain displacement, and growth/breakage of hydrate skins on gas/water interfaces. Large scale phenomena notably include the spatial distribution of hydrate saturation, especially when hydrate formation involves a free gas phase, and the morphology of hydrate, from lenses and filled fractures to veins and filled pores.

We developed a set of new models of relevant pore scale phenomena in this project, and these have been described in progress reports and a series of papers. This report focuses not on these models but on their application at the bed-scale to certain processes in hydrate-bearing sediments. One application is to sub-permafrost accumulations of hydrate, created as the base of the gas hydrate stability zone descended through previously established gas reservoirs. Another application is to sediments in deep water into which gas invasion occurs. The results provide useful insight into the factors governing the bed-scale behavior.

A major scientific contribution of this project is our identification of two broad regimes for gas displacing brine within sediments: a **fracturing** regime, which applies for low permeability sediments, and a **fingering** regime, which applies in higher permeability sediments. The fingering regime is subdivided into capillary fingering (classical invasion percolation) at small flow rates and viscous fingering at large flow rates. Many processes of interest in hydrate-bearing sediments can be better understood when placed in the context of the appropriate regime. For example, hydrate formation in sub-permafrost sediments falls in the capillary fingering regime, whereas gas invasion into ocean sediments is likely to fall into the fracturing regime.

The capillarity-controlled regime for sub-permafrost hydrate-bearing sediments means that certain parameters play a particularly important role. These include

- petrophysical properties for the sediment
 - the characteristic drainage and imbibition curves (capillary pressure vs. saturation)
 - relative permeability curves for the gas and brine phases
- geological properties
 - grain size distribution and its variation within the sediment,
- driving forces
 - capillary pressure of the gas phase and its variation with position and with gas column height

- gradients in saturation and capillary pressure.

Key Findings

Key findings for **sub-permafrost hydrate-bearing sediments** include:

- Variation in grain size distribution within a sediment layer can give rise to a hydrate saturation profile where sand-rich intervals containing little hydrate are interspersed between intervals containing large hydrate saturations.
- Viewed from the pore scale, conversion of a gas reservoir to hydrate is an imbibition process because the gas phase pressure decreases as the gas column height decreases. A pore-scale simulation of imbibition that assumes water reaches the gas-water interfaces very slowly yields an upper bound on final hydrate saturation of $S_{h,final} = S_{g,initial}$. Repeating the imbibition simulation with the assumption that water reaches interfaces very rapidly yields a lower bound on $S_{h,final}$. These bounds bracket saturation profiles reported for Mt Elbert and for Mallik.
- Viewed from the bed scale, conversion of a gas reservoir to hydrate is a transport problem: Large volumes of gas phase and brine phase (about two thirds of a pore volume of each phase) must enter the hydrate-bearing sediment during hydrate formation. A meter-scale laboratory experiment confirms that significant volumes of fluid phases move into the hydrate stability zone.
- Of the fluids that enter the hydrate-bearing sediment, the fraction which is gas determines the final hydrate saturation.
- The rate of hydrate formation, which is related to the rate of descent of the base of gas hydrate stability zone, and the relative permeabilities of gas and aqueous phases determine the gas phase fraction in the total fluids moving to the hydrate-bearing sediment.
- The accumulation of large hydrate saturations, like those reported at Mt Elbert and Mallik, require gas and brine phase transport from below the hydrate stability zone. This transport can be driven by capillarity along saturation gradients.
- Capillarity-controlled transport in turn requires relatively slow descent of the base of the gas hydrate stability zone. Otherwise, the rate of hydrate formation demands faster transport, which requires viscous forces to play a stronger role. Transport dominated by viscous forces approaches the solution given by fractional flow theory, in which a gas bank forms and aqueous phase cannot reach the hydrate stability zone, stopping the generation of hydrate at saturations much smaller than observed at Mt Elbert and Mallik.

Key findings for **deep-water hydrate-bearing sediments** include:

- “Capillary fracturing” is a dominant gas transport mechanism in low-permeability media.
- This phenomenon has been proposed based on grain-scale simulations in which we extended a discrete element mechanics code (PFC, by Itasca) to incorporate the dynamics of first single-phase and then multiphase flow, but was then confirmed experimentally in a set of laboratory experiments that demonstrate the different regimes of gas invasion in deformable sediments (capillary fingering, viscous fingering, and fracturing).

- Gas invasion regime is characterized by two dimensionless groups: a modified capillary number and a “fracturing number” that reflects the balance between the pressure forces that act to open conduits in the granular pack, and frictional forces that resist it.
- The morphology of the gas-invaded region exerts a fundamental control on the fabric of methane hydrate formation, and on the overpressures caused by methane hydrate dissociation.
- Methane transport in lake and oceanic sediments is controlled by dynamic conduits, which dilate and release gas as the falling hydrostatic pressure reduces the effective stress below the tensile strength of the sediments. This conceptual and mathematical model was tested against a four-month record of hydrostatic load and methane flux in Upper Mystic Lake, Mass., USA, and show that it captures the complex episodicity of methane ebullition.
- Our quantitative conceptualization opens the door to integrated modeling of methane transport to constrain global methane release from lakes and other methane-rich sediment systems, and to assess its climate feedbacks.

Development and Application of Bed Scale Models

Our analysis of pore-scale phenomena in this project has delineated three regimes that govern processes in which the gas phase pressure is increasing: fracturing, capillary fingering and viscous fingering. These regimes are characterized by different morphology of the region invaded by the gas (see Figure below).

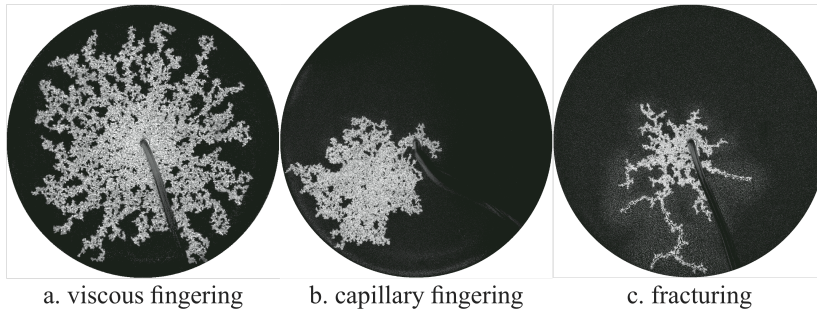


Figure. Different gas invasion regimes, observed experimentally [Holtzman et al., 2012]

The capillary fingering regime corresponds to a drainage displacement. On the other hand when the gas phase pressure is decreasing, the corresponding regimes are capillary fingering and compaction. In this case, the fingering corresponds to an imbibition displacement. Compaction corresponds to closure of fractures and tighter packing of grains. In this project, we studied all these regimes except compaction.

This section is the body of this report. It comprises two large subsections, one on *Capillarity Dominated Behavior*, the other on *Fracturing Dominated Behavior*.

The application focus of the *Capillarity Dominated Behavior* subsection is on subpermafrost accumulations of hydrate. Large saturations of hydrate in sand-rich sediments in the Arctic have drawn great interest. The leading hypothesis for the creation of these accumulations is that they are converted from existing gas reservoirs. The conversion to hydrate occurred when the base of gas hydrate stability descended through the reservoirs. The detailed mechanism by which this conversion occurs has not been elucidated. A major contribution of the research conducted in this project is the first quantitative and mechanistic model of the conversion process. We describe this process and several possible models. We show that field observations at Mt Elbert can be represented well by the limiting case of a closed system in which gas phase pressure decreases.

In the section on *Fracturing Dominated Behavior* we turn to cases in which gas phase pressure is increasing. The application focus is quite broad: relatively shallow sediments of relatively small permeability which are highly susceptible to fracturing as gas phase pressure increases. We demonstrate the existence of the different invasion regimes by means of controlled laboratory experiments in a radial cell. We collapse the behavior in the form of a phase diagram fully characterized by two dimensionless groups: a modified capillary number and a “fracturing number” that reflects the balance between the pressure forces that act to open conduits in the granular pack, and frictional forces that resist it. We use all this small-scale knowledge to propose simple mechanistic models of gas migration and hydrate formation at the geologic bed scale. We propose that methane transport in lake and oceanic sediments is controlled by dynamic conduits, which dilate and release gas as the falling hydrostatic pressure reduces the effective stress below the tensile strength of the sediments.

Capillarity Dominated Behavior

Geologic Context for Capillarity-Dominated Processes in Sub-Permafrost Hydrate-Bearing Sediments

Prospecting for gas hydrates as a resource has only recently begun to adopt the perspective of exploring for petroleum systems (Collett *et al.*, 2009). Gas hydrates are formed at low temperatures and generally high pressures (e.g. temperatures below 25°C and pressures greater than 1.5 MPa for natural gas hydrates) which are typical of relatively shallow depths in oceanic sediments (Kvenvolden, 1988; Koh *et al.*, 2002) or deeper sediments in the Arctic (Collett, 1993).

In deep ocean sediments hydrates occur in various morphologies (Sloan, 1998; Waite *et al.*, 2009). Hydrates have been observed as disseminated grains filling pores (Dallimore and Collett, 2005; Fujii *et al.*, 2008) and as complex networks of filled fractures and veins in fine grained sediments (Hadley *et al.*, 2008; Holland *et al.*, 2008). Beneath the Indian Ocean (offshore India) most of the recovered gas hydrate was found to exist in “combination reservoirs”, characterized as either pore-filling grains or particles disseminated (in coarser grain sediment) or as fracture-filling (in clay dominated sediments) (Collett *et al.*, 2009).

In the Arctic such as Alaska’s North Slope (ANS), strata several meters thick, containing large saturations (65%-75%) of gas hydrate are often separated by layers of varying thickness that contain little or no hydrate (Boswell *et al.*, 2011). In addition, gas hydrates in permafrost regions have been commonly reported to occur with pore-filling morphology in sand-rich sediments (Dallimore and Collett, 2005).

Hydrate formation in sediments, especially in marine environments, has been subject to series of analyses. Predictive models of the process can be divided into two categories: (A) Models assuming formation of hydrate from methane dissolved in water in which accumulation is driven by methane-saturated water entering the gas hydrate stability zone (GHSZ) or by providing methane from a biogenic source (Hyndman and Davis, 1992; Ginsburg, 1998; Xu and Ruppel, 1999; Buffett, 2000; Hensen and Wallmann, 2005; Bhatnagar *et al.*, 2007) and (B) models assuming formation of hydrate at the interface between gaseous and aqueous phases in which accumulation is driven by methane gas phase entering the GHSZ (Torres *et al.*, 2004; Liu and Flemings, 2006, 2007). One motivation for the latter class of models was that observed chloride concentrations and gas hydrate distributions could not be explained without assuming transport of free gas through GHSZ (Torres *et al.*, 2004).

The model categories (A) and (B), address marine hydrate reservoirs. While there is no comparably mechanistic model of hydrate formation for terrestrial hydrate accumulations, i.e. subpermafrost hydrate reservoirs, in the literature, the overall process has been delineated. Boswell *et al.* (2011) listed several aspects of gas hydrate accumulations in the Arctic that support the interpretation of conversion of free gas accumulation to gas hydrate accumulations. The accepted scenario for Arctic hydrate reservoirs such as those of the Prudhoe Bay and Kuparuk River area in ANS is that gas first accumulated in shallow traps when those traps were below the GHSZ. The gas reservoirs moved into the GHSZ in response to ancient climate cooling (Collett, 1993).

In this report a more detailed model of the process of hydrate accumulation is proposed, based on the latter Arctic scenario. A major difference between this model and the marine models (A) and (B) is that instead of presuming fluxes of fluid(s) to the GHSZ, we presume that the base of GHSZ moves down to (and through) an existing petroleum system. Fluid flux occurs in our model (and plays an important role in determining saturation) but only as a response to BGHSZ motion. This downward movement of the BGHSZ occurred in the ANS roughly 1.8 Ma (Collett, 1993; Dai *et al.*, 2011). For simplicity we also assume that CH₄ is the only constituent of the gas phase and the only guest molecule in the hydrate.

One motivation for a detailed process model is the observation in the well-characterized Milne Point Unit (MPU) hydrate accumulations, e.g. in Mount Elbert well, that hydrates are often restricted to the upper part of the sand units (Fig. 1b). Several explanations are possible. In the upper hydrate-bearing sand unit of Mount Elbert well, known as Unit D (Collett, 1993), this observation could be interpreted as the occurrence of high quality (large porosity and large intrinsic permeability) sand at the top of the unit. However, in the lower hydrate-bearing sand unit, known as Unit C (Collett, 1993), this is not the case (Boswell *et al.*, 2011). The top section of Unit C contains the major hydrate saturation (Fig. 1b) while it possesses a significantly lower porosity and intrinsic permeability than the lower section containing little or no hydrate (Boswell *et al.*, 2011). Moreover, reservoir sands in the MPU are only partially filled with hydrate and often exhibit a sharp basal contact. For example within the D Unit log and core data exhibit an abrupt decrease in hydrate saturation, S_h , from greater than 65% to less than 10% despite the gradational decrease in reservoir quality, reduced porosity and increased shale content (Boswell *et al.*, 2011). Hence it is difficult to postulate a straightforward relation between reservoir quality and hydrate saturation in the Mt. Elbert well.

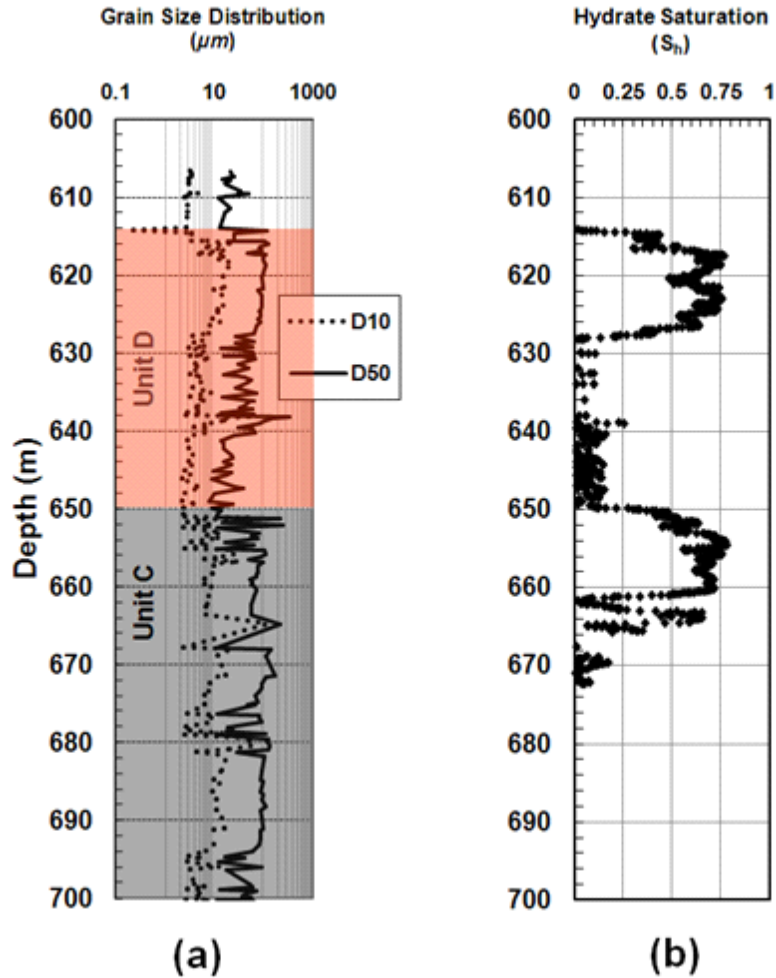


Fig. 1. Data from Mount Elbert stratigraphic test well, drilled in the Milne Point unit of Alaska North Slope: (a) 10th percentile, D_{10} , and 50th percentile, D_{50} , of grain size distribution versus depth determined from laser-grain-size analyses (Rose *et al.*, 2011); (b) Gas hydrate saturation, S_h , determined from the TCMR-repeat-pass-plus-density log based on NMR-DEN POR method (Lee and Collett, 2011). The shown interval of interest includes the informally labeled C and D units of Collett (1993).

Another possible explanation of these variations in hydrate saturation is that they simply reflect the variation of the original gas saturation distribution. Unit D may have been only partially filled with gas for a variety of reasons—a shallow spill point, the stratigraphic seal could hold only a modest gas column, or an interruption in the gas migration path caused insufficient charge, etc. But partial charge is not a necessary condition for variable hydrate saturation in an individual reservoir: the volume changes associated with hydrate formation mean that hydrate will occupy only the upper portion even of a fully charged reservoir. Whatever the extent of charge, this explanation assumes that the conversion to hydrate occurs after the reservoir is no longer connected to the source of gas.

The partial charge explanation becomes more critical in the case of a vertical sequence of partially filled hydrate reservoirs. This explanation would require Units D and C to have been charged separately, for example by migration along the individual layers from a conductive downdip fault connected to the gas source. It would also require no vertical communication between the gas accumulations, i.e. a sufficiently large capillary entry pressure for the sediment

at the base of Unit D. The requisite entry pressure depends in turn on the height of gas column resulting from the charge of Unit C.

Because the conversion to hydrate drives substantial fluid migration, the structural setting of the gas accumulations also affects the final hydrate distribution. The model analyzed here is for the limiting case of horizontal layers, in which fluid migration is only in the vertical direction. In this case the process is essentially one-dimensional. This is a reasonable approximation for the Mount Elbert prospect. The C and D Units occur within the non-marine Tertiary Sagavanirktok Formation and are laterally extensive throughout the Milne Point Unit (MPU) and beyond (Boswell *et al.*, 2011) covering approximately 360 km² (Collett, 1993; Winters *et al.*, 2011). A seismic survey (Inks *et al.*, 2009) suggests that hydrate-bearing intervals in the Mt. Elbert prospect are quite extensive in terms of areal distribution. The Mt. Elbert well is located on a monoclinical structure that dips less than 2° to the NNE (Collett, 1993; Inks *et al.*, 2009; Boswell *et al.*, 2011). The BGHSZ itself can be approximated as a horizontal surface, so its descent through laterally extensive gas accumulations within a nearly horizontal structure is also an approximately one-dimensional process. In this limiting case hydrate will form uniformly within the GHSZ, and any gas flow induced during hydrate formation must come from the accumulation still below the GHSZ. As the dip angle increases, gas can migrate along dip as well as vertically; the limiting case treated here provides a lower bound on the saturation profile for dipping beds. Conductive faults provide another possible route for fluid migration at Mt. Elbert well on the upthrown side of a large normal fault (Boswell *et al.*, 2011) which may have contributed to the flow at the time of hydrate formation, but we assume all faults are sealing in this work.

Thus the timing, the pathway, the extent of charge and the dip angle are key controls on final hydrate distribution in a multilayer column of sediment. The model presented here makes the partial charge explanation quantitative for noncommunicating layers, and more importantly it generalizes the partial charge model to show how a stack of partially filled hydrate reservoirs can result even from initially communicating layers that host a single continuous column of gas.

To summarize, applying the proposed 1-D model on field data from Mount Elbert well, we show that certain characteristic features associated with hydrate occurrence in the Arctic are consistent with three conditions: i) the establishment of gas phase saturation within the sediment when the base of gas hydrate stability zone (BGHSZ) was located above the sediment package; ii) sufficient variation of grain size distribution with depth and iii) volume reduction during hydrate formation, i.e. hydrate occupies less volume than its constituents (CH₄, H₂O) in their respective phases. The latter is presumably true in all natural hydrate-bearing sediments, including Arctic sediments. The first condition is also commonly satisfied in the Arctic; the second depends on local depositional history.

Physical Phenomena Critical to the Proposed Model

Grain size varies with depth in most depositional environments. When gas accumulates in a sediment, these variations play an important role on the gas/water saturation profile. Fig. 2a shows schematically a stack of four distinct sediment layers with different grain size distributions. Each layer thus has a different characteristic curve of capillary pressure versus saturation, as shown in Fig. 2b. Capillary pressure, P_c , is defined as the difference between the non-wetting phase pressure, in this case gas pressure P_g , and wetting phase, aqueous phase pressure P_w . Capillary pressure curve shows the relationship describing the capillary pressure required for establishing a given gas phase saturation in a sediment originally filled with water.

The top layer (layer 1) has the smallest grains, and the corresponding capillary pressure curve shows a much larger capillary entry pressure than other layers. If gas enters this stack of sediments from the bottom of layer 4 (Fig. 2a) and begins to accumulate, the capillary pressure increases with gas column height above the entry point as shown in Fig. 2c. The capillary pressure at any height combined with the corresponding drainage curve (Fig. 2b) yields the gas/water saturation profile shown in Fig. 2d. The fine-grained layer 1 acts as a seal for the gas accumulation in Fig. 2d. Note that the BGHSZ is above the gas column and thus no hydrate is present in Fig. 2d. Fig. 2e shows the situation when the BGHSZ has descended all the way down the gas column and thus the gas accumulation (Fig. 2d) has turned into hydrate. Note that the initially single gas column (Fig. 2d) turned into discrete, concentrated hydrate deposits at the top section of two of the formations (Fig. 2e). The resulting hydrate saturation profile in Fig. 2e exhibits a similar distribution to the Mount Elbert well (Fig. 1b). More detailed explanation of how vertical heterogeneity, i.e. grain size variation versus depth, can lead to such discrete, concentrated hydrate deposits is provided in a later section.

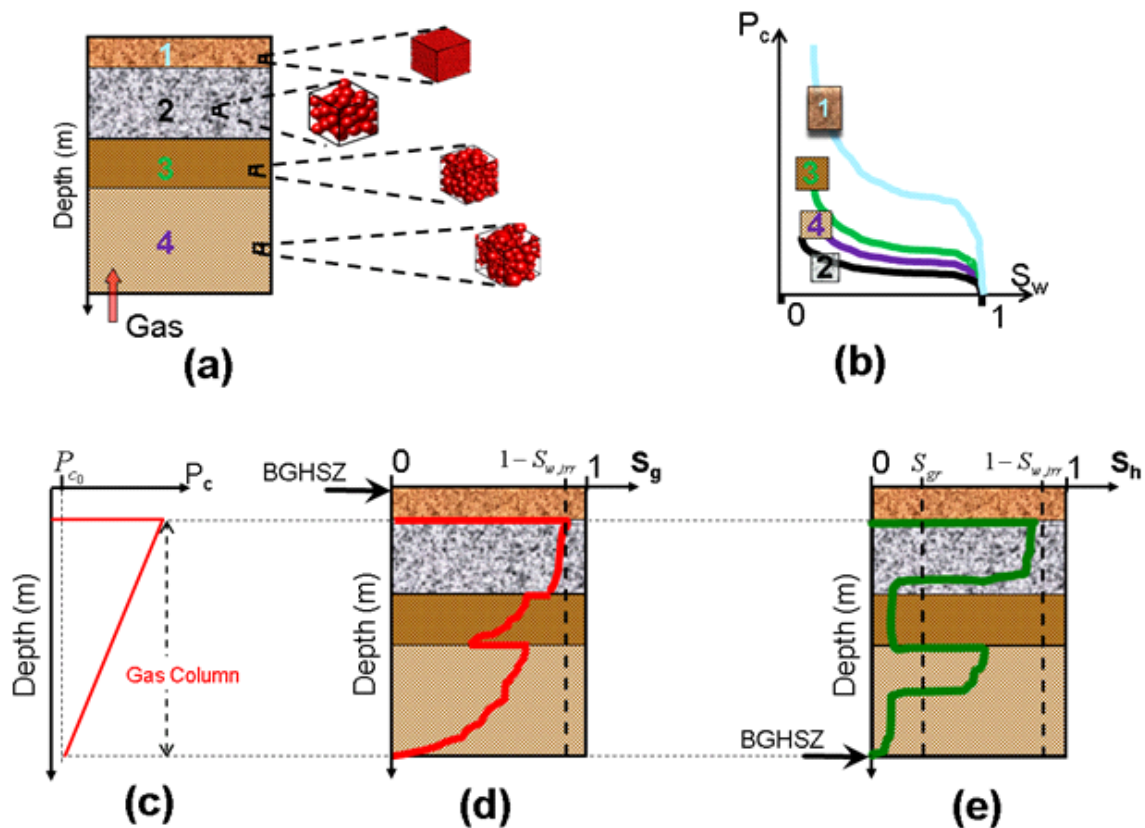


Fig. 2. (a) Sediment layers with different grain size distributions. The characteristic capillary pressure for each layer is shown in (b). Gas enters the bottom layer and accumulates below the fine-grained layer at top of sediment package. (c) Capillary pressure profile within the gas column, combined with the characteristic curves of (b), determines the gas saturation profile (d) through the sediments. Note that gas accumulation has occurred while BGHSZ is shallower than the gas column and thus no hydrate is being formed so far. (e) As BGHSZ descends along the sediment column, a hydrate saturation profile is established which can be very different from the initial gas saturation profile and need not correlate with sediment layering.

The other physical phenomenon essential to our model is that the volume occupied by a mole of methane hydrate, i.e. the amount of hydrate containing one mole of gas, is smaller than the

volume occupied by gas and aqueous phases containing the same number of moles of CH₄ and H₂O as the hydrate. This reduction in volume accompanying hydrate formation follows from hydration number, N , in the hydrate lattice, CH₄. N (H₂O), and typical densities of the respective phases. Hydrates are known to be non-stoichiometric, meaning that N varies with pressure, temperature and overall gas composition (Sloan, 2003), with values of $N = 6.05 \pm 0.6$ (Handa, 1986; Ripmeester and Ratcliffe, 1988) for methane hydrate. For simplicity we use a constant value of $N = 6$, which is consistent with an average density of 914 kg/m³ for methane hydrate (Sloan, 1998). As a numerical example of the volume reduction associated with hydrate formation, consider a vessel containing 0.5 m³ of methane and 0.5 m³ of pure water held at a constant pressure of 6.5 MPa and temperature of 2 °C during hydrate formation. At these conditions the phase densities are about 55 kg/m³ (gas) and 1000 kg/m³ (aqueous). For $N = 6$, the molecular weight of hydrate would be 124. All the gas will be consumed to form hydrate, and the hydrate volume is $V_h = 0.5 \times \frac{55}{16} \times \frac{124}{914} \approx 0.23 \text{ m}^3$. It can be shown that almost 0.18 m³ of water is used to form the latter amount of hydrate. Therefore, at the current thermodynamic condition the final hydrate volume, 0.23 m³, is almost one third of the consumed volumes of methane and water combined.

Conceptually, as hydrate forms from a fixed volume of gas phase in a sediment, void space becomes available. Here “void space” is shorthand for the volume change accompanying hydrate formation. The void space will either be filled by influx of fluid phase(s) or accommodated by compaction of the sediment. Here, we assume no compaction occurs during conversion to hydrate. We will see that in any case the volume changes are too large to be accommodated only by compaction. Methane which is transported to the GHSZ to help fill the void space is then converted to hydrate inside the GHSZ. As discussed below, the relative ratio of transported gaseous and aqueous phases affects the resulting hydrate saturation profile.

The rate of salinity transport can also affect the hydrate saturation profile. The inclusion of H₂O into the hydrate causes salinity to build up in the aqueous phase, potentially reaching the critical value at which hydrate is no longer stable at prevailing temperature and pressure. Here we assume that the aqueous phase has a small initial salinity. Furthermore, the descent of BGHSZ is assumed to occur over geologic time scales and thus any salinity buildup is dissipated into an unlimited reservoir of brine. Considering that heat diffusion (typically 10 m²/yr) is about 500 times faster than salinity transfer (typically 0.02 m²/yr) (Iversen and Jorgensen, 1993; Clennell *et al.*, 1999), we also neglect the effect of heat transfer.

We focus on the conversion of an accumulated gas saturation to hydrate as the BGHSZ moves down. Subsequently, hydrate dissociates if the BGHSZ moves upwards, leaving the gas bearing region out of GHSZ. Cycles of hydrate formation and dissociation could take place during geological time. For example, such movements of BGHSZ are reported in MacKenzie delta region (Majorowicz *et al.*, 2008; Torres *et al.*, 2011). Similar oscillations of the BGHSZ in Mount Elbert well were reported by Dai *et al.* (2011); however, the hydrate-bearing section of the Mount Elbert well remained well inside the GHSZ and not disturbed by the oscillations of the BGHSZ.

Volume Change for Hydrate Formation from Gas and Water

A box model is used to compute the volume change as hydrate forms. The box (with a volume V_{tot}) is originally filled by methane and water existing as two pure phases (Fig 3a). The initial gas/water volumes are prescribed and no hydrate is present initially. Temperature and

pressure are then adjusted to values at which hydrate is stable and held constant during hydrate formation. Phase densities are thus constant.

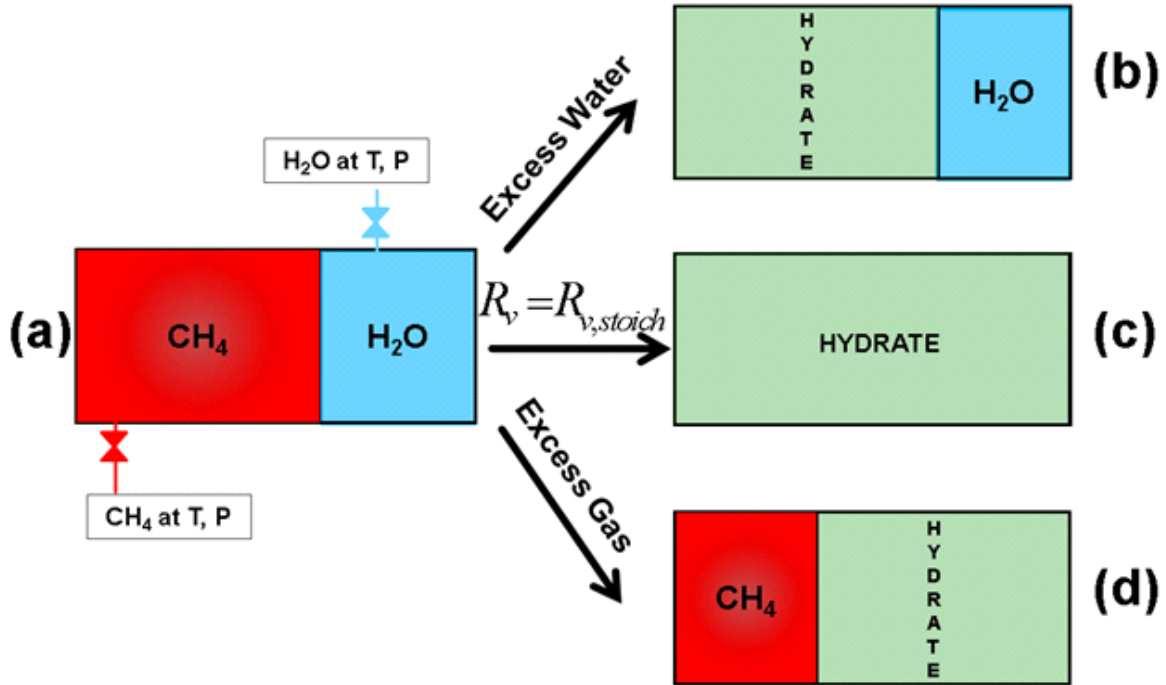


Fig. 3. (a) Hydrate formation in an open system: prescribed volumes of CH_4 and H_2O phases are initially present, and CH_4 and H_2O can enter so that T, P are constant during hydrate formation; (b) final state when the total amount of water (initial amount + the amount entered) is more than the stoichiometric requirement (excess water); (c) final state when the total amount of gas and water are at the exact stoichiometric ratio; (d) final state of the open system when the total amount of gas (initial amount + amount entered) is more than the stoichiometric gas requirement (excess gas).

Suppose an incremental volume of hydrate δV_h forms at the interface between gas and water phases as the result of stoichiometric, assuming constant hydration number $N = 6$, conversion of the corresponding increments of methane and water, δV_g and δV_w . For typical hydrate-stability subsurface conditions the phase densities are such that $\delta V_h < \delta V_g + \delta V_w$, and we write:

$$\delta V_h + \delta V = \delta V_g + \delta V_w \quad (1)$$

Here δV denotes the net change in volume occupied by fluids and hydrate. The consequence of this volume change depends on whether the box is closed or open.

For a closed box the only way to keep the pressure and temperature constant is by changing the volume of the box, i.e. V_{tot} decreases by δV . This would correspond to compaction (grain rearrangement to reduce porosity) in a natural system.

The sediments of interest behave more like open systems (fluid phases can leave or enter). In the model of Fig. 3, both water and methane can enter the box as needed to compensate for the volume reduction during hydrate formation and thus maintain the pressure. Hydrate will keep forming until one of the components (methane, water) inside the box is fully consumed. We define R_n as the ratio of number of gas phase moles, Δn_g , to the total number of moles of gas and aqueous phase, $\Delta n_g + \Delta n_w$, transported into the box. Two cases can be considered in terms of the initial and transported amounts of water, $n_{w,i}$ and Δn_w , and of methane, $n_{g,i}$ and Δn_g :

Excess Water: Total Water Exceeds Stoichiometric Requirement

In this case the total number of moles of water, $n_{w,i} + \Delta n_w$, is more than the stoichiometric amount of water required to convert the total amount of methane into hydrate, $N(n_{g,i} + \Delta n_g)$. Therefore, all the gas is consumed to form n_h moles, equivalent to a volume V_h , of methane hydrate and thus,

$$V_{w,f} = V_{tot} - V_h \quad (2)$$

where, V_{tot} denotes the total volume of the box and $V_{w,f}$ is the final water volume inside the box. Furthermore,

$$n_h = \frac{V_h}{\bar{V}_h} = (n_{g,i} + \Delta n_g) = \frac{V_{g,i} + \Delta V_g}{\bar{V}_g} \quad (3)$$

where $V_{g,i}$ denotes the initial gaseous phase volume in the box and ΔV_g is the gaseous phase volume transported into the box. \bar{V}_h and \bar{V}_g are the molar volumes of hydrate and methane, respectively. Molar volume of a component is equal to the molecular weight of the component divided by its density, i.e.:

$$\bar{V}_c = \frac{MW_c}{\rho_c} ; c = w, g, h \quad (4)$$

The final volume occupied by aqueous phase would be:

$$V_{w,f} = V_{w,i} + \Delta V_w - \underbrace{N \times V_h \frac{\bar{V}_w}{\bar{V}_h}}_{\text{Consumed } H_2O} \quad (5)$$

where $V_{w,i}$ and $V_{w,f}$ denote the initial and final water volume inside the box, respectively. ΔV_w is the volume of the aqueous phase transported into the box and N is the hydration number. Rewriting the right hand side of Eq. (5) in terms of moles yields:

$$V_{w,f} = [n_{w,i} + \Delta n_w - N(n_{g,i} + \Delta n_g)] \bar{V}_w \quad (6)$$

The hydrate volume can be written in terms of the initial moles of gas in the box and the molar ratio of gas transported, $R_n = \Delta n_g / (\Delta n_g + \Delta n_w)$, into the box:

$$V_h = \left[\frac{R_n (\bar{V}_g - \bar{V}_w) + \bar{V}_w}{R_n (\bar{V}_h - (N+1)\bar{V}_w) + \bar{V}_w} \right] n_{g,i} \bar{V}_h \quad (7)$$

Figure 3b illustrates a typical final state of the system in the case of excess water. Equations (2) and (5) give the total volume of water that entered the box, in terms of the final hydrate volume:

$$\Delta V_w = V_{tot} - V_{w,i} + V_h \left(N \frac{\bar{V}_w}{\bar{V}_h} - 1 \right) \quad (8)$$

Similarly, Eq. (3) gives the total volume of gas that entered the box:

$$\Delta V_g = \frac{\bar{V}_g}{\bar{V}_h} V_h - V_{g,i} \quad (9)$$

Equations (8) and (9) give the total phase volume transported into the box, $\Delta V_w + \Delta V_g$, as a function of the final hydrate volume, V_h :

$$\Delta V_w + \Delta V_g = K_{trans} V_h \quad (10)$$

where $K_{trans} = \frac{N\bar{V}_w + \bar{V}_g}{\bar{V}_h} - 1$. In fact, K_{trans} is the total phase (gaseous + aqueous) volume transported into the box (or any hydrate formation zone) per unit volume of hydrate formed, so that the total system volume is fixed. Note that K_{trans} is independent of the initial amount of gaseous and aqueous phase.

Excess Methane: Total Methane Exceeds Stoichiometric Requirement

In this case, there is more methane than the amount required to consume the total amount of water to form hydrate, i.e. $n_{g,i} + \Delta n_g > (n_{w,i} + \Delta n_w) / N$. Therefore, all the water is consumed to form n_h moles, equivalent to a volume V_h , of methane hydrate. Figure 3d illustrates a typical final state of the box in the case of excess methane. A development analogous to that in Section 2.1.1 yields the final hydrate volume as a function of R_n and the volumes of methane and water that enter the box:

$$V_h = \left[\frac{R_n (\bar{V}_g - \bar{V}_w) + \bar{V}_w}{R_n ((N+1)\bar{V}_g - \bar{V}_h) + (\bar{V}_h - \bar{V}_g)} \right] n_{w,i} \bar{V}_h \quad (11)$$

$$\Delta V_g = V_{tot} - V_{g,i} + V_h \left(\frac{\bar{V}_g}{\bar{V}_h} - 1 \right) \quad (12)$$

$$\Delta V_w = N \frac{\bar{V}_w}{\bar{V}_h} V_h - V_{w,i} \quad (13)$$

Equations (12) and (13) show that the total phase volume transported into the box, $\Delta V_w + \Delta V_g$, is governed by Eq. (10) regardless of having an excess water or excess methane case.

Figure 3c shows a special case where the final state of the system is having hydrate only. This happens only if

$$\frac{n_{w,i} + \Delta n_w}{n_{g,i} + \Delta n_g} = N \quad (14)$$

Combining Eqs. (3) and (14) gives $\Delta n_g = \Delta n_{g,stoich}$, required for the special case to happen, as:

$$\Delta n_{g,stoich} = \frac{V_{tot}}{\bar{V}_h} - n_{g,i} \quad (15)$$

Equations (14) and (15) give:

$$\Delta n_{w,stoich} = N \frac{V_{tot}}{\bar{V}_h} - n_{w,i} \quad (16)$$

Equations (15) and (16) show that the value of R_n for this special case, i.e. $R_{n,stoich} = \Delta n_{g,stoich} / (\Delta n_{g,stoich} + \Delta n_{w,stoich})$, depends on the initial state, $n_{g,i}$ and $n_{w,i}$. For a given initial phase content, $R_n < R_{n,stoich}$ represents an excess aqueous phase case while $R_n > R_{n,stoich}$ shows an excess gas case.

Based on the formulations above and assuming V_{tot} is fixed, two independent parameters exist. For example, one choice of independent parameters is $n_{g,i}$ and Δn_g , from which a final V_h and $V_{g,f}$ (or V_h and $V_{w,f}$ depending on values of independent parameters) is obtained. Another choice is $n_{g,i}$ and V_h from which Δn_g and Δn_w and thus R_n is obtained.

We now write the box model in terms of phase saturations in a volume of sediment. To do so, one pore volume of the sediment (porosity times total sediment volume) can be considered as the open box in the model. Dividing the preceding expressions by V_{tot} (=1 pore volume), $V_{g,i}$, $V_{g,f}$, $V_{w,i}$, $V_{w,f}$ and V_h are replaced by phase saturations, $S_{g,i}$, $S_{g,f}$, $S_{w,i}$, $S_{w,f}$ and S_h , respectively. Similarly, the transported phase volumes ΔV_w and ΔV_g are replaced by dimensionless volumes, $\Delta V_{w,d}$ and $\Delta V_{g,d}$. For instance, Eq. (10) can be extended to calculate the total pore volumes of gas and aqueous phase transported into a sediment as a function of hydrate saturation, as in Eq. (17).

$$\Delta V_{g,d} + \Delta V_{w,d} = K_{trans} S_h \quad (17)$$

We define R_v as a volumetric version of R_n , convenient for calculations in sediments, as $R_v = \Delta V_g / (\Delta V_g + \Delta V_w) = \Delta n_g \bar{V}_g / (\Delta n_g \bar{V}_g + \Delta n_w \bar{V}_w)$. It can be shown that R_v and R_n are related as:

$$R_v = \frac{R_n \bar{V}_g}{R_n (\bar{V}_g - \bar{V}_w) + \bar{V}_w} \quad (18)$$

When the model is applied to gas accumulations in sediment, two independent parameters are constrained accordingly. For example, one constrained parameter is the initial gas saturation inside the sediment, $S_{g,i}$. However, constraining ΔV_g (or R_v) requires more study. Here we treat R_v as a free parameter and examine how system behavior changes with R_v . An alternative is to consider $S_{g,i}$ and S_h as constrained parameters and determine R_v (or ΔV_g and ΔV_w).

Combining Eqs. (7) and (18) and replacing volumes with saturations, gives the final hydrate saturation for the excess water case as a function of R_v and initial gas saturation, $S_{g,i}$, as:

$$S_h = \frac{\bar{V}_h}{R_v (\bar{V}_h - \bar{V}_g - N \bar{V}_w) + \bar{V}_g} S_{g,i} \quad (19)$$

Similarly, for the excess methane case Eq. (20) holds.

$$S_h = \frac{\bar{V}_h}{R_v (-\bar{V}_h + \bar{V}_g + N \bar{V}_w) + \bar{V}_h - \bar{V}_g} (1 - S_{g,i}) \quad (20)$$

Figure 4 shows the corresponding curves for a set of values for initial gas/water saturation within a control volume of sediment. Temperature and pressure were assumed $T = 2 \text{ }^\circ\text{C}$ and $P = 6.5 \text{ MPa}$ (averaged temperature and averaged hydrostatic pressure over depth along the hydrate-bearing interval in the Mount Elbert well). In fact, the change in gas density due to change in pressure, with depth along the hydrate-bearing interval, is less than 5%; therefore, for simplicity the density of gas phase was assumed constant and corresponding to the averaged temperature and pressure. Using Peng-Robinson equation of state, methane density was calculated to be 55 kg/m^3 . Density of aqueous and hydrate phases were taken as 1000 kg/m^3 and 914 kg/m^3 (Sloan, 1998), respectively. Each curve in Fig. 4 passes through $S_h = 1$ when $R_v = R_{v,stoich}$. Regardless of the initial phase saturations, for values of $R_v < R_{v,stoich}$ the final state has only hydrate and water phases present (excess water) and for $R_v > R_{v,stoich}$ the final state has hydrate and gas phases only (excess gas).

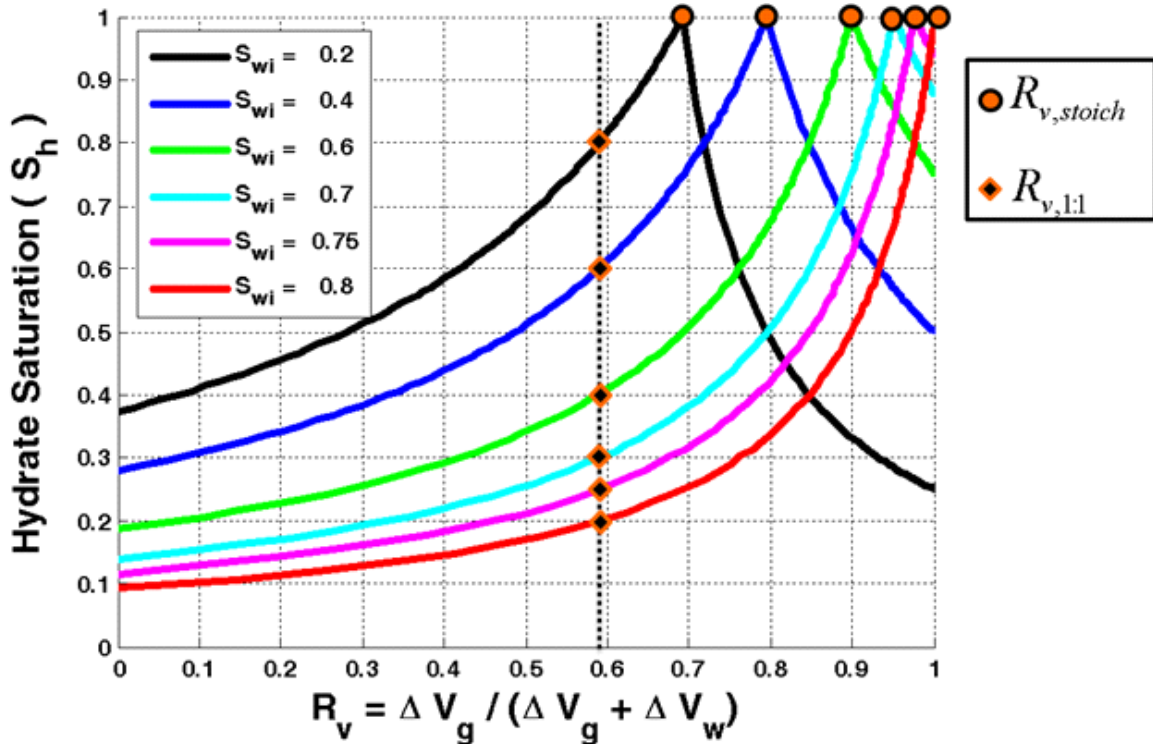


Fig. 4. Final hydrate saturation in an open volume of sediment at $2 \text{ }^\circ\text{C}$, 6.5 MPa depends strongly on initial water saturation and R_v . Special points at which S_h is the maximum possible value are shown as $R_{v,stoich}$ on the curves. To the left of $R_{v,stoich}$ the final state consists of hydrate and water; to the right, of hydrate and gas. Neutral points at which $S_h = S_{g,i}$ are shown as $R_{v,1:1}$ on the curves, which is equal to 0.59 at this temperature and pressure.

The value of R_v at which $S_h = S_{g,i}$ is denoted $R_{v,l:l}$, shown as diamonds in Fig. 4. If the final hydrate saturation S_h is larger than initial gas saturation $S_{g,i}$, then the final water saturation $S_{w,f}$ must be less than $S_{w,i}$. In this case the hydrate formation process must have involved drainage (reducing the wetting phase saturation). Conversely, if $S_h < S_{g,i}$, thus $S_{w,f} > S_{w,i}$, then the conversion required imbibition. The value of $R_{v,l:l}$ thus represents a neutral point between imbibition occurring during hydrate formation for $R_v < R_{v,l:l}$ and drainage occurring for $R_v > R_{v,l:l}$. It can be shown that the value of $R_{v,l:l}$ depends only on the phase densities and hydration number, N and is independent of initial saturations:

$$R_{v,l:l} = \frac{\bar{V}_g - \bar{V}_h}{N\bar{V}_w + \bar{V}_g - \bar{V}_h} \quad (21)$$

Gas reservoir Conversion to Hydrate: Bed-Scale Volumetric Considerations

Effect of Volume Change During Hydrate Formation on the Resulting Hydrate Saturation Profile from a Finite Column of Gas in a Homogeneous Sediment Column

The above analysis applies to a box of sediment with known initial gas/water saturation. By treating a sediment interval as a column of many such boxes, a given gas/water saturation distribution along the column and a chosen value for R_v uniquely determine the hydrate saturation profile. Accumulations are considered as a vertical stack of sediment boxes here since the model is 1-D. However, the latter consideration would not be appropriate for 3-D modeling because the box model does not account for lateral variations in sediment properties.

Consider a column of methane gas and water, in which the gaseous phase is no longer connected to original source of charge, established below a seal in a homogeneous sediment. Figure 5a shows gas saturation versus depth when BGHSZ is at the top of the gas column. As the BGHSZ descends, Fig. 5b, the gas and water above BGHSZ achieve the thermodynamic condition suitable for hydrate formation, hydrate forms, and the model of the preceding section applies.

Figure 5b shows the case in which both gaseous (red arrow) and aqueous (blue arrow) phases enter the vacant space created during hydrate formation. The phase volumes that enter depend on $S_{g,i}$ and R_v . The methane that enters is then converted to hydrate. As mentioned above, the gas column is assumed disconnected from the original source of charge; therefore, the transported methane is provided from below the hydrate formation zone within the same column of gas. Consequently, a volume of water ΔV_w^{GWC} imbibes from below the gas column to replace the transported gas. This causes the gas-water contact (GWC) to rise, establishing a residual gas saturation at the base of the accumulation, as shown in Fig. 5c. As the BGHSZ descends and the GWC rises, these two levels will meet at a certain depth and thereafter the BGHSZ enters the residual gas zone below the GWC. When the BGHSZ enters the residual gas zone, R_v is zero during hydrate formation since no gas can flow at residual gas saturation. The continuation of this process as the BGHSZ descends ultimately yields a hydrate profile with large saturations in the upper portion of the column and small saturations below (Fig. 5d). This profile differs qualitatively from the initial gas saturation profile (Fig. 5a) and is a characteristic result of the model.

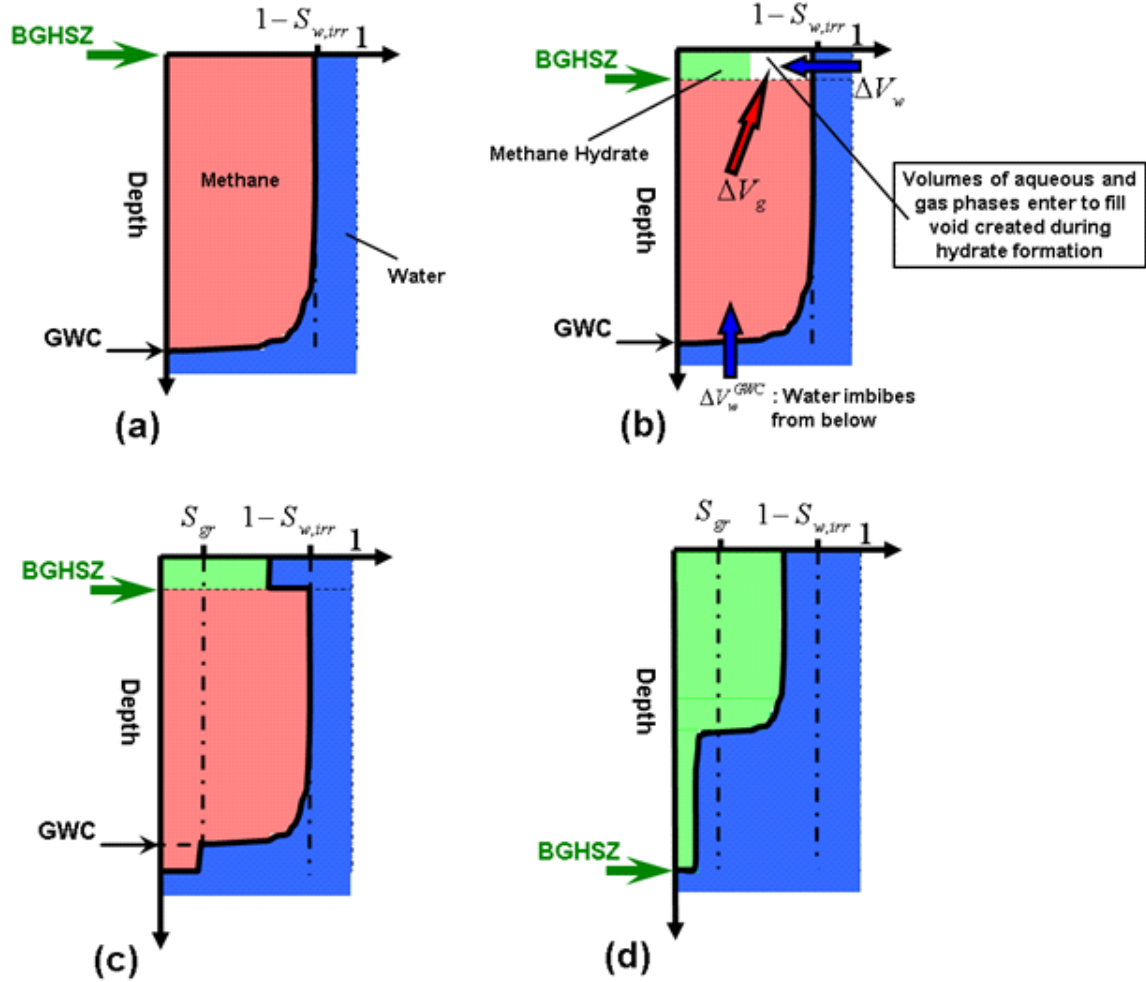


Fig. 5. (a) The initial state of a gas accumulation below a seal in a homogeneous sediment which is below the BGHSZ. (b) After little descent of the BGHSZ. The volume reduction during hydrate formation is shown in white. Gaseous and aqueous phases move into GHSZ to compensate for the volume change. (c) The migrated gas forms more hydrate; the final hydrate saturation in the sediment layer newly located in GHSZ can be estimated from the box model of Figs. 2 and 3 if a value of R_v is assumed. (d) The hydrate saturation profile $S_h(z)$ after the BGHSZ has descended to the lowermost part of the gas column differs significantly from $S_{g,i}(z)$ of (a). This is a consequence of the volume change during hydrate formation in a finite vertical column of gas.

Effect of Heterogeneity (Grain Size Variation along Depth) on Saturation Distribution

In contrast to the homogeneous sediment column shown in Fig. 5, heterogeneity is expected in natural sediments. Grain size variation with depth causes variation in capillary entry pressure along the sediment column.

The reduction in gas-water capillary pressure along the gas column, due to the rise of GWC, will have two implications in heterogeneous sediments. First, the gas phase saturation at each depth decreases, with the amount of decrease depending on the characteristic capillary curve for the sediment at each depth. Second, the capillary pressure at one or more depths may fall below the capillary entry pressure for sediment at that depth. If this occurs the initially single column of gas breaks into two (or more) columns of gas no longer in communication with each other.

Therefore, the capillary entry pressure profile is crucial in our model. Figure 6 illustrates hydrate formation from a pre-established gas accumulation below a seal in a heterogeneous sediment composed of four distinct homogeneous layers (Fig. 6a). The gas accumulation is cooled from the top, i.e. the BGHSZ descends, and consequently converted into hydrate. As the BGHSZ descends, the gas above the BGHSZ as well as some gas migrated from below would form hydrate above the BGHSZ. Similar to that for a homogeneous case, the migrated gas from below is replaced by aqueous phase, resulting in ascent of GWC. The gas-water capillary pressure decreases and intersects the capillary entry pressure at the top of the bottom-most layer and thus the initially single gas column breaks into two non-communicating gas columns: gas columns I and II (Fig. 6b). Therefore, gas column II would not contribute in further hydrate formation within gas column I. When the BGHSZ reaches the top of gas zone II, all the gas above this point is converted into hydrate (Fig. 6c). The final hydrate saturation profile (Fig. 6d), after the BGHSZ has descended to the lowermost part of the gas column, differs significantly from the initial gas saturation profile shown in Fig. 6a. This is a consequence of the volume change during hydrate formation in a finite column of gas, combined with the vertical variation in capillary entry pressure of the host sediment.

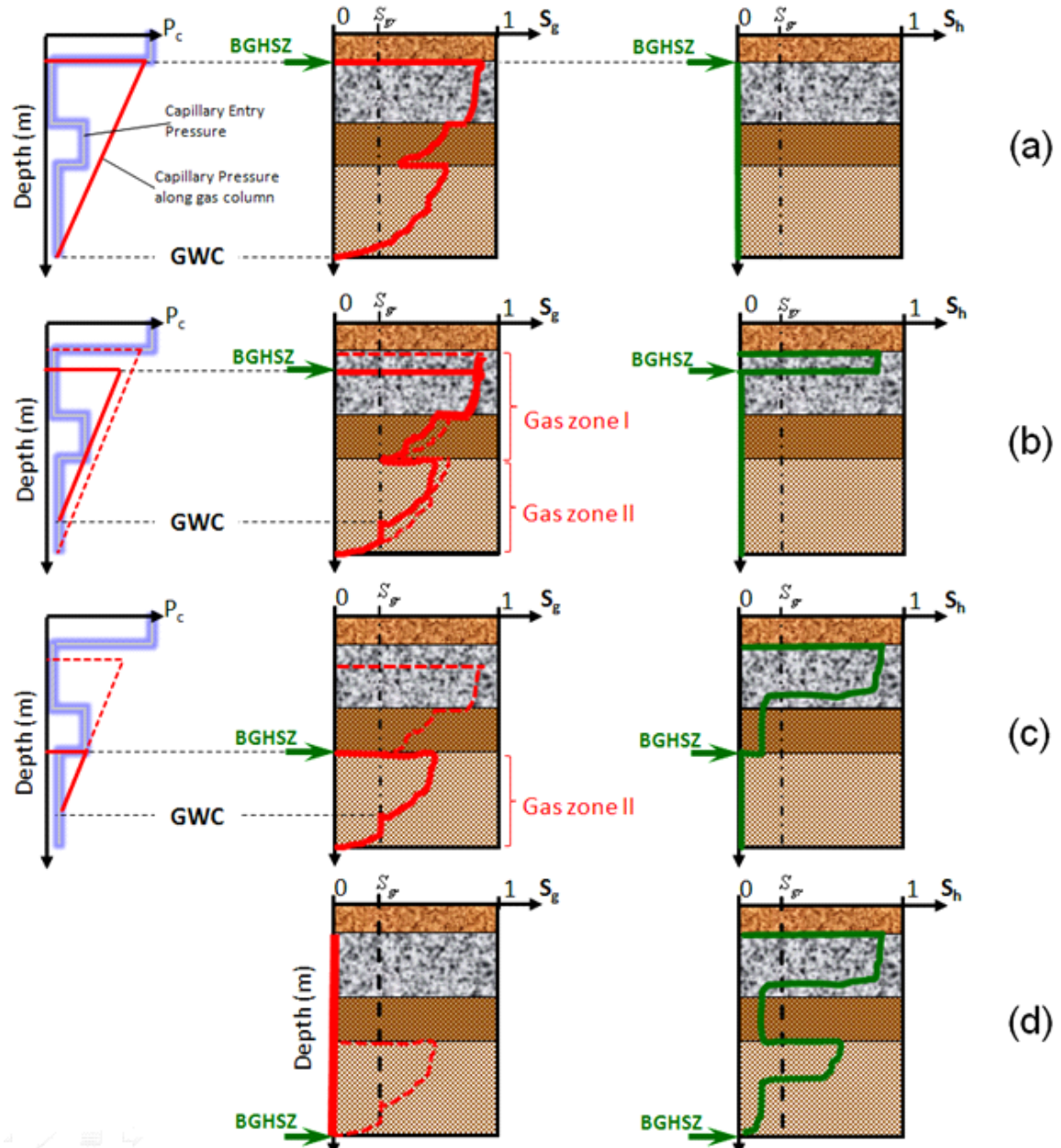


Fig. 6. Hydrate formation from a pre-established gas accumulation in a heterogeneous sediment. The gas accumulation is cooled from the top, i.e. the BGHSZ descends, and consequently converted to hydrate from top to bottom. The left column shows profile of capillary entry pressure versus depth (glowing blue line) as well as profile of capillary pressure along the gas column versus depth (red line). The middle column shows gas saturation versus depth along the sediment, and the right column shows hydrate saturation versus depth. (a) Capillary pressure, gas saturation and hydrate saturation versus depth when the BGHSZ is at the top of the gas column. (b) After little descent of the BGHSZ the gas above the BGHSZ as well as some gas migrated from below would form hydrate above the BGHSZ; the final hydrate saturation in the sediment layer newly located in GHSZ can be estimated from the box model of Figs. 2 and 3 if a value of R_v is assumed. The migrated gas from below is replaced by aqueous phase, resulting in ascent of GWC. The capillary pressure decreases and intersects the capillary entry pressure at the top of the bottom-most layer. Therefore, the gas below this point would not contribute in further hydrate formation above this point. Capillary pressure and gas saturation of the previous step is shown in dashed line. (c) When the BGHSZ reaches the top of gas zone II, all the gas above this point is converted into hydrate. (d) The hydrate

saturation profile $S_h(z)$ after the BGHSZ has descended to the lowermost part of the gas column differs significantly from $S_{g,i}(z)$ of (a).

Measurements of capillary entry pressure are rare, but grain size distributions are often available. Thus we develop a simple relationship between grain size parameters and capillary entry pressure.

The capillary entry pressure for a very well sorted granular media has been related to average grain radius, r_{avg} , as:

$$P_{c,entry} \approx \frac{6\sigma}{r_{avg}} \quad (22)$$

where σ is the interfacial tension between the two fluid phases (i.e. gaseous and aqueous phase). Eq. (22) has been shown both experimentally (Dawe *et al.*, 1992; Mason and Mellor, 1995; Hilpert *et al.*, 2000) and analytically (Mason and Mellor, 1995; Behseresht *et al.*, 2009).

In poorly sorted sediments Eq. (22) is not accurate. However capillary entry pressure is correlated with permeability, which in turn is correlated with grain size distribution. Breyer's equation, Eq. (23), relates hydraulic conductivity, K , to grain size distribution in sandy sediments.

$$K = 6 \times 10^{-4} \frac{\rho g}{\mu} \log\left(\frac{500}{U}\right) D_{10}^2 \quad (23)$$

where g is acceleration due to gravity, μ is the dynamic viscosity of the phase flowing through the sediment, ρ is the mass density of the flowing phase, D_{10} is the 10th percentile of grain size in the sediment and U , the coefficient of grain uniformity, is defined as:

$$U = \frac{D_{60}}{D_{10}} \quad (24)$$

Permeability, k , is related to hydraulic conductivity by:

$$k = K \frac{\mu}{\rho g} \quad (25)$$

Combining Eqs. (23) and (25) gives:

$$k = 6 \times 10^{-4} \log\left(\frac{500}{U}\right) D_{10}^2 \quad (26)$$

Since Eq. (22) works best for very well sorted granular media, we find an “equivalent” grain size, r_{eq} , of a very well sorted sand that has the same permeability as a poorly sorted sediment. The permeability of very well sorted sediments with grain radius, r , is (Bryant *et al.*, 1993):

$$k = 2.7 \times 10^{-3} r^2 \quad (27)$$

Combining Eq. (26) and (27) determines the “equivalent” grain size, r_{eq} :

$$r_{eq} = 0.4714 \sqrt{\log\left(\frac{500}{U}\right) D_{10}} \quad (28)$$

We next assume that the capillary entry pressure of the “equivalent well sorted sand” is a good estimate of the capillary entry pressure for the poorly sorted sediment. That is, Eq. (22) is used with $r_{avg} = r_{eq}$ to calculate the capillary entry pressure of sediment.

Application to Mount Elbert Well

The model was applied to field data from Mount Elbert gas hydrate stratigraphic test well. As discussed earlier, Mount Elbert well indicates two zones of large gas hydrate saturation (the D and C sand Units) in the stratigraphically highest portions of those sands (Boswell *et al.*, 2011). High resolution grain size distribution data are also available from the well (Winters *et al.*, 2011). In addition, as mentioned earlier, researchers have suggested that such hydrate accumulations are free gas accumulations converted to hydrate after being placed in the GHSZ (Boswell *et al.*, 2011; Collett *et al.*, 2011). Therefore, the Mount Elbert data should be a good test of the proposed model.

Analyzing the grain size distribution in different depths of Mount Elbert well data (Winters *et al.*, 2011) reveals that the coefficient of uniformity for majority of depths fall in the range of $1 < U < 20$. In addition, the grain sizes mostly fall between 60 μ m and 600 μ m. Therefore, the Breyer’s estimate of permeability should be applicable (Odong, 2008). Interfacial tension between gas and aqueous phases was estimated to be 65 mN/m at 2 °C and 6.4 MPa (Jho *et al.*, 1978). Brine salinity in Mount Elbert well is very small, 4 to 11 ppt, (Torres *et al.*, 2011) and thus has a density very close to that of fresh water, 1000 kg/m³. Based on these properties and Eq. (28), the capillary entry pressure versus depth was calculated from grain size distribution at each depth. Profiles of the 10th and 50th percentile of grain size in sand Units D and C are shown in Fig. 1a. The corresponding capillary entry pressure profile is shown as connected dots in Fig. 7a.

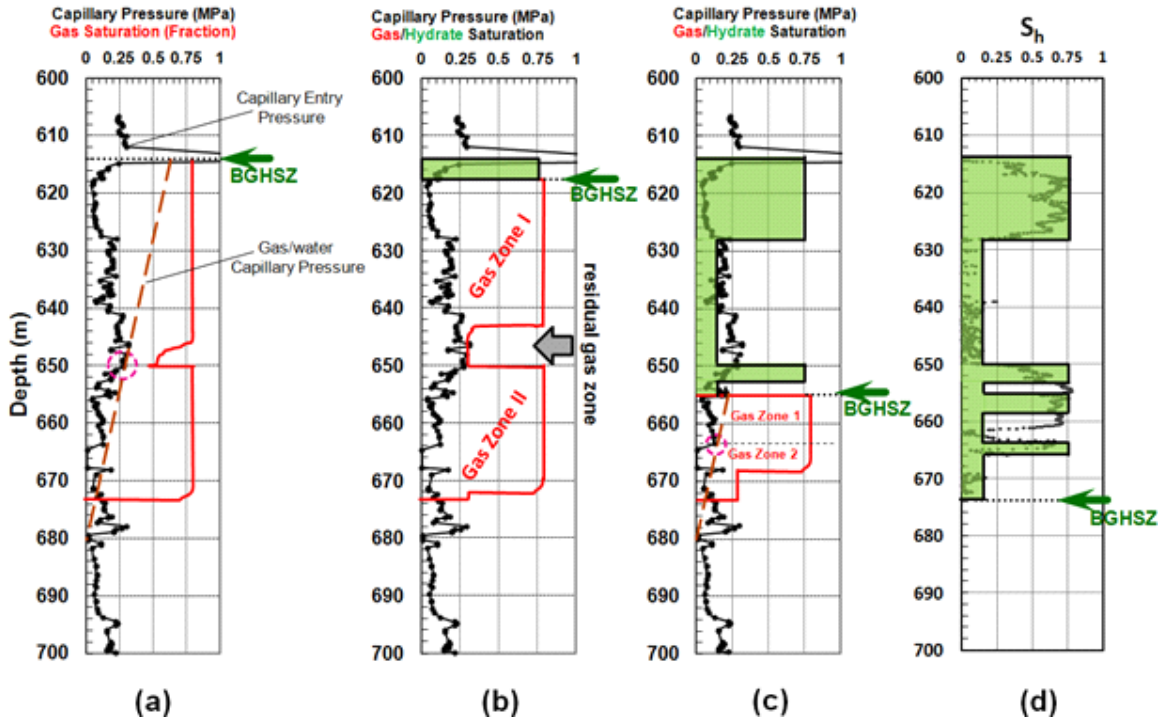


Fig. 7. (a) Capillary entry pressure, estimated from grain size distribution and Eqs. (22) through (28), versus depth (connected dots) along with estimated initial gas saturation (red solid line) when the BGHSZ was above the zone in which hydrate is currently present. Gas/water capillary pressure along the gas column is shown as dashed line. The gas saturation profile changes as the BGHSZ moves down through the gas column and hydrate forms. (b) The BGHSZ has moved 3.5 meters downward. Gas transported from the lower portion of Unit D and water imbibed from below to create gas zone I. Gas zones I and II are no longer in communication due to the capillary barrier between them (shown with a hollow circle) at 650 m. (c) Gas saturation profile (red) when BGHSZ has moved downward through the gas column to a depth of 655m and the resulting hydrate saturation (green fill). Indicated gas zones 1 and 2 are no longer communicating due to the capillary barrier (shown with a hollow circle) at 664 m. (d) Final hydrate saturation profile (using $R_v = 0.55$) after BGHSZ has moved below the bottom of gas column. The log derived hydrate saturations (Lee and Collett, 2011) are shown as dots.

We assume that the gas accumulated in the depth interval between 614 m and 673 m (i.e. within sand Units D and C) prior to the descent of BGHSZ. The estimated capillary entry pressure at depth 614m (Fig. 7a) indicates that such long free gas column could be maintained by the sealing lithology at this depth. Structural traps would have also augmented such conventional gas traps as Boswell *et al.* (2011) describe the accumulations in Mount Elbert well to be trapped by at least one western bounding fault and a four-way fold closure. It is also assumed that the accumulation was no longer connected to the source of charge. Figure 7a shows the estimated gas saturation profile (red solid line) in the gas reservoir prior to its conversion to hydrate. The profile is obtained from the capillarity characteristics of the host sediment and the presumed depth of the original GWC. The latter determines $P_c(z)$ the gas-water capillary pressure profile (dashed line in Fig. 7a), which in combination with the estimated capillary entry pressure determines the initial profile of S_g , similar to that explained in Fig. 2. For most of the gas column, gas saturation was estimated to be very large, close to $1 - S_{w,irr}$; which was then approximated by $1 - S_{w,irr}$ for simplicity. The smaller gas saturations between 646 m and 650 m are due to the fact that the capillary pressure is only slightly larger than the capillary entry

pressure in that interval. The irreducible water saturation, $S_{w,irr}$, is assumed to be 20% for the entire column (Behseresht *et al.*, 2009). Imbibition, i.e. aqueous phase displacing gas phase, does occur when hydrate begins to form, forcing gas phase to move upward to the hydrate stability zone. The residual gas saturation at the end of the imbibition, S_{gr} , is assumed to be 30% (Peng *et al.*, 2009).

This long column of gas was supported beneath the clay-rich layer observed at depth of 614 m in Fig. 7a. In the initial state the gas column is barely connected because the capillary pressure is very close to the capillary entry pressure value at the base of Unit D (depth 650 m, indicated with a hollow circle).

The final input for the model is the value of R_v . For this illustration we set $R_v = 0.55$ throughout the sediment. As described below this value makes physical sense and also gives a good match of observed hydrate saturation in Mount Elbert well. The effect of different values of R_v will be discussed in a later section.

As the BGHSZ moves downward into the gas column the GWC rises, the gas-water capillary pressure is reduced along the gas column, and the gas saturation decreases to residual saturation below the new position of the GWC. Crucially, the gas-water capillary pressure falls below the capillary entry pressure of the sediment at 650 m. Because the initial capillary pressure at 650 m is so close to the capillary entry pressure, this happens with the first increment of hydrate formation. Therefore, the originally connected gas column starts acting as two non-communicating columns of gas almost immediately after hydrate starts forming. Thus gas that migrates to the GHSZ in Unit D comes only from within Unit D itself. Fig. 7b shows an intermediate step when the BGHSZ is at a depth of about 618 m. Note that gas moving to fill the void due to hydrate formation now rises from the bottom of the upper portion of the accumulation, establishing a residual gas saturation between 644 m and 650 m. Water must imbibe into the base of Unit D to replace the migrated gas in this 1-D model.

Figure 7c illustrates the situation after the BGHSZ has descended to a depth of about 655 m. In addition to the initial gas saturation between 650 m and 655 m, some gas from the lower portion of Unit C has been used to form hydrate in the top section of this unit. For $R_v = 0.55$ the resulting hydrate saturation is 0.75 (cf. Fig. 4). The capillary pressure profile intersects the capillary entry pressure profile at a depth of 665 m. Thus the remaining gas column comprises two disconnected regions labeled gas zone 1 and gas zone 2 (Fig. 7c). As the BGHSZ keeps moving downward water imbibes from below into the lower part of gas zone 1 to compensate for the volume of gas that moves into the top section of gas zone 1 during hydrate formation. Meanwhile, gas zone 2 saturations remain essentially unchanged from their initial profile, because the gas zone 1 was disconnected from gas zone 2 prior to hydrate formation in gas zone 1.

The hydrate saturation profile once the BGHSZ has moved to the bottom of the gas column (a depth of about 673m) is shown in Fig. 7d. Our prediction is shown as green area and the log-derived hydrate saturations are shown as dots. In the imbibed portions of the gas zones (e.g. 629 m to 650 m in Unit D), R_v is zero; therefore, when the BGHSZ descends into these portions, only aqueous phase moves to fill the void space that accompanies hydrate formation. For $S_{gr} = 0.3$, Fig. 4 (curve for $S_{w,i} = 0.7$ evaluated at $R_v = 0$) yields a hydrate saturation $S_h = 0.13$. Thus the model predicts large hydrate saturations of 0.75 in the upper portions of Units C and D, and small hydrate saturations of 0.13 in the lower portions.

Comparing the Model Prediction with Log-Derived Observations

In Unit C in Mount Elbert well the zone of major hydrate saturation, which is located at the top of the formation, shows a considerably lower reservoir quality than that of the bottom adjacent part of the formation, bearing little or no hydrate saturation. The situation is similar in Unit D. A gradual decrease in reservoir quality but an abrupt reduction in S_h is observed in Unit D at around 629m. Though a small reduction in porosity or a small increase in shale content can lead to a significant reduction in permeability (Winters *et al.*, 2011), nevertheless Boswell *et al.* (2011) consider the lower portion of Unit D (below 629m) to possess sufficient quality to have held free gas. Furthermore, although the estimated capillary entry pressure values in the lower part of Unit D are significantly larger than those in the upper, above 629m, part of the unit (Fig. 7a) they are still smaller than the gas-water capillary pressure along the gas column. Therefore, major part of the lower D Unit seems to have small enough pore entry pressures to hold large free gas saturations, yet contains much less hydrate compared to that in the upper D Unit (Fig. 1).

The model predicts a uniform, small saturation of about 13% hydrate in the depth ranges of 628-650 and 666-674 meters. The prediction is consistent with observations. The log-derived hydrate saturation is small or zero in the same intervals, while pore fluid geochemical analysis based on dissolved chloride (Torres *et al.*, 2011) indicated the persistence of small values (10%-20%) of hydrate saturations in these depth ranges. The difference in hydrate saturation estimated from log interpretations and from geochemical analysis is attributed by Torres *et al.* (2011) to the effect of host sediment on parameterization of the saturation estimates. Lee and Collett (2011) argue that geochemically estimated hydrate saturations in Mount Elbert well may be quantitatively subject to error, as determining baseline salinity is complicated. Nevertheless, they emphasize that salinity data can certainly be used as a qualitative indicator of the presence of hydrates (Lee and Collett, 2011).

Assuming $R_v = 0.55$ yields a very good match with the log-derived hydrate saturation profile in Unit D. The model correctly predicts the break in hydrate saturation within Unit C at 663 m, but underestimates the thickness of the large hydrate saturation portion in Unit C between 650 m and 660 m. The mass of methane in the hydrate exceeds the mass of methane assumed in the initial gas accumulation in Unit C (Fig. 7a). As discussed in Section 4.4, increasing the initial gas charge does not change the predicted profile in Unit C. Thus it appears that more gas migrated into Unit C during hydrate conversion. One possibility is that the gas charge resumed as the BGHSZ descended, perhaps triggered by the large-scale fluid migration induced by hydrate formation. Another possible factor is the wider lateral extent of Unit C hydrate compared to Unit D. This could have enabled along-dip gas flow to contribute gas to the hydrate-bearing interval in Unit C but not in Unit D. This contribution is neglected in the 1D model, which thus provides a lower bound on the hydrate thickness.

Effect of R_v on Hydrate Saturation Profile

The model presented here imposes no a priori constraint on the value of R_v in the upper portions of Units C and D. It is of interest then to examine the effect of this parameter on the results. The value of $R_{v,stoich}$ for the Mount Elbert well case, with $S_{g,i} \approx 0.8$, is about 0.69 (see Fig. 4); therefore, for $R_v > 0.69$ the final state will be hydrate and gas phase only. At Mount Elbert well hydrate and water only are observed, (Lee and Collett, 2011) and thus we should have had $R_v < R_{v,stoich}$. Our model requires the GWC to move upward and gas-water capillary pressure along the gas column to decrease during hydrate formation. A consequence of this

decrease in capillary pressure is that some imbibition must occur throughout the gas zone, i.e. the aqueous phase saturation S_w must increase. In this case the value of R_v must be less than $R_{v,1:1}$ (the ratio at which S_w does not change from its initial value). For temperature and pressure conditions of the depth interval of interest, $R_{v,1:1}$ is about 0.59. This expectation is consistent with the value of $R_v = 0.55$ that gave a good match in Unit D (Fig. 7).

As R_v decreases, less gas enters and the final hydrate saturation decreases (see Fig. 4). Regardless of R_v the model converts the entire initial mass of methane in the gas column into hydrate. Thus, smaller R_v leads to greater thicknesses of hydrate at smaller saturations in the upper portion of each unit and correspondingly thinner intervals in which residual gas has been converted to hydrate. Figure 8 shows the hydrate saturation profile for R_v values of 0 (no gas movement at all), 0.23 and 0.48, along with the log-derived hydrate saturations in Mount Elbert well. Comparison with Fig. 7d suggests that while $R_v = 0.55$ is consistent with hydrate saturation profile in Unit D, R_v may have been smaller, i.e. some value between 0.23 and 0.48 which are shown in Fig. 8, as BGHSZ passed through Unit C. It can be shown that R_v is controlled not only by the relative mobilities of gaseous and aqueous phases and capillarity properties of the host sediment but also by the rate of hydrate formation. Therefore, value of R_v is expected to convey useful information about the multi-phase flow properties of host sediment, as well as the rate of hydrate formation. These issues will be discussed in detail in a future publication.

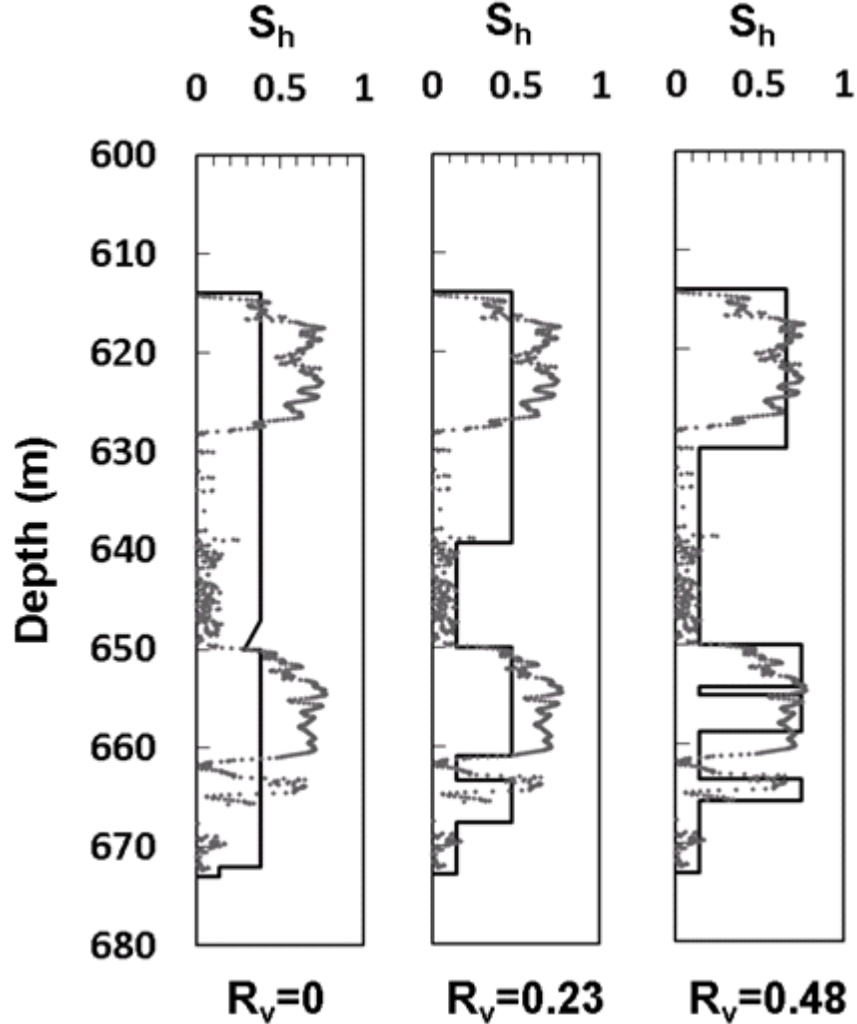


Fig. 8. Estimated hydrate saturation profile for three values of R_v along with log-derived hydrate-saturation data from Mount Elbert well (Lee and Collett, 2011). Note that mentioned values of R_v are used for non-residual gas saturations, forming the major hydrate saturations. For hydrate formation within imbibed intervals, i.e. where the gas saturation has decreased to its residual phase value (e.g. between 630 m and 650 m in the panel for $R_v = 0.48$), no gas flow is possible and $R_v = 0$ is used in those intervals.

Volume of Fluid Transported into the Hydrate-Bearing Zone

The total transported pore volumes of fluid change linearly with the final hydrate saturation, Eq. (10), with a slope of $K_{trans} \approx 1.9$ for the assumed P and T within the depth interval of interest in Mount Elbert well. Eq. (10) shows that the amount of fluid transported into the hydrate-bearing zone is substantial, around 1.4 pore volumes in upper portions of units C and D in Mount Elbert well (Fig. 9). Clearly such volume changes could not be accommodated by compaction of the sediment. In the lower portions of each unit, 0.3 PV of aqueous phase would have moved into the GHSZ to meet the stoichiometric requirement of converting gas to hydrate. In addition, 0.5 PV of aqueous phase, the difference between $S_{g,i}$ and S_{gr} ($\Delta V_{w,d}^{GWC}$ shown in dark blue in Fig. 9) had to enter to replace the gas transported from the imbibed zones (lower

portion of each disconnected gas sub-column). We will report in future on mechanisms by which this fluid movement could have occurred. We will show that capillary dominated, rather than pressure-driven viscous dominated, flow, is key to the required phase flow for converting a free gas accumulation, with large initial gas saturation, to large hydrate-saturation accumulations. This would also have useful implications in determining the time-scale over which such hydrate accumulations are formed. The magnitude of fluid phase transported is also important in hydrate-dissociation studies, e.g. when the BGHSZ rises through an existing hydrate accumulation, and pressure build-up evaluation when hydrate dissociates, because the same volume of fluid must be exported from the sediment.

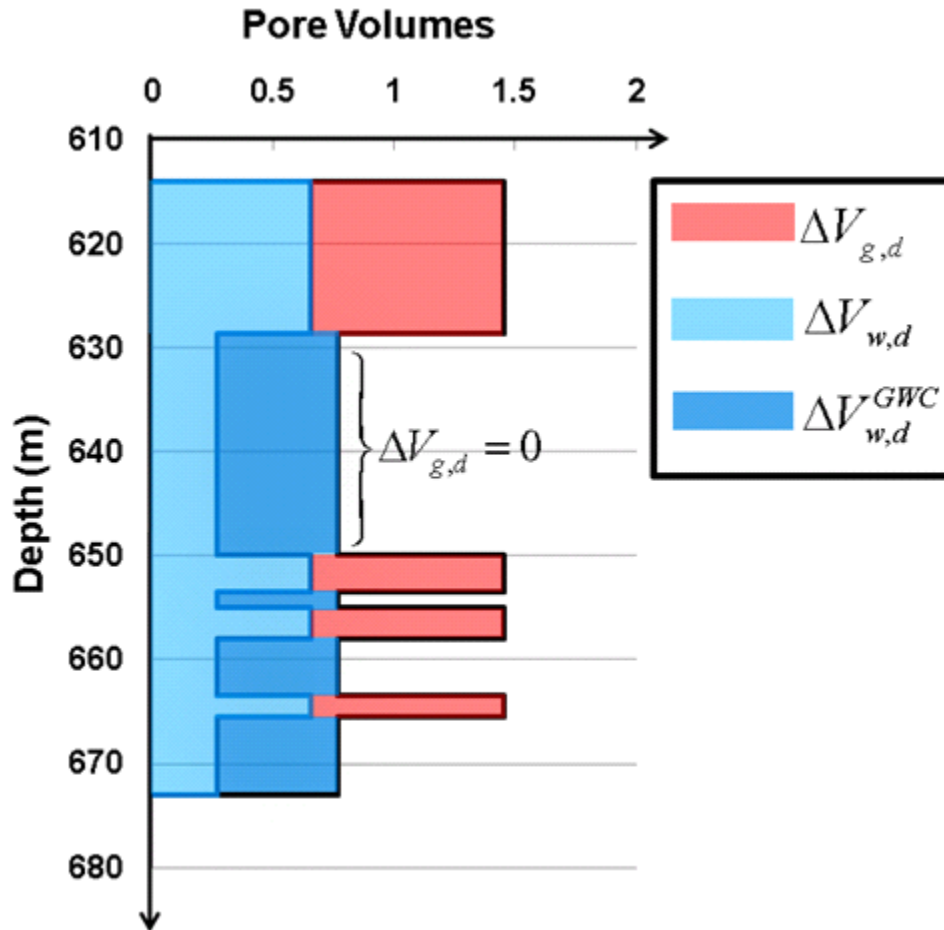


Fig. 9. The model predicts that considerable volumes of fluid (red: gas phase to GHSZ from deeper in the gas column; dark blue: aqueous phase to replace migrated gas; light blue: aqueous phase into GHSZ) have been transported during hydrate formation in Mount Elbert well. The upper portion of each unit accommodated a total of 1.4 pore volumes of gas and aqueous phases. This volume is in addition to the one pore volume initially filled with aqueous and gas phase.

Effect of the Extent of Initial Gas Charge on Modern Hydrate Saturation Distribution

We now consider two other initial gas saturation profiles: a) a partial charge that resulted in slightly thinner and consequently noncommunicating gas accumulations in Units D and C (Fig. 10a-1) and b) a greater charge that resulted in an initially continuous gas accumulation spanning Units D and C beyond the modern hydrate-bearing interval (Fig. 10b-1).

Figure 10a-1 shows the initial gas saturation profiles within Units C and D. The column height above the GWC at 668 m in Unit C does not provide enough capillary pressure to breach the seal at the base of Unit D. Thus the gas accumulations in zones I and II are noncommunicating. Furthermore, gas only partially fills the Unit D sand because the effective GWC is at the base of Unit D, and the capillary pressure thus does not exceed the capillary entry pressure at 640m. Figure 10a-2 shows the hydrate saturation profile after converting the gas accumulations (Fig. 10a-1) into hydrate. Much less hydrate forms in Unit D since much less gas is initially present. The model fails to predict the zones of minor hydrate saturation above the base of Unit D (between 640 m and 650 m) and between 668m and 673m in Unit C.

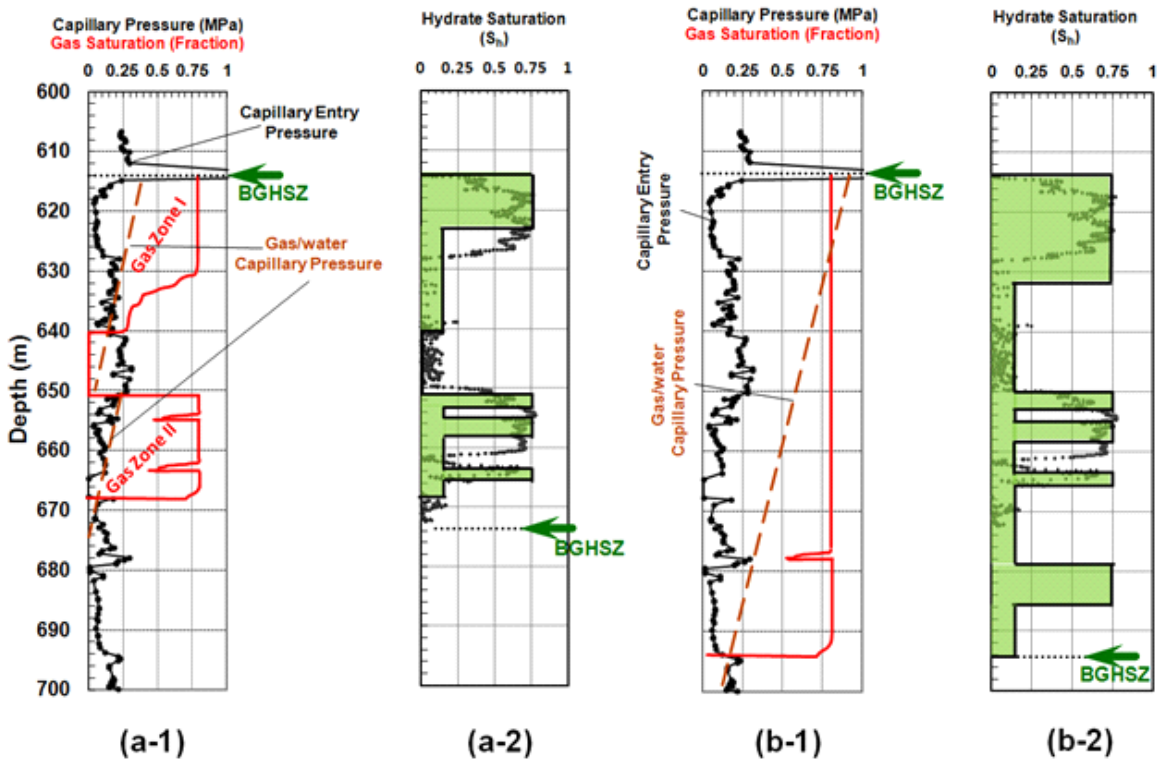


Fig. 10. Effect of initial gas charge on the resulting hydrate saturation profile: (a-1) shows two noncommunicating gas accumulations within the C and D Units of Mount Elbert well; (a-2) is the resulting hydrate accumulation after converting the gas accumulations in (a-1) into hydrate. Note that the hydrate-bearing interval in both Units C and D are underestimated. (b-1) shows a single long gas accumulation spanning through Unit D and part of Unit C when the BGHSZ is at the top of Unit D. In contrast to (a-1), the gas phase is connected between the units. The resulting hydrate accumulation (b-2) after converting this long gas column into hydrate exhibits the same profile in the upper portion of Unit C (650 m to 670 m), indicating initial gas charge has little effect on the behavior. Conversion also yields a large hydrate-bearing interval below 678m which is not observed in the logs. The hydrate-bearing interval in Unit D is overestimated, because the continuous gas column allows a significant amount of gas to migrate from Unit C into Unit D.

Figure 10b-2 shows the hydrate saturation profile after converting a thicker initial column of gas (Fig. 10b-1) for which the GWC is at 694m. In this case the hydrate saturation in Unit D is overestimated, because substantial gas moves into Unit D from Unit C before the two units are disconnected. The predicted profile between 650m and 673m is similar to that shown in Fig. 7d. This is because the gas column below 678 m becomes disconnected from the gas above that

point as the GWC rises. This creates a second effective GWC at 678 m, and when this secondary GWC rises to 673 m, the gas within Unit D becomes disconnected from that in Unit C just as in Fig. 7. Thus the absence of hydrate in the good quality sand below 665 m in Unit C is not necessarily an indication of insufficient original gas charge. The eventual conversion of the gas below 678 m yields another major hydrate-bearing interval, below 678m, which is not observed in Mount Elbert C Unit (Lee and Collett, 2011) in carefully retrieved cores (Rose *et al.*, 2011).

This analysis shows that the depth interval over which modern hydrate saturation is observed is expected to reflect the depth interval over which the original gas reservoir was established. That is why in the calculation above we tacitly assumed the initial gas column height was controlled by other factors (e.g. insufficient charge, a spill point elsewhere on the structure, the connection with the source simply happened to occur at 673 m, etc.). The proposed model predicts gas hydrate columns with the same length as the original gas column but with a very different shape of saturation profile.

Summary of Influence of Grain Size Variation and Phase Volume Changes on Hydrate Saturation Profiles

A 1-D model was proposed to predict/explain the hydrate saturation profiles in “converted free gas” hydrate reservoirs considering three key elements: (i) volume change during hydrate formation within an existing gas accumulation, (ii) the descent of the base of GHSZ through the accumulation, and (iii) sedimentological variation with depth that causes variation in capillary entry pressure. Applied to a gas accumulation no longer connected to the charge, these elements combine to drive gas migration within the accumulation to the GHSZ. Substantial aqueous phase migration to and through the sediment column to the GHSZ accompanies the gas migration and hydrate formation. This leads to large hydrate saturations in the upper portion of the column and small saturations in the lower portion, even if the lower portion is sand-rich. Internal gas migration raises the gas/water contact, raising the possibility of disconnection of the remaining gas column at layers having relatively large capillary entry pressure. When this occurs, the disconnected subcolumns also yield large and small hydrate saturations in their upper and lower portions, respectively. The hydrate saturation profile resulting from these processes is nonuniform with rather sharp basal contacts, i.e. large S_h values interspersed between small values, even if the initial gas saturation profile is uniform. The nonuniformity cannot be explained via association of major hydrate saturations with better quality sands.

The model was applied on data from Mount Elbert well located in one of the methane hydrate reservoirs in Alaskan North Slope. For a physically reasonable choice of the relative volumes of gas and aqueous phases that enter the hydrate zone, the model predictions match the field data satisfactorily. Of particular note, the model accounts for a twenty-meter interval of small hydrate saturation in fairly sand-rich sediment between two accumulations of large hydrate saturation. It also explains how in Unit C the major methane hydrate accumulation is at the top lower-quality sand but not in the lower better-quality deposit, even if the latter sand is originally charged with gas.

Material balance analysis shows that a considerable amount of fluid (of order 1 pore volume of gaseous and aqueous phases) needs to be transported during hydrate formation. In the 1D model analyzed here, all transport is vertical. This maximizes the influence of sedimentological control on the final hydrate distribution. As the areal extent of the gas accumulation increases or the dip of the structure increases, the contribution of along-dip flow to the required gas transport

increases, and the 1D model yields a lower bound on the thickness of the intervals with large hydrate saturation.

Gas Reservoir Conversion to Hydrate: Role of Pore-Scale Imbibition

The preceding sections have laid out the main physical phenomena that drive the conversion of a gas reservoir into a hydrate-bearing formation. We have assumed that during conversion the gas reservoir is no longer connected to the source of gas charge, and consequently the conversion of gas to hydrate causes the capillary pressure in the gas accumulation to decrease. We are thus led to consider in more detail the fluid phase displacement that must accompany this decrease in capillary pressure.

Viewed from the pore scale, conversion of a gas reservoir to hydrate is an imbibition process. Any reduction in capillary pressure will cause the aqueous phase to imbibe into the gas-saturated portion of the formation. In the gas column below the base of the gas hydrate stability zone, this imbibition behaves classically. That is, the gas saturation decreases, following the characteristic P_c - S_w curve for the sediment, and the gas-water contact at the base of the gas column rises. Imbibition at or within the hydrate stability zone introduces a novel aspect, however: the growth of hydrate at the gas/water interface makes that interface rigid. Because of the mechanical strength associated with the hydrate skin, displacing such an interface would in principle require a pressure difference over and above the capillary pressure needed to displace the geometrically equivalent fluid/fluid interface. We do not explicitly account for this mechanical strength in this work, not least because no measurements are available that would enable estimating its value. Instead, and more fundamentally, we propose in this research that the hydrate skin is likely to act as a permeable membrane, not as an impermeable barrier. Thus the aqueous phase can filter through the skin in response to a reduction in gas phase pressure.

This conceptual model leads to two useful limiting cases. In one limit, we assume water filters through the hydrate skin slowly, or, equivalently, we assume water moves very slowly from some large external source to the gas-hydrate-water interfaces. The slow arrival of water could be because of small permeability of the sediment through which the aqueous phase is transported, or because the driving force (saturation gradient or potential gradient or both) is small. The definition of “slow” is not absolute; the relevant measure is whether the rate of water supply is slow relative to the rate of hydrate formation. If so, then all water arriving at the gas-hydrate-water interface will be immediately incorporated into the hydrate phase, growing into the volume originally occupied by the gas phase.

In the other limiting case we assume that water filters through the hydrate skin rapidly, or equivalently that the rate of water supply is fast compared to the rate of hydrate growth. In this case, the gas/water interface is continually renewed. Thus it is possible for a traditional imbibition event to occur, in which two gas/water interfaces merge and enable gas to withdraw spontaneously from a pore as water fills the pore. Since we assume hydrate grows into the gas phase from a gas/water interface, the water in the newly imbibed pore will not be incorporated into the hydrate phase. Hydrate accumulates at an interface as long as the interface moves only incrementally in response to reductions in capillary pressure.

These two limiting cases should bracket the spectrum of behavior observed in nature. The remainder of this section explores in more detail the implications of this pore-scale perspective on hydrate growth.

Hydrate Formation and Growth in Pore Scale

It has been proved that hydrate formation can take place either from single phase (gas-saturated aqueous phase) or two phases (gaseous and aqueous phases) (Tohidi *et al.*, 2001; Katsuki *et al.*, 2006, 2007; Ohmura *et al.*, 2005; Teng *et al.*, 1995; Shindo *et al.*, 1995). However, forming hydrate from a single phase system is unlikely to obtain a high hydrate saturation, because of the low solubility of methane in aqueous phase (Handa, 1990). Thus for reservoirs in arctic regions where $> 70\%$ hydrate saturation is often observed, a two-phase system is required.

In the porous medium, the first nucleation of hydrate crystal occurs in low energy regions. In a two-phase system, one possible nucleation site is along the interface between gas and water. Later hydrate could possibly grow into either gaseous or aqueous phase. It seems the growth direction is controlled by the availability of gas or water. That is, if gas is limited, hydrate grows into the gaseous phase (Tohidi *et al.*, 2001; Katsuki *et al.*, 2007), while the limitation of water would let hydrate grow into the aqueous phase (Ohmura *et al.*, 2005; Dong Lee *et al.*, 2005). Another possible hydrate nucleation site is on the grain surface (Katsuki *et al.*, 2006). However, the grain surface is either exposed to gas or water, and therefore hydrate formation is restricted due to the lack of the other material.

After the first nucleation, hydrate growth requires the transportation of a material through the hydrate layer (if hydrate grows into gaseous phase, water must migrate through the hydrate layer to the gaseous phase, while growing in the other direction requires gas to migrate through the hydrate layer). Models were proposed to address such mechanism. In these models, micro defects in hydrate are considered as permeable conduits. (Mori and Mochizuki, 1997) suggested that water is able to pass through these conduits due to capillarity. Thus, hydrate formation is able to occur and grow into the gaseous phase. On the other hand, the model proposed by (Hirai *et al.*, 1996) argued that gas molecules can transport through the hydrate layer to the aqueous phase due to diffusion, and thus hydrate is able to grow into gaseous phase. However, the diffusion rate largely limits the hydrate formation rate, and therefore unlikely to capture the physics.

The different experimental observations and model descriptions suggest an on-going scientific debate on the hydrate growth in the porous medium, a reflection of our lack of understanding of the pore-level physics. In this section we examine the implications of the concept that proposed hydrate grows into the gaseous phase, due to the fact that in this work gas is the limiting resource in the reservoir.

This section focuses on pore scale processes. To explain the boundary conditions that will be applied to the pore scale model, we motivate this section with a recapitulation of the bed-scale process. Our field-scale model for the arctic region uses the concept of a petroleum system. Figure 11 shows the conceptual model. The reservoir was originally saturated with water. It was connecting to the deep gas source through faults and fractures. A capillary seal existed on top of the reservoir, and closures were capable of trapping the initial gas in the reservoir (not shown in the figure). BGHSZ originally was above the reservoir at an arbitrary depth. Permafrost extended from the ground surface to a depth that was shallower than BGHSZ. The distance between BGHSZ and the base of permafrost was in the magnitude of several hundred meters, as suggested by (Majorowicz *et al.*, 2008).

Over the geological time, thermogenic gas migrated upwards through these conduits (Fig. 11). Due to the low capillary entry pressure of the sediments and high capillary pressure between gas and water, it is likely that in most parts of the reservoir water was displaced to the irreducible

value (Peng, 2011). Gas slowly accumulated beneath the capillary seal, expanded downwards and finally filled the reservoir. When gas charge was complete, by assumption the communication between the reservoir and the deep gas source was lost. Therefore it became an isolated system for gas. We assume BGHSZ was still above the reservoir during this period, and thus no hydrate formed even though both gas and water were available.

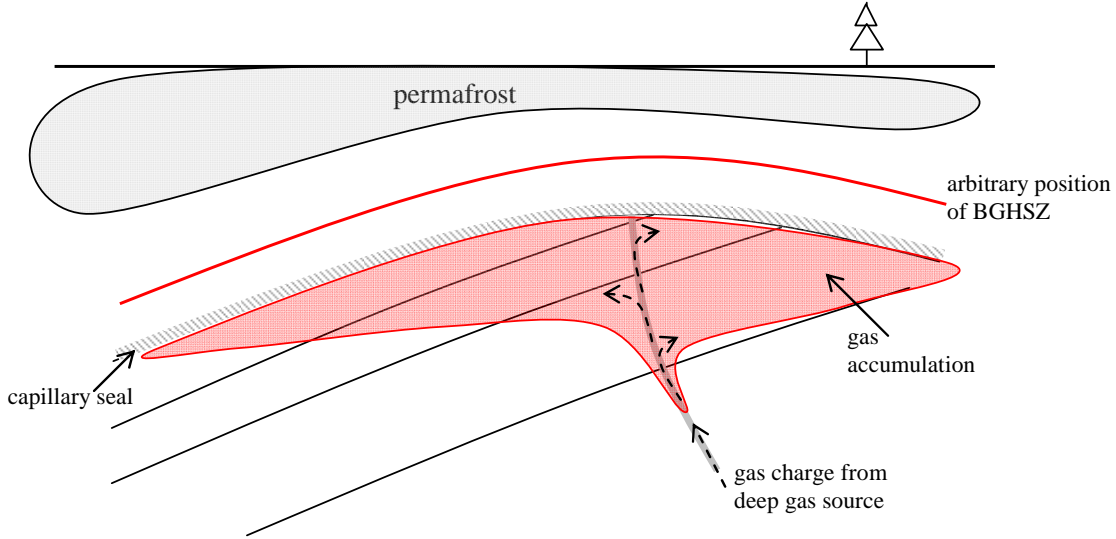


Fig. 11. A schematic of the initial gas charge in the reservoir and the position of permafrost and BGHSZ. Gas is in the red color.

BGHSZ began to descend when gas charge in the reservoir was complete (Fig. 12). In arctic regions, it is a general trend that BGHSZ has been moving downwards in the past several million years (Majorowicz *et al.*, 2008). When BGHSZ entered the reservoir, gas hydrate formed at BGHSZ. Hydrate formation from a two phase system (gas/water) is controlled by microscopic events, which will be investigated in the pore level (Section 2.1). The density of methane molecules in hydrate is computed by the following equation:

$$\rho_{g_hydrate} = \rho_h \frac{M_g}{M_g + NM_w} \quad (29)$$

where $\rho_{g_hydrate}$ is gas molecule density in the clathrate. ρ_h is hydrate density, which is 910 kg/m^3 (Sloan, 2003). M_g and M_w are the molecular weight of gas and water, respectively. N is the hydration number, and in our work it is 5.75. For ideal methane hydrate clathrate Eq. (29) gives $\rho_{g_hydrate} = 122 \text{ kg/m}^3$, which is much larger than the methane density in the reservoirs studied in this work (For example, methane density in Mount Elbert reservoir is $\sim 55 \text{ kg/m}^3$ and in Mallik reservoir is $\sim 90 \text{ kg/m}^3$). This result suggests that in the reservoir condition the volume of hydrate is smaller than the volume of gas converted to form hydrate (we assume water is the unlimited phase whose volume change is not considered). Thus the transportation of free methane and water into the local porous medium is required to fill the vacancy that would otherwise be created. The newly-fed gas and water were converted into gas hydrate, and further sucked in more gas and water from other lower reservoir layers. Such positive feedback continued until no more fluid invasion could occur, at which moment the porous medium was only filled by hydrate and water (the coexistence of hydrate and gas was not observed in either reservoir).

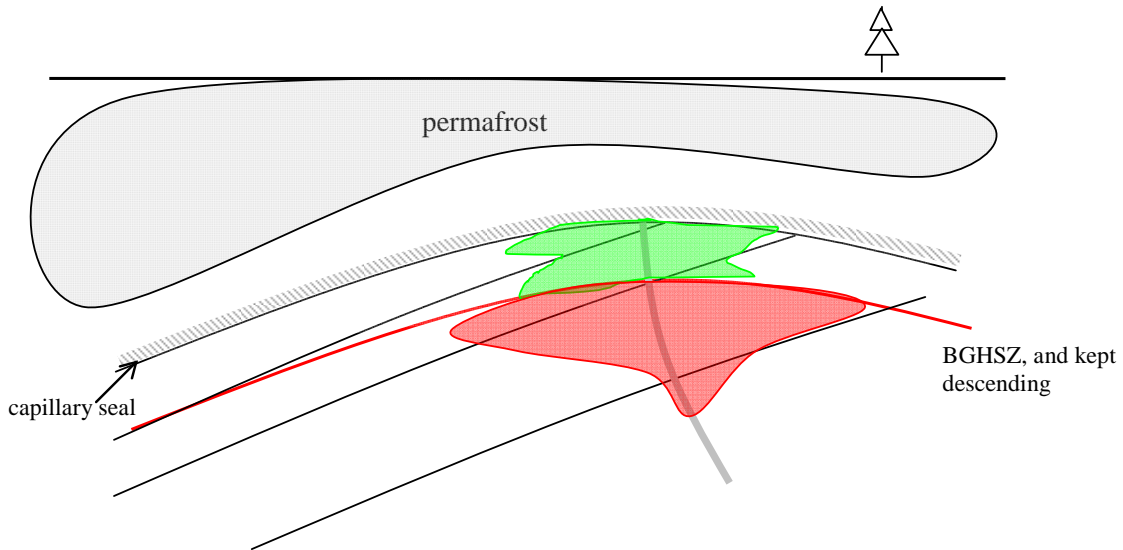


Fig. 12. A schematic of gas and hydrate distribution in the reservoir when BGHSZ was descending. Permafrost also expanded downwards. Gas is in the red color and hydrate is in the green color.

BGHSZ kept descending and converting gas and water into gas hydrate. Hydrate formation was complete when BGHSZ reached the base of the reservoir (the descending of BGHSZ from the top to the base of the reservoir took tens of thousands of years). The final hydrate profile differs from the initial gas/water distribution (Fig. 13). It has a characteristic pattern with two distinct regions of gas hydrate saturation.

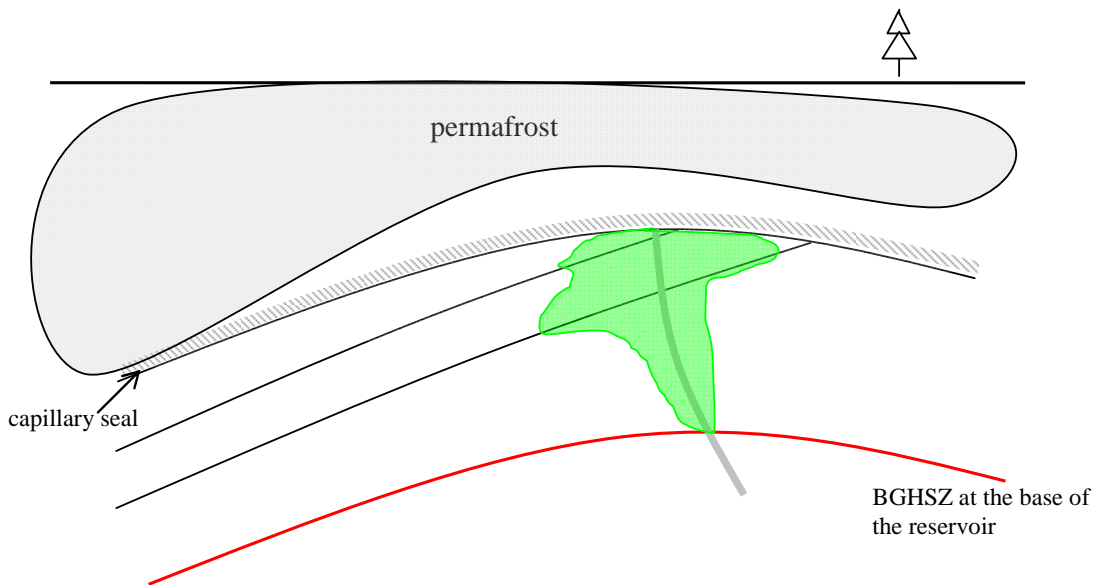


Fig. 13. A schematic of final hydrate distribution in the reservoir when BGHSZ reached the base of the reservoir. Hydrate saturation increases from base to the top of the reservoir. Permafrost expanded further to the deeper depth.

Scenarios of Hydrate Formation and Growth in Porous Medium

The initial gas and water distribution in the porous medium is controlled by drainage endpoint, at which gas displaces water to its irreducible value. We assume hydrate formation and growth follow the pathway of conventional imbibition, and thus a 2D simulation by LSMPQS is applied to show the detailed movement of gas/water interface during imbibitions (and also hydrate growth path). LSMPQS is a fundamental numerical technique that is capable of modeling capillarity-dominated process without any geometry simplification, with its accuracy and correctness widely tested against the experimental results (Prodanović and Bryant, 2006; Prodanović *et al.*, 2008). Two different hydrate formation scenarios are proposed by studying the imbibition process.

The hydrate formation and growth in the porous medium uses several general assumptions:

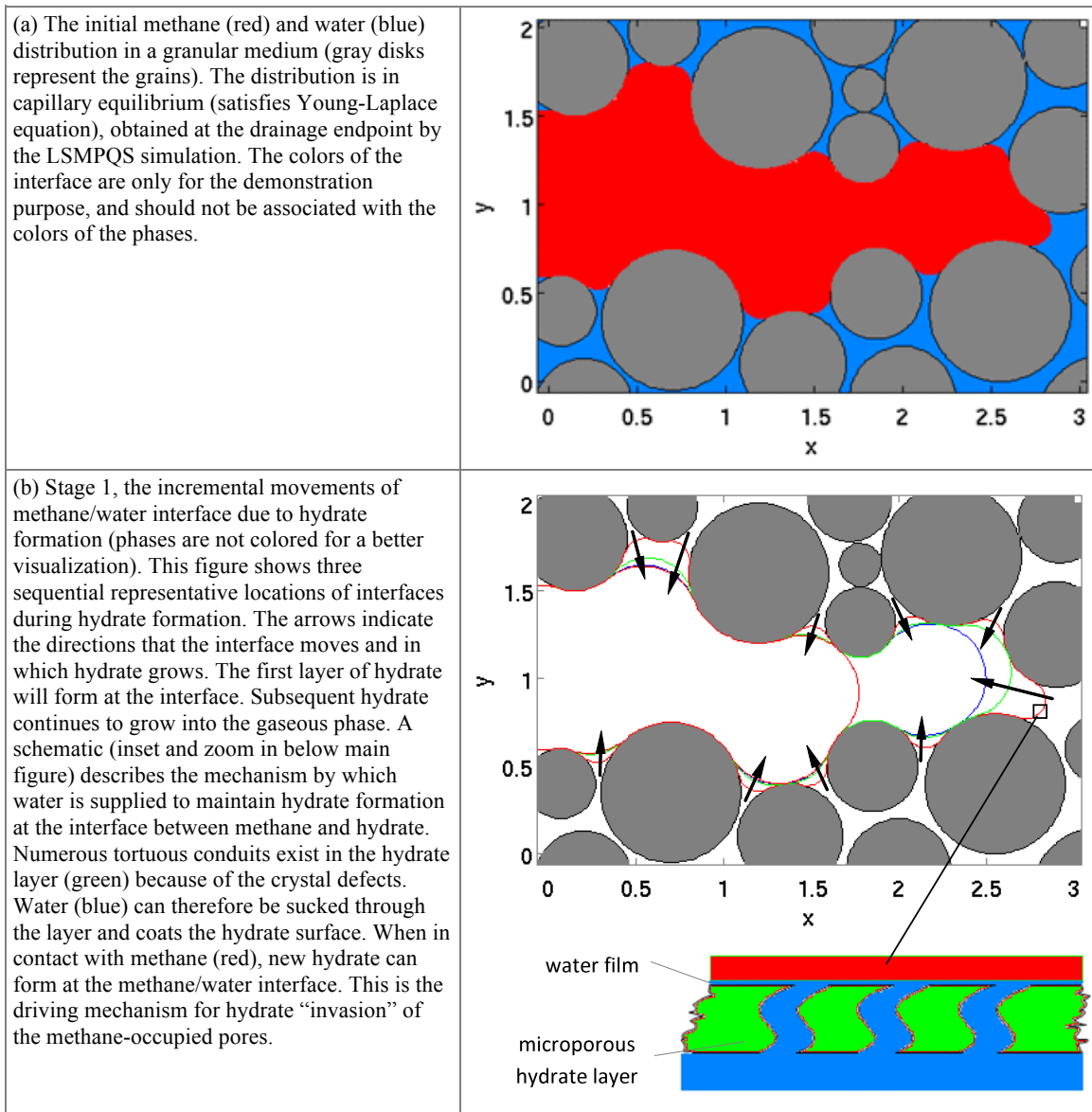
1. The gaseous phase (pure methane) and aqueous phase (water with constant salinity) are at capillary equilibrium, so that gas/water interfaces are static. Our model also assumes both gas and water are connecting to the bulk volume, and thus neither of them would be exhausted (that is, in the pore scale we do not apply the assumption of limiting gas and unlimited water). We consider the case that the salt ion diffusion rate is much higher than hydrate formation rate, and therefore salinity does not inhibit conversion.
2. The first layer of hydrate crystal forms along the interface between methane and water when the local temperature and pressure reach the phase equilibrium boundary (the hydrate-water/gas-water boundary).
3. Forming a layer of hydrate reduces the gaseous phase volume more than the aqueous phase, since volumetrically hydrate formation consumes more methane than water at typical hydrate stability conditions ($P = 5$ to 10 MPa, $T = 273$ to 283 K). Therefore, hydrate preferentially grows into the gaseous phase. In this fashion a layer of hydrate appears between gas and water, and the gas/water interface is replaced by a methane/hydrate interface, a thin hydrate layer, and a hydrate/water interface.
4. Continued growth of hydrate requires water to migrate from the aqueous phase in the sediment through microscopic defects (e.g. crystal defects within the hydrate, grain surface roughness, etc.) to the methane/hydrate interface.
5. The total vacancy (reduction in methane volume + reduction in water volume – increase in hydrate volume) generated when an incremental volume of hydrate forms is filled by aqueous phase. Depending upon the connectivity of the aqueous phase (between the interface where hydrate is forming and the bulk phase of formation water) and, more critically, upon the rate at which water can migrate through the existing hydrate in step (4), the rate of this filling may be faster or slower than the rate of hydrate formation at the interface.

In this model, hydrate saturation varies. If the water supply rate is much smaller than the hydrate formation rate, hydrate saturation will reach a maximum value. On the other hand if the water supply rate is much larger than the hydrate formation rate, hydrate saturation will reach the minimum value. We describe these two limiting scenarios next.

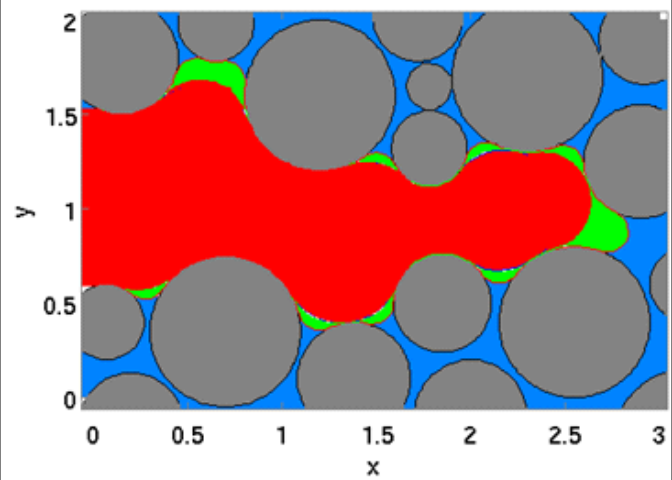
Hydrate Saturation and Distribution in Porous Medium, Scenario A: Water Supply Rate Much Smaller than Hydrate Formation Rate

Figure 14 shows a small 2D domain. It is a simple granular medium with large open spaces. The initial aqueous and gaseous phase distribution (Fig. 14a) is obtained by simulating a

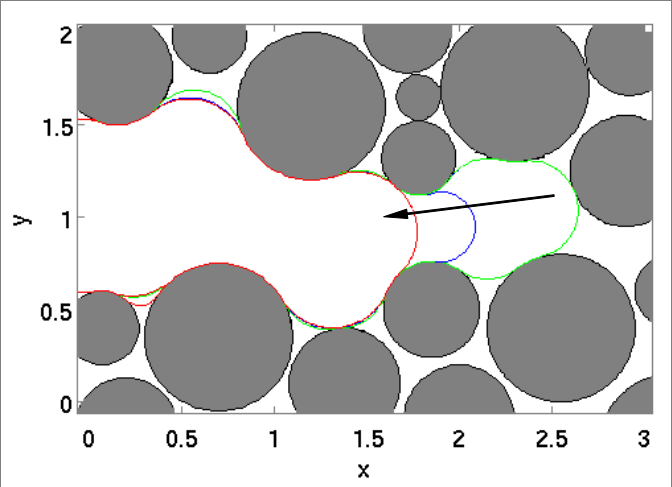
drainage endpoint using LSMPQS. The initial hydrate nucleation happens on gas (red)/water (blue) interface. The hydrate layer does not form as a single crystal. The microscopic defects within the layer of crystals allow water to imbibe through the hydrate layer and form a thin layer of water on the hydrate surface (Fig. 14b the zoom-in figure, notice the thin water layer (blue) on the gaseous phase (green)). Since hydrate formation is rapid compared to water supply, this water layer is quickly converted into hydrate. This further reduces the gaseous phase pressure (Figs. 14b and c) and water again imbibes onto the gas-hydrate interface. During this process, we assume that the curvature of hydrate layer maintains the curvature of capillary-equilibrium between gas and water, and therefore the hydrate invasion into the gaseous phase can be approximated as the imbibition process (the curves are computed by LSMPQS simulation). This stage of the hydrate formation (Figs. 14b and c) is referred to as stage 1.



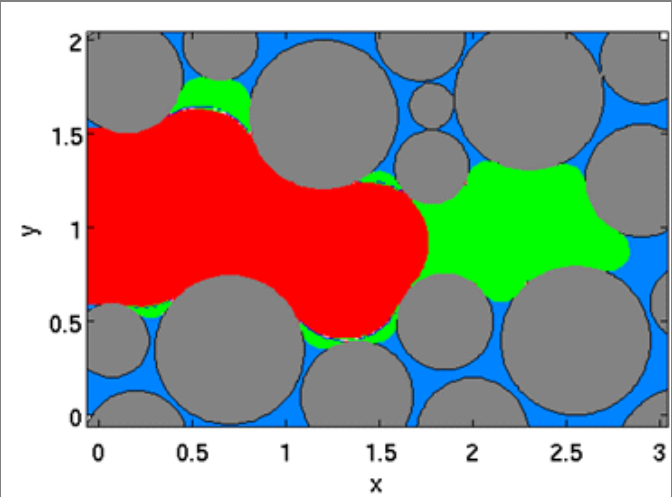
(c) Hydrate distribution (green) when the interface (indicated by the arrow) is at the critical point. From this point, an infinitesimal decrement of capillary pressure will make the interface unstable.



(d) Stage 2, the incremental movement of methane-water interface (from green to red interfaces; phases are not shown). The red curve is the capillary-equilibrium curve after an imbibition jump from the position indicated by the green curve, computed as if aqueous phase were displacing gas. Because the scenario considered here assumes that water can be supplied only very slowly, the Melrose jump cannot occur. Instead gradual incremental movement from green to red curves (blue curve is an example intermediate position) happens during this stage. The rapid formation of hydrate means that similar to B, hydrate grows from the water film on the methane/hydrate interface and gradually invades the gaseous phase.



(e) Hydrate distribution (green region) after stage 2. The total hydrate distribution is due to the hydrate formations in stages 1 and 2. Hydrate occupies the entire space that was taken up by methane before. That is, hydrate distribution replaces the initial methane gas distribution.



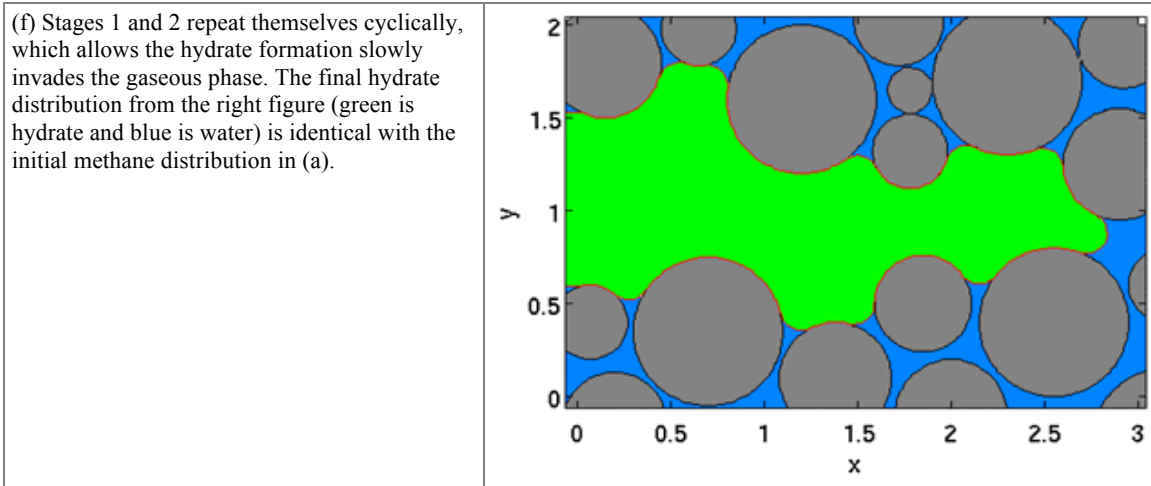


Fig. 14. Schematics of Scenario A that water supply rate is much smaller than hydrate formation rate, which gives the maximum hydrate saturation. The gray disks are sand grains, blue regions correspond to the aqueous phase, green region is hydrate, and the red region is gas phase.

The critical feature of this limiting case is that the gas/hydrate interfaces will gradually advance into the gas phase, so that adjacent interfaces eventually merge. This also means that separated gas/water interfaces merge as well, as water always coats the hydrate surface (Fig. 14b the zoom-in figure) because of capillarity. In classical imbibition, the interface will jump to a new location. This is the Melrose condition for imbibing a pore. However when two gas/hydrate interfaces (also gas/water interfaces) merge, a spontaneous Melrose imbibition event is not possible, because the fluid (water) is converted to a solid (hydrate) as soon as it reaches the gas/hydrate interface, and thus no extra water is available for the imbibition jump. In other words, the limiting water supply disables imbibition events, and only the slow and incremental movement of interface is allowed (Figs. 14d and e). This increment movement gives a similar pattern as of Figs. 14b and c. That is, water is sucked through the hydrate layer and coats the hydrate surface as a thin layer, of which the water is later converted into hydrate. This gradual movement of hydrate finally allows the interface to move into the following pores. We refer to this (Figs. 14d and e) as stage 2.

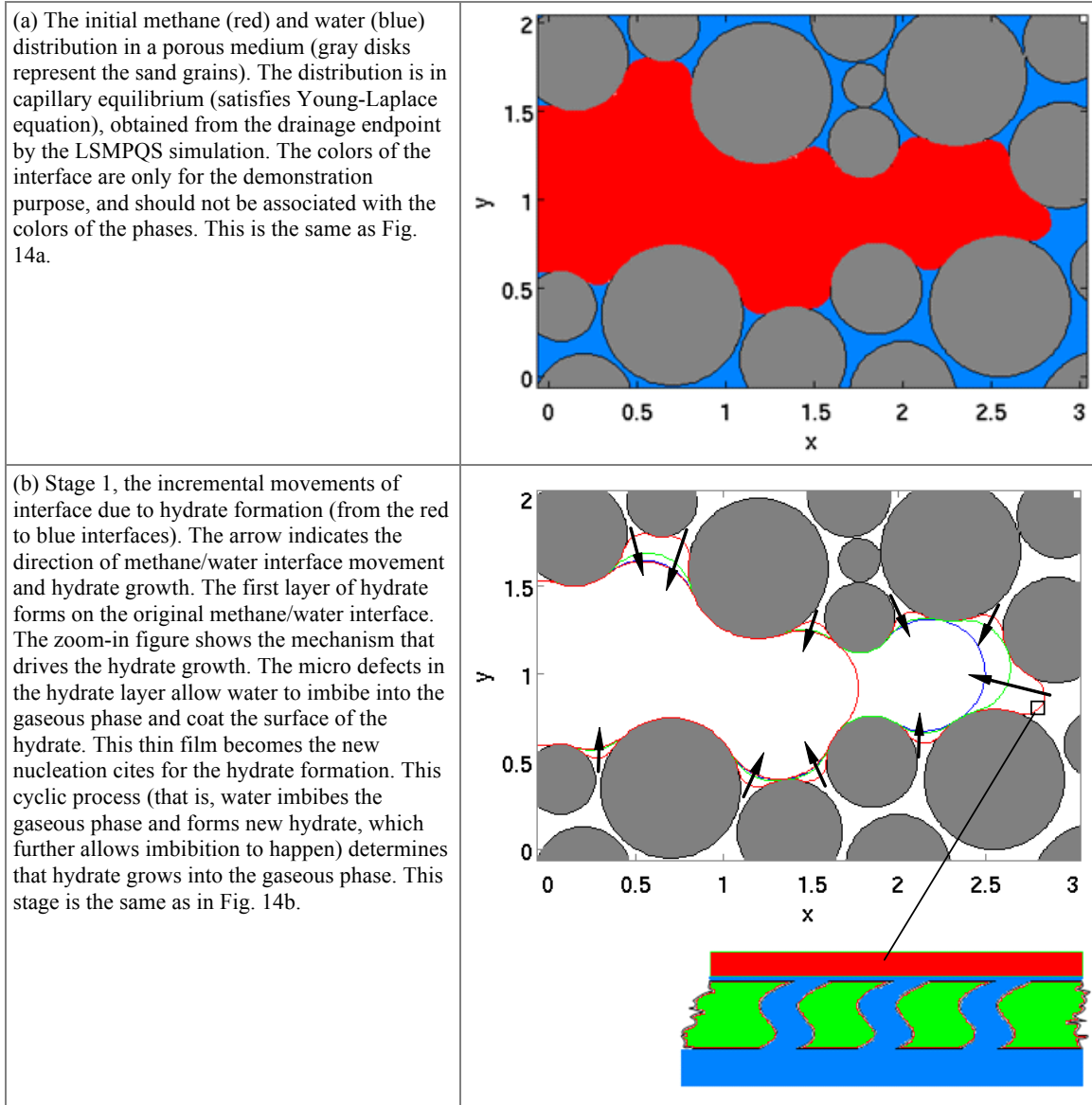
This incremental motion has an important implication: all the gas phase initially present is eventually converted to hydrate, and extra gas from other layers is required for the hydrate formation since the initial gas is insufficient. The final hydrate saturation has the same pore-scale “footprint” (occupies the same pores, throats, etc.) as the initial gas saturation (Fig. 14f), and it is the maximum value that can be predicted by this model.

These two stages have the same behavior but driven by different forces. Stage 1 is controlled by the capillary equilibrium, which is independent of the water supply rate. Stage 2, which would exhibit an imbibition jump if both phases at the interface were fluids, happens only because the water supply rate is slower than hydrate formation rate on the methane/hydrate interface. These two stages happen cyclically.

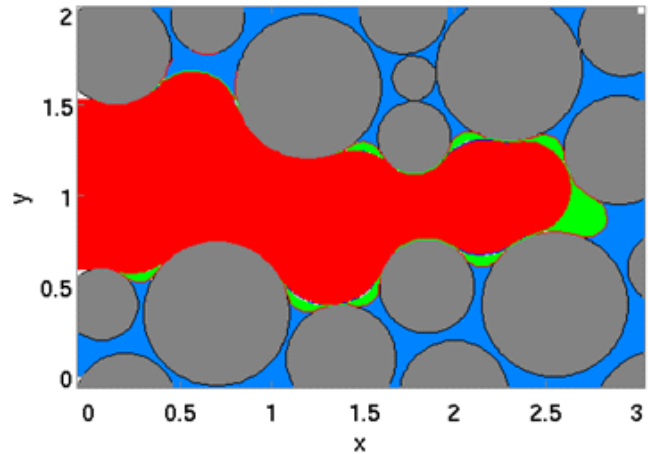
Hydrate Saturation and Distribution in Porous Medium, Scenario B: Water Supply Rate Much Greater than Hydrate Formation Rate

This scenario has the same stage 1 as scenario A: hydrate slowly invades gaseous phase (Figs. 15b and c). When the gas/water interface reaches the critical point at which two interfaces merge (the end of stage 1), the fluid behavior becomes different from scenario A. The

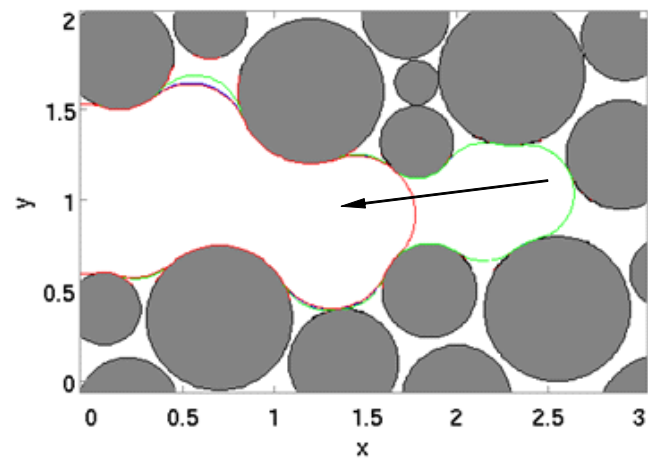
assumption that water supply rate is much larger than the hydrate formation rate indicates that water supply is no longer a constraint of imbibition. At the critical point, a Melrose imbibition jump takes place due to the unstable fluid/fluid interface, and invades gas-filled pores in an abrupt fashion.



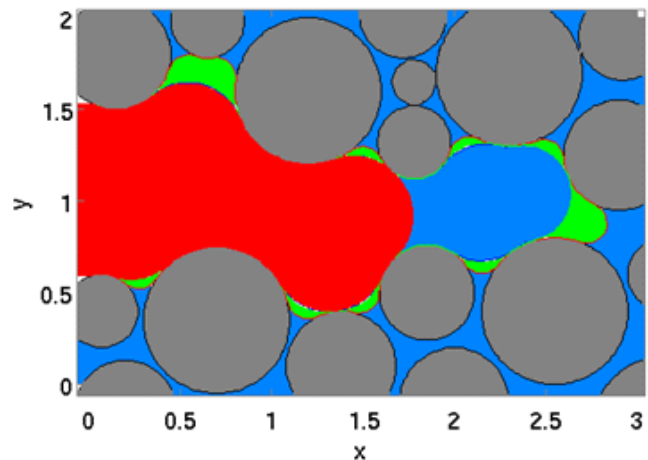
(c) Hydrate distribution (green) when the methane/hydrate interface is at the critical point. In contrast to Figure 4C, following this step, a slight decrement of curvature will result in a jump of interface to the left (Melrose imbibition jump). This is because the separate water films at the surface of the hydrate merge to form a single methane/water interface, which is unstable.



(d) Stage 2, the imbibition jump is an abrupt, instantaneous process. No intermediate steps, like the blue interface in Figure 4D, will be available. Thus the interface jumps as a gas/water interface to the next stable position, which is shown as the red curve.



(e) Imbibition jump sucks water to fill the pore (blue). A new, stable location of the gas/water interface is reached at the end of the jump. Since this is a sudden event that gives no time for hydrate formation, water can be maintained between the two interfaces. New hydrate can form along the newly-formed gas-water interface (boundary between red and blue regions), and only grows into the gaseous phase.



(f) Stages 1 and 2 repeat themselves cyclically. We only show here the final hydrate (green) and water (blue) distribution. The final distribution has a sandwich-like pattern: the water-filled pores are separated by hydrate shells of varying thickness. This gives the minimum hydrate saturation.

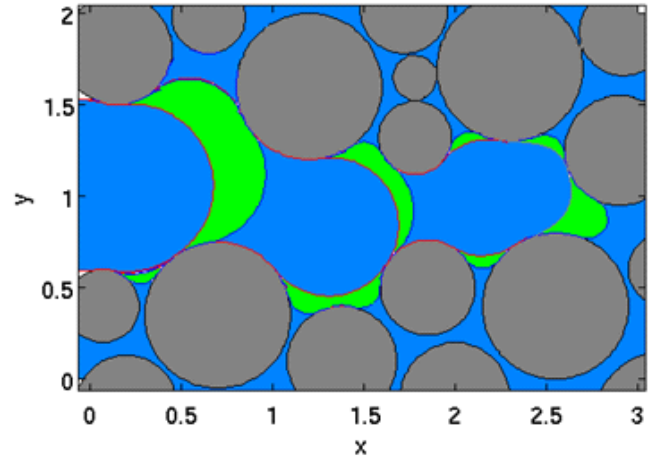


Fig. 15. Schematics of Scenario B that water supply rate is much larger than hydrate formation rate, which gives the minimum hydrate saturation. The color scheme is the same as in Fig. 14.

In Fig. 15c, Melrose jump of a gas/water interface takes place instead of the incremental movement. Consequently a large portion of the pore(s) will be filled by water. As stated by the assumption, hydrate grows only into the gaseous phase. Therefore, water invasion during the imbibition jump will not be converted into hydrate (Figs. 15d and e). Hydrate resumes growth only on the new stable locations of the gas/water interface(s), and into the gaseous phase as before. After several steps of incremental movement of the gas/hydrate interface into the gaseous phase, a Melrose imbibition jump happens again. This sequence of events leads to a sandwich-like pattern, illustrated at the imbibition endpoint in Fig. 15f: water droplets are encaged by hydrate shells in the porous medium.

It follows that this limiting case yields the minimum hydrate saturation. The original footprint of the gas phase is now occupied by water-filled pores and hydrate lenses of varying thickness, compared to the previous scenario where hydrate distribution completely follows the gas footprint. These two scenarios suggest the upper and lower limits of the hydrate saturation that could possibly happen in the porous medium: hydrate saturation is equal to the original gas saturation (upper limit, demonstrated in Fig. 14), and hydrate saturation is equal to the volume (area in 2D) swept by incremental movement (slow movement) of the interface (lower limit, demonstrated in Fig. 15). However, the requirement for the occurrence of these cases is that both methane and water are sufficient for hydrate formation (note that we do not constrain the availability of either water or methane in Scenarios A and B).

It is important to know the fraction of Melrose jump and incremental movement to estimate the hydrate saturation in Scenario B. In practice, we use network modeling to determine this value. Network modeling is a numerical tool that can be used to study drainage and imbibition (Blunt, 2001; Valvatne and Blunt, 2004; Valvatne *et al.*, 2005; van Dijke and Sorbie, 2003). Because of the assumptions and simplifications it applies, this technique is capable of modeling fluid flow in much larger samples than LSMPQS (Peng *et al.*, 2009). In our study, a model sediment containing 7000 monodisperse spheres is used. This model sediment is comparable to the real sediments in the hydrate reservoir, and therefore the simulation based on the model sediment is believed to represent the real fluid distribution in the porous media (Peng, 2011). By using network modeling, we obtain that Melrose jump takes 7% saturation unit during imbibition process, and the rest of imbibition events are all incremental movements.

The Effect of Gas Trapping on Hydrate Saturation in Porous Medium

One important behavior missing from the preceding analysis of scenarios A and B is the nonwetting phase trapping. The porous medium in Figs. 14 and 15 has large open space, and therefore does not permit trapping. In a sediments and sedimentary rocks, nonwetting phase is trapped at the imbibition endpoint, and disconnected from the bulk phase.

The trapping occurs due to two mechanisms. First, the continuous clusters of nonwetting phase are disconnected due to the imbibition happening in pores. Once the nonwetting phase loses its connection to the exit face (pores), it is trapped. Second, menisci at constraint geometries (for example, throats) merge at lower applied capillary pressure. This behavior snaps off and traps nonwetting phase in the pores. Both of the mechanisms require coalescence of separate menisci, that is, the Melrose event. A more detailed analysis can be found at (Gladkikh and Bryant, 2003).

Scenario A features a gradual invasion of hydrate, and there is no interface coalescence. Therefore, we do not consider nonwetting phase trapping in this scenario. With sufficient gas supply from other porous media, the hydrate saturation in Scenario A will be exactly the same as the initial gas saturation. On the other hand, Scenario B considers Melrose jump. Nonwetting phase will be trapped at the imbibition endpoint. When hydrate formation from the trapped gas is complete (in this case, no extra gas can be provided from the surrounding porous media), water comes in and fills the vacancy due to the hydrate formation. Much more water saturation is obtained by using this scenario.

1D Sedimentological Model

Although in Figs. 11 through 13, a 2D conceptual model is used to demonstrate hydrate formation with the descending BGHSZ, the field observation suggests that hydrate profile variation is much greater in the vertical direction than the horizontal direction (Dallimore and Collett, 2005). In the Arctic hydrate reservoirs, the lateral continuity of hydrate saturation is reasonable. We therefore simplify the previous conceptual model into 1D, which concerns only the vertical hydrate distribution. This simplification relies on the effect of grain size distribution described in the previous section. Here we extend the preceding analysis to include a highly simplified 1D model of the charging of the gas reservoirs. In effect, the model of gas charge assumes that the reservoirs are filled until the capillary barrier at the top of each reservoir is breached. It is beyond the scope of this work to consider in detail alternate schemes for gas charge, e.g. migration updip from a conductive fault. The main consequence of alternate schemes is that they need not fill the original gas reservoirs to the limits of their top seal capillary barriers. The resulting hydrate saturation profiles would still be characteristically “sandwich-like”, with large saturations in the upper portion of a reservoir decreasing sharply to small saturations in the bottom portion. The difference with the model examined here would be the fraction of reservoir in which large hydrate saturation occurs.

$$P_C^{entry} = \frac{2\sigma_{gw}}{R_{thr_ins}} \quad (30)$$

where P_C^{entry} is the capillary entry pressure, σ_{gw} is the interfacial tension between gaseous and aqueous phases. R_{thr_ins} is the throat inscribed sphere, whose value can be determined by using these approximations:

$$R_{thr_ins} = \begin{cases} \frac{1}{3}R_{grain} & \text{clean sand} \\ \frac{1}{6}R_{grain} & \text{shaly sand} \end{cases} \quad (31)$$

where R_{grain} is the median grain size of the sediment. Shale clogs the throats and therefore results in smaller throat sizes and higher capillary entry pressure. By using Eq. (31) we assume clay coats the grain uniformly in the porous medium. Equations (30) and (31) provide an approach to estimate capillary entry pressure at different layers from median grain size.

The capillary pressure between water and gas is zero at free water level (FWL), and increases almost linearly upwards. The comparison between the capillary entry pressure and capillary pressure allows the estimate of initial gas saturation in the reservoir.

Grain Size Variation and Gas Charge of Mount Elbert Hydrate Reservoir

Mount Elbert locates on the North Slope of Alaska. Cores are retrieved between 606 m to 760 m, from Mount Elbert test well (Hunter *et al.*, 2011; Rose *et al.*, 2011). Gas hydrate was discovered from 614 m to 672 m. Above 614 m, a thick layer of clay-rich silt exists as very strong capillary seal. Modern BGHSZ is believed to be at around 900 m, far below the depth where hydrate is observed. This observation indicates that the initial gas accumulation did not extend below this depth, and FWL (free water level) exists at 672 m.

Figure 16 shows the median grain size and the corresponding capillary entry pressure of the sediments. Capillary pressure between water and gas is also shown for comparison, which is much greater than the capillary entry pressure. The strong contrast is due to the facts that 1) gas and water have a large density difference, and thus large capillary pressure gradient; 2) sediments have large throat openings, which lead to low entry pressure. Capillary pressure is comparable to capillary entry pressure at 650 m. This is a potential capillary barrier to separate the reservoir into two units (Unit C and D by following Lee and Collett, 2011, and Anderson *et al.*, 2011).

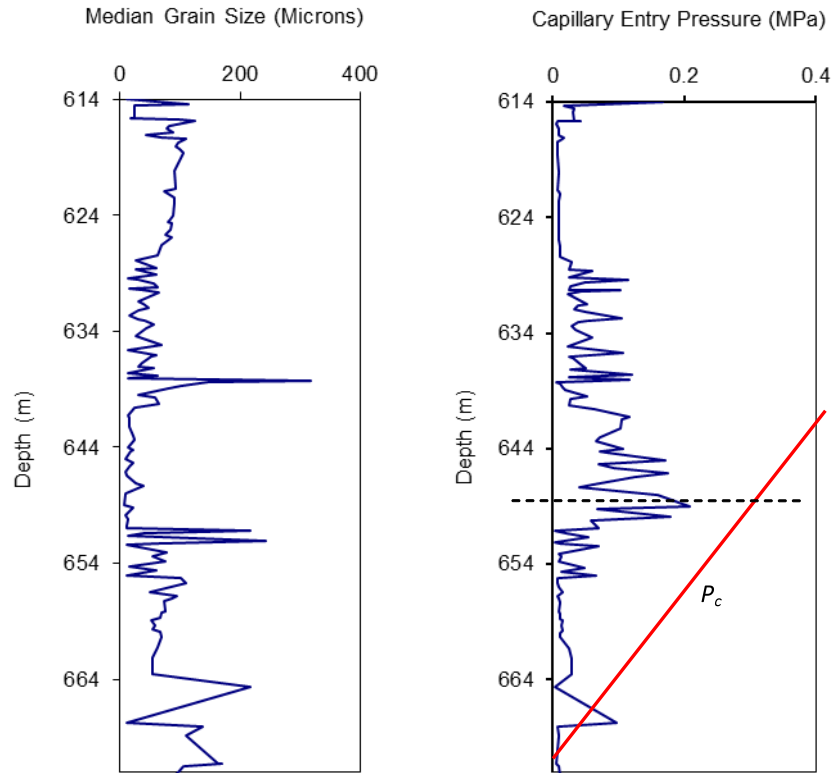


Fig. 16. The median grain size distribution and the capillary entry pressure, Mount Elbert hydrate reservoir. The capillary entry pressure is by using Eqs. (30) and (31), and the interfacial tension between water and methane to be 0.075 N/m (this is the surface tension of water at 300 K. This value is a weak function of salinity and pressure). The capillary pressure gradient between gas and water is 0.009 MPa/m, by assuming gas density to be 50 kg/m³ (at 6 MPa and 273 K) and water density to be 1000 kg/m³.

At the time when BGHSZ was still above Unit D, gas generated from deeper source migrated upwards and charged these two units. When the free gas reached the capillary barrier at 650 m, the capillary seal prohibited the further upward migration of gas. Gas therefore first accumulated in the upper region of Unit C (Fig. 17a), and expanded downwards. During the expansion, the capillary pressure at the top of Unit C increased. When the capillary pressure was able to exceed capillary entry pressure of the barrier between Unit C and D, gas kept migrating upwards, and accumulated from the top of Unit D (Fig. 17b). Gas slowly charged Unit D from top to bottom. This filling process continued in Unit C after Unit D was saturated by gas (Fig. 17c). Similar to Unit D, gas charged from top to bottom of Unit C. The final gas saturation profile gave a full gas column in both Unit C and D (Fig. 17d).

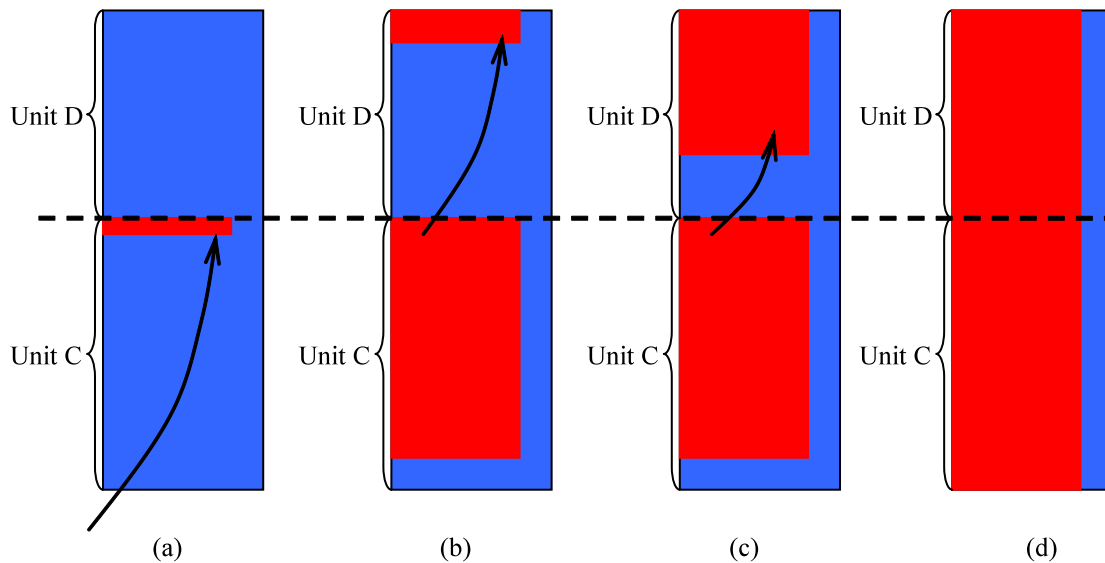


Fig. 17. Initial gas charge of Mt Elbert reservoirs subsequently converted to hydrate. (A) the upward-movement of free gas from deeper reservoir was blocked by the capillary barrier at 650 m. Gas accumulated beneath the capillary barrier and expanded downwards. (B) when the capillary pressure built up to exceed the entry pressure of the barrier, the upward migration restarted, and free gas began to fill the upper region of Unit D first, and expanded to the lower region (C). (D) both Unit C and D would eventually be filled up by gas.

In the current model, the initial gas saturation is uniform along the depth. This is an assumption based on the fact that capillary pressure is much higher than capillary entry pressure for most parts of the reservoir. Therefore we do not concern ourselves with the minor difference of gas saturation at different depths. We also ignore the capillary transition zone, as the length of this zone is negligible compared to the total length of the reservoir.

When BGHSZ descended and entered the gas reservoir, gas hydrate formed at BGHSZ. Depending upon the comparison between water supply rate and hydrate formation rate, different hydrate saturations were obtained (Scenarios A and B). In the following demonstration, we show only Scenario B.

Figure 18 shows the initial gas saturation, along with the capillary pressure and the sediment entry pressure. Hydrate formed at BGHSZ when it began to descend, and vacancies (due to hydrate formation) drew fluids (gas and water) from different zones: water was supplied from the capillary seal on top of the reservoir, where the permeability was comparable to the reservoir. Gas could only supply from the deepest depth where free gas was still available. At this depth, the pressure decrement due to gas loss was compensated by water invasion, from the aquifer below. The water invasion followed conventional imbibition process, where gas trapping also occurred.

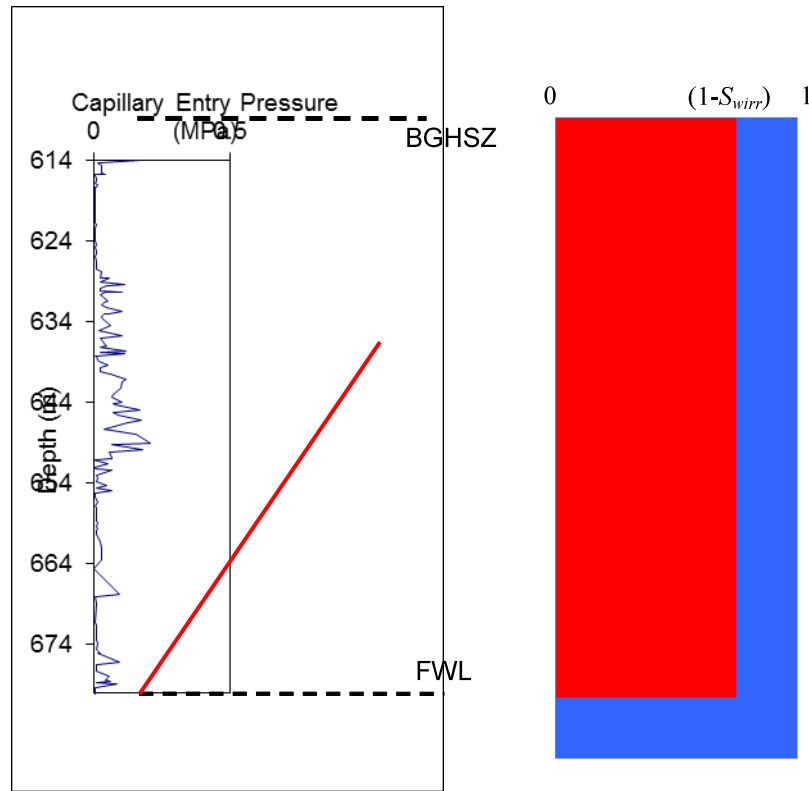


Fig. 18. The comparison of the capillary pressure and capillary entry pressure of the sediments before BGHSZ moves downwards (left), and the initial gas column (red) in the reservoir (water in blue).

The capillary pressure shifted upwards (from dashed to solid red line in Fig. 19), and reduced the difference with capillary entry pressure (Fig. 9). When the capillary pressure fell below the capillary entry pressure at 650 m (indicated by the arrow in Fig. 9), the gas communication between two units is terminated. We use a black line in the right panel of Fig. 9 to demonstrate this capillary barrier, which separates the gas column into upper and lower units (Unit C and D).

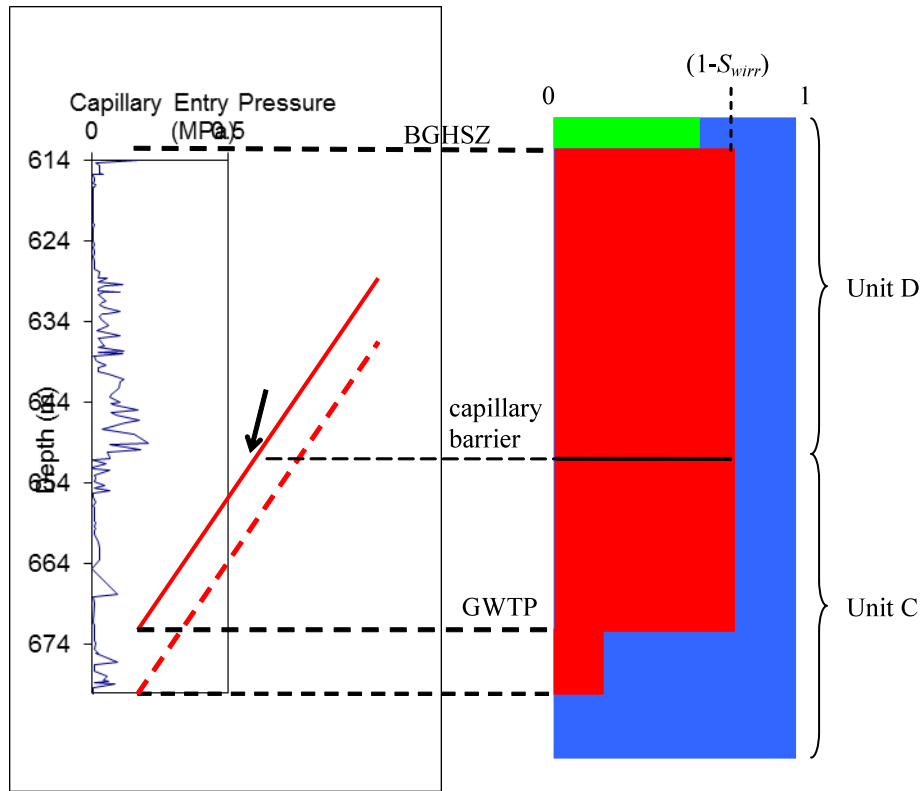


Fig. 19. The communication inside the gas column is restricted when capillary pressure decreases (from dashed to solid red line), for example due to rising gas-water contact, and becomes smaller than the capillary entry pressure. The black line on the right panel shows the possible capillary barrier that could separate the gas column into Unit C and D. GWTP stands for gas water transition point, which is the boundary between gas-saturated layers with residual-gas layers.

When BGHSZ further moved downwards, no free gas from Unit C migrated upwards due to the lack of hydraulic communication with Unit D. Instead, free gas from the bottom of Unit D (Fig. 20a) filled the vacancy created by hydrate formation and further facilitated hydrate formation.

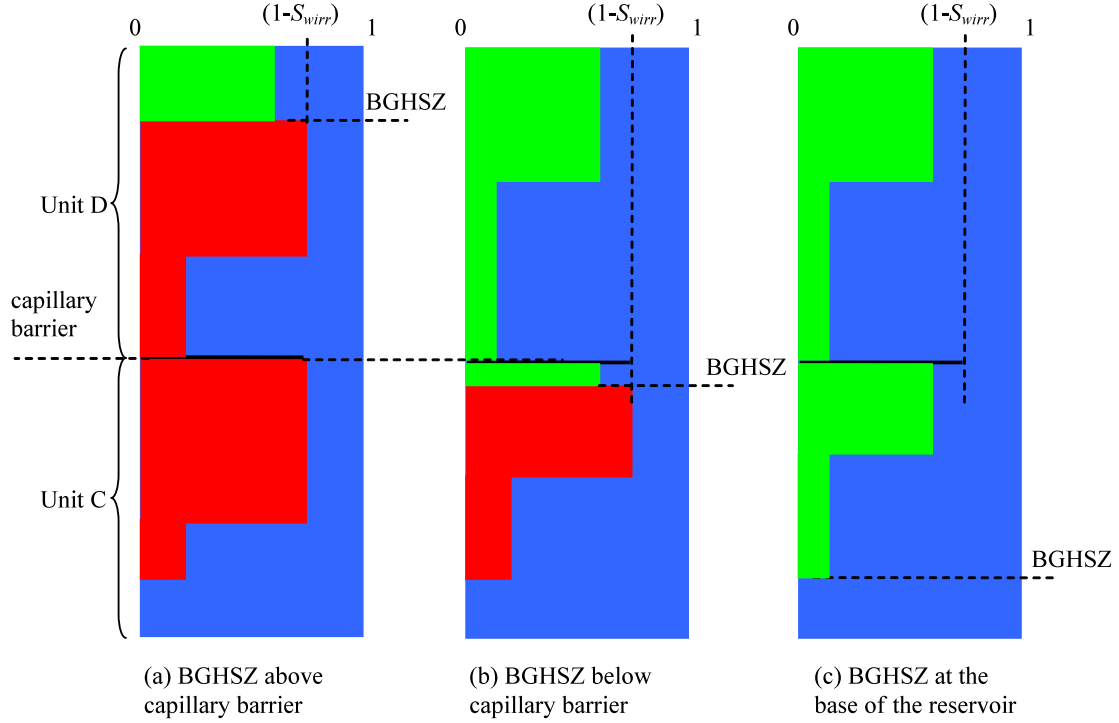


Fig. 20. Two intermediate steps when BGHSZ is above (a) and below (b) capillary barrier, and the final hydrate distribution when BGHSZ moves to the base of the reservoir (c). Almost all the free gas in (A) is supplied from the bottom of Unit D. In (b), the gas transportation is only within Unit C. The final hydrate distribution shows that Unit C and D share the similar hydrate profile.

When BGHSZ moved below the capillary barrier at 650 m, hydrate formation and gas transportation only took place in Unit C, and followed the same process as of Unit D. Unit D and C had the similar hydrate distribution pattern when hydrate formation was complete (Fig. 20c).

To predict hydrate profile, we subdivide the entire reservoir into finite number of layers (for example in Mount Elbert, each unit is divided into 200 layers). When BGHSZ reaches the base of each layer, we perform the following calculation:

- a. The model determines hydrate saturation in layer i , and calculates the equivalent amount of gas required to obtain the hydrate saturation. Here we assume that higher index means deeper layer. For Scenario A, the hydrate saturation is:

$$S_h = 1 - S_{wirr} \quad (32)$$

and for Scenario B:

$$S_h = 1 - S_{nwr} \left(1 - \frac{\rho_g}{\rho_h} \frac{M_g + NM_w}{M_g} \right) - S_{jump} - S_{wirr} \quad (33)$$

where S_h is hydrate saturation, S_{wirr} is irreducible water saturation, S_{nwr} is residual gas saturation. S_{jump} is the volume of Melrose jump in saturation unit. ρ_g and ρ_h are the density of gas and hydrate, respectively.

The total mass of gas (m_g) required to produce S_h is computed as

$$m_g = \rho_h S_h \phi \frac{M_g}{M_g + NM_w} \quad (34)$$

where ϕ is the porosity of layer i .

- b. The model then calculates the amount of gas needed from other layers (m_{g_extra} in Eq. (35)). This is simply the total mass of gas required to form hydrate (m_g) takes away the initial amount of gas in layer i .

$$m_{g_extra} = \rho_h S_h \phi \frac{M_g}{M_g + N M_w} - \rho_g S_g \phi \quad (35)$$

where S_g is the initial gas saturation of layer i .

- c. Starting from the bottom layer, the model searches upwards layer by layer for available free gas that can be transported into layer i . For example, if layer j ($j > i$) is already at the residual gas saturation, the model will search $j-1, j-2 \dots$ ($j-1, j-2 > i$), until free gas exists in that layer, say, $j-2$. If the amount of free gas in $j-2$ is not enough to compensate the amount by Eq. 35, free gas in upper layers ($j-3, j-4 \dots$, and $j-3, j-4 \dots < i$) should be added until the requirement is met.
- d. With the sufficient free gas coming from the deeper layer(s), layer i is filled by hydrate. Then BGHSZ moves to one deeper layer ($i+1$), and repeat steps (a) through (c). At the layers where gas saturation is already at the residual value, the model only needs to convert the residual gas into hydrate by using the following equation.

$$S_h = S_{nwr} \frac{\rho_g}{\rho_h} \frac{M_g + N M_w}{M_g} \quad (36)$$

Grain Size Variation and Gas Charge of Mallik Hydrate Reservoir

The Mallik hydrate reservoir is located on the coast of Beaufort Sea, northwest Canada (Dallimore and Collett, 2005). Most of the hydrate is found 300 to 700 m below the permafrost. Several test wells have been drilled since 2002, among which well 5L-38 is extensively studied. Research indicates hydrate occurrence between 890 m and 1110 m. BGHSZ is located at 1100 m. In Well 5L-38 a total of 120 m of hydrate column is identified, much longer than Mount Elbert.

Different from Mount Elbert, Mallik reservoir was likely to be separated into different units initially. Figure 21 shows a petrophysical description along the depth of 5L-38. At 941 m (the upper dashed line), the main-mode pore size (main-mode represents the dominant mode from the pore size distribution) and the gas permeability are all at their local minimum values. Since mercury porosimetry was used for the pore size determination, 'pore size' in Fig. 21 is in fact the throat size defined in this work. Therefore for 0.5 μm throat size, assuming gas/water interfacial tension to be 0.075 N/m we calculate the capillary entry pressure of this sediment to be 0.6 MPa. Using 0.009 MPa/m capillary pressure gradient, a 67 m of gas column, the same as the length of Unit B, must be established to overcome this capillary barrier. Therefore, an entire column of gas in Unit B will establish enough capillary pressure to barely exceed the capillary barrier at the base of Unit A.

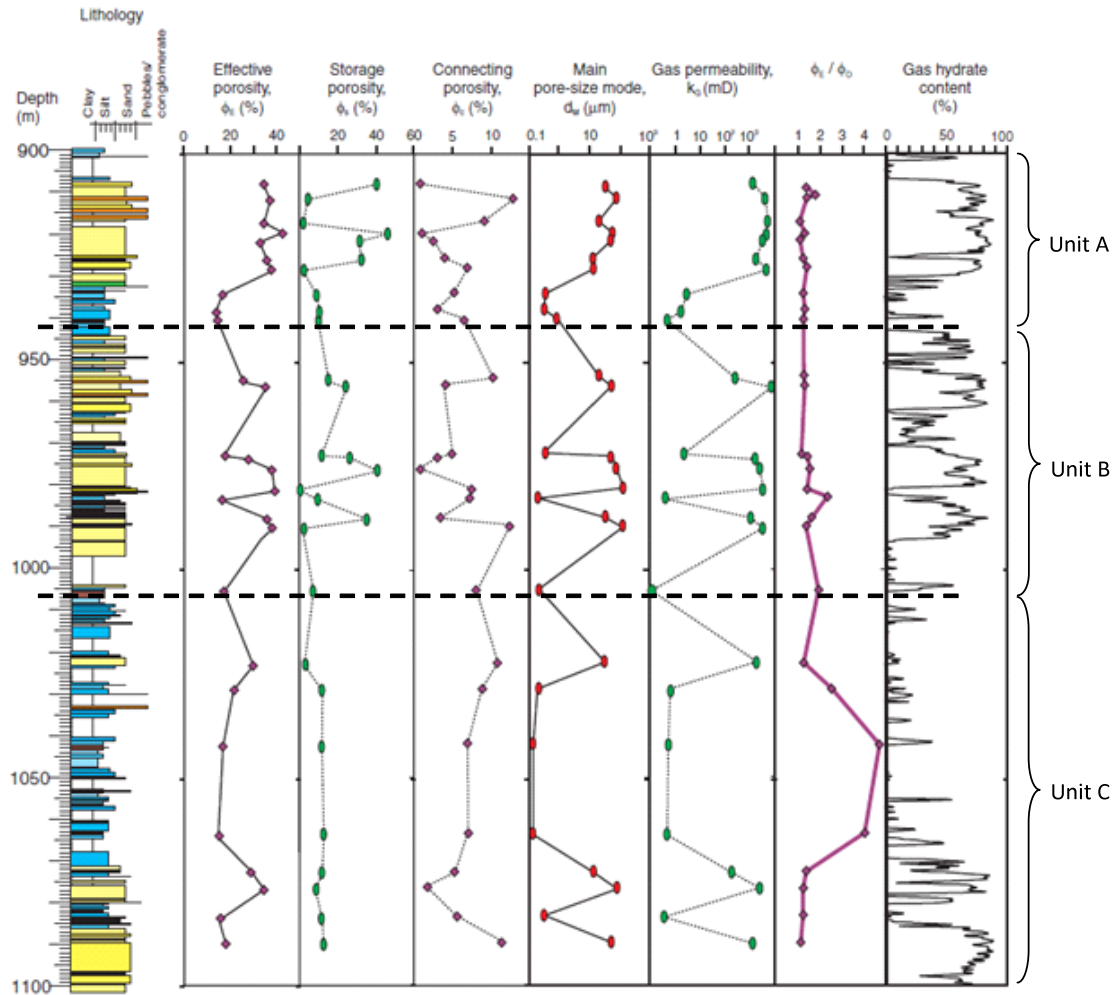


Fig. 21. The petrophysical properties from well 5L-38, Mallik hydrate reservoir. The properties are based on the lab measurements. From (Katsube *et al.*, 2011).

At 1006 m, near the base of Unit B, the gas permeability is at the smallest value of the entire depth, and also the main-mode pore size ($0.2\sim 0.3 \mu\text{m}$) is at its local minimum. Based on the same analysis as above, it therefore requires 1 to 1.5 MPa, or 111~167 m of gas column to overcome such barrier. This is close to the length of Unit C (95 m), considering our estimate of the ‘pore size’ from Fig. 21 is only approximate. We thus presume that once continuous gas column is established in Unit C, the capillary pressure at the base of Unit B would be just sufficient to overcome the capillary entry pressure at 1006 m.

The capillary barrier between Unit B and C separates the good lithology (Unit B) from the bad (sand-poor) lithology (Unit C). Below the barrier, except for an abnormal point (~ 1020 m), the petrophysical properties (from 1006 to 1072 m) all indicate very tight sediments. Along with the lithology description from (Uchida *et al.*, 2005), we infer that water, either capillary-bound or clay-bound, dominates this region. The gas saturation only just exceeded the critical saturation in Unit C (this value is the minimum gas saturation that can maintain a continuous gas cluster to allow gas flow through the porous medium) to enable the gas migration pathway. Therefore, the upper part of Unit C allowed gas to migrate to the units above but was not drained to large gas

saturation. This relatively small initial gas saturation explains the low hydrate saturation observed in this part of Unit C.

Another evidence of the capillary barriers is the capillary entry pressure of the sediments (Fig. 22), which is obtained by using the median grain size and Eqs. (30) and (31). In Mallik reservoir, due to the high content of shale, calculating the capillary entry pressure, especially at the shaly regions, is subject to large error. However, Fig. 22 still provides a relative comparison of the entry pressure at different depths, and therefore should only be used for identifying different regions.

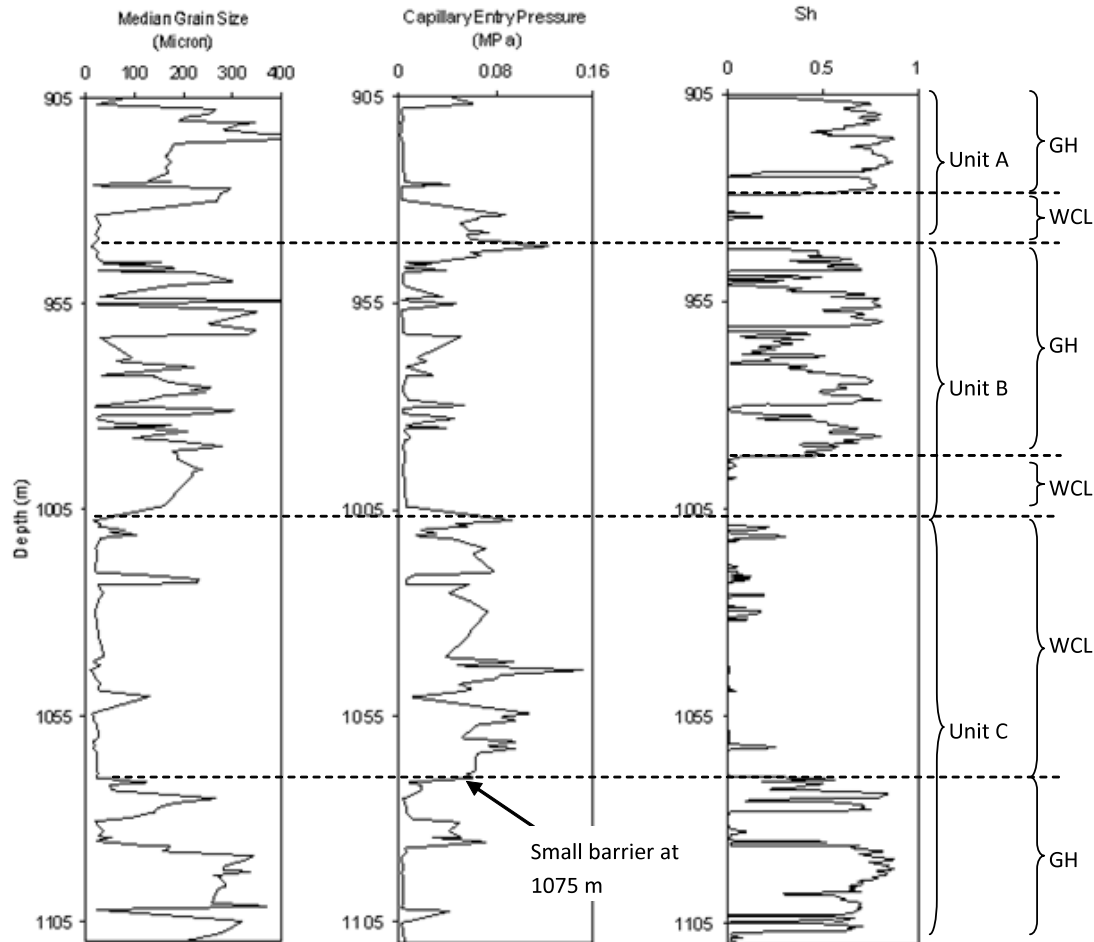


Fig. 22. The identification of different reservoir units from the capillary entry pressure, From well 5L-38, Mallik gas hydrate reservoir. The capillary entry pressure is computed by using Eqs. (30) and (31). This figure should only be used for the identification of different regions in Mallik gas hydrate reservoir, not for quantitative values of entry pressures.

To summarize the hypothesized initial distribution of gas saturation at Mallik, we assume the thermogenic gas from deeper sources migrated upwards through fractures. The migrating gas first encountered capillary barriers at 1075 m (Figs. 22 and 23a), thereby filling Unit C-GH (Figs 23a and 23b). The drainage curve for Unit C-GH sediments, Fig. 24, permitted buildup of large gas saturation. When the capillary pressure exceeded the entry pressure of WCL region, free gas began to migrate upwards into WCL, Fig. 13b (Recall that in Fig. 22, the capillary entry pressure

of Unit C-WCL region and its distribution along the depth are not to scale.) The drainage curves of Unit C-WCL have different characteristics than Unit C-GH and Unit B. Because of the wider grain size distribution and higher content of clay in Unit C-WCL, these sediments have higher entry pressure and much higher irreducible water saturation (Fig. 24).

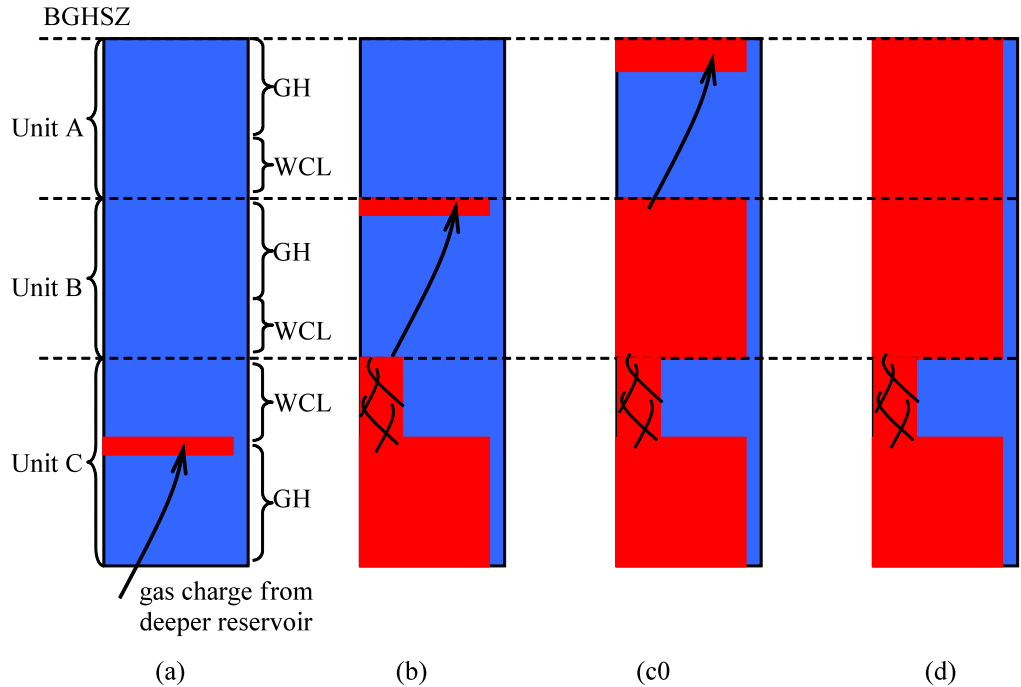


Fig. 23. Initial gas charge in the reservoir. (a) Gas invaded Unit C-GH from deeper gas source. (b) Gas filled Unit C-GH from top to bottom. When the capillary pressure exceeded the capillary entry pressure of Unit C-WCL (see WCL and GH regions in Fig. 22), gas migrated upwards through the pathways. However, the capillary pressure was not enough to allow gas to displace water in the sediments. At Unit B, gas was contained under the capillary barrier between Unit A and B, and expanded to the lower region. (c) When Unit B was almost filled up by gas, the capillary pressure exceeded the entry pressure of the barrier. Therefore, gas started to charge Unit A. Still the gas column accumulated at the top of Unit A and expanded downwards. (d) When gas charge was complete, Unit A, B and Unit C-GH were fully saturated with free gas. Unit C-WCL had small gas saturation (the minimum value to maintain the continuous cluster).

Therefore, gas column was incapable of fully draining Unit C-WCL, but was capable of maintaining the minimum saturation that would allow gas transport. When Unit C was filled by gas (95 m of gas column, with large saturation in Unit C-GH and small but connected saturation in Unit C-WCL), the gas phase capillary pressure at the base of Unit B was just enough to exceed the capillary entry pressure of that sediment, and thus free gas entered Unit B (Fig. 23b).

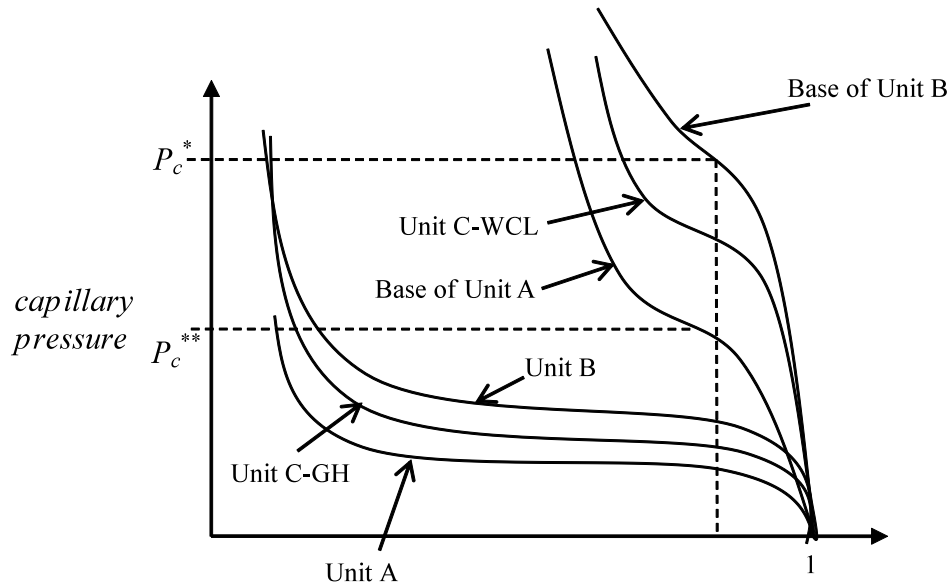


Fig. 24. Capillary entry pressure at different regions of Unit A, B and C. P_c^* corresponds to the capillary pressure at the base of Unit B when 95 m gas column occupies Unit C. At this capillary pressure, S_w is still large in Unit C-WCL, while Units C-GH and B are drained to $S_{w,irr}$. P_c^{**} corresponds to the capillary pressure at the base of Unit A when 67 m gas column occupies Unit B. At this capillary pressure, Unit A will drain to $S_{w,irr}$.

This behavior is also demonstrated by comparing the schematic drainage curves of Unit B and C in Fig. 24. The drainage curves for Unit B and Unit C-GH have a low entry pressure, and also a sharp percolation. These features arise because the sediments in these regions have larger grain size and relatively narrower grain size distribution than those in WCL region, whose drainage curves in Fig. 24 have higher entry pressure and do not exhibit sharp percolation. Unit C-WCL also has larger irreducible water saturation at drainage endpoint. The capillary pressure at the base of Unit B (P_c^* , corresponding to 95 m of gas column in Unit C) was just sufficient to break the capillary barrier at that depth. Once free gas entered Unit B, it displaced water to the irreducible value in accordance with the drainage curve in these coarser-grain sediments (Fig. 24).

The gas column continued to build up, until close to the base of Unit B. Because the capillary pressure at the base of Unit B was only just enough to allow gas to enter Unit B, the capillary pressure at the top of Unit B corresponds only to the thickness of the gas accumulation in this unit. As discussed above, in this situation capillary pressure at the top of Unit B was just enough to exceed the capillary entry pressure at the base of Unit A. In Fig. 24, P_c^{**} is the capillary pressure at the top of Unit B when the entire Unit B is filled by gas. When P_c^{**} overcomes the capillary entry pressure of the barrier, gas could easily fill Unit A because of its low percolation threshold. It then allowed gas to charge Unit A (Fig. 23c). No grain size measurements are available above Unit A, so we presume the capillary barrier at the top of Unit A is enough to hold the gas column in Unit A, which is about 35 m. At each layer except for Unit C-WCL, the initial gas saturation is set to be the constant $(1-S_{w,irr})$, because the capillary pressure between water and gas required to enter the base of each unit is more than enough to drain water to the irreducible saturation in the sands below each capillary barrier (Fig. 24).

We assume Unit A and B are not connected and thus apply the hydrate formation model to them separately. More precisely, it is assumed that the gas communication between Unit A and B

is barely available before hydrate formation, that is, the capillary pressure at the barrier between the two units only barely exceeds the capillary entry pressure of the barrier. When hydrate first formed at the top of Unit A-GH, the upward movement of gas would reduce the gas column height in Unit B. Thus the capillary pressure at the base of Unit A immediately dropped below the entry pressure, and terminated the gas communication between Units A and B. The same phenomenon occurred within Unit C and D in Mount Elbert discussed in the previous section.

As BGHSZ descends, hydrate starts to form at BGHSZ. The scenario follows the discussion of Mount Elbert: hydrate formation generates vacant spaces, and the invading gas and water to fill the vacant spaces also become the source for further hydrate generation. Two scenarios are considered, depending on the competition between water supply rate and hydrate formation rate, which yield upper and lower bounds of hydrate saturations. In the schematic of Fig. 25, we illustrate scenario B, that is, water supply rate is much greater than hydrate formation rate, so that water invasion by Melrose jump fills part of the void space. Free gas from the bottom of Unit A migrates to fill the void space, and allows for the water invasion happening below GWTP. During this process, the state of Unit B does not change. The capillary barrier at the base of Unit A prohibits the gas communication between the two units.

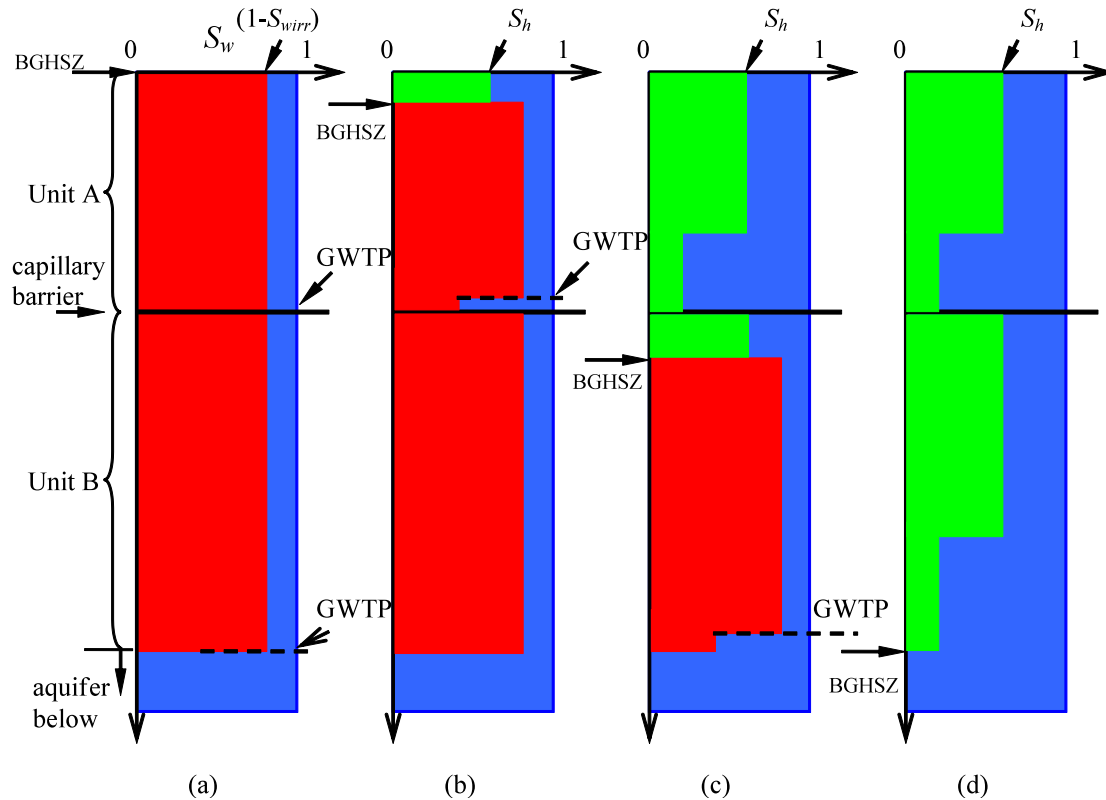


Fig. 25. A schematic of hydrate formation in Unit A and B. (a), (b), (c), and (d) show the distribution of hydrate, water and gas as BGHSZ moves downwards. It follows the similar procedure as Mount Elbert case shown in Fig. 20.

Gas in Unit A is converted into hydrate from the top down as BGHSZ moves downwards. Due to the gas redistribution within Unit A during the hydrate formation, the final hydrate distribution contains GH and WCL regions, similar to the case of Mount Elbert. GH region has the maximum hydrate saturation, while WCL region only has the hydrate saturation that is

converted from the residual gas. Figure 25c is an intermediate step after BGHSZ moves below the capillary barrier. The same hydrate formation process repeats in Unit B, and gives a final hydrate distribution as shown in Fig. 15d.

Predicting Hydrate Distribution with Pore-Scale Imbibition Model

We predict hydrate distribution in Mount Elbert and Mallik sites by applying the imbibition models described above as the BGHSZ descends through the initial gas saturation profile, while accounting for the possibility of the gas column being disconnected vertically during conversion. Two limiting cases are evaluated, which yield the maximum (Scenario A) and minimum (Scenario B) hydrate saturation according to whether the rate of water supply is slow or fast relative to the rate of hydrate growth, respectively. The gas reservoirs are assumed not to be connected to the deeper source during the descent of BGHSZ. The model predictions for both limiting cases are compared with the hydrate saturation profiles inferred from logs.

Predicted Hydrate Distribution in Mount Elbert Hydrate Reservoir

Several important parameters must be specified in order to apply the models. S_{wirr} and S_{nwr} are set to be 15% and 32%, respectively. These are the values from network modeling of a model sediment that accounts for periodic boundary condition, which is believed to represent the fluid distribution in the field (Peng, 2011). S_{nwr} is only relevant when Melrose jump occurs (Scenario B). The saturation change associated with Melrose jumps, S_{jump} , is 7%, from Section 2.1. The density of methane (ρ_g) is computed by using the EOS proposed by Soave, Redlich and Kwong (Sandler, 2006). Hydrate density is 910 kg/m^3 , with the hydration number being 5.75 (Sloan, 2003). The water density is assumed to be 1000 kg/m^3 . The porosity of the sediment varies with lithologies, and can be found in (Winters *et al.*, 2011).

Several approaches are employed to obtain a reasonable field estimate of the hydrate saturation in the reservoir condition. These approaches include interpretations from density, resistivity, and acoustic logs (Lee and Collett, 2011), and also from core-derived chloride concentrations (Torres *et al.*, 2011). These data are cross-verified, and thus are considered to reflect the real hydrate distribution in Unit C and D.

Figure 26 shows a comparison of the model-predicted hydrate distribution with the field data. The left panel is Scenario A where water supply rate is much smaller than hydrate formation rate. Based on the previous analysis, hydrate therefore can fill up the volume of all the original gas, and the hydrate saturation in the GH region becomes the same as the initial gas saturation in the sediment, which is 85% ($1-S_{wirr}$). This overestimates the saturation value from the field observation.

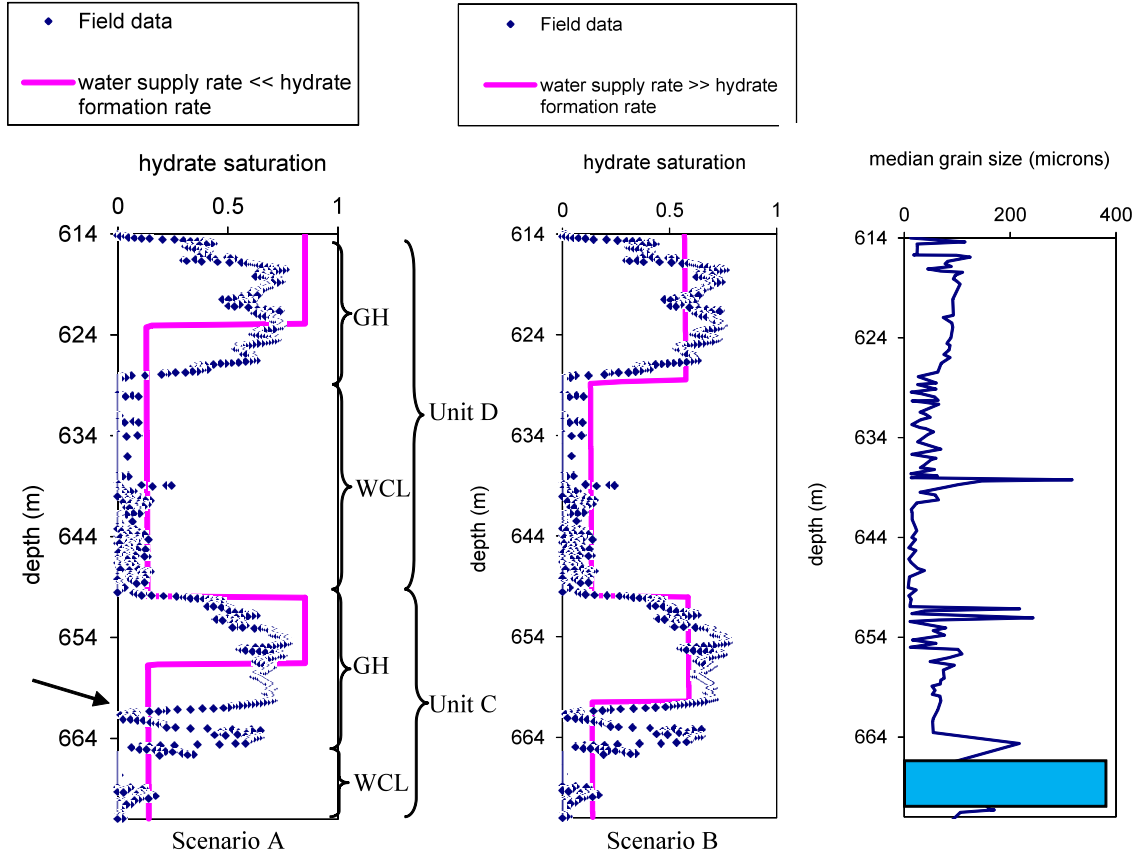


Fig. 26. A comparison of model prediction and field data of hydrate distribution, Mount Elbert hydrate reservoir (left and middle panels for slow and fast water supply, respectively) based on the pore-scale imbibition model, and the median grain size distribution along the depth (right panel).

Hydrate formation in GH region of each unit drains the free gas from WCL region, and leaves behind only the residual gas. Under the in-situ temperature and pressure, 32% S_{nwr} yields about 10% S_h , the remaining 20% void space will be filled by water. Because Unit C and D are assumed to have no communication (Fig. 19), the same pattern of hydrate distribution is observed in both units, with higher saturation region (GH) on top and the lower saturation region (WCL) at the bottom.

When the water supply rate is greater than the hydrate formation rate (scenario B, middle panel of Fig. 26), another imbibition event (Melrose jump) occurs. In this scenario, the void space created owing to hydrate formation will be filled by both hydrate (because of incremental movement) and water (because of Melrose jump), which gives lower hydrate saturation than Scenario A. Furthermore, gas trapping occurs at imbibition endpoint. Melrose jump disconnects gas bubbles from the bulk phase. Such behavior further increase water saturation, and gives the lower bound of hydrate saturation in the porous medium.

The hydrate saturation predicted from Scenario B is about 58%, a much smaller value than Scenario A. With the same amount of initial gas in place, the lengths of GH region for two scenarios are different. The length in Scenario B is much longer than Scenario A, a reflection of the different maximum hydrate saturations.

The field data (blue squares in Figure 16) have the similar pattern, where GH region lays on top of WCL region. The highest hydrate saturation is around 80%, lower than 85% (scenario A)

but much higher than 58% (scenario B). However, sediments with this saturation do not prevail along the entire GH region. In Unit D-GH and C-GH the average hydrate saturation is about 57% and 60%, respectively. Thus Scenario B not only predicts similar hydrate saturation with the field data, but also the length of GH region. The length of GH region from prediction shows 14 m of Unit D-GH and 10 m of Unit C-GH. The corresponding values from the field data are 14 m of Unit D-GH and 16 m of Unit C-GH. We obtain a satisfactory agreement in Unit D-GH for both average hydrate saturation and unit length; however, we significantly underestimate the length of Unit C-GH.

The comparison between Scenario A and field data does not yield good agreement (Fig. 26a). The estimated hydrate saturation is much higher than, and the estimated length of GH region is much smaller than, the field data. Such comparison suggests that hydrate formation does not simply fill up gas-filled pores, but involves more complex processes (Melrose jump, Scenario B). The final hydrate saturation is a result of both of the incremental movement (hydrate filling) and Melrose jump (water filling). The good comparison between Scenario B and the field data (Fig. 26b) confirms this conclusion.

A hydrate saturation discontinuity exists at about 661 m (indicated by the black arrow in Fig. 26a). Our model does not predict hydrate distribution at this layer. The model estimation from Scenario B only predicts that Unit C-GH extends to 660 m, and below that depth hydrate saturation drops to a very low value.

It is a common argument that hydrate saturation is a strong function of lithology: good lithology (clean sands with large grains) is the ideal environment for hydrate preservation (Rose *et al.*, 2011; Winters *et al.*, 2011), and therefore should have large hydrate saturation. In Mount Elbert case, between 662 m and 672 m (the deepest depth where hydrate is observed) we observe a good lithology (right panel of Fig. 26). However, large hydrate saturation only extends to 665 m. Between 665 m and 672 m (indicated by the blue box) only a small amount of hydrate is observed. Based on our model prediction, we argue that such behavior is due to the fluid redistribution during hydrate formation. As demonstrated by Figs. 18 through 20, hydrate formation draws free gas from the base of each unit. Even though initially the entire unit is charged to the same gas saturation, the gas saturation is reduced to the residual value in WCL regions. The residual gas only yields a low hydrate saturation in the porous medium. Thus even though good lithology exists in WCL region it need not host high hydrate saturations after conversion of the gas reservoir.

Predicted Hydrate Distribution in Mallik Hydrate Reservoir

We use the same EOS as in the previous section on Mt. Elbert to compute gas density. Most of the properties are the same as specified in the previous section. The only different value is the hydration number. For this hydrate reservoir, this value was measured by (Ripmeester *et al.*, 2005), who gave an average value of 6.1 over the depth. Porosity information is obtained at individual depths from (Winters *et al.*, 2005).

The left panel of Fig. 27 shows the comparison between simulation by Scenario A and field data. In Unit A, the model prediction agrees with the maximum hydrate saturation observed in the field (85%). However, only several layers could reach such high saturation. Only less than 20 m thickness of Unit A-GH is predicted, while the field data show 29 m. The model prediction is 1/3 smaller than the field observation. In Unit A-WCL, we predict roughly 20% hydrate saturation in Unit A-WCL, which is converted from the residual gas saturation ($S_{nwr} = 32\%$). The field data, on the other hand, shows very low hydrate saturation. Since the logging data (where

hydrate saturation data are derived from) might not be reliable when hydrate saturation is low, we do not attempt to compare the hydrate saturation in WCL region with the field data. This is also the case in Unit B-WCL.

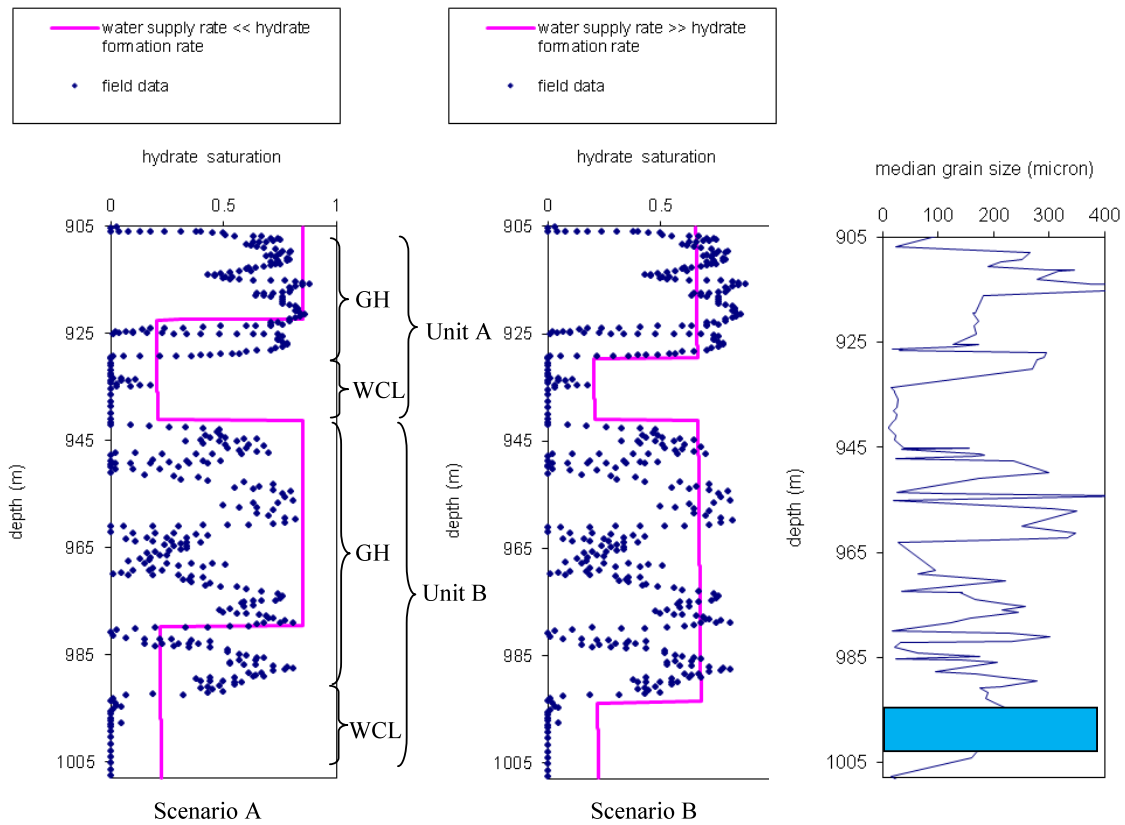


Fig. 27. A comparison of predicted and measured hydrate distribution, Mallik hydrate reservoir (left and middle panels for slow and fast water supply, respectively) based on the pore-scale imbibition model, and the median grain size distribution along the depth (right panel).

The hydrate saturation from field data has more variations in Unit B-GH. It varies between 30% to 85%, which is largely dependent on the facies. In general, maximum hydrate saturation occurs in the clean sands, while the organic rich or dolomite-cemented sands have less hydrate content. Silty sands have the minimum hydrate saturation due to the higher content of clay and the secondary porosities associated with it (Winters *et al.*, 2005). Our model does not take into consideration these features and predicts uniform hydrate saturation in Unit B-GH (left panel of Fig. 27). The prediction underestimates the thickness of GH region. By using Scenario A, we only predict 38 m of Unit B-GH, while the field data give 53 m of this region.

We study the hydrate distribution by using scenario B in the middle panel of Fig. 27. This scenario assume water supply rate to be much greater than hydrate formation rate, and therefore allows for water invasion. The maximum hydrate saturation by this scenario is lower than scenario A. It has a more satisfactory agreement with the field data. In Unit A-GH, the model prediction suggests 63%-65% hydrate saturation, which well matches the average saturation of the field data. The model also yields 15 m of the GH region, same with the field observation. We have a similar comparison in Unit B-GH: The model predicts almost uniform hydrate saturation ($S_h = 65\% \sim 68\%$) and similar thickness of Unit B-GH.

Similar to Mount Elbert, we observe cases where good lithology does not correspond to high hydrate saturation. Between 1000 and 1005 m (indicated by the blue box) of the Mallik reservoir, clean sands with large grain size are identified. However, little hydrate is discovered in this region. Based on our analysis, we argue that this behavior is the consequence of fluid redistribution during hydrate formation. In WCL region, free gas that originally fills the porous medium is transported upwards to fill the vacancy in the shallower layers during hydrate formation. Thus only residual gas is left behind to form hydrate. This process creates hydrate depletion zone, which does not have a strong correlation with the lithology in the reservoir.

Influence of Model Assumptions on Hydrate Saturation Profiles

Salinity Effect

In the above model we assumed that solute diffusion rate is much faster than hydrate formation rate, so that the buildup of salinity in the aqueous phase in the hydrate stability zone does not inhibit hydrate formation. We now consider the opposite limiting case, in which solute does not diffuse away. Then salinity excluded from the hydrate accumulates in the remaining aqueous phase and thereby may limit the ultimate hydrate saturation.

In Mount Elbert hydrate reservoir, the background water salinity is 0.47 wt%, which is likely to be the salinity when hydrate began to form 2.5 Ma years ago (Torres *et al.*, 2011). For Scenario A, we start from $S_{wirr} = 15\%$, and obtain 85% hydrate saturation. Expressed in saturation units, the total volume of water required to generate this amount of hydrate is 77.3%, calculated from hydrate and water densities, which are 910 kg/m³ and 1000 kg/m³. Salt ions excluded from 77.3% water will remain in a volume of aqueous phase equivalent to 15% saturation when hydrate formation is complete. The salinity of the remaining aqueous phase therefore increases from its initial value of 0.43% to a final value of 2.6%. For Scenario B, the same procedure can be applied, and the salinity in the aqueous phase after conversion is computed as 1.0%, and tabulated in Table 1.

Table 1. Salinity Buildup During Hydrate Formation Without Salt Ion Diffusion, Mount Elbert Hydrate Reservoir

Scenario	Hydrate saturation, S_h	Water saturation, $S_w = 1 - S_h$	Initial salinity (weight percentage)	Salinity after hydrate formation (weight percentage)
A	85%	15%	0.43%	2.6%
B	58%	42%	0.43%	1.0%

In Mallik hydrate reservoir, to our best knowledge there is no information of the water salinity at the time when hydrate formed. For the sake of illustration let us suppose that the salinity at the time of hydrate formation was 2.3%, the same as the present-day value (Matsumoto *et al.*, 2005). Based on the above analysis, we can also calculate the salinity after hydrate formation. The results are tabulated in Table 2.

Table 2. Salinity Buildup During Hydrate Formation Without Salt Ion Diffusion, Mallik Hydrate Reservoir

Scenario	Hydrate saturation, S_h	Water saturation, $S_w = 1 - S_h$	Initial salinity (weight percentage)	Salinity after hydrate formation (weight percentage)
A	85%	15%	2.3%	15.3%
B	58%	42%	2.3%	5.5%

Figure 28 shows the maximum salinity under which hydrate can be stable in Mount Elbert and Mallik reservoirs. For Mount Elbert, hydrate is stable until salinity reaches up to 8%, which is much higher than the maximum salinity we predict by assuming no salt ion diffusion (Table 1). Therefore for both scenarios in Mount Elbert case, salt accumulation does not inhibit hydrate formation.

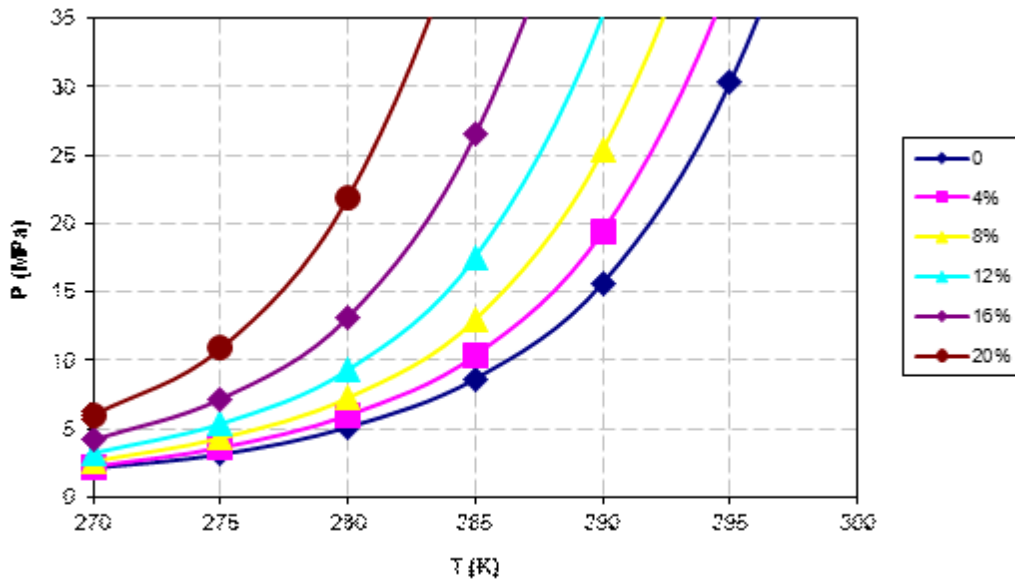


Fig. 28. GHSZ (gas hydrate stability zone) variation as a function of pressure, temperature and salinity. At each salinity, above the curve hydrate is stable, while below the curve hydrate is unstable. The pressure and temperature range of Mount Elbert and Mallik reservoirs are shown. See <http://www.geochem-model.org/models/ch4-sea/> (Sun and Duan, 2007).

In Mallik reservoir, temperature ranges from 280 to 285 K, and pressure ranges from 8 to 10 MPa. For Scenario A, the entire reservoir is in a region where hydrate is unstable: the salinity increases to 15.3% in Table 2, and the curve of 16% salinity lies well above the box showing Mallik conditions. This observation suggests that for Scenario A, 85% hydrate saturation cannot be obtained without salt ion diffusion. Scenario B, on the other hand, only has 5.5% salinity. The entire reservoir is therefore in the region where hydrate is stable. Salt ion accumulation does not inhibit hydrate formation in Scenario B.

The comparison suggests that in Scenario A the hydrate saturation should be smaller than 85%. We thus would gain a similar profile with that of Scenario B (lower hydrate saturation, but longer length of GH region), and better comparison with the field observation.

The Direction of Hydrate Growth in the Porous Medium

It is an assumption in our model that hydrate grows into the gaseous phase once the first nucleation occurs at the gas/water interface. Here we discuss another possibility. That is, hydrate grows into the aqueous phase instead of the gaseous phase. Based on the density of the phases, an irreducible water saturation of 15% will be converted into only 16.5% hydrate, leaving the rest of the pore space to be filled by gas (83.5%). This result does not match the field observation from two aspects. First, the hydrate saturation in the GH region, for both reservoirs, is more than 50%. Thus the prediction (16.5%) is much lower than the field observation. Second, from the field observation only hydrate and water coexist, and no free gas is present. These two observations invalidate the possibility that hydrate grows into the aqueous phase.

Summary of Influence of Pore-Scale Imbibition on Hydrate Saturation Profiles

The imbibition model is a novel method for predicting the saturation profile of a hydrate accumulation resulting from conversion of a gas reservoir in the Arctic. The model relies on the basic physics of pore-scale processes occurring during hydrate formation. It does not account for larger-scale considerations such as the source of water supplied to the hydrate stability zone, nor the factors that control the rate of supply. Instead the model invokes the two limiting cases regarding supply rate. The results should bound what is observed in nature.

The pore scale model is inspired by the conventional imbibition process: the reduction in capillary pressure induced by hydrate formation allows water to advance into pores as gas withdraws. In the hydrate stability zone, an unconventional feature arises: hydrate forms on gas-water interfaces. Crucially, we assume the hydrate skin on a gas-water interface is permeable, allowing water to imbibe through the skin and come into contact with the gas phase. The model assumes that hydrate grows only into the gaseous phase.

The rate of permeation of water through the hydrate skin plays a significant role in determining hydrate saturation. Two limiting cases were studied. Scenario A limits the water supply rate (relative to the rate of hydrate formation), and thus prohibits the Melrose event by which most pores are filled during convention imbibition; this prohibition also eliminates the possibility of disconnecting gas phase within clusters of pores, so gas trapping does not occur. Consequently, hydrate grows to occupy exactly the same “footprint” occupied by the initial gas saturation. The final hydrate saturation and distribution is therefore identical to the initial gas. Scenario B, on the other hand, allows water supply freely, i.e. rapid compared to rate of hydrate formation. In this case the hydrate formation process at the pore scale looks more like conventional imbibition, where both Melrose jumps and the disconnection and trapping of gas in pores take place. The model identifies incremental movement of gas-hydrate-water interfaces in pore throats and at pendular rings during imbibition as well as Melrose events, in which water invades a pore or cluster of pores in a spontaneous jump. Hydrate is assumed to continue to grow at interfaces as they move incrementally. But since hydrate grows into the gas phase, the water-filled pores cannot be converted to hydrate. On the other hand all the trapped gas is converted into hydrate. The net effect is that Scenario B yields a smaller hydrate saturation, and the hydrate occupies only a subset of the initial “footprint” of the gas phase.

The pore scale model is based on the presumption that both gas and water are sufficient for hydrate formation. This does not preclude the other assumption in the field scale, that is, the reservoir gas is the limiting phase. In this model, we assume a conventional gas reservoir before hydrate formation occurs. Gas is disconnected from the source. Thus when BGHSZ moves downwards into the reservoir (originally above the reservoir), water invasion has to occur to

compensate the fluid loss and pressure decrease due to hydrate formation, and changes the initial fluid distribution in the field scale. Based on this mechanism, a characteristic hydrate distribution pattern is obtained. The distribution features two distinct regions: the one with high hydrate saturation and the one with low hydrate saturation. Depending on the reservoir connectivity, the pattern is often repeated in the reservoir.

Both Mallik and Mount Elbert hydrate reservoirs have hydrate distribution profiles that fall between the limiting cases predicted by the imbibition model. In fact model predictions based on Scenario B gives reasonable agreement with the field data. This suggests that the rate of water supply was large during the descent of BGHSZ.

Gas Reservoir Conversion to Hydrate: Role of Pressure-Driven Fluid Phase Transport at Bed-Scale

Overview

The immediately preceding section describes the behavior associated with conversion of gas reservoirs to hydrate reservoirs from the pore-scale perspective. That perspective did not account explicitly for the mechanism by which gas and water were supplied to the hydrate stability zone. We now turn to examine this transport problem from the bed scale. The basic premise is simple: the same decrease in gas phase pressure that drives imbibition (by reducing the capillary pressure) can also drive viscous flow of both gas and aqueous phases to the hydrate stability zone. In the earlier sections of this report that treated the overall volumetric changes associated with hydrate formation, we saw that the fraction of fluid flow made up by the gas phase controlled the hydrate saturation in the upper portions of the reservoirs. Here we develop a model of pressure-driven transport and determine whether the calculated phase fluxes yield the hydrate saturation profile observed in Mt Elbert.

The model is based on the same conceptual model for the conversion process used in previous sections. In summary, the conversion results from the descent of the base of gas hydrate stability zone (BGHSZ) through gas accumulated in a sediment. Given the measured grain size distribution in the sediment column, the initial gas phase saturation is estimated from the profile of capillary entry-pressure with depth. The gas accumulation is assumed to be isolated so that methane transport occurs only within it. We will show that if water transport occurs only by co-current flow of gaseous and aqueous phases up to the hydrate stability zone (HSZ), it is not possible to create large hydrate saturations from large initial gas saturations. This is because typical relative permeability curves impose strong limitations on water flux. Thus the large hydrate saturations observed in Mt. Elbert and Mallik above the current BGHSZ suggest another form of water flow: water moves down through accumulated hydrate from above. This requires the aqueous phase to remain connected within the hydrate-bearing sediment. The ratio of aqueous phase permeability in the hydrate-bearing sediment to the aqueous phase relative permeability at residual gas saturation determines hydrate saturation profile.

We begin this section by setting the context for the bed-scale transport model. The goal is to recapitulate essential features from the preceding sections of this report, so that the model development is self-contained.

Context for Pressure-Driven Transport Model

Substantial amount of research has been conducted to provide predictive models of hydrate formation in sediments. Available models can be divided into three main categories: (1) models

predicting hydrate formation from methane-saturated water as it enters the gas hydrate stability zone (GHSZ) or by providing methane from a biogenic source in the GHSZ (Ginsburg 1998; B. Buffett 2000; Hensen & Wallmann 2005; Bhatnagar *et al.* 2006; Bhatnagar *et al.* 2007; Bhatnagar *et al.* 2008; Phirani *et al.* 2009), (2) models assuming hydrate formation at the interface between gas phase and aqueous phase as the methane gas phase enters the GHSZ (Xiaoli Liu & P. B. Flemings 2007; X Liu & P. Flemings 2006; Torres *et al.* 2004), and (3) model presuming that the base of GHSZ moves through pre-established gaseous and aqueous phases instead of presuming fluxes of fluid(s) into the GHSZ (Behseresht & Bryant 2011b). One motivation for the latter model was that some hydrate accumulations in the arctic such as that in Mt. Elbert, located in the southeastern portion of the Milne Point Unit (MPU) within the Alaska North Slope (ANS), are believed to be pre-established free gas columns converted into hydrate after being placed in the GHSZ (Boswell *et al.* 2009; T. S. Collett 1993; T. Collett 2002).

Adapting the latter model, Behseresht and Bryant (2011) achieved satisfactory matches with the hydrate saturation distribution from field data. They used a stoichiometric fixed-pore-volume model of hydrate formation from water and methane. Through considering the vertical variation in capillary entry pressure, i.e. variation in grain size distribution, as well as volume reduction during hydrate formation, leading to continuous flow of fluid phases during hydrate formation, they could mechanistically explain/predict the currently observed hydrate saturation distribution in the Mt. Elbert well deposits. Notably, the model explains why in unit C (Fig. 29a) the major methane hydrate accumulation is at the top lower-quality sand rather than the bottom better-quality deposit, and how a nearly uniform initial gas saturation profile leads to a sandwich-like hydrate saturation profile.

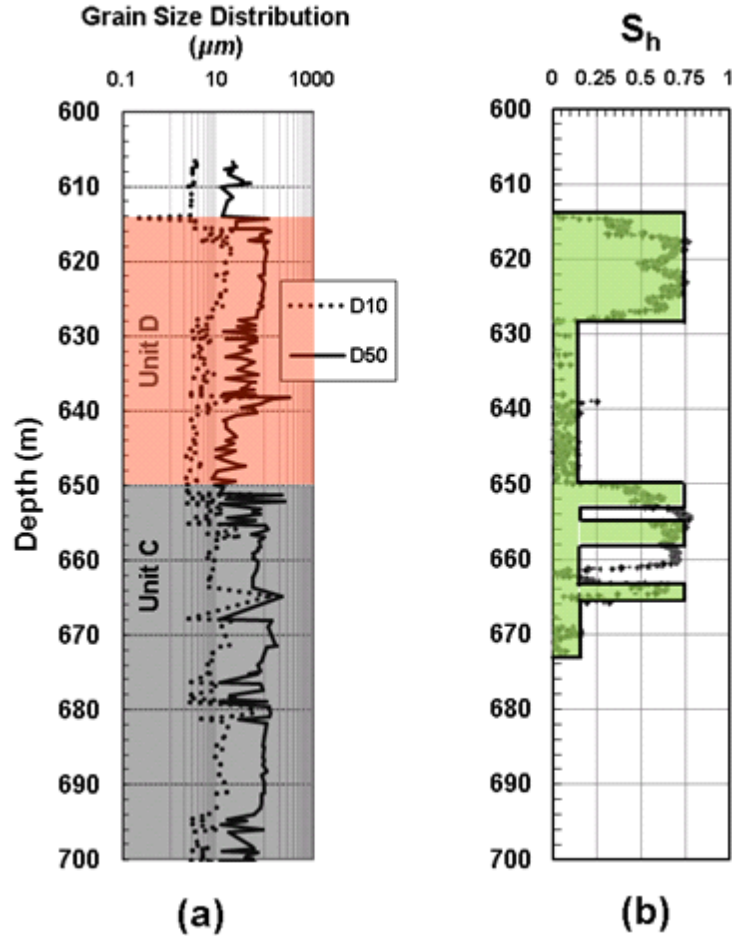


Fig. 29. (a) The 10th (D₁₀) and 50th (D₅₀) percentile of grain size extracted from core data (Rose *et al.* 2011) versus depth in Mt. Elbert well. The depth range shown, 600-700m, includes two sand units informally designated as sand unit D and C by Collett (T. S. Collett 1993). (b) Predicted final hydrate saturation (green area) by Behseresht and Bryant model forms a sandwich of large and small values. An R_v value of ≈ 0.55 was used in this case. The log derived hydrate saturations are shown as dots (Behseresht & Bryant 2011b).

It was shown that to have a hydrate saturation distribution as currently observed in Mt. Elbert, abundant amount of fluids, up to 1.4 pore volumes for Mt. Elbert case, should have been transported into the hydrate-bearing zones. It was also shown that the gas phase volume fraction, R_v in Eq. (37), of the total transported fluid volume, $\Delta V_g + \Delta V_w$, is directly related to the final hydrate saturation in a sediment zone, given the initial fluid phase saturations, $S_{w,i}$ and $S_{g,i}$. (Behseresht & Bryant 2011b). That work did not propose a mechanism for the fluid transport, however.

$$R_v = \frac{\Delta V_g}{\Delta V_g + \Delta V_w} \quad (37)$$

In this section we review some key elements of the stoichiometric model applied to model hydrate formation in porous media and then discuss an important new aspect of the model: What parameters control the value of R_v and thus the resulting hydrate saturation in the host sediments. It is assumed that the alternative to fluid movement as a result of volume reduction associated with hydrate formation, which is compaction or grain rearrangement within the sediment, can be

neglected (Behseresht & Bryant 2011b). We also assume that methane that moves to the GHSZ is subsequently converted to hydrate. For simplicity we also assume that CH₄ is the only constituent of the gas phase and the only guest molecule in the hydrate. We assume that the aqueous phase has a small initial salinity and that any buildup in salinity caused by incorporation of H₂O into hydrate is rapidly dissipated into an unlimited reservoir of brine. The gas column is assumed to be no longer connected to its source and thus the gas mass is fixed. Finally, the heat diffusion coefficient is about 500 times larger than the salinity transport coefficient, so we neglect the effect of heat transfer on limiting hydrate formation.

Figure 30 shows a box of sediment with total pore volume V_{tot} containing an initial water saturation and methane saturation of $S_{w,i}$ and $S_{g,i}$, respectively. For the sake of visualization, the gas and aqueous phases are shown as if they occupied separate subvolumes. The box of sediment is assumed to be open to methane and water flow to compensate for the volume reduction associated with the hydrate formation inside the box. It is assumed that the thermodynamic condition, P and T , is appropriate for hydrate formation inside the box and hydrate keeps forming until one of the constituents inside the box, water or methane, is entirely consumed. The final hydrate saturation, $S_{h,f}$ inside the box is governed by the proportion of gas and water entering the sediment, i.e. R_v , as shown in Eq. (38).

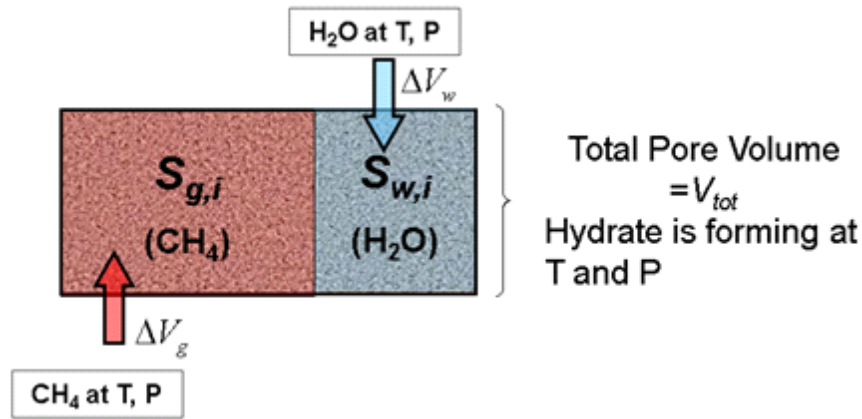


Fig. 30. Sediment box with total pore volume V_{tot} filled with water and methane. The sediment is under a pressure/temperature suitable for hydrate formation. The box is open to water and methane flow from outside.

$$S_{h,f} = \begin{cases} \frac{\bar{V}_h}{R_v(\bar{V}_h - \bar{V}_g - N\bar{V}_w) + \bar{V}_g} S_{g,i} & ; R_v < R_{v,stoich} \\ 1 & ; R_v = R_{v,stoich} \\ \frac{\bar{V}_h}{(\bar{V}_h - \bar{V}_g)(1 - R_v) + N\bar{V}_w R_v} S_{w,i} & ; R_v > R_{v,stoich} \end{cases} \quad (38)$$

Here \bar{V}_h , \bar{V}_w and \bar{V}_g are hydrate molar volume, water molar volume and methane molar volume at pressure P and temperature T . $R_{v,stoich}$ is defined as a value of R_v for which $S_{h,f}=1$. It can be shown that $R_{v,stoich}$ is related to the initial gas saturation by Eq. (39).

$$R_{v,stoich} = \frac{\bar{V}_g - \bar{V}_h S_{g,i}}{\bar{V}_g + N\bar{V}_w - \bar{V}_h} \quad (39)$$

Given an initial gas/water saturation inside the sediment box in Fig. 30, the dimensionless volume of fluids transported into the sediment, $\Delta V_{g,d}$ and $\Delta V_{w,d}$, is related to the final hydrate saturation inside the sediment by Eqs. (40) and (41). Dimensionless volumes are in units of pore volume and are calculated by dividing the absolute volumes, ΔV_g and ΔV_w , by the total pore volume of the sediment, V_{tot} .

$$\Delta V_{g,d} = R_v \left(\frac{N\bar{V}_w + \bar{V}_g}{\bar{V}_h} - 1 \right) S_{h,f} \quad (40)$$

$$\Delta V_{w,d} = (1 - R_v) \left(\frac{N\bar{V}_w + \bar{V}_g}{\bar{V}_h} - 1 \right) S_{h,f} \quad (41)$$

The gas phase fraction denoted by $R_{v,1:1}$ represents a neutral point between imbibition (i.e. increase in S_w from its initial value, $S_{w,i}$) occurring during hydrate formation for $R_v < R_{v,1:1}$ and drainage (i.e. decrease in S_w from its initial value, $S_{w,i}$) occurring for $R_v > R_{v,1:1}$. They showed that the value of $R_{v,1:1}$ is independent of initial saturations (Eq. (42)):

$$R_{v,1:1} = \frac{\bar{V}_g - \bar{V}_h}{N\bar{V}_w + \bar{V}_g - \bar{V}_h} \quad (42)$$

In summary, this model allows the full range of behavior, from only aqueous phase entering the sediment box to fill the volume ($R_v = 0$) to only gas phase entering ($R_v = 1$). For $0 < R_v < R_{v,1:1}$ the aqueous phase coexists with hydrate at the final state and $S_{w,f} = 1 - S_{h,f} < S_{w,i}$, so that imbibition occurs during hydrate formation. For $R_{v,1:1} < R_v < R_{v,stoich}$, aqueous phase and hydrate coexist at the final state, but some drainage has occurred, so that $S_{w,f} = 1 - S_{h,f} > S_{w,i}$. Finally, for $R_{v,stoich} < R_v < 1$, the gas phase coexists with hydrate at the final state, with $S_{g,f} = 1 - S_{h,f}$. The situation commonly encountered in regions between the base of permafrost and the BGHSZ is an aqueous phase coexisting with hydrate. The hydrate phase can be present in trace amounts, $S_h < 0.10$, or in rich layers (many meters of sediment) with $0.5 < S_h < 0.8$. In the latter case, of order one pore volume of gas and aqueous phases must move into the layer, with roughly equal volumes of each phase.

Flow Model for Gaseous and Aqueous Flow into the GHSZ

The driving force for fluid phase movement is the reduction in volume occupied by the gas/aqueous/hydrate phases when hydrate forms from gas and aqueous phase components. We wish to determine gas phase and aqueous phase movements independently, and thereby determine the value of R_v . To do this it is first necessary to know the mechanisms through which gaseous and aqueous phase arrive into the zone of hydrate formation while hydrate is forming in an interval newly introduced into the GHSZ. Figure 31 illustrates a sand unit with a gas column established below a seal at depth, h_1 .

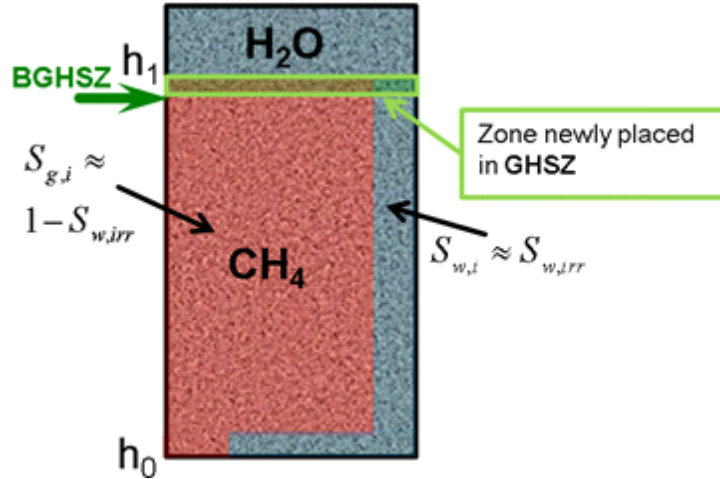


Fig. 31. A sand unit having a seal at depth, h_1 is shown. A gas accumulation is established below the seal. The BGHSZ was above the gas column when the gas column was established. The BGHSZ is descending through the sediment column. The zone recently placed in the GHSZ is shown within a green fill on the sediment column.

The BGHSZ has just moved into the gas-bearing zone and hydrate can form inside the zone shown with a green box. Because of the very low ratio of aqueous to gas phase mobilities, steady co-current flow of aqueous phase and gas phase from below the BGHSZ cannot supply the amount of water required, $\Delta V_{w,d}$ (Behseresht & Bryant 2011a). Instead, a piston-type movement of gas would arise, with the aqueous phase following much more slowly from below, as shown in Fig. 32.

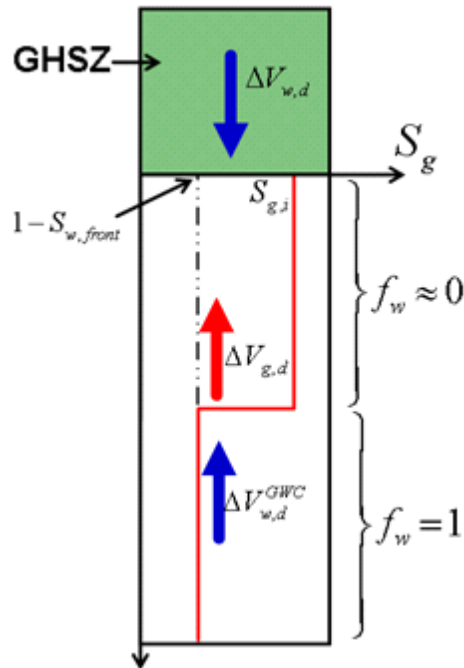


Fig. 32. Schematic for the transported volumes of aqueous and gas phase when hydrate is forming at the base of GHSZ. Fractional flow theory proves it unlikely that the required amount of aqueous phase, $\Delta V_{w,d}$, has been transported through an upward co-current flow with the gas phase. Instead we suppose it to have come through the hydrate-bearing sediment above BGHSZ.

Because aqueous phase viscosity is much larger than that of the gas phase, the aqueous phase mobility λ_w is much smaller than that of the gas phase λ_g for almost any reasonable set of relative permeability curves (Behseresht & Bryant 2011a). Consequently, the saturation just upstream of the front, $S_{w,front}$, would be almost the same for all initial water saturations: $S_{w,front} \approx 1 - S_{gr}$, where S_{gr} is the residual gas saturation. The corresponding fractional flow of water would be $f_{w,front} \approx 1$. Just ahead of the front, the water saturation is $S_w = S_{w,i}$ and $f_w \approx 0$. Thus only gas is arriving ($f_g = 1 - f_w \approx 1$) at the BGHSZ. This piston type movement of a methane bank ahead of the water bank can provide the upper zones in which hydrate is forming with the needed gas, $\Delta V_{g,d}$. Simultaneously this piston type movement of aqueous phase would require the transport of water, $\Delta V_{w,d}^{GWC}$, to replace transported gas from below and thereby raise the gas-water contact (GWC). But clearly the cocurrent flow cannot have transported water into the zone of hydrate formation.

The need for considerable amount of water, $\Delta V_{w,d}$, during hydrate formation requires a different route for water flow. We propose that water moves down through accumulated hydrate from the unfrozen water above (Fig. 32). (Such water exists, because the base of permafrost is always above the BGHSZ.) For this to happen the water phase must remain connected within the hydrate-bearing sediment. This requires the final hydrate saturation at the upper zones to be less than $1 - S_{w,irr}$ so the aqueous phase is connected at the final water saturation. Behseresht and Bryant (2011b) predict that this condition will arise, because imbibition occurs in the upper zones as the GWC rises and causes the capillary pressure to decrease as the height of the gas column decreases.

In the following, the model illustrated in Fig. 32 is formulated and applied on one of the sand units in Mt. Elbert well. Gas is assumed to have a piston type cocurrent flow. Figure 33 shows the sand unit in Fig. 31 when the BGHSZ has moved down through a portion of the original gas column. The figure shows the situation once the BGHSZ has moved from depth, $h_1 + L_h$ to $h_1 + L_h + \Delta L_h$. The gas accumulation between h_1 and $h_1 + L_h$ has been fully consumed to form hydrate and the pore space is filled with hydrate and water only, i.e. $R_v < R_{v,stoich}$. As hydrate forms in the ΔL_h interval newly placed in the GHSZ, the flow of aqueous phase, q_w , and gas phase, q_g , takes place. Aqueous phase pressure is assumed hydrostatic and the pressure at depths h_1 and h_0 are assumed undisturbed, i.e. hydrostatic, by the change in pressure due to the volume change associated with the hydrate formation in the ΔL_h interval (Fig. 33). At the moment shown in Fig. 33, the GWC is at a depth of $h_0 - L_w$. As hydrate forms in the ΔL_h interval, GWC keeps moving upward to accommodate the transport of gas to the zone of hydrate formation above. Permeability to aqueous phase flow in the hydrate-bearing zone in the interval $[h_1, h_1 + L_h]$ is denoted as $k_{w,h}$. The permeability to gas phase flow in the interval $[h_0 - L_w, h_0 - L_i]$ is denoted as k_g and the permeability to aqueous phase flow below the depth of $h_0 - L_w$ is shown as k_w .

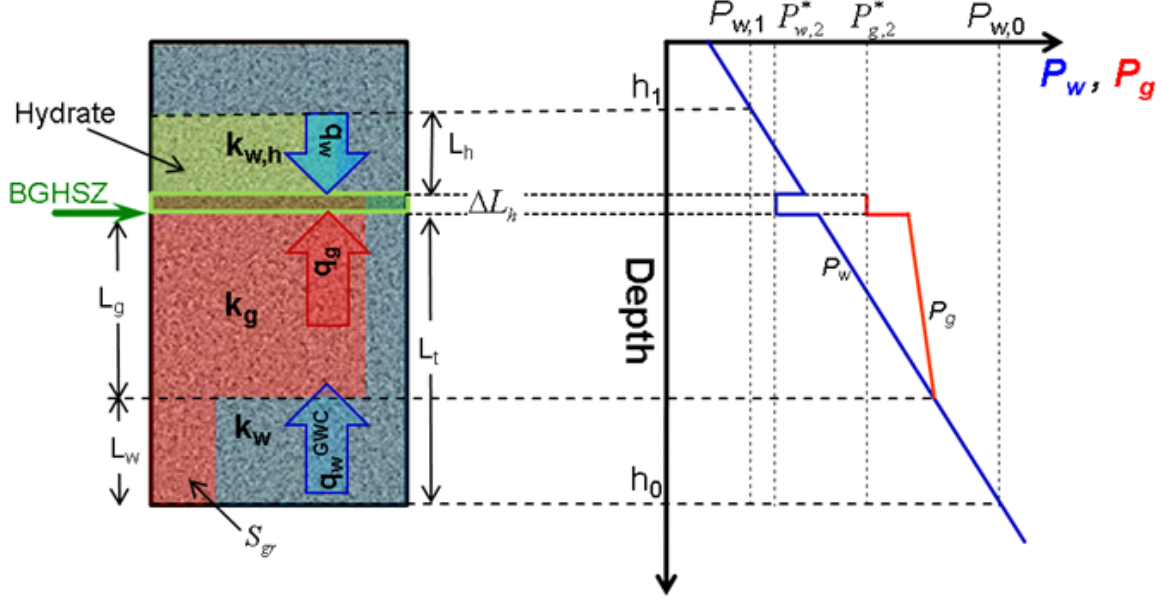


Fig. 33. The sand unit of Fig. 31 when the BGHSZ has moved down through a portion of the gas column. There is L_h meters accumulation of hydrate above the current location of the BGHSZ. The GWC has moved upward (compare to Fig. 31) to depth $h_0 - L_w$. The gas below the GWC has been transported upward and the gas saturation is S_{gr} . The phase pressure state inside the sediment is shown by a companion graph of pressure versus depth. The capillary pressure $P_g - P_w$ is zero at the GWC. The decrement in pressure at the BGHSZ indicates schematically the effect of the phase volume reduction accompanying hydrate formation.

The volume reduction associated with hydrate formation in the interval ΔL_h in Fig. 33 is assumed to decrease the aqueous phase pressure at the BGHSZ to a value $P_{w,2}^*$ from its original hydrostatic value $P_{w,2} = P_{w,1} + \rho_w g L_h$. For an increment of hydrate, dS_h , the corresponding consumed amount of water and gas is calculated from Eqs. (43) and (44) (Behseresht & Bryant 2011a).

$$dS_w^{used} = \frac{N\bar{V}_w}{\bar{V}_h} dS_h \quad (43)$$

$$dS_g^{used} = \frac{\bar{V}_g}{\bar{V}_h} dS_h \quad (44)$$

For the initial fluid phase saturations, a total fluid compressibility can be calculated as:

$$c_t = S_{w,i}c_w + S_{g,i}c_g \quad (45)$$

If no fluid were to enter the interval ΔL_h then the pressure change, dP , associated with the consumed volume of gaseous and aqueous phase, is calculated from Eq. (46).

$$dP = -\frac{1}{c_t} \frac{dV}{V_{tot}} = -\frac{1}{c_t} dS = -\frac{1}{c_t} (dS_w^{used} + dS_g^{used} - dS_h) \quad (46)$$

Combining Eqs. (43), (44) and (46) gives:

$$dP = \frac{-1}{c_t} \left(\frac{N\bar{V}_w + \bar{V}_g}{\bar{V}_h} - 1 \right) dS_h \quad (47)$$

Therefore, the pressure, $P_{w,2}^*$, after a decrement of dS_w^{used} and dS_g^{used} is calculated as:

$$P_{w,2}^* = [1 - \frac{1}{P_{w,2} \times c_t} (\frac{N\bar{V}_w + \bar{V}_g}{\bar{V}_h} - 1) dS_h] P_{w,2} = [1 - \frac{1}{(P_{w,1} + \rho_w g L_h) c_t} (\frac{N\bar{V}_w + \bar{V}_g}{\bar{V}_h} - 1) dS_h] (P_{w,1} + \rho_w g L_h) \quad (48)$$

The reduction in pressure will induce flow in both gaseous and aqueous phases. From Darcy's law, the downward flow of water through the hydrate-bearing zone, q_w , would be:

$$q_w = \frac{A k_{w,h}}{\mu_w} [\frac{P_{w,1} - P_{w,2}^*}{L_h} + \rho_w g] \quad (49)$$

where A is the cross sectional area, g is the acceleration due to gravity and ρ_w is density of aqueous phase. Substituting Eq. (48) in (49) after simplifying gives:

$$q_w = A \frac{1}{c_t} \frac{N\bar{V}_w + \bar{V}_g}{\bar{V}_h} \frac{k_{w,h}}{L_h \mu_w} dS_h \quad (50)$$

A check for the above equation is that if no hydrate forms, $dS_h = 0$, and thus $q_w = 0$, as is expected.

For the upward piston type flow of gas and water from below Darcy's law can be applied as:

$$\begin{cases} q_w^{GWC} = \frac{A k_w}{\mu_w} [\frac{P_{w,0} - P}{L_w} - \rho_w g] \\ q_g = \frac{A k_g}{\mu_g} [\frac{P - P_{g,2}^*}{L_g} - \rho_g g] \end{cases} \quad (51)$$

where P is the flowing water pressure at the GWC and can be calculated from Eqs. (53) and (54). For the vertical flow of gaseous and aqueous phases we make the usual fractional flow theory assumption that:

$$q_w^{GWC} = q_g \quad (52)$$

Combining the two equations in Eq. (51) and the equation in Eq. (52) gives:

$$\begin{cases} P_{w,0} - P = q_g \frac{L_w}{A \lambda_w} + \rho_w g L_w \\ P - P_{g,2}^* = q_g \frac{L_g}{A \lambda_g} + \rho_g g L_g \end{cases} \quad (53)$$

Adding the two equations in Eq. (53) and simplifying gives:

$$q_g = \frac{A}{\frac{L_w}{\lambda_w} + \frac{L_g}{\lambda_g}} [(P_{w,0} - P_{g,2}^*) - (\rho_w L_w + \rho_g L_g) g] \quad (54)$$

Similar to $P_{w,2}^*$, the corresponding pressure for the gas phase in the hydrate formation zone, $P_{g,2}^*$, when an increment of hydrate, dS_h , forms can be expressed in terms of the equilibrium gas pressure, $P_{w,2} + \Delta\rho_w g L_g$, and Eq. (47):

$$\begin{aligned} P_{g,2}^* &= \left(1 - \frac{1}{P_{g,2} c_t} \frac{N \bar{V}_w + \bar{V}_g}{\bar{V}_h} dS_h\right) P_{g,2} \\ &= \left(1 - \frac{1}{(P_{w,0} - \rho_w g L_t + \Delta\rho_w g L_g) c_t} \frac{N \bar{V}_w + \bar{V}_g}{\bar{V}_h} dS_h\right) (P_{w,0} - \rho_w g L_t + \Delta\rho_w g L_g) \end{aligned} \quad (55)$$

Combining Eqs. (44), (54) and (55) gives the upward gas flow as:

$$q_g = \frac{1}{c_t} \frac{N \bar{V}_w + \bar{V}_g}{\bar{V}_h} \frac{A}{\frac{L_w}{\lambda_w} + \frac{L_g}{\lambda_g}} dS_h \quad (56)$$

We now have the rate of aqueous phase transport to the BGHSZ from above, Eq. (50), and the rate of gaseous phase transport to the BGHSZ from below, Eq. (56). We use these in the next section to determine R_v as a function of the phase relative permeabilities.

Calculating R_v from Aqueous and Gaseous Phase Flows

For this one-dimensional flow, Eq. (57) holds.

$$\frac{q_g}{q_w} = \frac{u_g}{u_w} \quad (57)$$

By definition, $R_v = \frac{q_g}{q_g + q_w}$ and thus:

$$\frac{u_g}{u_w} = \frac{R_v}{1 - R_v} \quad (58)$$

Based on the Buckley-Leverett shock (Buckley & Leverett 1942), shown in Fig. 32, the upward Darcy velocity of gaseous phase, u_g , can be expressed in terms of the water front speed, dL_w/dt as in Eq. (59).

$$u_g = (S_{g,i} - S_{gr}) \phi \frac{dL_w}{dt} \quad (59)$$

where ϕ is the average porosity of the porous media through which the flow is taking place. Dividing Eq. (56) by Eq. (50) gives the left side of Eq. (57) from which R_v can be calculated:

$$\frac{u_g}{u_w} = \frac{k_w}{k_{w,h}} \frac{L_h}{M L_t + L_w(1 - M)} \quad (60)$$

where M is the mobility ratio defined as:

$$M = \frac{k_w / \mu_w}{k_g / \mu_g} \quad (61)$$

Defining a length L_w^* so that $u_w = \frac{dL_w^*}{dt}$ we express the ratio of phase velocities as:

$$\frac{u_g}{u_w} = \frac{(S_{g,i} - S_{gr})\phi \frac{dL_w}{dt}}{\frac{dL_w^*}{dt}} = \frac{(S_{g,i} - S_{gr})\phi \times dL_w}{dL_w^*} = (S_{g,i} - S_{gr})\phi \frac{\Delta L_w}{\Delta L_w^*} \quad (62)$$

R_v can be evaluated from Eqs. (58) and (62) as:

$$R_v = \frac{(S_{g,i} - S_{gr})\phi \Delta L_w}{(S_{g,i} - S_{gr})\phi \Delta L_w + \Delta L_w^*} \quad (63)$$

Combining Eqs. (60) and (62) gives:

$$\frac{(S_{g,i} - S_{gr})\phi \times dL_w}{dL_w^*} = \frac{k_w}{k_{w,h}} \frac{L_h}{ML_t + L_w(1 - M)} \quad (64)$$

$$\Rightarrow \frac{dL_w}{dL_w^*} = \frac{\xi}{ML_t + L_w(1 - M)} \quad (65)$$

where,

$$\xi = \frac{k_w}{k_{w,h}} \frac{L_h}{(S_{g,i} - S_{gr})\phi} \quad (66)$$

The dynamic quantity in Eq. (66) is the thickness of the hydrate zone L_h and the overall permeability of the hydrate-bearing interval, $k_{w,h}$. Thus Eq. (64) relates the rate at which the gas-water contact moves to the thicknesses of the hydrate zone, the remaining gas column L_t and the residual gas zone L_w . The influence of the relative permeability curves appears in the mobility ratio M because of co-current flow in the gas column. These curves also determine the ratio of aqueous phase permeability below the GWC, k_w , to the aqueous phase permeability in the hydrate-bearing sediment, $k_{w,h}$, which affects the magnitude of ξ in Eq. (66). Rearranging and integrating Eq. (65) gives:

$$\int_0^{\Delta L_w} (1 - M)L_w dL_w + \int_0^{\Delta L_w} ML_t dL_w = \int_0^{\Delta L_w^*} \xi dL_w^* \quad (67)$$

Hence,

$$\Delta L_w^* = \frac{1}{\xi} \left[\frac{(1 - M)}{2} \Delta L_w^2 + ML_t \Delta L_w \right] \quad (68)$$

Based on the above discussion, when the BGHSZ moves down from $h_1 + L_h$ to $h_1 + L_h + \Delta L_h$, the following algorithm can be used to calculate R_v and thus hydrate saturation, S_h , in the ΔL_h interval newly introduced in the GHSZ:

- a. Start with an initial guess for $R_v = R_{v,temp}$

- b. Calculate ΔL_w from Eq. (34).

The required pore volume of gas required to be transported into the ΔL_h interval, $\Delta V_{g,d}$, which is a function of R_v can be calculated from Eq. (40). This amount of gas will be provided through sweeping ΔL_w meters of the gas column by the water front from below; therefore:

$$A\phi(S_{g,i} - S_{gr})\Delta L_w = A\phi\Delta L_h\Delta V_{g,d} \quad (69)$$

Hence,

$$\Delta L_w = \frac{\Delta V_{g,d}}{S_{g,i} - S_{gr}} \Delta L_h \quad (70)$$

- c. Calculate ΔL_w^* from Eq. (68).
d. Update the value of $R_{v,temp}$ using Eq. (63).
e. If $|R_v/R_{v,temp} - 1| > 0.001$ go to Step a.
f. $R_v = R_{v,temp}$ is the final calculated R_v for forming hydrate in the interval ΔL_h .

From the calculated value of R_v , the final hydrate saturation in the ΔL_h new hydrate-bearing interval is calculated from Eq. (38) Hence this model provides an *a priori* method of estimating R_v , the gas phase fraction of the total phase volume arriving at the BGHSZ. We use the above algorithm to predict the hydrate saturation distribution, given the initial distribution of phase saturations (before descent of BGHSZ), the P and T of the GHSZ, the residual gas saturation, the relative permeabilities of gaseous and aqueous phases, and the aqueous phase relative permeability when hydrate occupies sediment pore space.

$$k_{w,h} = \frac{L_h + \Delta L_h}{\frac{L_h}{k_{w,L_h}} + \frac{\Delta L_h}{k_{w,\Delta L_h}}} \quad (71)$$

There are several models to estimate the aqueous phase permeability in the presence of hydrate. Here, we assume that hydrate fills center of the pores and thus a pore-filling permeability model applies. Let the permeability of non-hydrate-bearing sediment in the ΔL_h interval be denoted k . Based on the pore-filling model (Kleinberg *et al.* 2003), if the hydrate saturation in the interval is S_h , the permeability to aqueous phase of the hydrate-bearing ΔL_h interval, $k_{w,\Delta L_h}$ is calculated from Eq. (72).

$$k_{w,\Delta L_h} = \frac{(1 - S_h)^{n+2}}{(1 + \sqrt{S_h})^2} k \quad (72)$$

where n is the hydrate saturation exponent. Neglecting the effect of capillary pressure, the saturation exponent increases from $n = 0.4$ at $S_h = 0.1$ to unity at $S_h = 1$ (Spangenberg 2001; Kleinberg *et al.* 2003).

Application of Transport Model to Mt Elbert

The above model is applied on the D sand unit of Mt. Elbert well. First, the profile of absolute permeability of the sand unit versus depth is established. For the grain size distribution in Mt. Elbert well, Eq. (73) can be used to estimate the permeability at each depth as a function of grain size distribution at that depth:

$$k = 6 \times 10^{-4} \log\left(500 \frac{D_{10}}{D_{60}}\right) D_{10}^2 \quad (73)$$

where, D_{10} and D_{60} are the 10th and 60th percentile of the grain diameter distribution, respectively (Behseresht & Bryant 2011b). Figure 34 shows the estimated permeability versus depth in the D sand unit based on the grain size distribution shown in Fig. 29a.

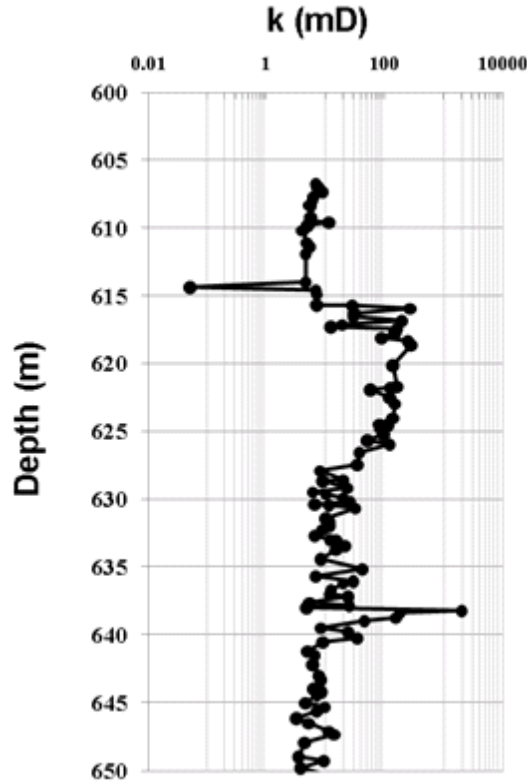


Fig. 34. Estimated permeability from Eq. (73) based on grain size distribution data for the D sand unit in Mt. Elbert well. Grain size variation versus depth is shown in Fig. 29a.

To calculate the mobility ratio, M , of aqueous to gaseous phase, for the upward piston type co-current flow, the end-point relative permeabilities of aqueous and gaseous phase are needed. Here a typical pair of end-point relative permeability values for water-wet sediments is used: 0.3 for water and 0.7 for methane, as shown on the typical relative permeability curve for water-wet sediment in Fig. 35. Dynamic methane viscosity, μ_g , is estimated to be 1.2×10^{-5} Pa.s at the current depth-averaged pressure and temperature of the sand unit ($P = 6.5$ MPa and $T = 2^\circ\text{C}$) (Huang *et al.* 1966). At the same thermodynamic condition, viscosity of water, μ_w , is estimated to be 1.7×10^{-3} Pa.s (Stanley & Batten 1969). Thus M is 3×10^{-3} . Note that due to the hundred-fold difference in gas and aqueous phase viscosities, we have $M \ll 1$ for typical ratios of end point relative permeabilities.

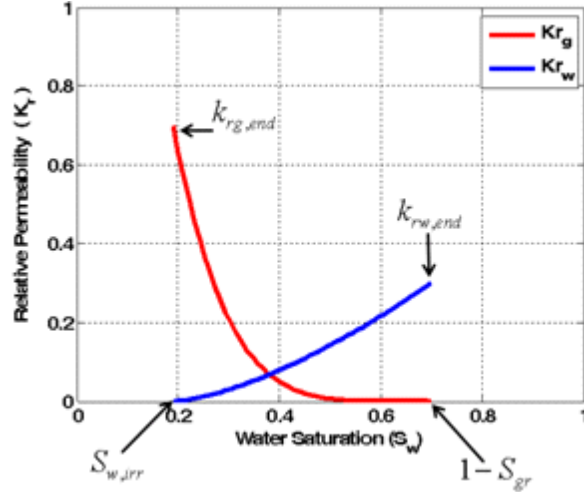


Fig. 35. Typical relative permeability curves for a water-wet sediment; red represents the relative permeability of gaseous phase and blue represents that of the aqueous phase. The end point relative permeabilities, along with the end point saturations are shown on the graph.

We apply the above model (Fig. 31), starting with the same initial gas saturation profile as that estimated by Behseresht and Bryant (2011b) based on the capillary entry pressure profile calculated from the grain size distribution at each depth. The initial gas saturation profile in the D sand unit can be approximated by that shown in Fig. 31 having $h_0 = 650$ m, $h_1 = 614$ m, $S_{w,irr} = 0.18$ and $S_{gr} = 0.3$ (Behseresht *et al.* 2009).

Figure 36a shows the calculated R_v versus depth with a solid black line as the BGHSZ moves down through the methane/water bearing sediment. The reason that R_v values increase with depth from the upper part of the unit is that as the BGHSZ moves downward and the length of hydrate-bearing sediment, L_h , increases, the overall permeability of the hydrate bearing sediment, $k_{w,h}$ decreases. This reduces the water flow rate from above which is equivalent to an increase in R_v . The R_v in the imbibed zone below 630 m, swept by water to the end-point saturation $1 - S_{gr}$, is zero. This is because when BGHSZ descends into the residual gas zone, no more gas is available to flow upwards as all gas saturation below BGHSZ is at residual. Examination of Eqs. (63) and (68) shows that the calculated R_v , and hence the predicted hydrate saturation profile, is independent of the porosity, ϕ . In fact, for a given initial gas water saturation, the ratio $k_w/k_{w,h}$ is the main parameter governing R_v under a fixed thermodynamic condition (i.e. at fixed T and P , hence $\bar{V}_g / N\bar{V}_w = const$).

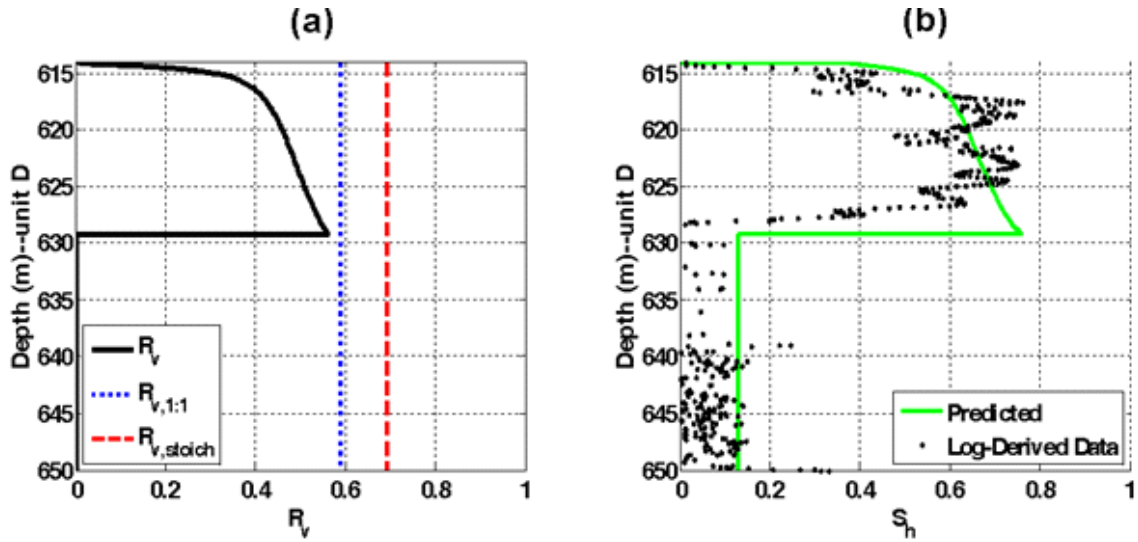


Fig. 36. Application of the pressure-driven fluid transport model to the D sand unit in Mt. Elbert well using an end-point $k_{r,w}=0.3$. $k_{w,h}$ is determined from Eq. (71). (a) R_v versus depth shown in solid black line. R_v is zero below 629 m because the gas saturation dropped to residual there as gas moved upward to the BGHSZ. The values of $R_{v,1:1}$ and $R_{v,stoich}$ are shown in dotted line and dashed line, respectively. (b) Predicted hydrate saturation profile in green solid line. Dots represent the log-derived hydrate saturation data (Rose *et al.* 2011).

The calculated value of R_v determines the hydrate saturation at each depth. Figure 36b shows the predicted hydrate saturation profile along with the log-derived hydrate saturation data of the D sand unit in Mt. Elbert well (Rose *et al.* 2011). Note that the hydrate saturation profile shown in green solid line (Fig. 36b) evolved from an initially uniform gas saturation profile with $S_{g,i} \approx 1 - S_{w,irr} = 0.8$ filling almost the entire D sand unit. The agreement with the measured values of S_h is reasonable. The trend of increasing S_h from 614 m to 620 m is evident, as is the small but nonzero S_h between 630 m and 650 m.

Applying the model on D sand unit in Mt. Elbert well with a smaller end-point relative permeability for aqueous phase compared to that in Fig. 35, $k_w = 0.1$, predicts a longer hydrate column but at smaller saturation as shown in Fig. 37. The reason is that the smaller aqueous phase end-point relative permeability slows the rate at which gas can move to the BGHSZ, causing R_v to be smaller, and hence S_h to be smaller. The mass of gas converted to hydrate is the same as in Fig. 36, so the smaller S_h requires a longer column in the upper hydrate-bearing zone than in Fig. 36.

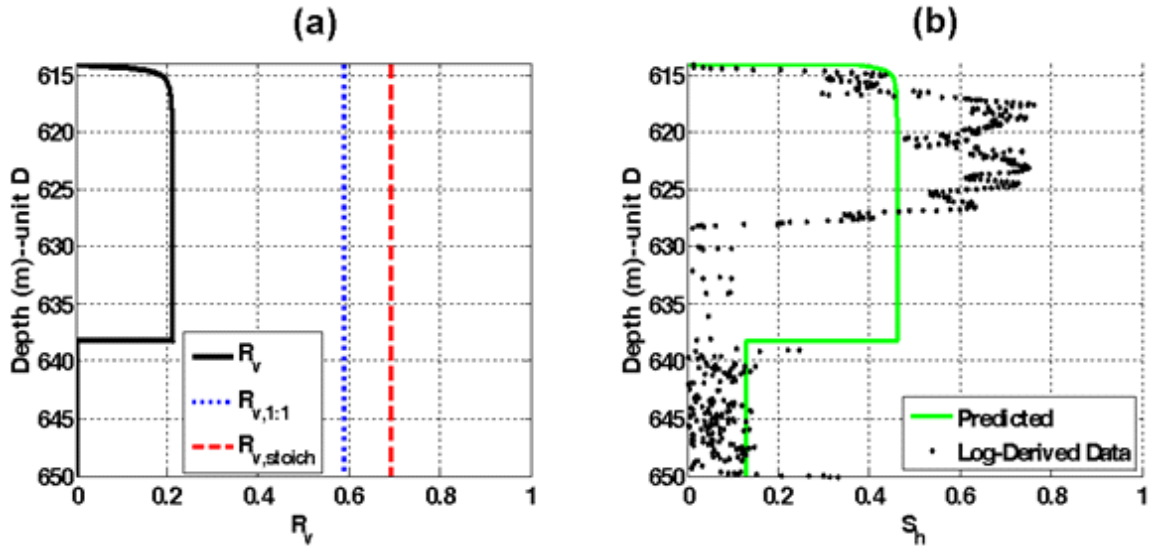


Fig. 37. Application of the pressure-driven fluid transport model to the D sand unit in Mt. Elbert well using an end-point $k_{r,w} = 0.1$ yields smaller R_v and correspondingly thicker upper zone of hydrate at a smaller saturation than in Fig. 36. (a) R_v versus depth shown in solid black line. (b) Predicted hydrate saturation profile in green solid line. Dots represent the log-derived hydrate saturation data (Rose *et al.* 2011).

Figure 38b shows the predicted hydrate saturation profile when the end-point relative permeability to aqueous phase is changed from 0.3 (in Fig. 35) to 0.5. The larger value enables more rapid transport of gas to the BGHSZ, causing R_v to increase. This results in larger hydrate saturations. This reduces the aqueous phase permeability in the hydrate-bearing sediment, causing R_v to increase further. In the present model, this feedback leads to complete conversion of aqueous phase saturation to hydrate, yielding $S_h = 1$ in the upper part of the column. This prevents subsequent transport of water from above the BGHSZ. Thus the hydrate saturation below this point corresponds only to converting the existing initial water saturation, and a large gas saturation is predicted to remain unconverted (pink box in Fig 38). Neither the hydrate saturation profile nor the presence of a gas saturation is consistent with observations.

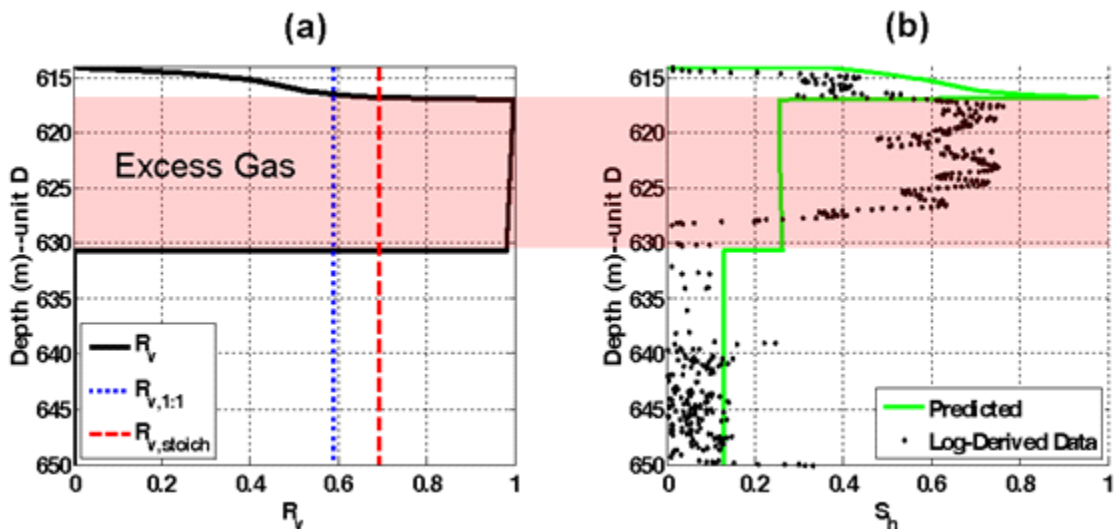


Fig. 38. Applying the fluid model along with the stoichiometric model on the D sand unit in Mt. Elbert well using an end-point $k_{r,w} = 0.5$ yields a qualitatively different behavior than Figs. 36 and 37. (a) R_v versus

depth shown in solid black line. Calculated R_v from the flow model exceeds $R_{v,stoich}$ in part of the sand unit which is shown with a red fill. (b) Predicted hydrate saturation profile in green solid line. The zone identified with red fill contains hydrate and gas only which is in contradiction to the observed profile in field having hydrate and water only.

Discussion of Pressure-Driven Transport Model

Comparing the above figures it is evident that Mt. Elbert agrees more with $k_{rw,end} = 0.3$, Fig. 36. Therefore, the proposed model is consistent with typical relative permeability curves and typical end-point relative permeabilities. However, the model is sensitive to the endpoint aqueous phase effective permeability $k_{rw,end}$. In fact, the ratio of $k_{rw,end}/k_{w,h}$ is also crucial to the behavior of the model. The same sensitivity shown in Figs. 37 and 38 would also apply if the value of permeability to aqueous phase in the hydrate-bearing sediment $k_{w,h}$ were to change by a factor of two. Laboratory experiments reported in the literature suggest that this permeability is highly sensitive to hydrate saturation, and in any case it will also depend strongly on the variation in grain size within the hydrate-bearing sediment. Moreover the model contains a feedback loop, in that larger $k_{rw,end}$ yields larger hydrate saturations, which cause smaller values of $k_{w,h}$. This is the cause of the increase in S_h with depth between 614 and 629 m in Fig. 36, and between 614 m and 617 m in Fig. 38. The hydrate saturation profiles predicted for smaller or larger values of $k_{rw,end}/k_{w,h}$ shown in Figs. 37 and 38 respectively, are not observed at Mt Elbert (M. W. Lee & T. Collett 2011).

Numerous hydrate accumulations in the Alaska North Slope exhibit saturation profiles qualitatively similar to Mt Elbert. Yet the pressure-driven transport model yields the behavior observed at Mt Elbert only for a rather narrow range of choices of $k_{rw,end}/k_{w,h}$. The range of choices seems particularly narrow considering the likely range of values in different accumulations. For these reasons, it seems unlikely that pressure-driven flow is responsible for supplying gas and aqueous phases to the hydrate stability zone during conversion. Physically, the problem with this model is that pressure-driven flow cannot supply aqueous phase from below the BGHSZ. The gas phase is supplied from below the BGSHZ at a rate proportional to $k_{rw,end}$ while the aqueous phase must be supplied from above at a rate proportional to $k_{w,h}$. The ratio $k_{rw,end}/k_{w,h}$ fixes the relative rates of gas and aqueous phase transport. These rates must be rather finely balanced to yield the observed saturation profiles.

The pressure-driven model neglects an important aspect of fluid flow in porous media, especially when water saturation approaches $S_{w,irr}$: capillary pressure gradients causing an extra water suction to keep the aqueous phase connected, i.e. $S_w \geq S_{w,irr}$. This is in analogy with the observed induced water suction during frost heave formation, which keeps the aqueous phase connected for continued heave formation (Penner 1959; Hermansson & Spencerguthrie 2005). Formation of hydrate is analogous in several respects to frost heave formation (Cook *et al.* 2008; J. Y. Lee *et al.* 2011; Rees *et al.* 2011). Once the aqueous phase saturation becomes close to the $S_{w,irr}$, further decrement of the aqueous phase saturation due to hydrate formation would cause a large capillary pressure gradient. This would transport aqueous phase to the zone to counteract the decrement in saturation. Because the gradient dP_c/dS_w is largest near $S_{w,irr}$, this mechanism is likely to prevent R_v from increasing beyond $R_{v,1:1}$. Figure 39 shows the model prediction for the same parameters as in Fig. 38, but assuming R_v cannot exceed $R_{v,1:1}$. The predicted hydrate saturation matches the log-derived data and predicts an excess water situation (having hydrate and water only) which is expected.

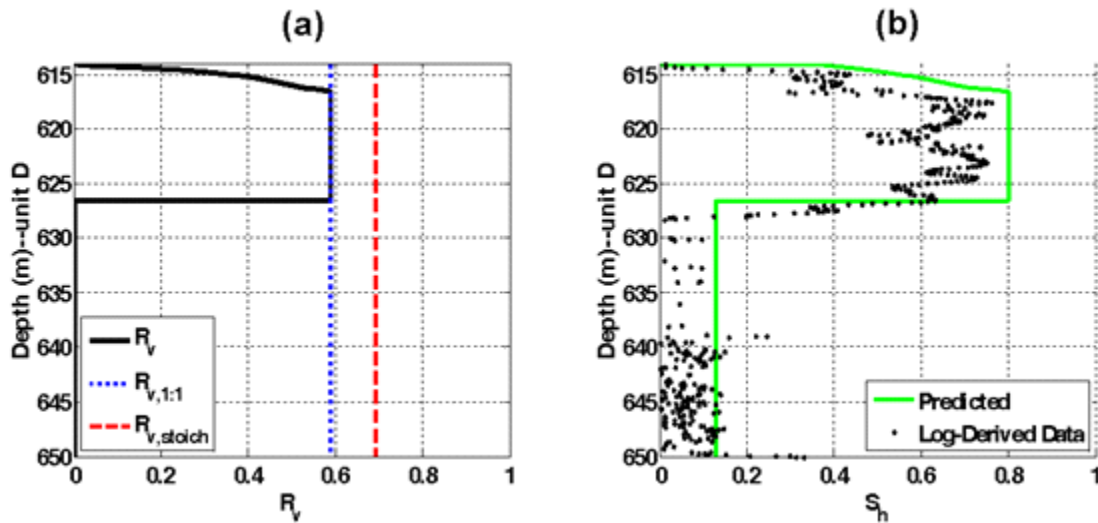


Fig. 39 Applying a constrained pressure-driven fluid transport model along with the stoichiometric model on the D sand unit in Mt. Elbert well using an end-point $k_{r,w} = 0.5$; the constraint is that R_v is not allowed to exceed the value $R_{v,1:1}$. The predicted hydrate saturation profile overestimates the measurements in the upper part of the unit and yields a slightly thinner accumulation. The small hydrate saturation below 627 m is the result of converting residual gas saturation to hydrate.

Of course the constraint of R_v is entirely *ad hoc*. The fact that overriding the pressure-driven flow model in this way yields a saturation profile close to what is observed raises the interesting hypothesis that capillarity-driven transport is a more general means of accounting for the behavior during conversion to hydrate. This observation is the motivation for the next section of this report.

Summary of Applicability of Pressure-Driven Transport Model for Conversion of Gas Reservoirs to Hydrate

The conversion of a gas accumulation into hydrate reduces the volume occupied by fluid phases and thus drives the flow of fluid phases toward the zone of hydrate formation. Assuming this flow is driven by gradient in potential has significant implications for the applicability of the model. In particular, a *co-current flow* of gas and aqueous phases from below a descending base of gas hydrate stability zone (BGHSZ) upward into the hydrate stability zone (GHSZ) *cannot provide the required amount of water* for hydrate formation. This is because the rising gas phase forms a sharp front, in accord with fractional flow theory, ahead of which only gas flows. Thus the pressure-driven model must transport water to the GHSZ from above. That is, water moves down into the GHSZ through accumulated hydrate from overlying aquifers, while gas rises to the GHSZ from the remaining gas reservoir.

With suitable choices of the key transport coefficients (effective permeability to aqueous phase at the residual gas endpoint, and effective permeability to aqueous phase of sand containing large hydrate saturation), the *countercurrent transport* of gas and aqueous phases *provides the large volumes of both components needed* to form large hydrate saturations observed in Arctic sediments. The large saturations occur only in the upper portion of the original gas accumulation, with the thickness and the saturation depending on the ratio of aqueous phase end point relative permeability to aqueous phase permeability in hydrate-bearing sediment. A column of small hydrate saturations (10-15%) forms below the upper zone; this lower zone is where residual gas phase saturation was established as gas flowed upward to the

GHSZ and aqueous phase imbibed. During hydrate formation in the imbibed zones the only phase flowing into the GHSZ due to the volume change is the aqueous phase.

For plausible endpoint relative permeabilities for aqueous phase and for a reasonable choice of a relationship between water effective permeability and hydrate saturation, the model prediction agrees with behavior observed in the Mt. Elbert well. However the model prediction is highly sensitive to the ratio of these transport coefficients. Small variations in grain size distribution, end point relative permeability, or hydrate saturation dependence yield large variations in predicted hydrate profiles, including qualitatively different behavior, e.g. preservation of a large gas phase saturation. Thus the pressure-driven fluid transport model is unlikely to provide a robust explanation of the mechanism of conversion. Instead it offers useful insight into the likely role of capillarity-driven transport, which is discussed in the next section of this report.

Gas Reservoir Conversion to Hydrate: Role of Capillarity-Driven Fluid Phase Transport at Bed-Scale

The preceding section shows that pressure-driven, viscous-dominated flow is unlikely to account for observed hydrate saturation distributions at Mt Elbert or elsewhere in the subpermafrost accumulations. In this section we generalize the fluid flow model to account for capillarity-driven transport. For this application, saturation gradients provide the driving force. The model is otherwise the same as described in the preceding section. Here we recapitulate the main features of that model and include the relevant terms for capillarity-driven transport.

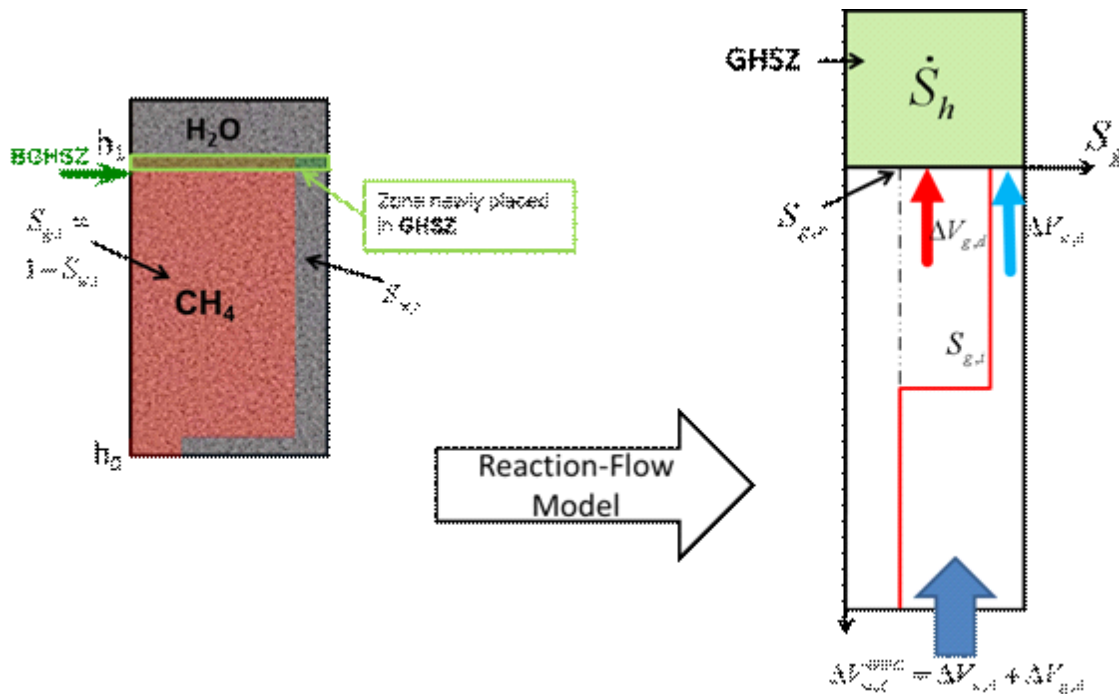


Fig. 40. Schematic of fluid flow induced by hydrate formation during descent of BGHSZ.

Assume that flow of gaseous and aqueous phases occurs only from below in response to the generation of hydrate, as shown in Fig. 40. The flow of gaseous, u_g , and aqueous phase, u_w , are as follows:

$$u_w = -k\lambda_w \left(\frac{\partial P_w}{\partial z} - \rho_w g \right) \quad (74)$$

$$u_g = -k\lambda_g \left(\frac{\partial P_g}{\partial z} - \rho_g g \right) \quad (75)$$

where,

$$\lambda_i = \frac{k_{r,i}}{\mu_i} \quad ; i = w, g \quad (76)$$

As mentioned in earlier sections, the difference between the gaseous phase pressure, P_g , and aqueous phase pressure, P_w , is known as capillary pressure, P_c . Therefore, the gradients of the two phase pressures are related as follows:

$$\frac{\partial P_g}{\partial z} = \frac{\partial P_w}{\partial z} + \frac{\partial P_c}{\partial z} \quad (77)$$

Defining u_T as the total flux of gaseous and aqueous phases combined with Eq. (77) gives:

$$u_T = u_w + u_g = -k\lambda_w \left(\frac{\partial P_w}{\partial z} - \rho_w g \right) - k\lambda_g \left(\frac{\partial P_w}{\partial z} + \frac{\partial P_c}{\partial z} - \rho_g g \right) \quad (78)$$

Eq. (78) can be further simplified as follows:

$$u_T = -k(\lambda_w + \lambda_g) \frac{\partial P_w}{\partial z} + k(\lambda_g \rho_g + \lambda_w \rho_w)g - k\lambda_g \frac{\partial P_c}{\partial z} \quad (79)$$

Solving for the aqueous phase pressure gradient from Eq. (79), and substituting in Eq. (74) gives:

$$u_w = \underbrace{\frac{\lambda_w}{\lambda_w + \lambda_g} u_T}_{Viscous} + \underbrace{k \frac{\lambda_w \lambda_g}{\lambda_w + \lambda_g} \frac{\partial P_c}{\partial z}}_{Capillary} + \underbrace{k \frac{\lambda_w \lambda_g}{\lambda_w + \lambda_g} (\rho_w - \rho_g)g}_{Gravity} \quad (80)$$

As indicated in Eq. (80), three contributions to the water flux are viscous (pressure driven), capillary (saturation gradient driven) and gravity (buoyancy).

Furthermore, the mass balance equations for both gaseous and aqueous phases are as follows:

$$\phi \frac{\partial}{\partial t} S_w + \frac{\partial}{\partial z} u_w + \alpha_w \dot{S}_h = 0 \quad (81)$$

$$\phi \frac{\partial}{\partial t} S_g + \frac{\partial}{\partial z} u_g + \alpha_g \dot{S}_h = 0 \quad (82)$$

α_w and α_g are stoichiometric conversions relating hydrate formation rate to consumption rate of water and methane; for simplicity we assume pure phases so that aqueous and gaseous phase saturations are synonymous with water component and methane component concentrations, respectively:

$$\alpha_w = \phi \frac{N \bar{V}_w}{\bar{V}_h} \quad (83)$$

$$\alpha_g = \phi \frac{\bar{V}_g}{\bar{V}_h} \quad (84)$$

where ϕ is porosity and \bar{V}_w , \bar{V}_h and \bar{V}_g are the molar volumes of water, hydrate and methane, respectively.

Summation of Eqs. (81) and (82) gives:

$$\phi \frac{\partial}{\partial t} (S_w + S_g) + \frac{\partial}{\partial z} (u_w + u_g) + (\alpha_w + \alpha_g) \dot{S}_h = 0 \quad (85)$$

Substituting $S_w + S_g = 1 - S_h$ in Eq. (85) and simplifying gives:

$$(\alpha - \phi) \dot{S}_h + \frac{\partial}{\partial z} u_T = 0 \quad (86)$$

where $\alpha = \alpha_w + \alpha_g$.

The final system of equations is as follows:

$$\left\{ \begin{array}{l} \phi \frac{\partial}{\partial t} S_w + \frac{\partial}{\partial z} \left\{ \underbrace{\frac{\lambda_w}{\lambda_w + \lambda_g} u_T}_{\text{Viscous}} + k \underbrace{\frac{\lambda_w \lambda_g}{\lambda_w + \lambda_g} \frac{\partial P_c}{\partial S_w} \frac{\partial S_w}{\partial z}}_{\text{Capillary}} + k \underbrace{\frac{\lambda_w \lambda_g}{\lambda_w + \lambda_g} (\rho_w - \rho_g) g}_{\text{Gravity}} \right\} + \underbrace{\alpha_w \dot{S}_h}_{\text{Sink}} = 0 \\ (\alpha - \phi) \dot{S}_h + \frac{\partial}{\partial z} u_T = 0 \end{array} \right. \quad (87)$$

The solution to Eq. 87 depends on several rock and fluid properties: the relative permeability curves (for the phase mobilities), the capillary pressure curve (for the gradient of capillary pressure vs. saturation) and phase densities (for buoyancy). All flows are driven by rate of hydrate formation, which is prescribed as a boundary condition in the model. The domain includes the gas reservoir plus a finite volume of aquifer below the gas/water contact, which is assumed to be at constant pressure equal to hydrostatic. The top of the gas reservoir is assumed to be sealed to fluids (both gas and water).

The model assigns the rate of hydrate formation in a finite volume of sediment. It computes fluxes in the gas/water region below the BGHSZ and fluxes within the GHSZ. The latter depends on the permeability to fluids in the presence of hydrate, for which we use an empirical correlation. Note that $\dot{S}_h = f(z, t)$ is a function of space and time. In fact we impose a moving boundary condition on the above system of equations to mimic the descent of the BGHSZ happened in response to surface temperature cooling in the Arctic.

$$\dot{S}_h(z, t) = \begin{cases} \dot{S}_h & ; \quad z \leq z_{BGHSZ} \\ 0 & ; \quad z > z_{BGHSZ} \end{cases} \quad (88)$$

where z_{BGHSZ} is the depth of the BGHSZ which in turn is a function of time, $z_{BGHSZ} = f(t)$.

In the following results, the applied rates of descent of the BGHSZ are assumed constant. It is also possible to assign variable, with time t , rates of descent of the BGHSZ. The main output of the model is profiles of flux and saturation for each phase. The three contributions to the flux of each fluid phase can also be extracted.

Illustration of the pressure-driven and capillarity-driven model

In this section we consider an initial gas reservoir through which gaseous and aqueous phase saturations are distributed based on capillarity/gravity equilibrium. Then a top section of the gas reservoir is placed inside the GHSZ and the emerged gaseous and aqueous phase fluxes are predicted. We show that the rate of hydrate formation multiplied by the rate of descent of the BGHSZ plays a key role in determining the final hydrate saturation as well as the final state of the system, i.e. hydrate coexists with aqueous phase vs hydrate coexists with gas phase. To simplify the interpretation of the model, we fix the level of the BGHSZ at 5 meters below the seal (top of the gas column) and use three different magnitudes for the rate of hydrate formation, \dot{S}_h .

In Cases 1, 2 and 3 the capillarity and relative permeability characteristics of the host sediment are fixed as shown in Fig. 41 and 42.

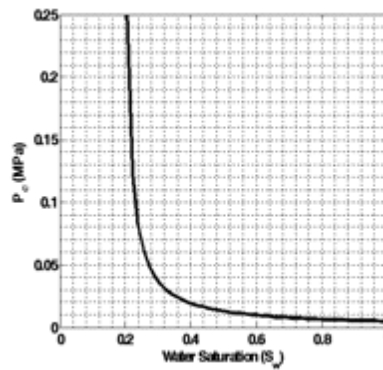


Fig. 41. Rock properties used in capillarity-driven flow model: Capillary pressure vs water saturation.

In case 4, the same rate of hydrate formation as that in Case 2 is used, but different capillarity and relative permeability characteristic, as shown below, are used. The host sediment in Case 4 is more water-wet and exhibits a sharper capillary percolation compared to that of Cases 1, 2 and 3.

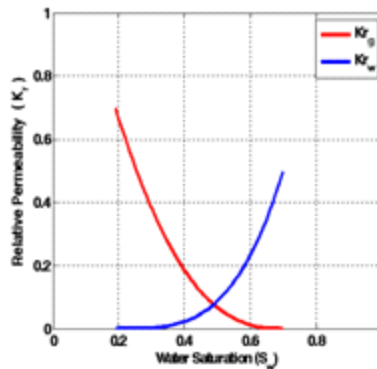


Fig. 42. Rock properties used in capillarity-driven flow model: Gas and water relative permeability curves.

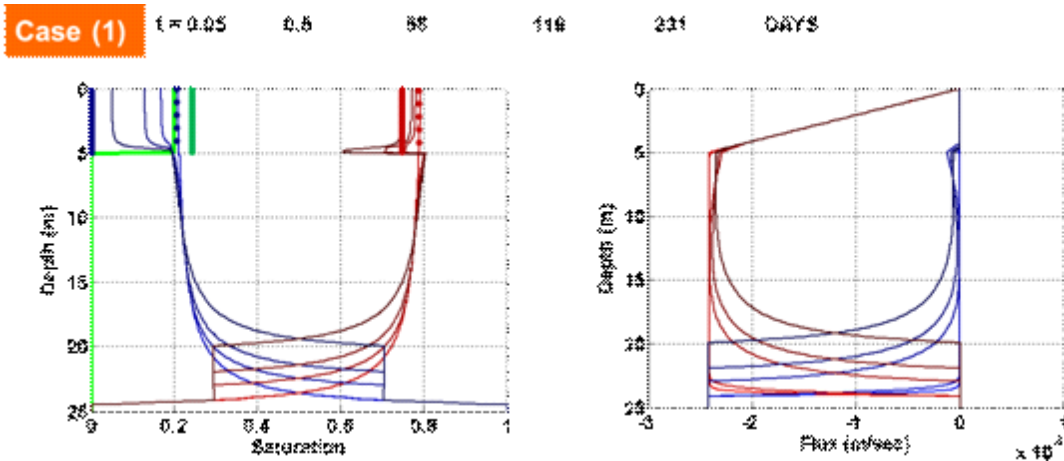


Fig. 43. Model results for Case 1, in which large hydrate growth rate imposed in a 5 m layer of sediment at the top of a 25 m thick formation. The lower 20 meters of the formation are below the BGHSZ. (left). Saturation profiles (blue = water, red = gas, green = hydrate) at the times indicated at the top of the image. Darker shades correspond to later times. Initial and final saturations in the 5 m layer shown as dotted and heavy lines, respectively. (right) Phase fluxes (blue = water, red = gas) in the formation at the times indicated at top of image. Darker shades correspond to later times. Negative values of flux mean upward flow. The flux of water phase is forced to nearly zero between 5 m and 15 m by the large flux of gas phase, which has much larger mobility. Thus hydrate formation ends after all the water in the top 5 m of the sediment is consumed (note final saturations in left panel, indicated by heavy lines in top 5 m).

Case 1

A large rate of hydrate growth (6 m/y) is imposed in the example shown in Fig. 43. Large growth rates require large fluxes of gaseous and aqueous phases. These can be provided only by pressure driven flow; the product of saturation gradient and the slope of the P_c-S_w characteristic curve is simply not large enough to provide large water flux. Thus the large rate of hydrate growth leads to a viscous-dominated fractional flow in which gas flux overwhelms the capacity for water flux. The GWC rises at the speed of the classical Buckley-Leverett shock front (Fig. 43, left panel); above the GWC the saturation profile has a short transition zone then is essentially constant. The flux of aqueous phase is negligible above the GWC (Fig. 43, right panel). Since only gas is arriving at the GHSZ at 5 m depth, hydrate formation is limited to the water available in the GHSZ. The final state in the GHSZ shows a modest S_h of 25% (heavy green line, Fig. 43 left panel) and gas saturation of 75% (heavy red line, Fig. 43, left panel), slightly below the initial value of 80%.

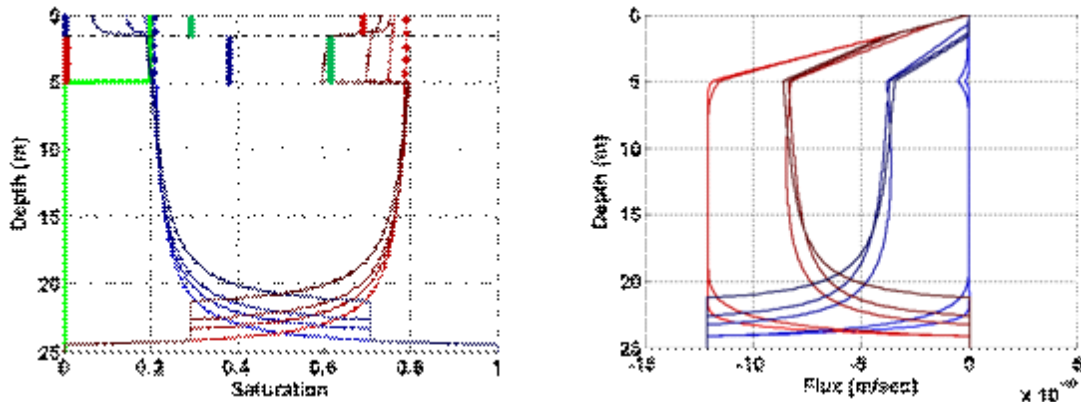


Fig. 44. Model results for Case 2, in which rate of hydrate growth is moderate. (left). Saturation profiles (blue = water, red = gas, green = hydrate). Darker shades correspond to later times. Initial and final saturations in the 5 m layer shown as dotted and heavy lines, respectively. (right) Phase fluxes (blue = water, red = gas) in the formation at the times indicated at top of image. Darker shades correspond to later times. Negative values of flux mean upward flow. The flux of water phase at early times is essentially zero because the saturation gradient is too small to sustain the rates required by hydrate growth; thus in the top 1.5 m of the GHSZ, all the water is consumed to form hydrate. At later times the water phase saturation gradient can sustain the needed upward flux of 4×10^{-10} m/s, while the upward gas phase flux is twice the water flux. The final saturation of hydrate is large (62%), and the final water saturation is 38%.

Case 2

Moderate rates of hydrate growth (0.3 m/y) require moderate fluxes of water and gas phases (Fig. 44). These can be provided by a combination of pressure-driven and capillarity-driven flow. Though the saturation profiles are similar to Case 1, the flux profiles are quite different, with water flux being about half the gas flux. The water and gas fluxes reach a steady value in the upper part of the domain below the GHSZ; they vary with time in the lower part as the GWC rises. As a result hydrate formation proceeds with all the gas arriving at the GHSZ being converted to hydrate. Thus in contrast to Case 1, the final state in the lower 3 m of the GHSZ in Case 2 shows a large S_h of 62% and no remaining gas saturation; instead the final water saturation is 38%. The top 2 m of the GHSZ show a similar final state to Case 1 because during early time the flux of water to the top 2 m could not be sustained.

Case (3)

t = 0.0127 0.1269 15.9849 31.9430 47.4069 YEARS

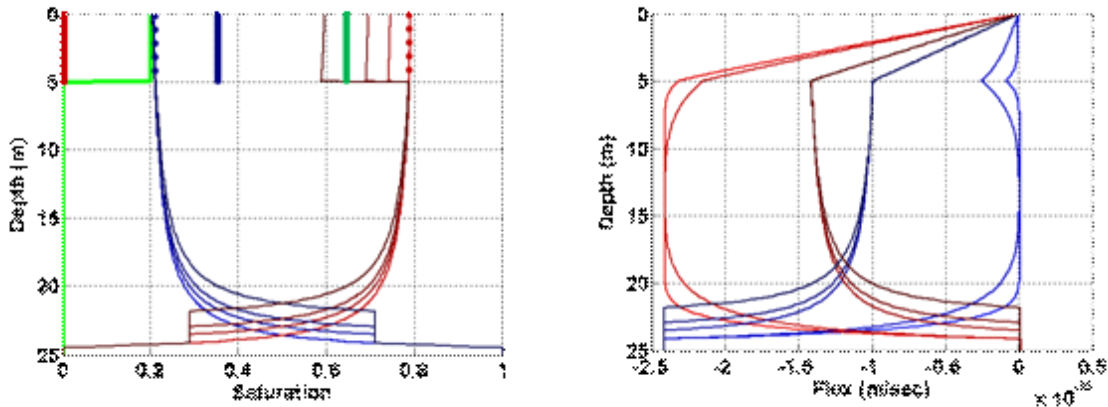


Fig. 45. Model results for Case 3, in which small hydrate growth rate is imposed. (left). Saturation profiles (blue = water, red = gas, green = hydrate) at the times indicated at the top of the image. Darker shades correspond to later times. Initial and final saturations in the 5 m layer shown as dotted and heavy lines, respectively. (right) Phase fluxes (blue = water, red = gas) in the formation at the times indicated at top of image. Darker shades correspond to later times. Negative values of flux mean upward flow. The flux of water phase quickly approaches a steady value of 1×10^{-10} m/s, while the upward gas phase flux is 1.4×10^{-10} m/s.

Case 3:

If the rate of hydrate growth is small (0.06 m/y), then the required fluxes of gas and water are proportionately smaller, as seen in Fig. 45 (right panel). In this case, the pressure-driven flow is quite small, and the saturation-gradient driven flow accounts for most of the aqueous phase flux. The systems quickly approaches a pseudo-steady state, in which the GWC rises slowly while the saturation profiles above the GWC stay nearly the same shape (Fig 45, left panel). Thus the fluxes of both phases are nearly constant (Fig 45, right panel). In other words, the small steady rate of hydrate growth imposed on the system leads to small steady capillarity-dominated fluxes of fluids into the GHSZ. These steady phase fluxes determine the value of R_v , the fraction of total flux which is gas phase, to approach 0.59 at a depth of 5 m, where the fluids enter the GHSZ. The flux of water is almost entirely due to capillarity.

As described in the discussion of volumetric considerations earlier in this report, the value of R_v and the initial gas saturation determine the final hydrate saturation and the saturation of the other phase (gas or water). During the times shown here, the water saturation in the GHSZ (top 5 m of formation) is remaining steady at just over its initial value of 20%, and the hydrate saturation increases as the gas saturation decreases. Thus from Fig. 4 we expect the final S_h to be 80%. But in the transport model we find S_h is about 65% (heavy green line in left panel of Fig 45). The difference is due to the relative permeability curves, which show a residual gas saturation of 0.30 (Fig. 42). Thus the pressure-driven transport of gas into the GHSZ stops when S_g reaches 0.3 in the GHSZ, and subsequently only water flows into the GHSZ from below. During this period R_v is zero, and the remaining gas phase is converted to hydrate. Consequently the final hydrate saturation is smaller than expected from Fig. 4, since Fig. 4 ignores any transport limitations. In effect Fig. 4 assumes zero residual gas saturation, and thus provides an upper bound on the final hydrate saturation.

We may also place the results of the capillarity-driven transport model for Case 3 in the context of the pore-scale imbibition model developed earlier in this report. The volumetric model depicted in Fig. 4 neglects all considerations of transport mechanism, and a value of $R_v = 0.59$ in this model yields a final hydrate saturation that corresponds to the initial gas saturation. The pore-scale imbibition model ignores transport at the bed scale. Scenario A of this model, in which water arrives very slowly to the gas/hydrate/water interface, also yields a final hydrate saturation equal to the initial gas saturation, cf. Fig. 14. Scenario A assumed no limitation on the gas phase transport. Thus a common factor in these predictions of large final hydrate saturation is the absence of constraints on gas transport. In contrast the capillarity-driven flux model explicitly accounts for both phase fluxes at the bed scale and therefore must account for the effect of residual gas saturation. It thus yields a smaller final hydrate saturation as discussed above. Similarly, Scenario B of the pore-level imbibition model accounted for the possibility of trapping residual gas, Fig. 15. This yields a smaller final hydrate saturation; compare left and middle panels of Fig. 27, for example. The common factor to the predictions of not-quite-as-large final hydrate saturation is the constraint on gas transport that applies when gas saturation declines to residual.

This analysis shows that the pore-scale imbibition model can be incorporated into the bed-scale transport model described in this section via the residual gas saturation. If pore-scale considerations suggest that water reaches the gas/hydrate/water interface in individual pores slowly compared to the rate of hydrate growth at that interface, then the effective residual gas saturation is zero. It is clear that moving the gas relative permeability curve endpoint to $S_w = 1$ in Fig. 42 would yield a prediction of $S_h = 80\%$ in the transport model. The pore-scale imbibition model scenarios show that the characteristic rock properties for the gas/hydrate/water system need not be the same as for the gas/water system. Thus we conclude that the capillarity-driven transport model should in general account for two sets of curves, one set that applies in the GHSZ where three phases (gas, water, hydrate) can co-exist in the pore space, and another conventional set that applies in the not-yet-converted gas reservoir below the GHSZ.

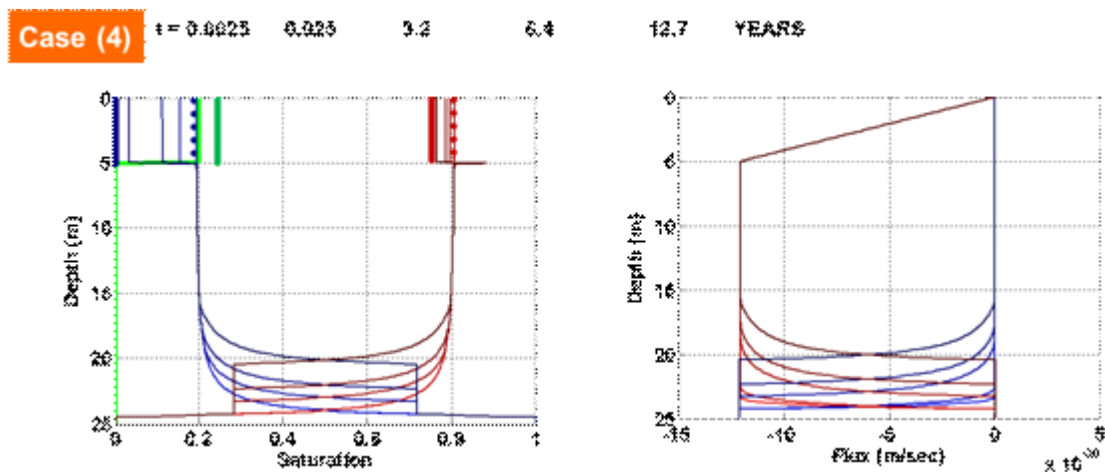


Fig. 46. Model results for Case 2 with a flatter capillary pressure curve. (left) Saturation profiles (blue = water, red = gas, green = hydrate). Darker shades correspond to later times. Initial and final saturations in the 5 m layer shown as dotted and heavy lines, respectively. (right) Phase fluxes (blue = water, red = gas) in the formation at the times indicated at top of image. Darker shades correspond to later times. Negative values of flux mean upward flow. In contrast to Case 2 (Fig. 44) the flux of water phase is essentially zero because dP_c/dS_w is smaller. Thus the capillarity-driven flux is too small to sustain the rates required by hydrate growth, and all the water in the GHSZ is consumed to form hydrate.

Case 4

To confirm the importance of the contribution of capillarity to the water phase flux, we rerun Case 2 with a shallower capillary pressure curve. This means that the gradient of P_c vs S_w is smaller. Consequently the capillarity-driven flux is smaller for same saturation gradient. The smaller capillarity-driven flux of water proves insufficient to supply the imposed rate of hydrate growth. Hence the flow in this case reverts to the viscous dominated flow of gaseous and aqueous phases as in Case 1. Therefore, the gas flux becomes dominant and prevents any water reaching the GHSZ. Thus the resulting hydrate saturation is about 25%, and a gas saturation remains in the GHSZ. Comparing Cases 2 and 4 shows that for the same rate of hydrate formation, the final state of the system is determined by the characteristic capillarity and relative permeability curves of the host sediment.

If in nature the rate of hydrate formation is limited by the rate of descent of the BGHSZ, which is in order 10^{-3} m/y or less for the relevant cooling period for the Alaska North Slope, then we are in a regime like Case 3 where capillarity driven flux is the primary means of transporting fluid to GHSZ. We conclude that the proportion of gas and water fluxes to the GHSZ (the quantity R_v) is controlled by the relative permeability and capillary pressure characteristics of the domain. For typical capillary and relative permeability characteristics the value of R_v converges to values a little less than $R_{v,1:1}$ and remains at this value until S_g reaches $S_{g,r}$ at which point R_v goes to zero. Thus we get S_h not quite as large as $S_{g,i}$ in the top of the gas reservoir. The rest of the profile can therefore be estimated with the same average value of R_v , using the simpler model that accounts only for volumetric changes and sedimentology, described in previous section of this report.

Summary of Applicability of Capillarity-Driven Transport Model for Conversion of Gas Reservoirs to Hydrate

We conclude that capillarity-driven transport to the GHSZ from below is the key mechanism of fluid transport when a gas reservoir is converted to hydrate by a descending BGHSZ. The model computes fluxes due to buoyancy, pressure gradient and saturation gradient in response to the volume changes associated with hydrate formation. The model predicts that capillarity-driven flux is dominant mode of water transport and that this flux is sufficient to supply the needs of relatively slow rates of hydrate formation. The model yields an *a priori* value of R_v , the volumetric parameter (fraction of total fluid phases movement made up by gas) which determines the final hydrate saturation, given the initial gas saturation. For typical multiphase flow characteristics (relative permeability and capillary pressure) the predicted R_v gives a large hydrate saturation close to those observed in Mt. Elbert and Mallik wells.

Only if the rate of descent of BGHSZ is large (and hence the rate of hydrate generation is large) is the rate of water flux too small to supply the need. In this case the model predicts smaller hydrate saturations and large gas saturation. Since gas saturations are not observed in the GHSZ at Mt. Elbert and Mallik wells, this suggests that the rate of fluid transport may control the rate of hydrate formation if the BGHSZ descends rapidly. This is consistent with the experimental results presented in the next section, in which the BGHSZ was moved 1 m in 15 days or about 25 m/y. Hydrate formation occurred at a steady rate that was considerably lagged the rate of cooling.

These considerations suggest that in nature, fluxes of gas and water from below the GHSZ establish saturation profiles that balance the gradients due to buoyancy, pressure and capillarity. At any given location of the BGHSZ, the balance leads to a characteristic value of R_v , the

fraction of fluid phase transport made up of gas. This value combined with the presumed value of residual gas saturation in the GHSZ leads to hydrate saturations less than or equal to the initial gas saturation at that location, depending on the magnitude of residual saturation. This is the reason that the simpler bed-scale model (presented in earlier sections of this report, and which accounts for volumetric changes and sedimentological variation for a user-prescribed value of R_v) correctly predicts the Mt. Elbert well saturation profile when the appropriate value of R_v is given.

Gas Reservoir Conversion to Hydrate: Experimental Validation of Fluid Transport in Response to Hydrate Formation

Descending Bottom of Methane Gas Hydrate Stability Zone Experiment Description

Overview

In collaboration with Dr. Timothy Kneafsey of Lawrence Berkeley National Laboratory, an experiment was conducted in which the base of gas hydrate stability was slowly moved down a sandpack containing gas and water. The apparatus was built in Dr. Kneafsey's lab at LBNL, and the experiment was conducted there in the summer of 2011.

A pressure vessel was packed with alternating 'fine' and 'coarse' fractions of silica sand (US Silica F-110, ~120 μm mean diameter), which were previously separated using a mechanical sand shaker. The pressure vessel was saturated with de-ionized water, filling the pore space. A vacuum was drawn on the reservoir before it was pressurized with methane to ~800psig. To establish initial gas saturation in the sand pack, a valve on the bottom of the pressure vessel was opened and water was allowed to flow into the reservoir, replaced by methane gas at the top and mid point of the sand pack. About 360 g of water was present in the reservoir at the end of the water displacement. Thus the corresponding volume of methane, ~360 mL, had been distributed in the sand pack. Porosity of the sandpack is $\approx 36\%$. The vessel cooling jackets were progressively switched from 10°C to 1.5°C coolant from top to bottom, bringing a larger top portion of the sand pack into the hydrate stability zone each time. A cooling jacket was only switched over once minimal incremental hydrate formation was taking place.

A summary of different steps of the apparatus setup is as follows:

- 3'' diameter, 40'' long, 4554mL vessel dry packed with alternating layers of 'fine' and 'coarse' sand, leaving 1633mL pore volume \rightarrow Porosity: $\phi \approx 36\%$.
- Vessel vacuum saturated with de-ionized water (1633mL of water added to system)
- 3707mL reservoir evacuated, then pressurized with methane (3707mL of methane at 18°C and 800psig added to system)
- System closed while 300mL of water drained and pumped from vessel to reservoir, leaving 300mL of gas in vessel
- Vessel uniformly cooled to 10°C, then each cooling loop changed to 1.5°C coolant from top to bottom progressively

Grain Size Distribution

Silica sand (US Silica F-110, ~120 μm mean diameter) was separated into a 'fine' fraction and a 'coarse' fraction using a mechanical sand shaker. To measure the grain size distribution of each fraction, three ~100 g samples of each fraction were each further separated by grain size.

Two different stacks of six progressively smaller sieves were used in a mechanical sand shaker. The results of these measurements are shown in Figs. 47 and 48.

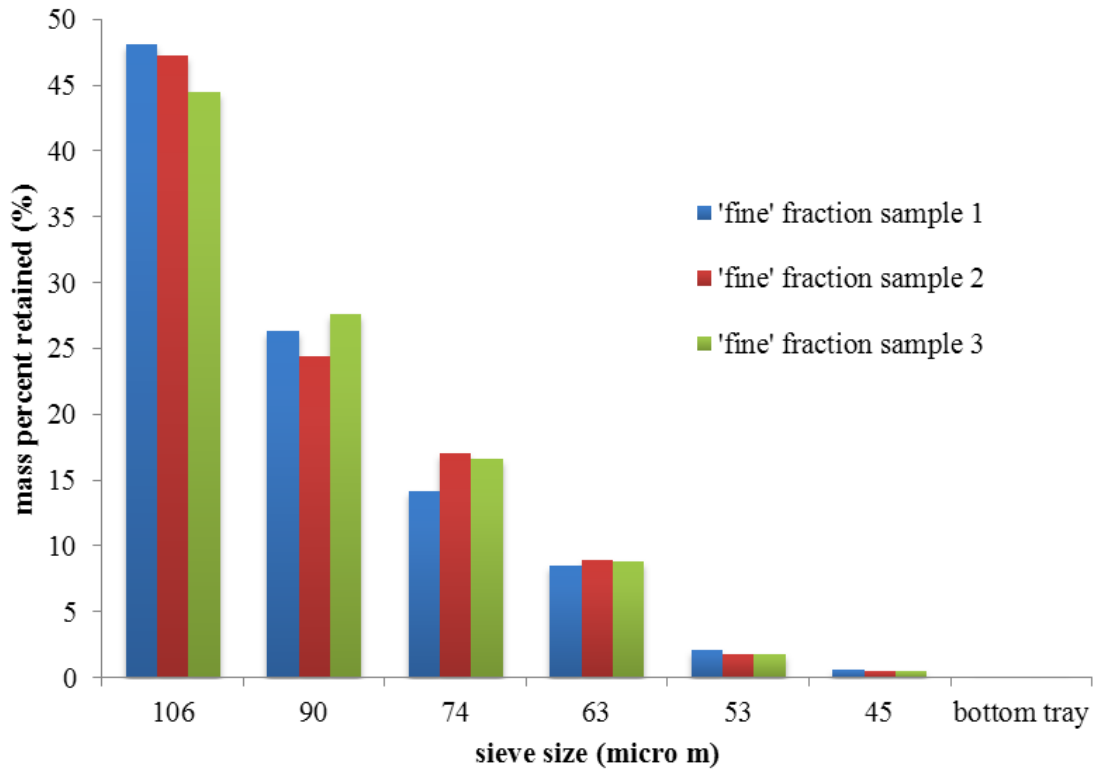


Fig. 47. Fine fraction mass percent sand retained versus sieve size.

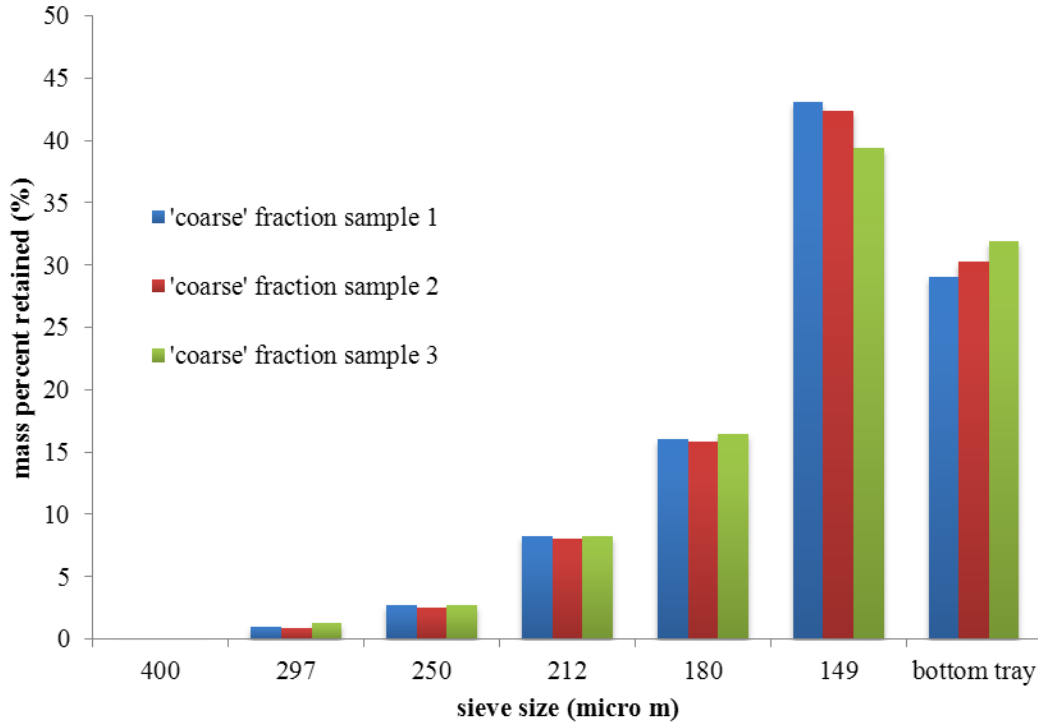


Fig. 48. Coarse fraction mass percent retained versus sieve size.

Drainage Capillary Pressure Curve

To measure the drainage capillary pressure versus water saturation curve of each fraction, three ~60 g samples of each fraction were tested using the 'porous plate method'. The samples were placed in cups with porous ceramic bases (soil retainer assemblies, part number 0676, Soilmoisture Equipment Corp.). The samples were then vacuum saturated with de-ionized water, weighed and placed in a vessel fitted with a porous plate (5 bar pressure plate extractor, part number 1600, Soilmoisture Equipment Corp.). See Fig. 49.

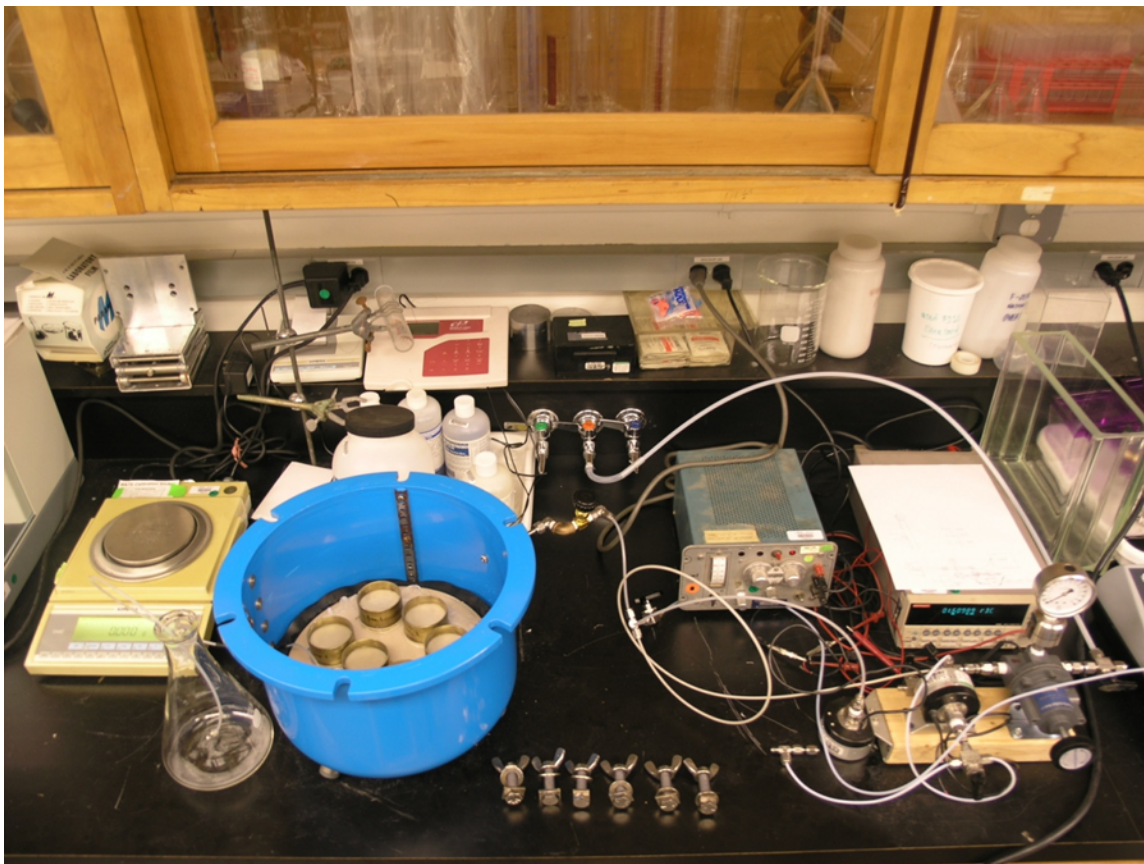


Fig. 49. The porous plate capillary pressure vessel and associated equipment in the laboratory of Dr. Tim Kneafsey at Lawrence Berkeley National Laboratory.

The vessel was closed and pressurized with laboratory air at controlled pressure via a forward pressure regulator. Displaced de-ionized water accumulated in a flask. The system was left at each pressure for sufficient time to reach capillary equilibrium, determined by observation of no further water displacement from the vessel. At this time the vessel was opened and each sample cup weighed. The cups were then returned to the vessel and the air pressure increased by ~ 0.5 psi. This process was repeated up to a pressure of 3psi.

The results of these measurements are shown in Fig50.

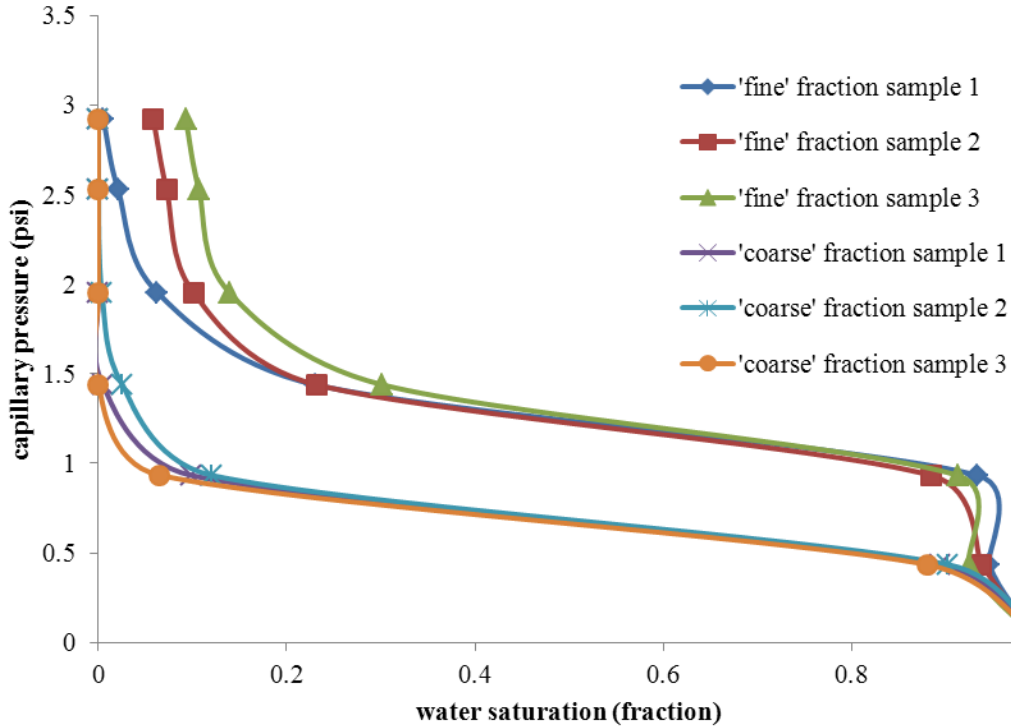


Fig. 50. Capillary pressure versus water saturation for fine and coarse fractions of sand.

Experimental Hardware Description

Two ‘thermocouple strings’ were constructed to allow the measurement of temperature at multiple points along their length. Each ‘thermocouple string’ was a 3/8 inch OD aluminum tube, fitted with ten type T thermocouples that were each spaced 4 inches apart, filled with epoxy. The two thermocouple strings were fitted to an end cap of a 3 inch diameter x 40 inch long aluminum pressure vessel, one in the center and one offset from center. These twenty thermocouples were labeled T1 to T10, top to bottom, for the sensors in the center mounted thermocouple string and T11 to T20, top to bottom, for the sensors mounted in the outer thermocouple string. Two pressure transducers were fitted to the vessel, one at each end and labeled upper and lower.

The pressure vessel was mounted vertically. Ten discrete cooling jackets were constructed from multiple wraps of soft rubber tubing. These were labeled 1 to 10 from top to bottom. The vessel and cooling jackets were insulated with closed cell foam. Two chillers were filled with ethylene glycol. One chiller was set at 10 °C (a temperature outside the hydrate stability zone) and the other set at 1.5 °C (a temperature inside the hydrate stability zone for the range of pressures expected). The chillers were connected to the ten cooling loops via insulated tubing, manifolds, valves and Y connectors, allowing the coolant temperature circulated through each cooling jacket to be selected independently. A thermocouple was placed in the ethylene glycol tank of the chiller set to 1.5 °C and labeled chiller temperature.

A one-gallon pressure vessel, termed the ‘reservoir’ (part number 304L-HDF4-1GAL, Swagelok) was fitted to a stand and set at an angle of ~45 degrees from horizontal. The vessel was placed on a balance (Sartorius). A thermocouple was placed on the reservoir and labeled reservoir temperature.

The top of the reservoir was connected to the top of the pressure vessel and a point halfway between the top and bottom of the pressure vessel. The bottom of the reservoir was connected to

the bottom of the pressure vessel. Flexible PEEK pressure lines were used for the connections to the reservoir to minimize external forces applied, allowing the mass of the reservoir and fluids to be accurately recorded by the balance. A schematic and photo of the experimental setup are shown in Figs. 51 and 52.

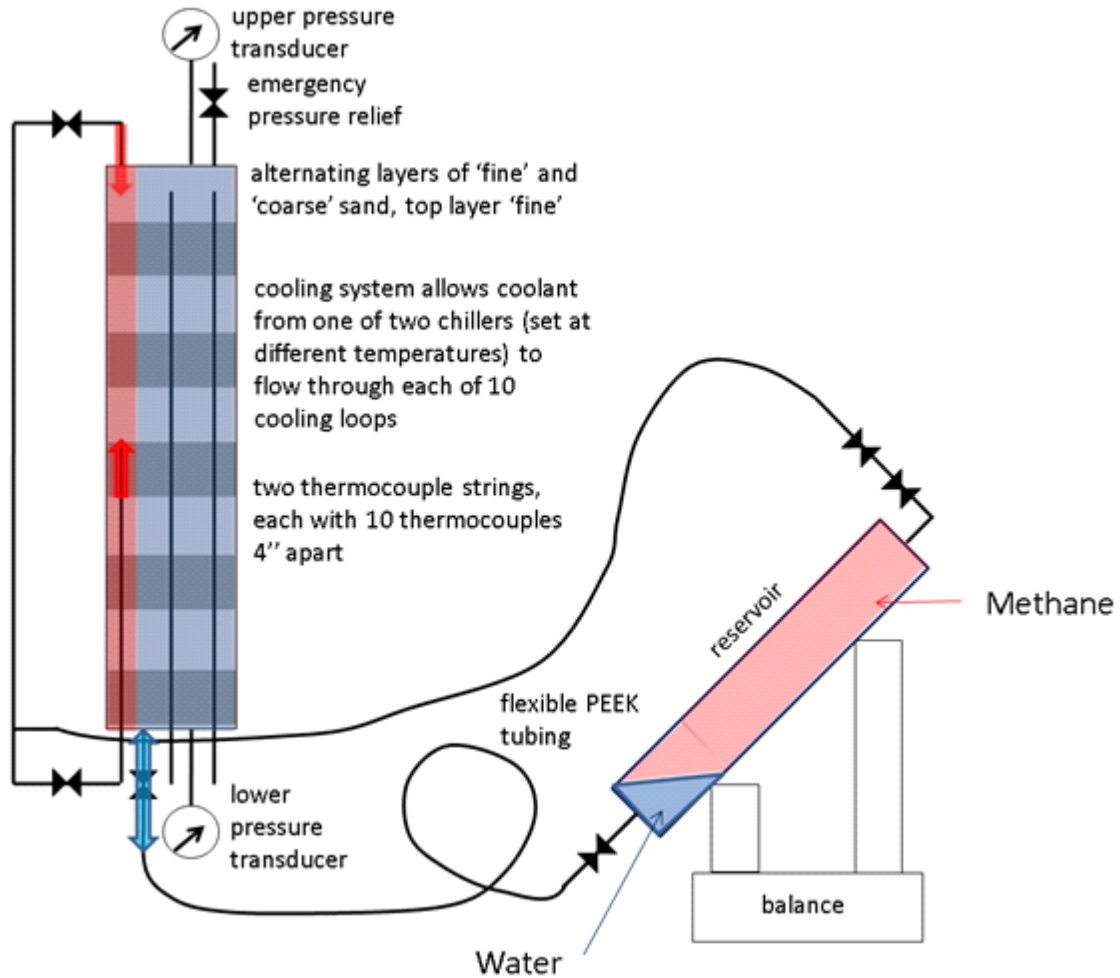


Fig. 51. Schematic of the descending BGHSZ experiment.

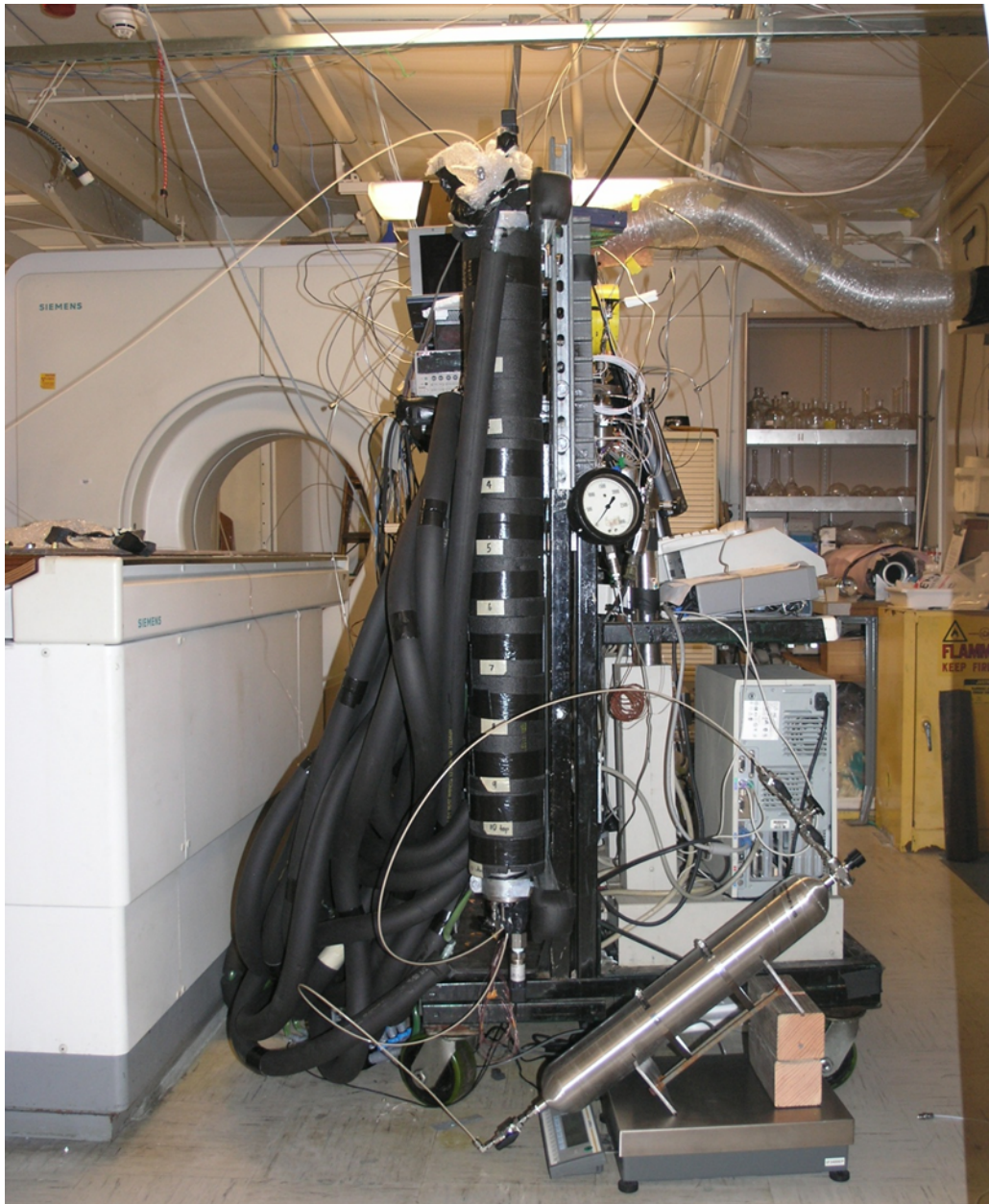


Fig. 52. Descending BGHSZ experimental setup in the laboratory of Dr. Tim Kneafsey at Lawrence Berkeley National Laboratory.

The twenty-two thermocouples and two pressure transducers were logged using a Keithley data logger writing to an Excel spreadsheet. The balance was logged using a software wedge writing to a text file.

Setting up the Sand Pack, Water and Methane

The vessel was packed with alternating fractions of coarse and fine fractions of silica sand. Each fraction was poured into the pressure vessel in small stages and tamped with a plastic rod. The height and mass of each fraction of sand is shown in Table 3.

Table 3. Height and Mass of Each Alternating Sand Fraction

	Fraction	Height (in)	Mass (g)
Top	fine	4.6	641.8
	coarse	3.9	741.0
	fine	4.0	751.8
	coarse	3.4	670.0
	fine	3.9	706.5
	coarse	3.3	734.3
	fine	4.5	795.3
	coarse	4.0	751.5
	fine	4.5	883.2
	Bottom	coarse	3.9

The pressure vessel internal volume minus that occupied by internals was 4551.1 mL. The volume of sand packed into the vessel was 2918.1 mL, calculated from the total mass and density ($\rho_{\text{sand}} = 2.65 \text{ g/mL}$). The difference was 1633.0 mL of pore volume or an average of 35.9% porosity.

The sand filled pressure vessel was evacuated with a vacuum pump and then scanned with a medical computed tomography (CT) scanner. The pressure vessel was then saturated with de-ionized water, filling the pore space with 90.64 moles of water ($\rho_{\text{water}} = 1.00 \text{ g/mL}$). The sand and water filled pressure vessel was then re-scanned with the CT scanner. A vacuum was drawn on the reservoir before it was pressurized with methane to ~800 psig.

Methane density data versus temperature and pressure was obtained from the NIST Chemistry WebBook, which uses a custom equation of state for methane (Setzman and Wagner, 1991). Methane density was calculated across the temperature and pressure range of interest for the experiment at isotherms from 0 °C to 22 °C in one-degree increments and across a pressure range of 644.7 psia to 854.7 psia. Each isotherm (density versus pressure) was fitted with a linear trend-line. The slope and intercept of each trend-line was plotted versus temperature and quadratic functions fitted. This allowed a simple equation of state proxy for methane to be formulated, one that matches the NIST data to 0.2% for density. Using the equation of state proxy described, the reservoir temperature and upper pressure transducer pressure, along with the reservoir volume of 3706.8 mL, 9.53 moles of methane was supplied to the system during pressurization.

The gas phase was assumed to be pure methane, since at such low temperatures the water vapor pressure contributes a very small mole fraction of water to the vapor phase. The solubility of methane in water is very small and as such methane dissolution into the aqueous phase is neglected.

Experimental Procedure

To establish initial gas saturation in the sand pack, a valve on the bottom of the pressure vessel was opened and water was allowed to flow into the reservoir, replaced by methane gas at the top and mid point of the sand pack. Once the indicated mass on the balance reached close to a steady state due to capillary equilibrium, an ISCO syringe pump was used to withdraw small (20 mL and 50 mL) volumes of methane from the reservoir and inject them into the top of the sand pack, leading to further displacement of water into the reservoir. After a small number of cycles of methane reinjection, no significant change in mass indicated on the balance was observed,

indicating methane breakthrough. At this time hydraulic connectivity was re-established between the bottom of the reservoir and the bottom of the pressure vessel.

359.7 g of water was present in the reservoir at the end of the gravity and gas injection driven water displacement, with the balance remaining in the sand pack. Thus the same volume of methane, 359.7 mL, had been distributed in the sand pack.

All pressure vessel cooling jackets were set to the 10 °C chiller and the sand pack cooled from room temperature. After reaching a steady state of 10 °C, the pressure vessel cooling jackets were progressively switched from 10 °C to 1.5 °C coolant from top to bottom, bringing a larger top portion of the sand pack into the hydrate stability zone each time. A cooling jacket was only switched over once minimal incremental hydrate formation was taking place.

At one point the pressure had dropped sufficiently that the system was re-pressurized to ensure adequate methane availability for hydrate formation.

The temperatures measured on the outer thermocouple string are shown in Fig. 53. From 359980 s, cooling loop 2 has been switched to 1.5 °C coolant. Cooling loop was already circulating 1.5 °C coolant at that time. From 392600 s two distinct spikes in temperature are seen, as a result of heat produced during rapid hydrate formation.

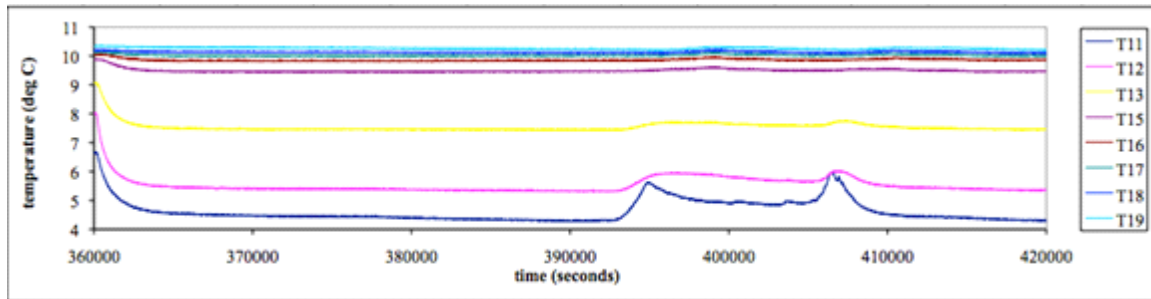


Fig. 53. Outer thermocouple string temperatures versus time.

The variations in reservoir temperature, driven by the ambient conditions prevailing in the room, are shown in Fig. 54.

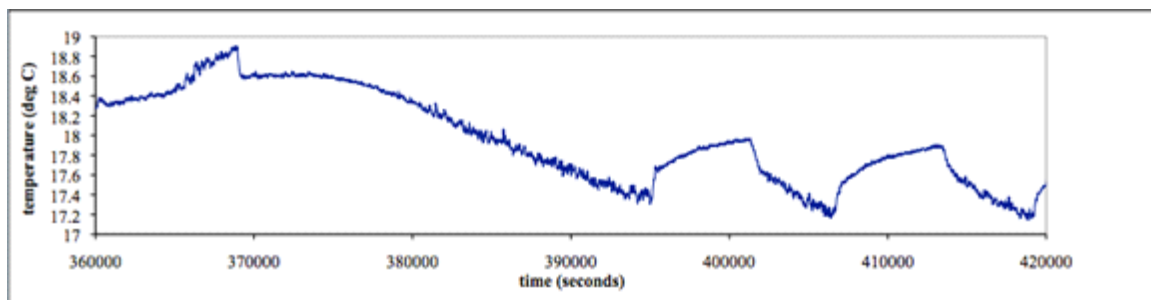


Fig. 54. Room temperature versus time.

The system pressure drop associated with the formation of gas hydrate is shown in Fig. 55.

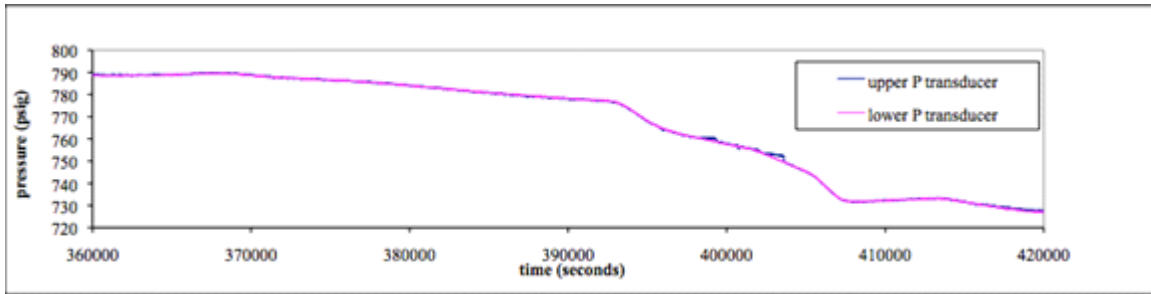


Fig. 55. Pressure versus time.

The indicated mass on the balance is shown in Fig. 56.

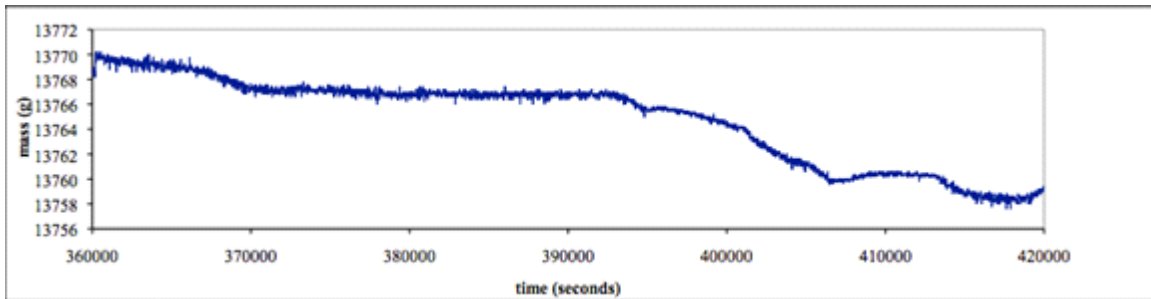


Fig. 56. Indicated mass on balance versus time.

Once the entire sand pack had been brought into the hydrate stability zone, the pressure vessel was scanned once more with the CT scanner, as shown in Fig. 57.

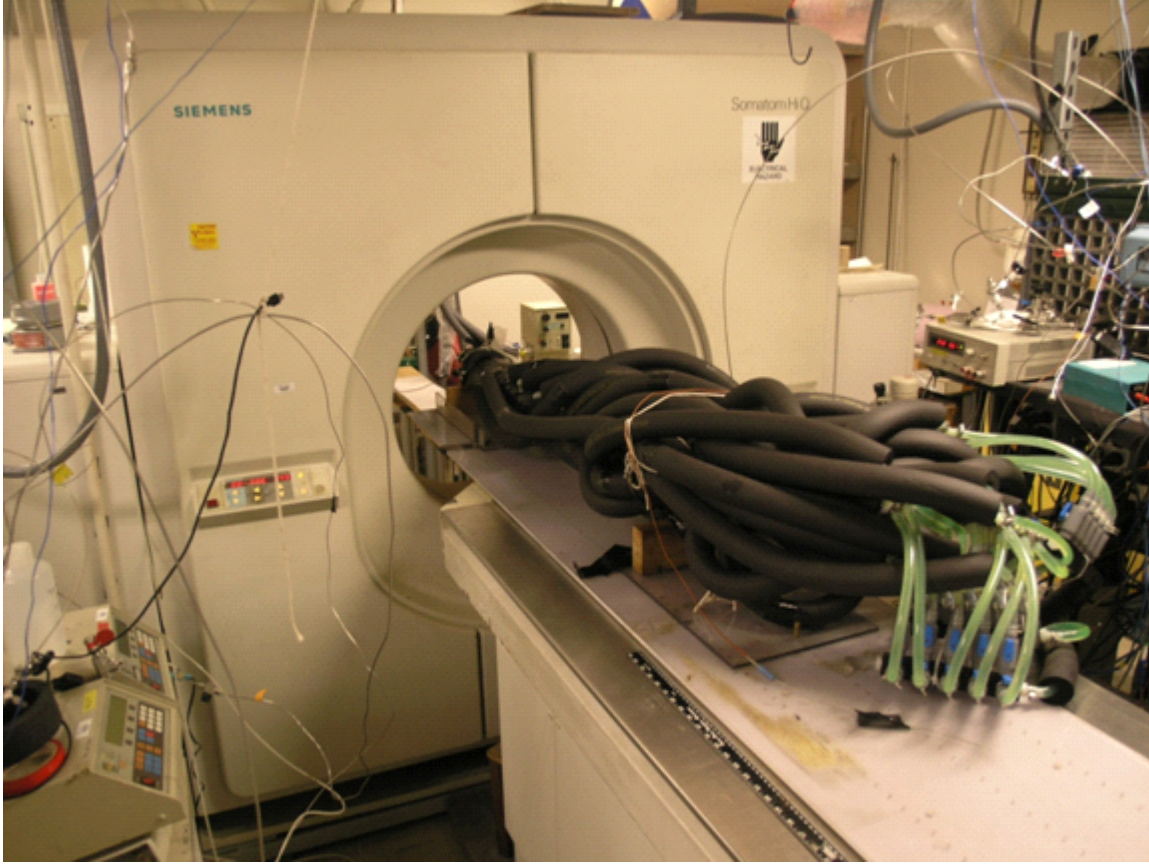


Fig. 57. Scanning pressure vessel, sand pack and hydrate with medical CT scanner in the laboratory of Dr. Tim Kneafsey at Lawrence Berkeley National Laboratory.

Calculations from Raw Data

At any time during the experiment, the mass indicated on the balance is a sum of the following:

$$m_{balance} = m_{reservoir} + m_{waterreservoir} + m_{methanereservoir} + m_{verticalline} \quad (89)$$

where:

- $m_{balance}$ = mass indicated on balance (g)
- $m_{reservoir}$ = mass of reservoir (g)
- $m_{waterreservoir}$ = mass of water in reservoir (g)
- $m_{methanereservoir}$ = mass of methane in reservoir (g)
- $m_{vertical line}$ = vertical component of force applied to reservoir, as apparent mass (g)

From the volume of the reservoir, the prevailing gas density from the equation of state proxy detailed above and assuming a water density, $\rho_{water} = 1.00\text{g/mL}$, an expression for the mass of water in the reservoir at any time during the experiment can be arranged:

$$m_{waterreservoir} = \frac{m_{balance} - m_{reservoir} - m_{verticalline} - 3706.8 * \rho_{methane}}{1 - \rho_{methane}} \quad (90)$$

The results from Eq. 90 are shown in Fig. 58.

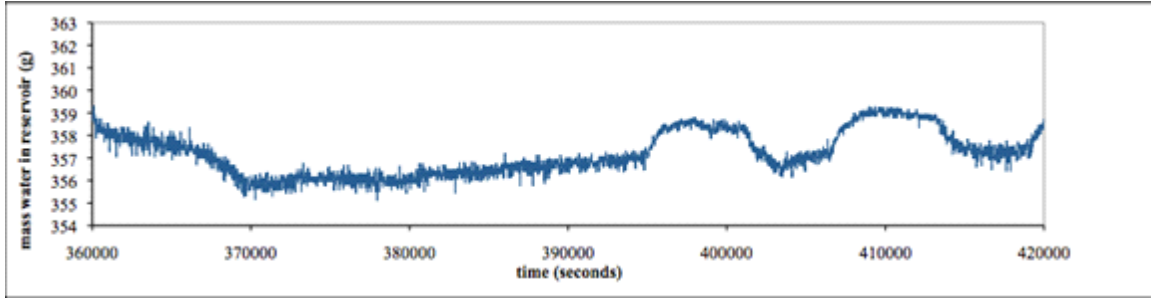


Fig. 58. Mass of water in reservoir versus time.

To approximate the quantity of hydrate formed at any time during the experiment, it was assumed that hydrate occupies the same volume as the water consumed during its formation. This assumption leads to the volume occupied by methane gas remaining unchanged in the presence of hydrate formation. The equation of state proxy was used for gas density, along with the gas volume, 3706.8 mL, to calculate the moles of methane present in gas phase and by difference to the total moles of methane in the system, that present in hydrate. The results of this calculation are shown in Fig. 59.

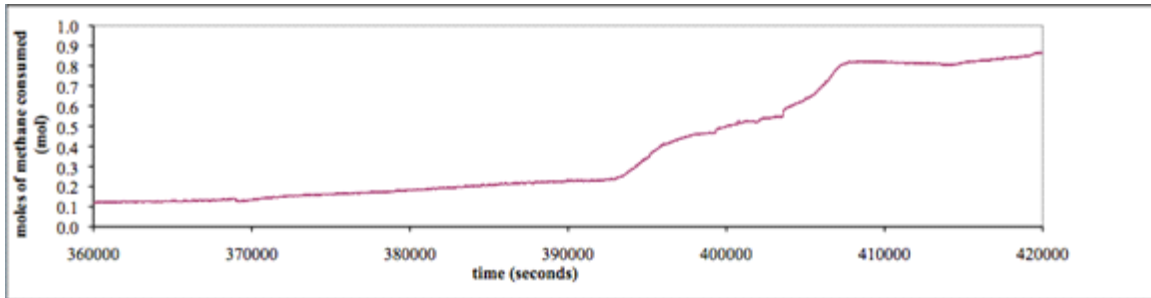


Fig. 59. Methane consumed versus time.

The location of the BGHSZ at the end of each period of cooling was determined from a linear interpolation of the location of the equilibrium temperature read by the outer thermocouple string, at the prevailing pressure. The results are presented in Table 4.

Table 4. BGHSZ Location and Quantity of Hydrate Formed After Each Period of Cooling

Bottom Cooling Loop Circulating 1.5 °C Coolant	Time (s)	Distance from Top of Sediment Column to BGHSZ (in)	Cumulative Moles of Hydrate Formed at End of Time Period (mole)	Cumulative Volume of Hydrate Formed (cm ³)
1	351940 - 359980	3.7	0.07	9.7
2	359980 - 446260	8.1	0.85	113.7
3	446260 - 529080	11.8	1.73	232.6
3	529080 - 544080	15.2	1.80	241.2
4	544080 - 705240	17.4	2.46	330.4
5	705240 - 783060	20.8	3.03	406.4
6	783060 - 862840	24.5	3.18	427.2
7	862840 - 943720	28.0	3.38	452.9
8	943720 - 982960	32.3	3.52	472.6
9	982960 - 1029780	36.0	3.60	483.5
10	1029780 - 1114100	39.9 (entire column)	3.74	502.2

Note: the system was re-pressurized from 529080 s. The entries at 529080 s show the location of the BGHSZ and moles of hydrate formed just prior to re-pressurization.

At select times of interest, an accurate calculation of the quantity of hydrate formed was completed. This was done by again using the equation of state proxy for methane, though applied to two separate volumes of gas phase methane. At the temperature indicated by the reservoir thermocouple and the pressure indicated by the upper pressure transducer, one volume of methane occupies the volume of the reservoir not occupied by the volume of the water in the reservoir.

$$n_{methane} = \frac{(3706.8 - \frac{m_{water}}{\rho_{water}})}{v_{methane}} \quad (91)$$

where

- $n_{methane}$ = number of moles of methane in reservoir (mol)
- $v_{methane}$ = molar volume of methane (mL/mol)

The remainder of the methane is present in the sand pack in gas phase below the BGHSZ or in hydrate phase within the GHSZ. A fractional term apportioning methane between the two phases was solved for, such that the volume of liquid water plus gas phase methane plus gas hydrate was equal to the total pore volume.

$$\text{pore volume} = V_{watersandpack} + V_{methanesandpack} + V_{hydrate} \quad (92)$$

where

- pore volume = pore volume (mL)
- $V_{watersandpack}$ = volume of water in sand pack (mL)
- $V_{methanesandpack}$ = volume of methane in gas phase (mL)
- $V_{hydrate}$ = volume of hydrate (mL)

A hydration number of 6 and hydrate density of 0.925 g/mL was assumed. The quantity of methane hydrate formed at the end of each time period calculated by this approach is included in Table 4. This method is more accurate than the approximate method used to produce Fig. 59. However, when comparing the two calculation techniques for all but the first calculation, a

maximum percentage difference in the number of moles of hydrate calculated is 5%, which is relatively small. The first calculation is based on such a small change in pressure that other effects may dominate the results calculated.

Results–Distribution of Density at End of Experiment

Figure 60 shows the results of preliminary processing of the CT images acquired in the water-saturated sandpack prior to gas invasion (left panel of Fig. 60) and after the experiment ended, i.e. when the entire column had been cooled to be in the GHSZ and no more water remained in the reservoir (right panel of Fig. 60). The left panel reveals minor variations in packing density within the column. The right panel shows two main regions of relatively low density material (cold colors) in the two coarse-sand layers in the top half of the column. Smaller amounts of low-density material are present in the two uppermost fine-sand layers (orange colors). The preliminary image processing cannot unequivocally attribute the low density regions to hydrate rather than gas. However it is clear that hydrate formed in the experiment, and if that hydrate were concentrated in the upper coarse-sand layers then the CT image would look very much like the right panel in Fig. 60. Thus for the purpose of analyzing this experiment, we will assume that regions of maximum density (yellow) are sand completely saturated with water, while regions of less than maximum density contain hydrate and water.

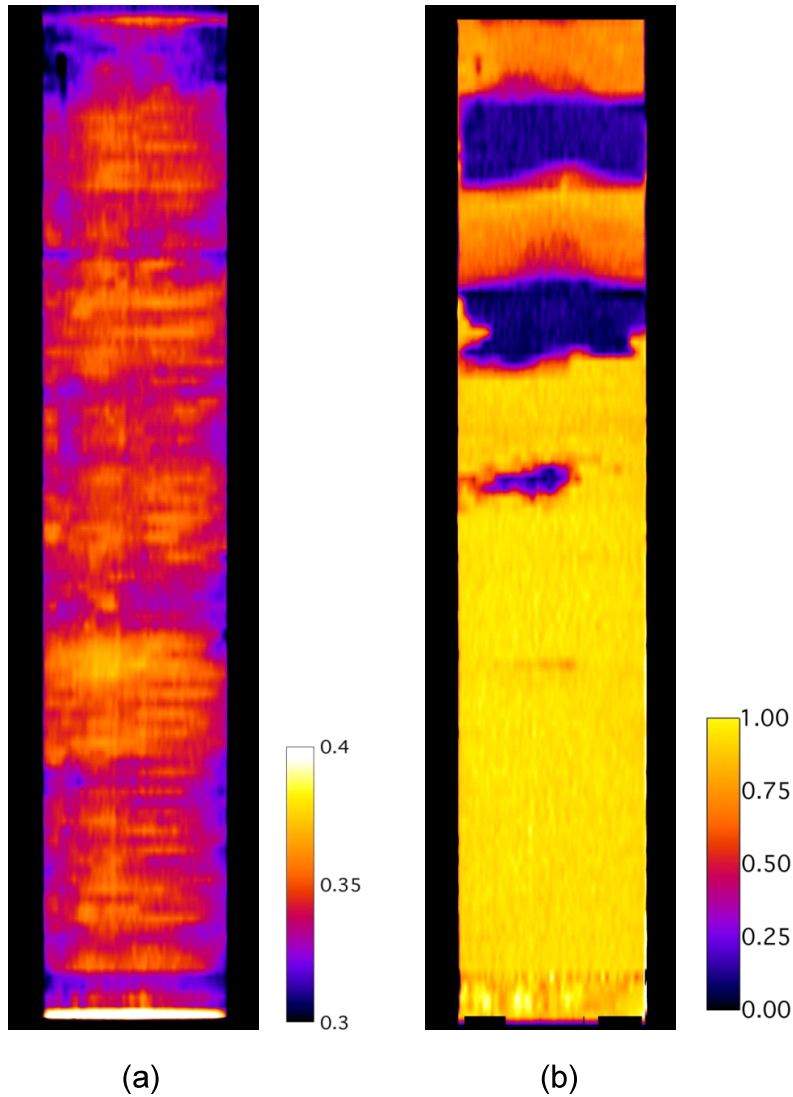


Fig. 60. (a) The porosity calculated from CT scans of the sand pack prior to hydrate formation. (b) The ‘total saturation’ of the sand pack after hydrate formation is complete, also calculated from CT scans. This is mathematically the saturation if only water and gas are present. This calculation is an intermediate step to calculating the hydrate saturation. What it shows clearly is greater hydrate saturation in the ‘coarse’ layers than in the ‘fine’ layers, for the top half of the column. For the bottom half of the column there does not appear to be a significant difference, though this will be investigated further.

Fluid Phase Transport Model (During Hydrate Formation)

Initial condition

An average gas saturation of 22% is initially placed into the sandpack before cooling starts. Based on the capillarity characteristics of the coarse and fine grained sections it is possible to estimate the layer-by-layer distribution of the overall 22% gas saturation. Figure 61 shows the gas saturation profile which satisfies the capillarity/gravity equilibrium along with the characteristic capillary curves of the fine and coarse sections. Based on the capillary curves it is expected that a large gas saturation, i.e. $S_g = 0.9$, is established within the coarse layers and a much smaller gas saturation, i.e. $S_g = 0.1$, within the fine grained layers. Based on the CT images

of the sandpack at the end of experiment the bottom half of the sandpack is almost fully saturated with water. Therefore, the gas phase must have channeled through the bottom half of the sandpack establishing a very low gas saturation, e.g. $S_g = 2\%$, just enough to make a connected path of gas phase throughout the sandpack. An evidence of such connected path of gas throughout the sandpack is that the top and bottom pressure transducers essentially read the same pressure values during major part of the experiment. Note that the average gas saturation of the gas profile shown in Fig. 61 is also 22%.

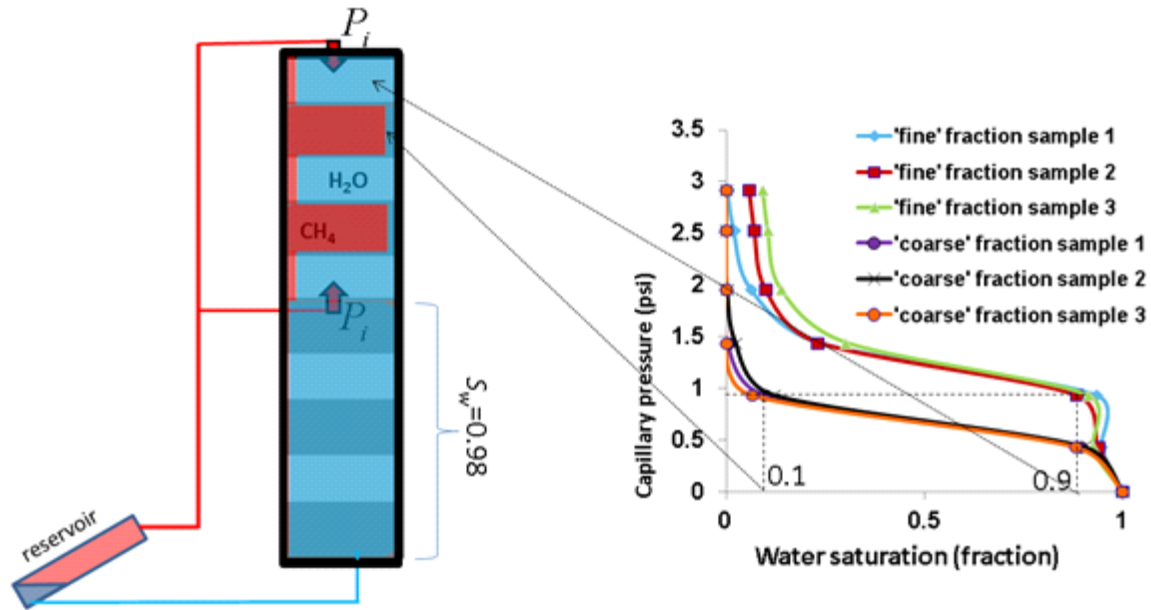


Fig. 61. The initial gas saturation profile within the sandpack determined from the characteristic capillary curves of the coarse and fine layered sections.

The graph of final hydrate saturation for the three initial gas saturations of interest here is shown in Fig. 62. As discussed in previous sections hydrate formation from gas and water requires flow of gaseous and aqueous phase into the GHSZ. The gaseous/aqueous phase proportion of the transported phase was shown to have a first order effect on the final hydrate saturation profile.

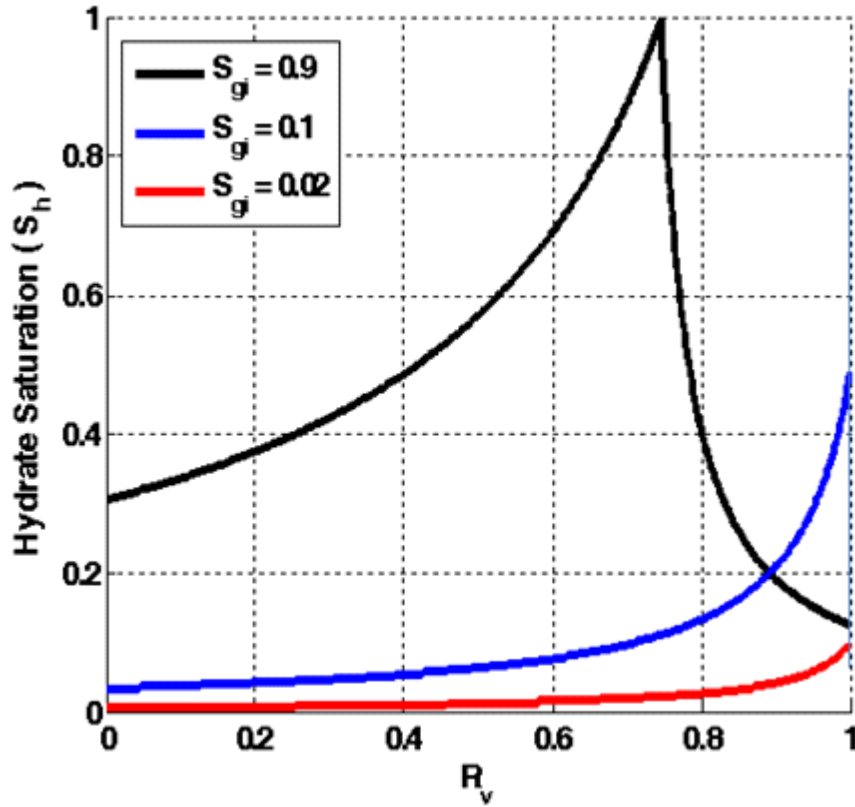


Fig. 62. Final hydrate saturation, S_h , versus gas volume fraction of the total phase fluxes, R_v , for the initial gas saturations in the layers shown in Fig. 61. Methane density is ~ 40 kg/m³ at the operating temperature $T \sim 5$ °C and average pressure of 750 psi.

Formulation of the Driving Force

Assume hydrate is forming in a portion of the sandpack containing an initial uniform gas saturation. We adopt a quasi-steady state method to estimate the gas/water fluxes transported into the hydrate-formation zone during hydrate formation. We denote the pressure (gas pressure) inside the hydrate-formation zone as P_j (containing n_j moles of gas), and the pressure of the gas elsewhere inside the system as P_i (containing n_i moles of gas). Obviously, before any hydrate is forming and the system is in equilibrium $P_i = P_j$; therefore, no flow is taking place when no hydrate is forming.

Assume that at time t^- when gas saturation is $S_g^{t^-}$ (containing $n_j^{t^-}$ moles of methane) and water saturation is $S_w^{t^-}$, a saturation increment of hydrate, dS_h , forms inside the hydrate formation zone. For this to happen, an incremental saturation of gas $dS_g^{used} = \frac{\bar{V}_g}{\bar{V}_h} dS_h$ and an increment $dS_w^{used} = N \frac{\bar{V}_w}{\bar{V}_h} dS_h$ water were consumed. \bar{V}_g, \bar{V}_w , and \bar{V}_h are molar volumes of

methane, water and methane hydrate, respectively. The number of moles of gas inside the hydrate formation zone would also drop to $n_j^t = n_j^{t-} - \frac{dS_h}{\bar{V}_h}$. The gas phase is assumed to expand

and fill the void space instantly and thus $S_g^t = S_g^{t-} + dS_w^{used} - dS_h$. Therefore, the pressure at the hydrate formation zone would drop. Since the system pressure is controlled by the gas phase, the pressure at the hydrate-formation zone would drop to:

$$P_j^t = P_i^t \left(\frac{S_g^{t-} - dS_g^{used}}{S_g^{t-} + dS_w^{used} - dS_h} \right) = P_i^t \left(\frac{S_g^{t-} - dS_g^{used}}{S_g^t} \right) \quad (93)$$

assuming the ideal-gas law is valid.

The number of gas moles outside the hydrate formation zone and thus its pressure is assumed to remain unchanged, $n_i^t = n_i^{t-}$ and $P_i^t = P_i^{t-}$, right before gas starts flowing to the hydrate formation zone.

$P_j^t < P_i^t$ implies a gas flow from outside the zone of hydrate-formation into the hydrate formation zone. Moreover, the aqueous phase would also experience this drop of pressure and would flow towards the zone of hydrate-formation. Flow of gas and water takes place until the pressure outside and inside of the hydrate-stability zone becomes equal again, i.e. $P_i = P_j$.

Formulation of the Phase Fluxes

We consider two cases for the mode of fluid transport. First we assume no capillarity-driven flow so that only pressure-driven viscous dominated flow occurs. We further assume that the saturation profile below the GHSZ does not change as hydrate forms and fluids flow to the GHSZ. We will show that in this case the proportion of gaseous phase flow, R_v , is not consistent with the large observed (inferred from CT image, Fig. 60 right panel) hydrate saturation within coarse layers. In the second case, we consider capillarity-driven flow together with pressure-driven flow, the former resulting from a capillary pressure gradient imposed by aqueous phase consumption during hydrate-formation. We will show that for the time-scale of this experiment the capillary-driven flow must have played a key role in forming large hydrate saturations from initial large gas saturations within the coarse layers as observed at the end of the experiment.

Case 1: Viscous Dominated Flow

Flow rate for water and gas is estimated from Darcy equation at each step. The increment in potential difference that each phase experiences would be $P_i - P_j$. Based on the apparatus setup, aqueous phase is fed only from below the hydrate formation zone while gas phase is supplied from the top and from the midpoint of the sandpack. The water flow rate in the infinitesimal time

interval $[t, t + dt]$ is assumed constant, $q_w = \frac{kk_{rw}}{\mu_w} A \frac{P_i^t - P_j^t}{\frac{L}{2} + L_2}$, where L is the length of the

sandpack. Similarly, gas flow rate in the time interval $[t, t + dt]$ would be:

$$q_g = \frac{k_1 k_{rg}}{\mu_g} A \frac{P_i^t - P_j^t}{L_1} + \frac{k_2 k_{rg}}{\mu_g} A \frac{P_i^t - P_j^t}{L_2} \quad (94)$$

Using the above gas and aqueous phases flow rates, P_i^{t+dt} is calculated as:

$$P_i^{t+dt} = P_i^t \left(1 - \frac{\frac{q_g dt}{\bar{V}_g}}{n_i^t} \right) \quad (95)$$

Since gas and water both would flow towards the hydrate formation zone, and since water is the incompressible phase, S_g^{t+dt} would decrease from S_g^t by the amount of water (pore volumes) that is supplied to the hydrate formation zone, i.e. $S_g^{t+dt} = S_g^t - q_w dt / PV_{HSZ}$, wherein PV_{HSZ} denotes the pore volume inside the hydrate formation zone. In fact, both water flow and the moles of gas transported, $q_g dt / \bar{V}_g$, into the hydrate formation zone contribute to increasing P_j (while P_i is decreasing due to loss of moles of gas). Therefore, P_j^{t+dt} is calculated as in Eq. (96).

$$P_j^{t+dt} = P_j^t \left(\frac{n_j^t + \frac{q_g dt}{\bar{V}_g}}{\frac{S_g^{t+dt}}{\frac{n_j^t}{S_g^t}}} \right) = P_j^t \left(\frac{S_g^t}{S_g^{t+dt}} \right) \left(\frac{n_j^{t+dt}}{n_j^t} \right) \quad (96)$$

Note that, this increase in P_j and the corresponding decrease in P_i continues until $P_i = P_j$ and the gas/water flow stops. This analysis is carried forward through incremental time steps, dt , and the system approaches an equilibrium state until another increment of hydrate dS_h forms and the above can be applied similarly.

Application of Pressure-Driven Viscous Flow Model to Stage 2 of Experiment

To illustrate the application of the above model, we analyze the hydrate formation within the coarse layer when the BGHSZ is at depth 8.1" from the top of the sandpack. Since we only consider the pressure-driven viscous dominated flow, R_v is basically governed by the ratio of phase mobilities, $\frac{\lambda_{g,eff}}{\lambda_{w,eff} + \lambda_{g,eff}}$. Note that since we have two inlets for the gas phase and only

one inlet for water from below, R_v is slightly greater than $\frac{\lambda_{g,eff}}{\lambda_{w,eff} + \lambda_{g,eff}}$.

Inferred data from the experiment corresponding to this step is presented in Fig. 63. The number of moles of methane consumed was inferred from the pressure change in the system (which was measured by two pressure transducers, one at the top and one at the bottom). The following table summarizes the amount of methane that was used and the resulting amount of methane hydrate. Density of water was assumed to be $\rho_w = 1000 \text{ kg/m}^3$, density of methane was assumed to be $\rho_h = 914 \text{ kg/m}^3$ (Sloan, 1998) and the density of methane at $P = 788 \text{ psig}$ (system pressure right before hydrate formation starts) was calculated to be $\rho_g \approx 44 \text{ kg/m}^3$. During the analysis as the pressure of the gas is decreasing, the density value and thus the methane molar volume is updated. Molar volumes of water, hydrate and methane at $P = 788 \text{ psig}$ and $T = 5 \text{ }^\circ\text{C}$ are reported in Table 5.

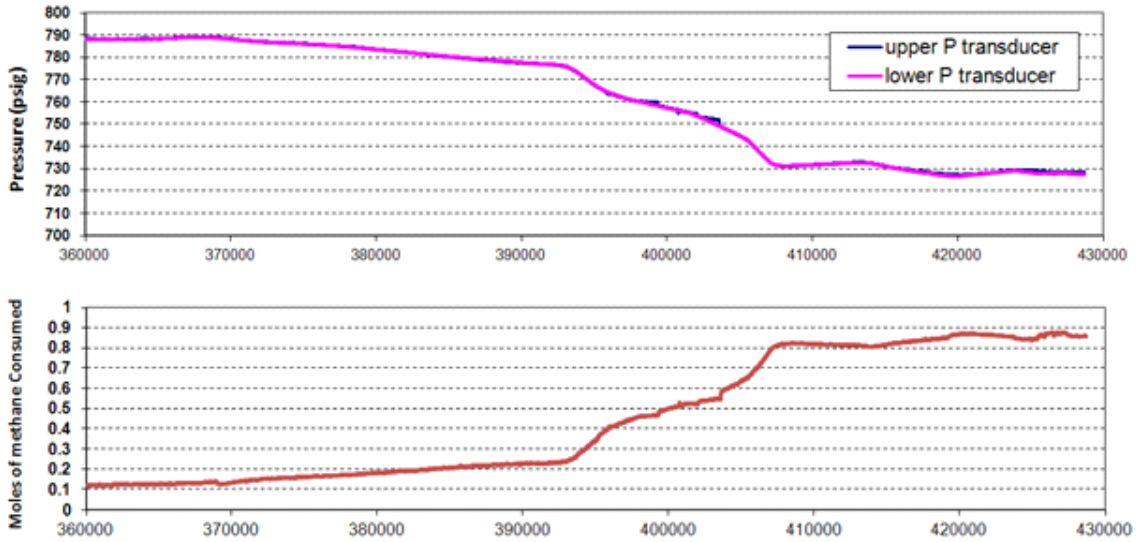


Fig. 63. Experiment results: BGHSZ descends from $z=0$ to $z=20.6 \text{ cm}$ and stays at 20.6 cm for about 24 hours. Horizontal axis shows time in seconds. The moles of methane consumed (bottom panel) are computed from the pressure in the reservoir (top panel) and the mass of water in the reservoir (not shown).

Table 5. Experiment Data: Hydrate is Assumed to Form Within the Height Interval $[0, 20.6] \text{ cm}$ of the Sandpack

Molar volumes (m ³ /kmole)			HSZ pore volume $PV_{HSZ} \text{ (cm}^3\text{)}$	Inferred information from experimental data		
\bar{V}_w	\bar{V}_g	\bar{V}_h		Moles of CH ₄ converted (moles)	Average Hydrate Saturation, S_h	Water Entered Sandpack (g)
0.018	0.363	0.136	336.4	≈ 0.8	$\approx 33\%$	≈ 12

We impose the hydrate-formation rate inferred from the experiment data as a boundary condition on the model. The goal in doing this is to determine from the model how the fluids phases will move in response to this condition. An average hydrate saturation of $S_h = 0.33$ was formed in the GHSZ in the time interval $[3.6 \text{ } 4.2] \times 10^5 \text{ sec}$; therefore, an average rate of hydrate formation (sat unit/sec) may be extracted. However, based on the graph of consumed moles of methane versus time (Fig. 63) it is clear that there are three different major rates of hydrate formation over the course of time within the interval $[3.6 \text{ } 4.2] \times 10^5 \text{ sec}$: slow between $3.6 \times 10^5 \text{ s}$ and $3.9 \times 10^5 \text{ s}$, fast between $3.9 \times 10^5 \text{ s}$ and $4.08 \times 10^5 \text{ s}$, and slow again for the remainder of the

interval. Therefore, in the modeling the rate of hydrate formation appropriate to each time interval was imposed. An intrinsic permeability of 10 Darcy was assumed for the sandpack and the relative permeability shown in Fig. 64 was used.

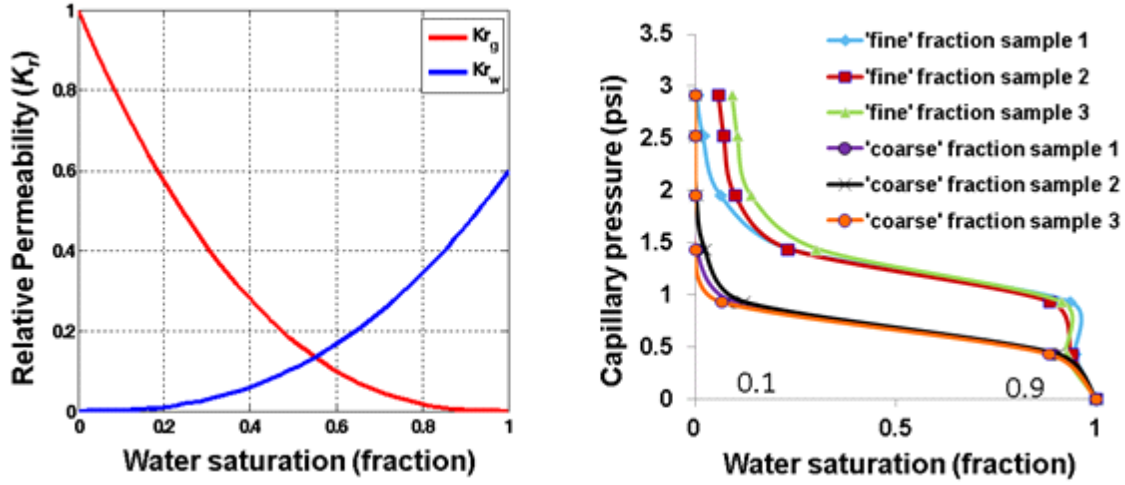


Fig. 64. Left: Assumed characteristic relative permeability curves for both coarse and fine layers; Right: Experimental capillary curves of fine and coarse layers based on porous plate method.

The effective mobilities used for flow into the top coarse layer, shown in Fig. 65, are calculated using the harmonic average the mobility of the layers below the coarse layer as follows:

$$\lambda_{w,eff} = \frac{0.8}{\frac{0.5}{\lambda_w|_{S_g=0.02}} + \frac{0.2}{\lambda_w|_{S_g=0.1}} + \frac{0.1}{\lambda_w|_{S_g=0.9}}} \quad (97)$$

$$\lambda_{g,eff} = \frac{0.3}{\frac{0.2}{\lambda_g|_{S_g=0.1}} + \frac{0.1}{\lambda_g|_{S_g=0.9}}} \quad (98)$$

There will be another effective mobility calculated for gas flow from above which can be calculated similar to Eq. (98). The effective mobilities of gaseous and aqueous phase flowing from below are $\lambda_{g,eff} = 394.5$ and $\lambda_{w,eff} = 8.7$; consequently R_v is almost 1.

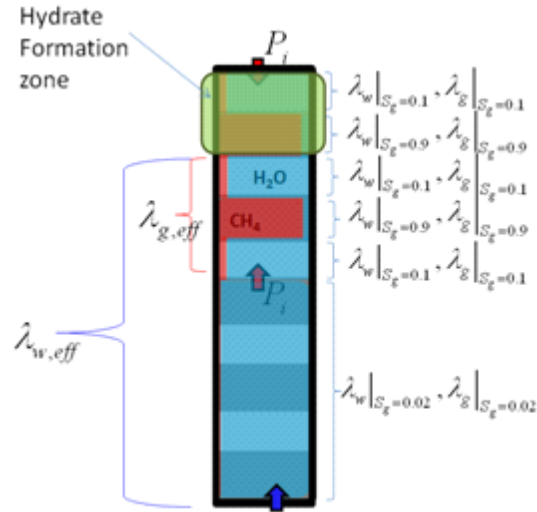


Fig. 65. Illustration of the effective mobilities used in the viscous dominated flow calculations.

Using these mobilities, the model predicts that hydrate formation stops at about 13% hydrate saturation, (Fig. 66), far less than the observed average value of 33% (Table 3). This limited hydrate saturation of 13% is what we would expect from Fig. 62 and R_v nearly unity. In effect the GHSZ runs out of aqueous phase because the water phase mobility is so much smaller than the gas phase mobility. Note that the model predicts that the remaining pore space in the layer would be filled with gas, not water. However, based on the final CT-scan images a large hydrate saturation of about 80%-90% was established within the top coarse layer sections. This indicates that viscous dominated flow cannot explain the experimental observations.

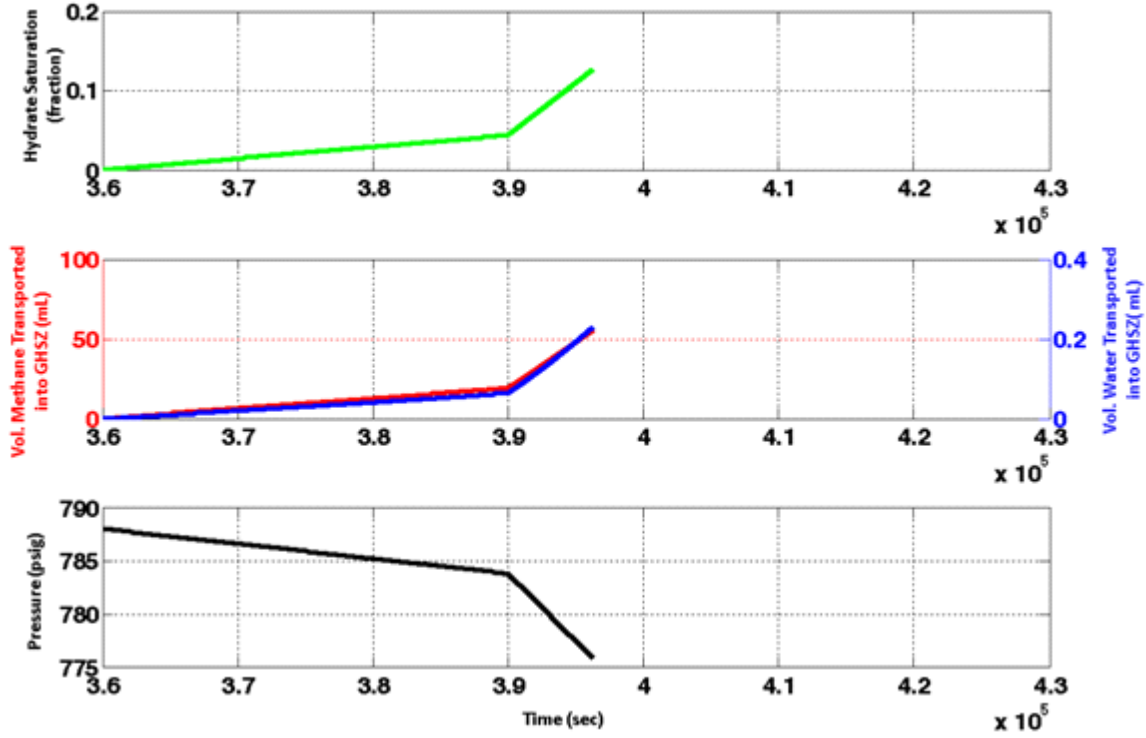


Fig. 66. Simulation results for hydrate formation within the coarse layer between [9.4 cm 20.6 cm] when only viscous dominated flow is taken into account. BGHSZ descends from $z = 0$ to $z = 20.6$ cm and stays at 20.6 cm for about 24 hours. Rate of hydrate formation determined from Fig. 63 was imposed on the model as a boundary condition.

Case 2: Pressure-Driven + Capillarity-Driven Flow

This case accounts for another contribution to aqueous phase flow towards the GHSZ, the flow due to a capillary-pressure gradient imposed by aqueous phase consumption during hydrate formation. Similar to the discussion above, when a saturation increment of hydrate, dS_h , forms inside the GHSZ, $dS_g^{used} = \frac{\bar{V}_g}{\bar{V}_h} dS_h$ saturation of gas and $dS_w^{used} = N \frac{\bar{V}_w}{\bar{V}_h} dS_h$ saturation of water were used to form the latter increment of hydrate. The gas phase is assumed to expand and fill the void space instantly and thus $S_g^t = S_g^{t^-} + dS_w^{used} - dS_h$. The water saturation decreases to $S_w^t = S_w^{t^-} - dS_w^{used}$ at the same moment. This reduction in water saturation would be equivalent to an increase of the capillary pressure from the initial capillary pressure, i.e. equilibrium state. The capillarity contribution to water flow is:

$$u_{w,cap} = k \frac{\lambda_w \lambda_g}{\lambda_w + \lambda_g} \left(\frac{\partial P_c}{\partial z} + (\rho_w - \rho_g)g \right) \quad (99)$$

Note that in the above equation downward direction is the + direction. When the system is in equilibrium we have $-\frac{\partial P_c}{\partial z} = (\rho_w - \rho_g)g$; therefore, $u_{w,cap}=0$. When an increase in capillary

pressure takes place due to a reduction in aqueous phase saturation $-\frac{\partial P_c}{\partial z} > (\rho_w - \rho_g)g$ and thus a nonzero flux of water flows towards the GHSZ due to a gradient in capillary pressure.

Figure 67 shows the modeling results when we account for the capillary-driven flows. A clear increase in magnitude of water flowing into the GHSZ is observed in Fig. 67 compared to that in Fig. 66. This substantial increase in the amount of water flux is due to the capillarity-driven flow. At the time, $t = 420,000$ sec when $S_h=33\%$, the gaseous and aqueous phase saturations are $S_g=58.54\%$ and $S_w=8.46\%$, respectively. Note that the initial gaseous and water saturations were $S_{g,i} = 90\%$ and $S_{w,i} = 10\%$, and thus it is clear that gaseous phase saturation is decreasing much faster than that of aqueous phase. In fact, capillary-dominated flow is crucially contributing toward maintaining the water saturation to make formation of large hydrate saturations possible.

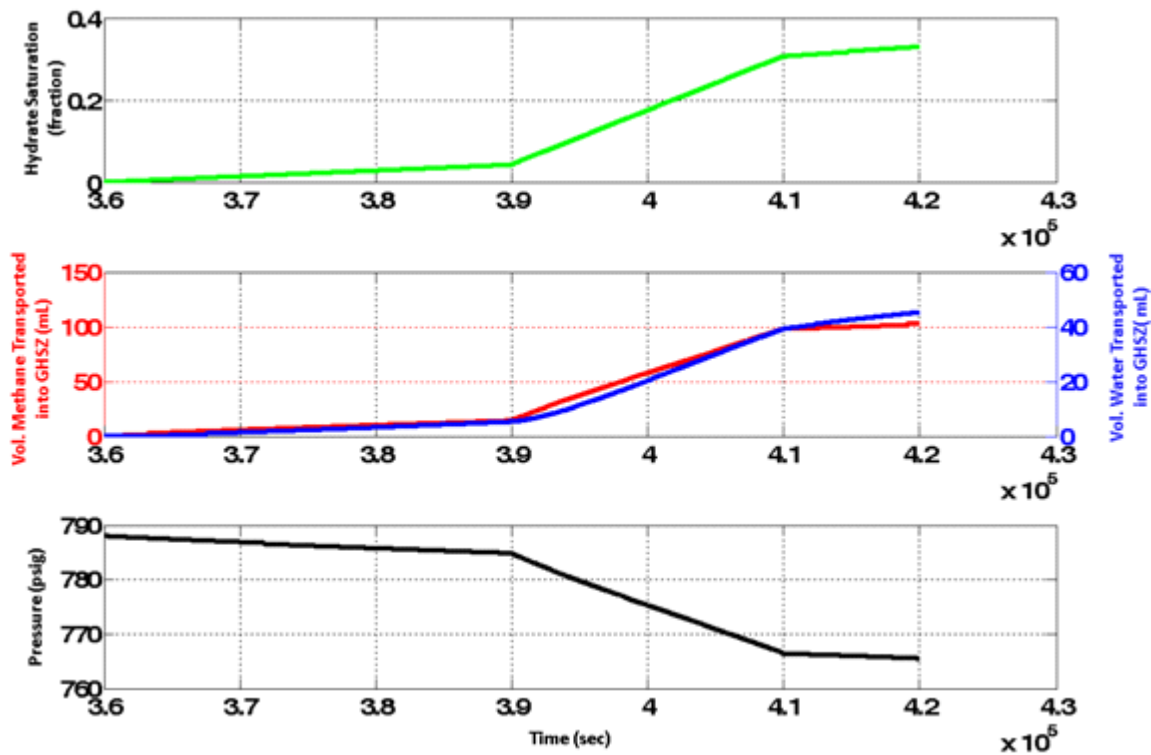


Fig. 67. Simulation results for hydrate formation within the coarse layer between [9.4 cm 20.6 cm] when both viscous dominated and capillarity-driven flows are taken into account. BGHSZ descends from $z = 0$ to $z = 20.6$ cm and stays at 20.6 cm for about 24 hours. Rate of hydrate formation was adopted from the experiment.

Is Hydrate Formation Controlled by the Rate of Fluid Transport?

The preceding analysis shows that capillarity-driven movement of water enables flow at rates sufficient to supply the observed rate of hydrate formation. Moreover the model indicates that neglecting capillarity-driven movement causes the GHSZ to be water-starved. This is a limiting case as very large saturation gradients would obviously arise long before the water saturation in the layer were completely consumed. This suggests that even if the flow were pressure-driven (viscous dominated) for some period of time, the system would evolve to a state in which

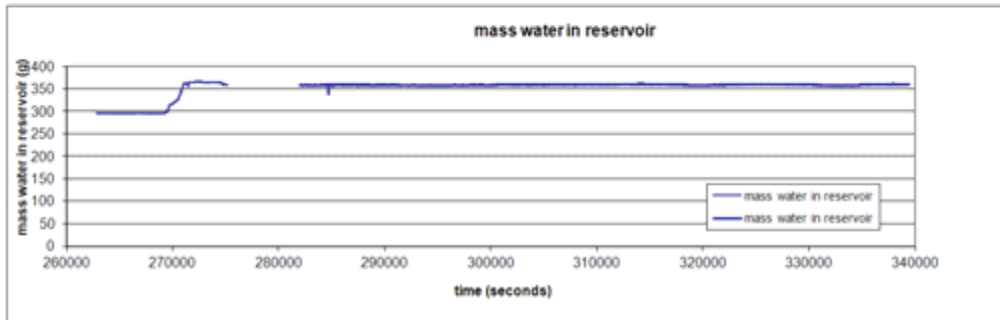
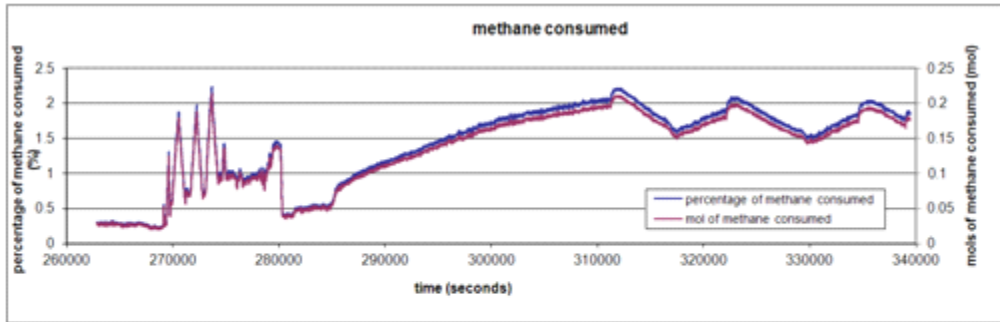
capillarity-driven flow must occur. These considerations raise an interesting speculation: the rate at which hydrate can be formed from a gas accumulation is ultimately limited by the rate at which the aqueous phase can be supplied to the GHSZ.

The experiment provides some support for this speculation. The images on the following pages show the moles of gas converted into methane hydrate in each step of descent of the BGHSZ as well as the mass of water in the reservoir versus time. In the first three steps, methane is consumed intermittently at large rates ($> 3 \times 10^{-5}$ gmol/s), while the net amount of water sucked into the sandpack from the reservoir is small. In fact the mass of water in the reservoir fluctuates rather wildly in steps 2 through 4. In fact sometimes water enters the reservoir from the sandpack. The model shows that large rates of hydrate formation cannot be sustained with only viscous flow. The fluctuations in the water flux between reservoir and sandpack may be a manifestation of this limit, as the system may have become starved of water in various locations during the intervals of rapid hydrate formation. The starvation would have caused hydrate formation to stop, halting the requirement for influx of fluids. Meanwhile local capillarity-driven flow restored water in other locations, enabling hydrate formation to resume.

A transition from viscous-dominated to flow with a significant contribution from capillarity seems to have occurred after step 4. Unlike steps 1 through 4, the behavior does not change qualitatively during steps 5 through 8. The rate of hydrate formation is steady, decreasing slowly with time and accompanied by a steady draining of water from the reservoir into column. The rate of hydrate formation is much smaller throughout this period than it was during the large-rate-of-formation intervals in steps 2 and 3. The small rate was not for lack of gas to be converted; at the end of step 4, the cumulative gas converted was just 64% of the value at the end of the experiment. Nor is the small rate due to lack of hydrate stability: the BGHSZ is far below the upper portion of the column where the hydrate is forming, and no salinity builds up during hydrate formation because the aqueous phase is distilled water. The simplest explanation for the late-stage behavior is that the system has settled into a balanced state. The rate of hydrate formation is just large enough to impose pressure and capillary pressure gradients that in turn are just large enough to induce the rates of gas and water transport needed to support hydrate formation. Since even the smaller rate of hydrate formation cannot be supplied only by pressure-driven viscous flow, this suggests that capillarity-driven flow of water is essential to the formation of hydrate. Moreover, the rate of capillarity-driven flow determines the rate of hydrate formation.

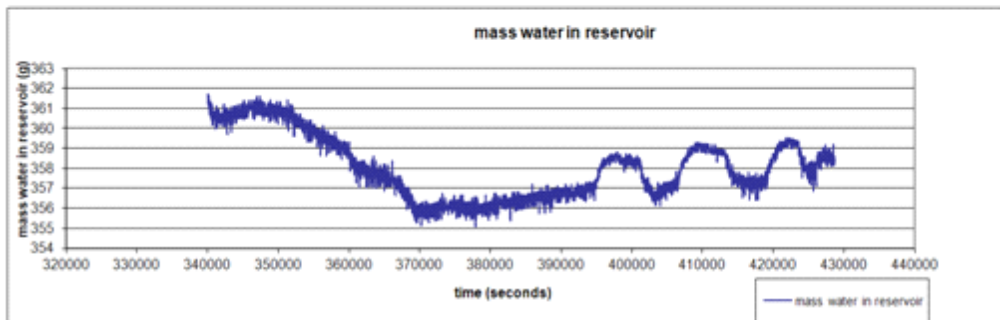
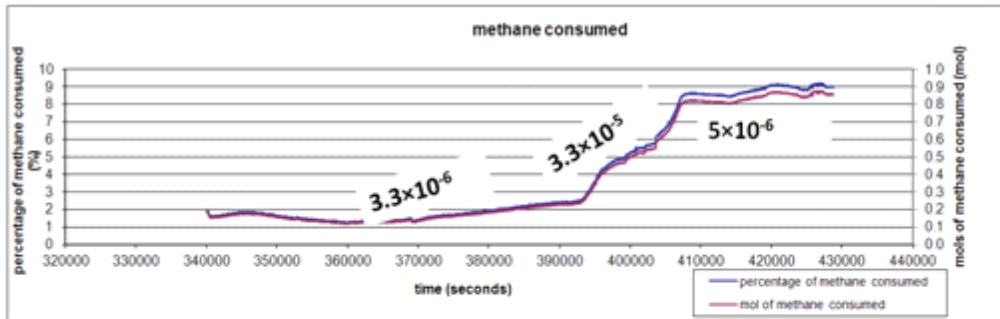
Rate of Hydrate formation
= 5×10^{-6} (moles hydrate/second)

Step 1



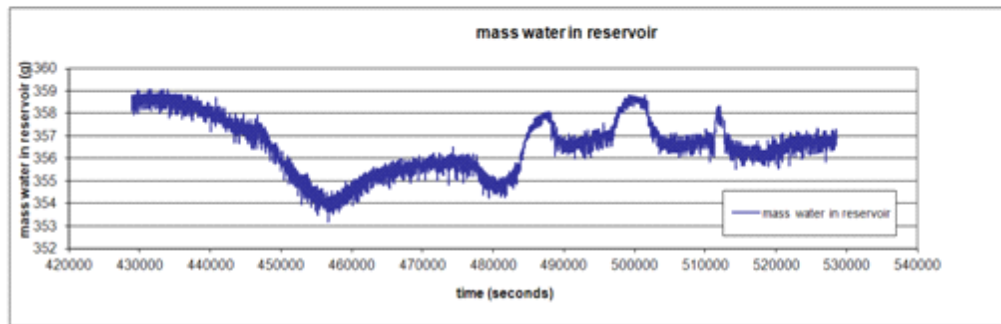
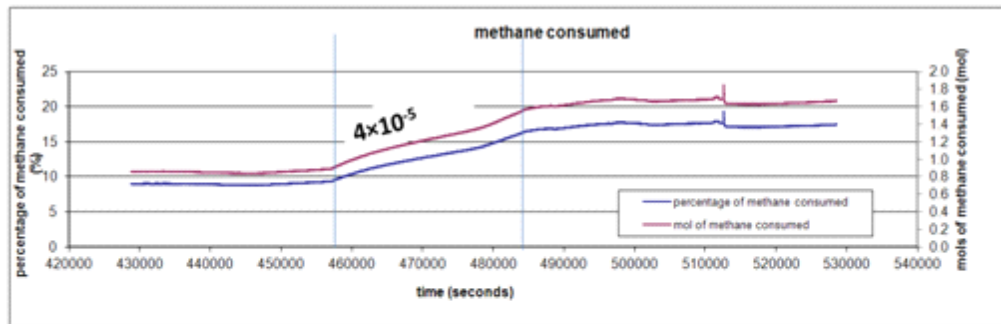
Rate of Hydrate formation
=Shown on Graph

Step 2



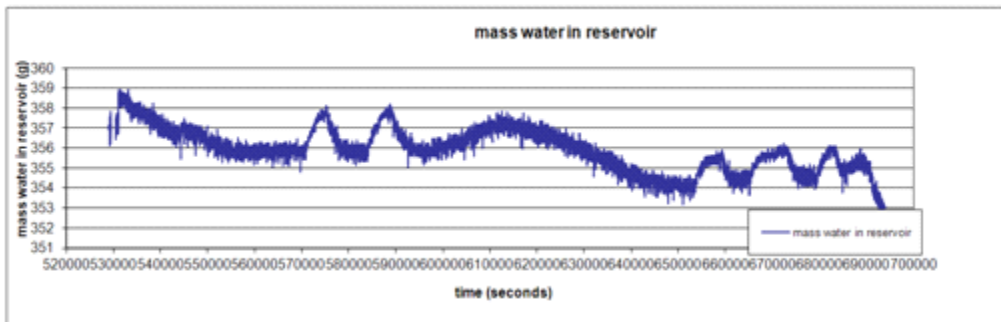
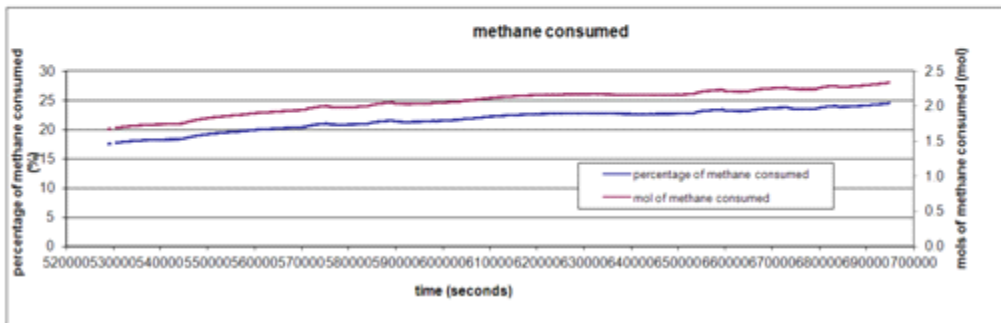
Rate of Hydrate formation
= Shown on Graph

Step 3

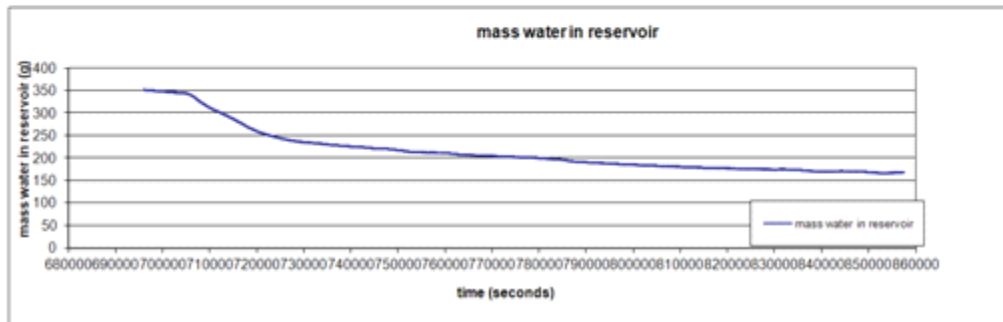
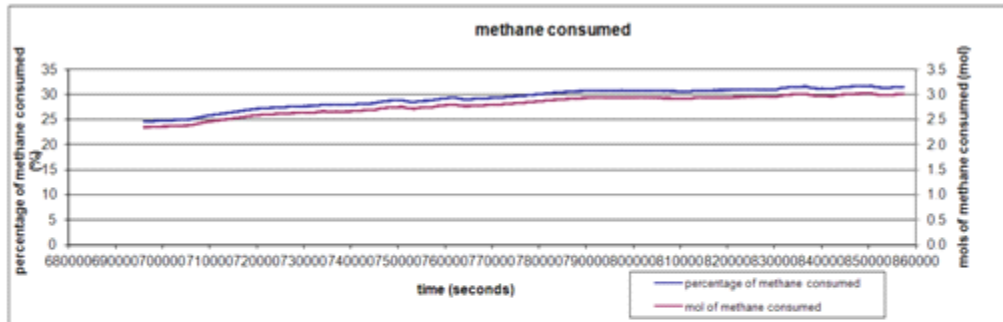


Rate of Hydrate formation
= 3.6×10^{-6} (moles hydrate/second)

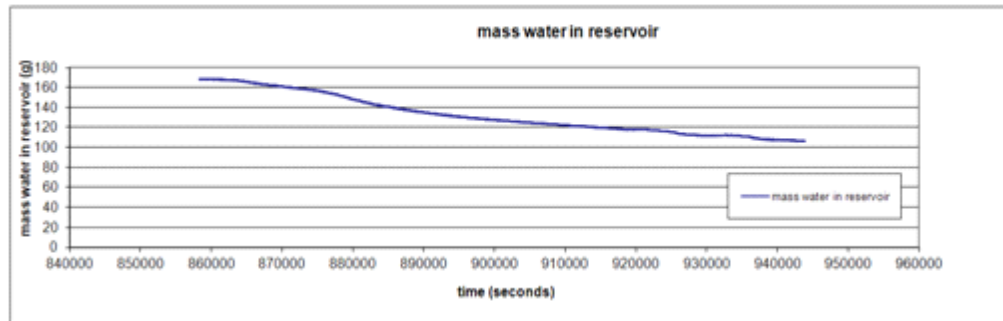
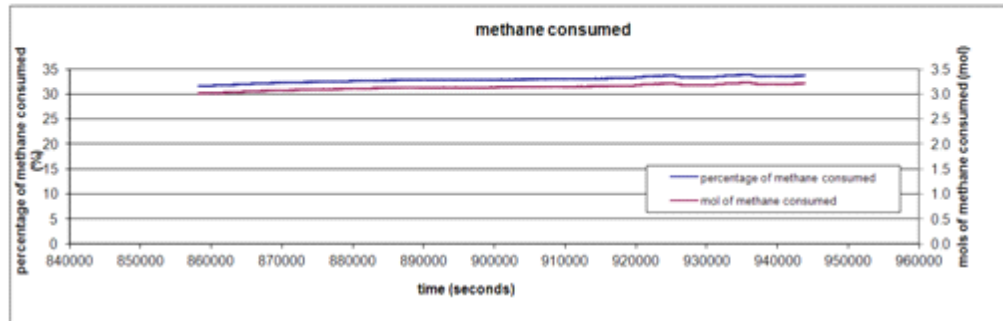
Step 4



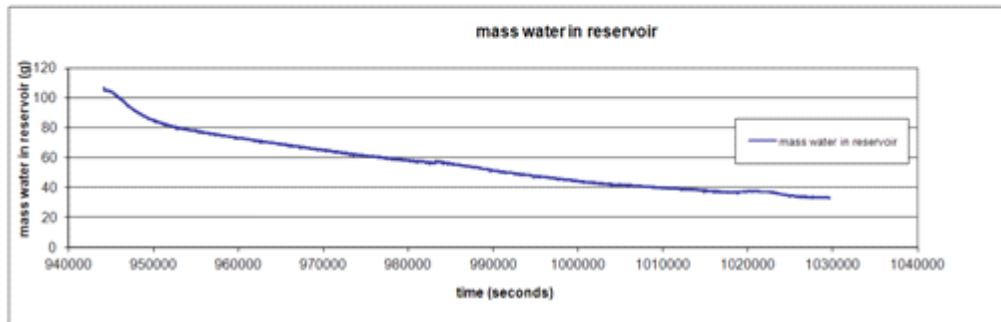
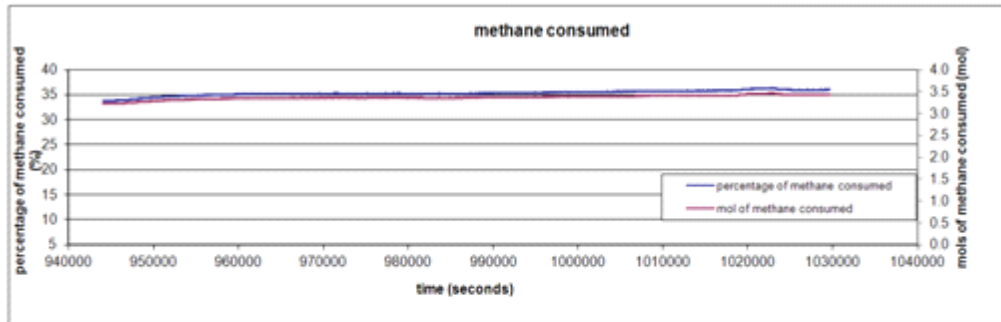
Rate of Hydrate formation
 $=4.2 \times 10^{-6}$ (moles hydrate/second) **Step 5**



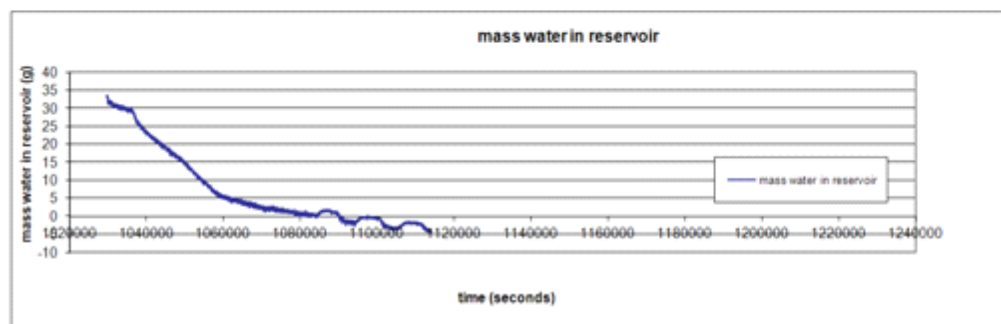
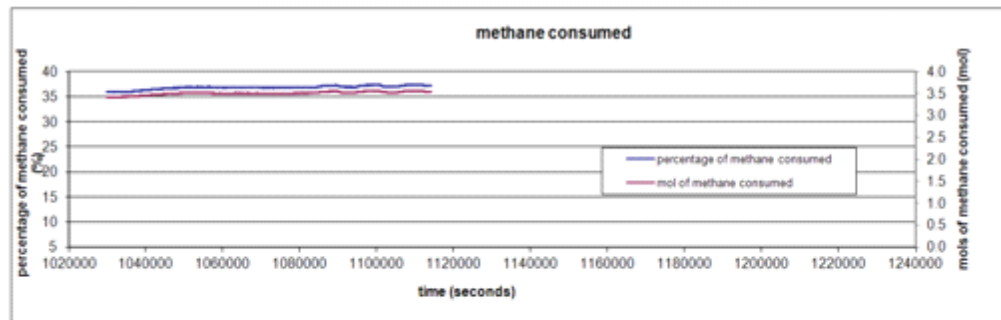
Rate of Hydrate formation
 $=2.4 \times 10^{-6}$ (moles hydrate/second) **Step 6**



Rate of Hydrate formation
 $=2.4 \times 10^{-6}$ (moles hydrate/second) **Step 7**



Rate of Hydrate formation
 $=1.3 \times 10^{-6}$ (moles hydrate/second) **Step 8**



Discussion of Findings from Experimental Descent of Gas Hydrate Stability Zone

The experimental boundary conditions do not replicate the situation in gas reservoirs converted to hydrate in the Arctic. The key differences are that in the experiment water can move

to the hydrate stability zone only from below, while in nature water can move from below and from above. In experiment gas can move to the hydrate stability zone from below and from above, while in nature it can move only from below. Finally, the fluid phase pressures decrease with time in the experiment (though the conditions remain within the hydrate stability field throughout), while the water phase pressure does not change with time in nature. These differences are minor and do not alter the essential similarities to the natural situation. In the experiment and in nature, the base of the gas hydrate stability zone descends gradually through an existing gas accumulation, and fluid phases are free to move in response to any gradients that arise as hydrate forms. The latter point is important: no fluid flow (neither pressure-driven nor capillarity-driven) is imposed in the experiment. Instead the system evolves a combination of buoyancy-, pressure- and capillarity-driven fluxes of the gas and water phases, and these fluxes balance the various resistances to transport.

The model predicts that the contribution of capillarity-driven flux is significant in these experiments. In fact $R_v \sim 0.69$ when capillary-dominated flow is taken into account while $R_v \sim 1$ when only the viscous dominated portion of the flow was considered. This is consistent with our findings in previous sections of this report, namely, pressure-driven flow cannot supply water from below the BGHSZ fast enough to sustain hydrate formation. Moreover the model predicts that the amount of gas flows to the GHSZ from above quickly diminishes as both the effective permeability, due to hydrate formation within the GHSZ, and gaseous phase relative permeability, due to decrease in gas saturation within the GHSZ, decrease. Therefore, the main contribution for gas flow would be flow from the middle gas inlet. While the gas flux from above and from below could not be independently measured in this experiment, the consistency of the model with other observations suggests that all the fluids needed during conversion to hydrate can be supplied from below. But this is possible only if capillarity-driven flux is accounted for.

The consistency of the capillarity-driven flux model with the experimental observations suggests that the finding in the previous section, viz. that the observed hydrate saturation profile in Mt. Elbert arises naturally from the capillarity-driven fluxes, is not a coincidence. That is, these findings suggest that the gas reservoir conversion process is slow, that it introduces modest, even negligible pressure gradients but impose significant gradients in saturation which, along with gas buoyancy, feed the appropriate volumes of fluids to the GHSZ.

A complete validation of the model would compare the predicted hydrate saturation profile to the observed profile in Fig. 60. Unfortunately this is not possible because we do not know the initial gas saturation profile. The required horizontal positioning of the column during scanning would have disrupted the gas-water saturation distribution achieved in the vertical orientation of the experiment. Thus the experiment proceeded with knowledge only of the mass of gas in the column and the observation that gas was produced from the bottom of the column during injection. This is sufficient only to bound the possible initial saturation profile, e.g. if it were uniform, the initial gas phase saturation would have been 0.20. As discussed above, it is possible to make a plausible estimate of the original gas saturation profile, and this does lead to a prediction consistent with the final profile. It would be valuable to repeat the experiment and eliminate this uncertainty.

The coarse/fine layering in the sand pack was intended to represent the variation that allows for disconnection of the gas column as the gas-water contact rises during conversion to hydrate. This is a key mechanism leading to large saturations in the upper portions of layers, separated by regions of small hydrate saturation. The experiment did not test this mechanism directly, because the pressure in the gas phase probably was controlled by gas column height. Though the

gas/water contact presumably rose during the experiment as water entered the bottom of the sandpack, the gas phase in the sandpack was always connected to the gas reservoir pressure by the inlets at the top and at the midpoint of the sand pack. Thus disconnection of the gas column across fine sand layers probably did not occur, and the gas phase was able to flow anywhere within the top half of the sandpack throughout the experiment.

Conclusions from Experiment on Descending Base of Gas Hydrate Stability Zone

After establishing a gas saturation within a long (1 m) sand column, short (10 cm) sections of the column were sequentially (from top to bottom) cooled to conditions at which hydrate was stable. While the boundary conditions (a source of gas and water phases at same pressure, with gas line connected to the top and midpoint of the sand column and water line connected to the bottom) were not the same as those during the descent of the base of gas hydrate stability zone through gas reservoirs in the Arctic, the driving force for fluid phase movement was identical: the consumption of gas and water and the reduction in phase volume accompanying hydrate formation. A mathematical model of fluid phase transport that accounts for fluxes due to buoyancy pressure gradient and capillary pressure gradient correctly predicted the movement of gas phase and water phase into the sand column from the reservoir, given the observed rate of hydrate formation and the observed pressure history. The agreement with observation is significant, since it requires achieving the correct balance between the different driving forces.

Capillarity-driven fluxes are essential for explaining the observed hydrate distribution. The experiment thus supports the hypothesis that saturation gradients are a key mechanism in the process of converting gas reservoirs to hydrate in the Arctic.

References for Capillarity Dominated Behavior in Hydrate-Bearing Sediments

- Anderson, B., Hancock, S., Wilson, S., Enger, C., Collett, T., Boswell, R., and Hunter, R., 2011, Formation pressure testing at the Mount Elbert Gas Hydrate Stratigraphic Test Well, Alaska North Slope: Operational summary, history matching, and interpretations: *Marine and Petroleum Geology*, v. 28, no. 2, p. 478-492.
- Behseresht, J., Bryant, S.L., Sepehrnoori, K., 2009. Infinite-Acting Physically Representative Networks for Capillarity-Controlled Displacements. *Soc. Petrol. Eng. J.* 14, 568-578.
- Bhatnagar, G., Chapman, W.G., Dickens, G.R., Dugan, B., Hirasaki, G.J., 2007. Generalization of gas hydrate distribution and saturation in marine sediments by scaling of thermodynamic and transport processes. *Am. J. Sci.* 307, 861-900.
- Blunt, M., 2001, Flow in porous media -- pore-network models and multiphase flow: Current Opinion in Colloid & Interface Science, v. 6, no. 3, p. 197-207.
- Boswell, R., Rose, K., Collett, T.S., Lee, M., Winters, W.J., Lewis, K.A., Agena, W.F., 2011. Geologic controls on gas hydrate occurrence in the Mount Elbert prospect, Alaska North Slope. *Mar. Pet. Geol.* 28, 589-607.
- Bryant, S.L., King, P.R., Mellor, D.W., 1993. Network model evaluation of permeability and spatial correlation in a real random sphere packing. *Transp. Porous Media.* 11, 53-70.
- Buffett, B., 2000. Formation of gas hydrate from dissolved gas in natural porous media. *Mar. Geol.* 164, 69-77.
- Clennell, B.M., Hovland, M., Booth, J.S., Henry, P., Winters, W.J., 1999. Formation of natural gas hydrates in marine sediments 1. Conceptual model of gas hydrate growth conditioned by host sediment properties. *J. Geophys. Res.* 104, 22985-23003.
- Collett, T., and Lee, M., 2005, Electrical-resistivity well-log analysis of gas hydrate saturations in the JAPEX/JNOC/GSC *et al.* Mallik 5L-38 gas hydrate production research well: Scientific results from the Mallik 2002 Gas hydrate Production Research Well Program, Mackenzie Delta, Northwest Territories, Canada.
- Collett, T.S., 1993. Natural Gas Hydrates of the Prudhoe Bay and Kuparuk River Area, North Slope, Alaska. *Am. Assoc. Pet. Geol. Bull.* 77, 793-812.
- Collett, T.S., Johnson, A., Knapp, C., Boswell, R., 2009. Natural Gas Hydrates – A Review, in: *Natural Gas Hydrates – Energy Resource Potential and Associated Geologic Hazards*, Mem. Am. Assoc. Pet. Geol. 89, 146–219.
- Collett, T.S., Lee, M.W., Agena, W.F., Miller, J.J., Lewis, K.A., Zyrianova, M.V., Boswell, R., Inks, T.L., 2011. Permafrost-associated natural gas hydrate occurrences on the Alaska North Slope. *Mar. Pet. Geol.* 28, 279-294.
- Dai, S., Lee, C., Santamarina, J.C., 2011. Formation history and physical properties of sediments from the Mount Elbert Gas Hydrate Stratigraphic Test Well, Alaska North Slope. *Mar. Pet. Geol.* 28, 427-438.
- Dallimore, S.R., Collett, T.S., 2005. Scientific results from the Mallik 2002 gas hydrate production research well program, Mackenzie delta, Northwest Territories, Bull. Geol. Surv. Can., 585.
- Dawe, R.A., Wheat, M.R., Bidner, M.S., 1992. Experimental investigation of capillary pressure effects on immiscible displacement in lensed and layered porous media. *Transp. Porous Media.* 7, 83-101.

- Dong Lee, J., Susilo, R., and Englezos, P., 2005, Methane-ethane and methane-propane hydrate formation and decomposition on water droplets: *Chemical Engineering Science*, v. 60, no. 15, p. 4203-4212.
- Fujii, T., Saeki, T., Kobayashi, T., Inamori, T., Hayashi, M., Takano, O., Takayama, T., Kawasaki, T., Nagakubo, S., Nakamizu, M., Yokoi, K., 2008. Resource Assessment of Methane Hydrate in the Eastern Nankai Trough, Japan. Presented in Offshore Technology Conference, 5-8 May 2008, Houston, Texas, USA.
- Ginsburg, G.D., 1998. Gas hydrate accumulation in deep-water marine sediments. *J. Geol. Soc. (London, U.K.) Special Publications*. 137, 51-62.
- Gladkikh, M., and Bryant, S., 2005, Prediction of imbibition in unconsolidated granular materials: *Journal of Colloid and Interface Science*, v. 288, no. 2, p. 526-539.
- Hadley, C., Peters, D., Vaughan, A., Bean, D., 2008. Gumusut-Kakap Project: Geohazard Characterisation and Impact on Field Development Plans, Presented in International Petroleum Technology Conference, 3-5 December, Kuala Lumpur, Malaysia.
- Handa, Y., 1990, Effect of hydrostatic pressure and salinity on the stability of gas hydrates: *The Journal of Physical Chemistry*, v. 94, no. 6, p. 2652-2657.
- Handa, Y.P., 1986. Calorimetric determinations of the compositions, enthalpies of dissociation, and heat capacities in the range 85 to 270 K for clathrate hydrates of xenon and krypton. *J. Chem. Thermodyn.* 18, 891-902.
- Hensen, C., Wallmann, K., 2005. Methane formation at Costa Rica continental margin—constraints for gas hydrate inventories and cross-décollement fluid flow. *Earth Planet. Sci. Lett.* 236, 41-60.
- Hilpert, M., McBride, J.F., Miller, C.T., 2000. Investigation of the residual–funicular nonwetting-phase-saturation relation. *Adv. Water Resour.* 24, 157-177.
- Hirai, S., Okazaki, K., Araki, N., Yazawa, H., Ito, H., and Hijikata, K., 1996, Transport phenomena of liquid CO₂ in pressurized water flow with clathrate-hydrate at the interface: *Energy Conversion and Management*, v. 37, no. 6-8, p. 1073-1078.
- Holbrook, S., Hoskins, H., Wood, W., Stephen, R., and Lizarralde, D., 1996, Methane Hydrate and Free Gas on the Blake Ridge from Vertical Seismic Profiling: *Science*, v. 273, no. 5283, p. 1840 -1843.
- Holland, M., Schultheiss, P., Roberts, J., Druce, M., 2008. Observed gas Hydrate morphologies in marine sediments. Presented in the 6th International Conference on Gas Hydrates, Vancouver, British Columbia, Canada.
- Hunter, R., Collett, T., Boswell, R., Anderson, B., Digert, S., Pospisil, G., Baker, R., and Weeks, M., 2011, Mount Elbert Gas Hydrate Stratigraphic Test Well, Alaska North Slope: Overview of scientific and technical program: *Marine and Petroleum Geology*, v. 28, no. 2, p. 295-310.
- Hyndman, R., and Spence, G., 1992, A Seismic Study of Methane Hydrate Marine Bottom Simulating Reflectors: *Journal of Geophysical Research*, v. 97, no. B5, p. PP. 6683-6698.
- Hyndman, R.D., Davis, E.E., 1992. A Mechanism for the Formation of Methane Hydrate and Seafloor Bottom-Simulating Reflectors by Vertical Fluid Expulsion. *J. Geophys. Res.* 97, 7025-7041.
- Inks, T., Lee, M., Agena, W.F., Taylor, D., Collett, T.S., Hunter, R., Zyrianova, M., 2009. Seismic prospecting for gas hydrate and associated free gas prospects in the Milne Point area of northern Alaska, in: Collett, T.S., Johnson, A., Knapp, C., Boswell R., eds., *Natural Gas Hydrates – Energy Resource Potential and Associated Geologic Hazards*. Mem. Am. Assoc. Pet. Geol., 89.

- Iversen, N., Jorgensen, B., 1993. Diffusion coefficients of sulfate and methane in marine sediments: Influence of porosity. *Geochim. Cosmochim. Acta.* 57, 571-578.
- Jho, C., Nealon, D., Shogbola, S., King, A.D., 1978. Effect of pressure on the surface tension of water: Adsorption of hydrocarbon gases and carbon dioxide on water at temperatures between 0 and 50°C. *J. Colloid Interface Sci.* 65, 141-154.
- Katsube, T., Dallimore, S., Jonasson, I., Connell-Madore, S., Medioli, B., Uchida, T., Wright, J., and Scromeda, N., 2005, Petrophysical characteristics of gas-hydrate-bearing and gas-hydrate-free formations in the JAPEX/JNOC/GSC *et al.* Mallik 5L-38 gas hydrate production research well: Geological Survey of Canada, Scientific results from the Mallik 2002 Gas hydrate Production Research Well Program, Mackenzie Delta, Northwest Territories, Canada.
- Katsuki, D., Ohmura, R., Ebinuma, T., and Narita, H., 2006, Formation, growth and ageing of clathrate hydrate crystals in a porous medium: *Philosophical Magazine*, v. 86, no. 12, p. 1753-1761.
- Katsuki, D., Ohmura, R., Ebinuma, T., and Narita, H., 2007, Methane hydrate crystal growth in a porous medium filled with methane-saturated liquid water: *Philosophical Magazine*, v. 87, no. 7, p. 1057-1069.
- Kleinberg, R., Flaum, C., and Collett, T., 2005, Magnetic resonance log of JAPEX/JNOC/GSC *et al.* Mallik 5L-38 gas hydrate production research well: gas hydrate saturation, growth habit, and relative permeability: Geological Survey of Canada, Scientific results from the Mallik 2002 Gas hydrate Production Research Well Program, Mackenzie Delta, Northwest Territories, Canada.
- Koh, C., Westacott, R., Zhang, W., Hirachand, K., Creek, J., Soper, A., 2002. Mechanisms of gas hydrate formation and inhibition. *Fluid Phase Equilib.* 194-197, 143-151.
- Kvenvolden, K., 1988. Methane hydrate — A major reservoir of carbon in the shallow geosphere? *Chem. Geol.* 71, 41-51.
- Lee, M., and Collett, T., 2005, Assessment of gas hydrate concentrations estimated from sonic logs in the JAPEX/JNOC/GSC *et al.* Mallik 5L-38 gas hydrate research production well: Geological Survey of Canada, Scientific results from the Mallik 2002 Gas hydrate Production Research Well Program, Mackenzie Delta, Northwest Territories, Canada.
- Lee, M.W., Collett, T.S., 2011. In-situ gas hydrate saturation estimated from various well logs at the Mount Elbert Gas Hydrate Stratigraphic Test Well, Alaska North Slope. *Mar. Pet. Geol.* 28, 439-449.
- Liu, X., and Flemings, P., 2007, Dynamic multiphase flow model of hydrate formation in marine sediments: *Journal of Geophysical Research*, v. 112, no. B3.
- Liu, X., Flemings, P.B., 2006. Passing gas through the hydrate stability zone at southern Hydrate Ridge, offshore Oregon. *Earth Planet. Sci. Lett.* 241, 211-226.
- Lorenson, T., Collett, T., and Hunter, R., 2011, Gas geochemistry of the Mount Elbert Gas Hydrate Stratigraphic Test Well, Alaska North Slope: Implications for gas hydrate exploration in the Arctic: *Marine and Petroleum Geology*, v. 28, no. 2, p. 343-360.
- Majorowicz, J., Osadetz, K., and Safanda, J., 2008, Onset and stability of gas hydrates under permafrost in an environment of surface climatic change - past and future, *in* Vancouver, Canada.
- Majorowicz, J.A., Osadetz, K., Safanda, J., 2008. Modeling temperature profiles considering the latent heat of physical-chemical reactions in permafrost and gas hydrates: The Mackenzie

- Delta terrestrial case, Presented in the Ninth International Conference on Permafrost, Fairbanks, Alaska USA, pp. 1113-1118.
- Mason, G., Mellor, D.W., 1995. Simulation of Drainage and Imbibition in a Random Packing of Equal Spheres. *J. Colloid Interface Sci.* 176, 214-225.
- Matsumoto, R., Tomaru, H., Chen, Y., Lu, H., and Clark, I., 2005, Geochemistry of the interstitial waters of the JAPEX/JNOC/GSC *et al.* Mallik 5L-38 gas hydrate production research well: Geological Survey of Canada, Scientific results from the Mallik 2002 Gas hydrate Production Research Well Program, Mackenzie Delta, Northwest Territories, Canada.
- Mori, Y., and Mochizuki, T., 1997, Mass transport across clathrate hydrate films -- a capillary permeation model: *Chemical Engineering Science*, v. 52, no. 20, p. 3613-3616.
- Odong, J., 2008. Evaluation of Empirical Formulae for Determination of Hydraulic Conductivity based on Grain-Size Analysis. *J. Am. Sci.* 4, 1-6.
- Ohmura, R., Matsuda, S., Uchida, T., Ebinuma, T., and Narita, H., 2005, Clathrate hydrate crystal growth in liquid water saturated with a guest substance: Observations in a methane + water System: *Crystal Growth & Design*, v. 5, no. 3, p. 953-957.
- Peng, Y., 2011, Study of methane hydrate formation and distribution in arctic regions: from pore scale to field scale [PhD dissertation]: The University of Texas at Austin.
- Peng, Y., Prodanovic, M., Bryant, S.L., 2009. Improving Fidelity of Network Models for Drainage and Imbibition. Presented in SPE Annual Technical Conference and Exhibition, 4-7 October, New Orleans, Louisiana.
- Prodanović, M., and Bryant, S., 2006, A level set method for determining critical curvatures for drainage and imbibition: *Journal of Colloid and Interface Science*, v. 304, no. 2, p. 442-458.
- Prodanović, M., Bryant, S., and Karpyn, Z., 2008, Investigating matrix-fracture transfer via a level set method for drainage and imbibition, *in* Proceedings of SPE Annual Technical Conference and Exhibition.
- Ripmeester, J., Lu, H., Moudrakovski, I., Dutrisac, R., Wilson, L., Wright, F., and Dallimore, S., 2005, Structure and composition of gas hydrate in sediment recovered from JAPEX/JNOC/GSC *et al.* Mallik 5L-38 gas hydrate production research well, determined by X-ray diffraction and Raman and solid-state nuclear magnetic resonance spectroscopy: Geological Survey of Canada, Scientific results from the Mallik 2002 Gas hydrate Production Research Well Program, Mackenzie Delta, Northwest Territories, Canada.
- Ripmeester, J.A., Ratcliffe, C.I., 1988. Low-temperature cross-polarization/magic angle spinning ¹³C NMR of solid methane hydrates: Structure, cage occupancy, and hydration number. *J. Phys. Chem.* 92, 337-339.
- Rose, K., Boswell, R., Collett, T.S., 2011. Mount Elbert Gas Hydrate Stratigraphic Test Well, Alaska North Slope: Coring operations, core sedimentology, and lithostratigraphy. *Mar. Pet. Geol.* 28, 311-331.
- Setzmann, U.; Wagner, W., A New Equation of State and Tables of Thermodynamic Properties for Methane Covering the Range from the Melting Line to 625 K at Pressures up to 1000 MPa, **J. Phys. Chem. Ref. Data**, 1991, 20(6), 1061-1151.
- Ruppel, C., Boswell, R., and Jones, E., 2008, Scientific results from Gulf of Mexico Gas Hydrates Joint Industry Project Leg 1 drilling: Introduction and overview: *Marine and Petroleum Geology*, v. 25, no. 9, p. 819-829.
- Shindo, Y., Fujioka, Y., Takeuchi, K., and Komiyama, H., 1995, Kinetics on the Dissolution of CO₂ into Water from the Surface of CO₂ Hydrate at High Pressure: *International Journal of Chemical Kinetics*, v. 27, p. 569-575.

- Sloan, E., 2003, Fundamental principles and applications of natural gas hydrates: *Nature*, v. 426, no. 6964, p. 353-363.
- Sloan, E., and Koh, C., 2008, *Clathrate hydrates of natural gases*: CRC Press.
- Sloan, E.D., 1998. *Clathrate hydrates of natural gases*. 2nd ed. Marcel Dekker, New York.
- Sun, R., and Duan, Z., 2007, An accurate model to predict the thermodynamic stability of methane hydrate and methane solubility in marine environments: *Chemical Geology*, v. 244, no. 1-2, p. 248-262.
- Teng, H., Kinoshita, C., and Masutani, S., 1995, Hydrate formation on the surface of a CO₂ droplet in high-pressure, low-temperature water: *Chemical Engineering Science*, v. 50, no. 4, p. 559-564.
- Tohidi, B., Anderson, R., Clennell, M., Burgass, R., and Biderkab, A., 2001, Visual observation of gas-hydrate formation and dissociation in synthetic porous media by means of glass micromodels: *Geology*, v. 29, no. 9, p. 867-870.
- Torres, M.E., Collett, T.S., Rose, K.K., Sample, J.C., Agena, W.F., Rosenbaum, E.J., 2011. Pore fluid geochemistry from the Mount Elbert Gas Hydrate Stratigraphic Test Well, Alaska North Slope. *Mar. Pet. Geol.* 28, 332-342.
- Torres, M.E., Wallmann, K., Tréhu, A.M., Bohrmann, G., Borowski, W.S., Tomaru, H., 2004. Gas hydrate growth, methane transport, and chloride enrichment at the southern summit of Hydrate Ridge, Cascadia margin off Oregon. *Earth Planet. Sci. Lett.* 226, 225-241.
- Tréhu, A., Flemings, P., Bangs, N., Chevallier, J., Gràcia, E., Johnson, J., Liu, C., Liu, X., Riedel, M., and Torres, M., 2004, Feeding methane vents and gas hydrate deposits at south Hydrate Ridge: *Geophysical Research Letters*, v. 31, p. 4 PP.
- Uchida, T., Tsuji, T., Takahashi, T., Okui, T., and Minagawa, H., 2005, Petrophysical properties and sedimentology of gas-hydrate-bearing sediments in the JAPEx/JNOC/GSC *et al.* Mallik 5L-38 gas hydrate production research well: Geological Survey of Canada, Scientific results from the Mallik 2002 Gas hydrate Production Research Well Program, Mackenzie Delta, Northwest Territories, Canada.
- Valvatne, P., and Blunt, M., 2004, Predictive pore-scale modeling of two-phase flow in mixed wet media: *Water Resources Research*, v. 40, no. W07406.
- Valvatne, P., Piri, M., Lopez, X., and Blunt, M., 2005, Predictive pore-scale modeling of single and multiphase flow: *Transport in Porous Media*, v. 58, no. 1, p. 23-41.
- van Dijke, M., and Sorbie, K., 2003, Pore-scale modelling of three-phase flow in mixed-wet porous media: multiple displacement chains: *Journal of Petroleum Science and Engineering*, v. 39, no. 3-4, p. 201-216.
- Waite, W.F., Santamarina, J.C., Cortes, D.D., Dugan, B., Espinoza, D.N., Germaine, J., Jang, J., Jung, J.W., Kneafsey, T.J., Shin, H., Soga, K., Winters, W.J., Yun, T.S., 2009. Physical properties of hydrate-bearing sediments. *Rev. Geophys.* 47, RG4003.
- Winters, W., Dallimore, S., Collett, T., Medioli, B., Matsumoto, R., Katsube, T., and Brennan-Alpert, P., 2005, Relationships of sediment physical properties from the JAPEx/JNOC/GSC *et al.* Mallik 5L-38 gas hydrate production research well: Geological Survey of Canada, Scientific results from the Mallik 2002 Gas hydrate Production Research Well Program, Mackenzie Delta, Northwest Territories, Canada.
- Winters, W., Walker, M., Hunter, R., Collett, T., Boswell, R., Rose, K., Waite, W., Torres, M., Patil, S., and Dandekar, A., 2011, Physical properties of sediment from the Mount Elbert Gas Hydrate Stratigraphic Test Well, Alaska North Slope: *Marine and Petroleum Geology*, v. 28, no. 2, p. 361-380.

Xu, W., and Ruppel, C., 1999, Predicting the occurrence, distribution, and evolution of methane gas hydrate in porous marine sediments: *Journal of Geophysical Research*, v. 104, p. 5081-5095.

Fracturing Dominated Behavior

Preferential mode of gas invasion in sediments: Grain-scale mechanistic model of coupled multiphase fluid flow and sediment mechanics

Introduction

Gas migration through water-filled soft sediment is an essential component of the dynamics of the seafloor. It governs, for instance, the spatiotemporal characteristics of natural gas seeps and vent sites [Judd et al., 2002; Heeschen et al., 2003; Best et al., 2006], the biochemical processes in the shallow sub-seafloor as well as the ocean floor [Suess et al., 1999], the mechanical and acoustic properties of submarine sediments [Anderson and Hampton, 1980; Anderson et al., 1998; Waite et al., 2008], the creation of pockmarks in the ocean floor [Hovland et al., 2002; Sahling et al., 2008], and the accumulation of gas hydrate (notably methane) in ocean sediments. Understanding gas transport in soft sediments is also key to assessing the viability of carbon dioxide sequestration in the sub-seafloor, either by hydrate formation [Koide et al., 1995, 1997b] or gravitational trapping [Koide et al., 1997a; House et al., 2006; Levine et al., 2007; Goldberg et al., 2008].

Methane hydrates—crystalline ice-like compounds composed of methane molecules caged in a lattice of water molecules [Sloan, 1998]—form naturally at high pressures and low temperatures, like those typical of most of the ocean floor. It is believed that an enormous pool of carbon exists in the form of methane gas and methane hydrate in the ocean floor along the continental margins [Kvenvolden, 1988; Sloan, 2003], although the global estimates of the energy resource are highly uncertain. It also seems likely that this pool of carbon plays an important role in massive submarine landslides [Paull et al., 2003] and in the global carbon cycle [Dickens, 2003]—its sudden or gradual release has been hypothesized to be the cause of past and future climate change [Dickens et al., 1995; Buffett and Archer, 2004; Archer et al., 2009].

Methane hydrate systems in ocean sediments have been the subject of intense research in recent years. A significant component of that effort is directed towards gaining a better conceptual picture of the hydrogeological environment of gas hydrate systems. Particular attention has been devoted to the two end-members [Trehu et al., 2006b]:

1. The hydrogeologically more active, dynamic end-member, exemplified by Hydrate Ridge, offshore Oregon [Suess et al., 1999; Tryon et al., 2002; Heeschen et al., 2003; Trehu et al., 2004b; Weinberger et al., 2005].
2. The hydrogeologically less active, quiescent end-member, illustrated by Blake Ridge, offshore South Carolina [Holbrook et al., 1996; Dickens et al., 1997; Hornbach et al., 2007].

One of the fundamental observations at these two sites is the co-existence of methane hydrate, gas and brine within the hydrate stability zone (HSZ). This is especially noticeable in dynamic environments [Wood et al., 2002; Milkov et al., 2004; Torres et al., 2004; Zühlsdorff and Spiess, 2004; Heeschen et al., 2007; Sahling et al., 2008], but has been observed in low-flux hydrate provinces [Gorman et al., 2002]. It seems clear that, in some geologic settings, methane transport

through the HSZ cannot occur solely as diffusive and advective transport of dissolved methane in the aqueous phase [Torres et al., 2004; Trehu et al., 2004a; Liu and Flemings, 2006].

The scientific community is now undergoing a heated debate as to what are the reasons for co-existence of hydrate and gas [Milkov and Xu, 2005; Torres et al., 2005; Ruppel et al., 2005], which include: (1) kinetics of hydrate formation [Torres et al., 2004]; (2) regional geotherms [Wood et al., 2002]; (3) hypersaline brines as a result of hydrate formation [Milkov et al., 2004]; and (4) fast, focused flow of free gas through fractures and high-permeability conduits [Flemings et al., 2003; Hornbach et al., 2004]. The importance of methane migration as a separate gas phase, and the need to account for multiphase flow effects coupled with hydrate formation, have already been pointed out over a decade ago [Ginsburg and Soloviev, 1997; Soloviev and Ginsburg, 1997].

It has been proposed that free gas accumulation beneath the HSZ may reach a critical thickness to dilate fractures or activate pre-existing faults that will serve as conduits for fast upwards gas migration [Wood et al., 2002; Flemings et al., 2003; Trehu et al., 2004a; Hornbach et al., 2004; Zühlsdorff and Spiess, 2004; Obzhairov et al., 2004; Netzeband et al., 2005; Weinberger and Brown, 2006; Liu and Flemings, 2006, 2007]. Although they did not address the problem at the grain scale, Liu and Flemings [2007] also predicted that at fine grain size and high capillary entry pressure, fracture propagation would dominate the process as gas pressure exceeded the horizontal stress. In this case, it is clear that the study of the hydrate system must be coupled with the mechanical response of the host sediments containing hydrate.

Our hypothesis is that coupling of multiphase fluid flow and sediment mechanics leads—under certain conditions to be described below—to preferential fracturing of the sediment. The creation of these capillary pressure-driven fractures provides fast paths for upwards migration of methane gas through the HSZ, which in turn explains the co-existence of methane gas and hydrate [Behseresht et al., 2008; Jain and Juanes, 2008].

In this paper, we support this hypothesis by developing a mechanistic model at the *grain scale*. We develop a discrete element method (DEM) to model the strong coupling between the pore fluids and the mechanical behavior of the sediment. We rigorously account for the presence of one or more fluids in the pore space by incorporating additional sets of forces due to pore fluid pressures and interfacial tension between the fluids. We demonstrate the DEM's ability to reproduce core-scale behavior, as measured by triaxial laboratory experiments and fluid flow tests. The proposed methodology elucidates the depositional environments (grain size and earth stresses) under which migration of methane gas by fracturing of the sediment is favored over capillary invasion. This determines the distribution of methane gas and hydrate, and the likelihood that gas and hydrate will co-exist. Even though the analysis is done at the grain scale, these results have important implications at the geologic or planetary scale, such as for estimating the magnitude of methane fluxes into the ocean, and the overall size of the hydrate energy resource.

Theory, Formulation and Methods

The Discrete Element Method (DEM) [Cundall and Strack, 1979] has proved a valuable tool to study the mechanisms for deformation and failure of granular materials with variable degree of cementation [Bruno and Nelson, 1991]. Moreover, based on simple geometric arguments, stress variations (and subsequent deformation) have been shown to affect flow properties such as porosity and permeability [Bruno, 1994].

Each element or grain is identified separately by its own mass, moment of inertia and contact

properties. For each grain, its translational and rotational movements are described by solving Newton's second law of motion. The mechanical behavior at the deformation region of grain contact is approximated by introducing a grain contact model, such as a system of a spring, dashpot and slider (Figure 69).

Micromechanics of “dry” media

The movement of a grain is dictated by the net force and moment acting on it. For a *dry model*, that is, one in which pore pressures are negligible, the forces for each grain may include: (1) a contact force \mathbf{F}_c due to the deformation at the grain contacts, (2) a damping force \mathbf{F}_d due to grain non-elastic collisions; (3) an external force \mathbf{F}_b due to gravity and prescribed tractions at the boundaries. The contact force \mathbf{F}_c can be further split into normal and tangential components, \mathbf{F}_c^n and \mathbf{F}_c^s , respectively.

The simplest (linear elastic) mechanical behavior at the grain contacts is described by the following equations:

$$F^n = k_n U_n, \quad \Delta F^s = -k_s \Delta U_s, \quad (1)$$

where U_n is the overlap, ΔU_s is the tangential displacement, and k_n and k_s are the normal and shear stiffness at the contact, respectively [ITASCA, 2004; Potyondy and Cundall, 2004]. Inelastic behavior emerges due to either slip between grains, or breakage of contact bonds. Inelasticity is reflected by the constraints:

$$F^s \leq \bar{\mu} F^n, \quad F^n \leq \varphi_n, \quad F^s \leq \varphi_s, \quad (2)$$

where $\bar{\mu}$ is the contact friction coefficient, and φ_n and φ_s are the normal and shear strengths (in force units) of the contact.

Bulk behavior of a granular system is a collective response determined by all the individual grain–grain interactions. For dry sample analyses, the interparticle interactions can be associated with a network of grain–grain contact forces connecting the centroids of grains that are in contact.

Given the set of forces \mathbf{F}_j and moments \mathbf{M}_j acting on the i th particle, its motion is described by the following equations:

$$m_i \ddot{\mathbf{x}}_i = \sum_j \mathbf{F}_j, \quad (3)$$

$$I_i \ddot{\theta}_i = \sum_j \mathbf{M}_j. \quad (4)$$

Here, \mathbf{x}_i and θ_i are the position vector of the grain centroid and the angle vector of rotation about the centroid; the double dots denote second time derivatives of the position and rotation angle; m_i is the mass; and I_i is the tensor of moments of inertia, respectively. The equations of motion (3)–(4) must be solved simultaneously for all grains in the system via a numerical integration scheme. A commercial three-dimensional DEM code, PFC2D [ITASCA, 2004], was used to integrate these equations in time.

Micromechanical vs. Macroscopic Parameters The parameters that need to be defined at the grain-scale level are ρ_s (grain density), $\bar{\mu}$, k_n , k_s , φ_n and φ_s , as well as the grain size distribution, which we shall characterize simply by the grain radius interval $[r_{\min}, r_{\max}]$.

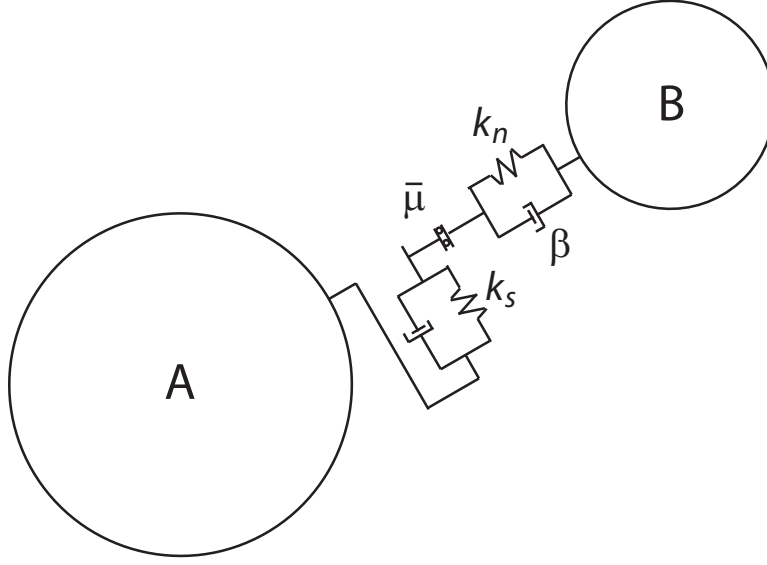


Figure 69: Schematic diagram of a grain–grain contact in a Discrete Element Model. Elastic forces are represented by springs, with normal stiffness k_n and shear stiffness k_s . The contact model includes inelastic and irreversible mechanics through friction (a slider with friction coefficient $\bar{\mu}$), viscous damping (dashpots with damping coefficient β), and bond rupture.

From DEM simulations of biaxial tests, the linear elastic *macroscopic* parameters (Young modulus E and Poisson ratio ν), as well as strength properties (yield stress σ_y , friction angle φ , cohesion c , etc.) may be computed. In order to obtain macroscopic parameters that are independent (or only slightly dependent) on the grain size, the contact strengths must scale with the grain size [Potyondy and Cundall, 2004]:

$$\varphi_n = \bar{\sigma}_c 2r_g w, \quad \varphi_s = \bar{\tau}_c 2r_g w, \quad (5)$$

where $\bar{\sigma}_c$ and $\bar{\tau}_c$ are the normal and shear contact strengths (in stress units)—assumed to be independent of grain size—and w is the width of the 2D assembly in the third dimension.

Time Step Selection for Mechanics Simulation Since explicit time integration is used, the time step is bounded by stability considerations. The characteristic time required to capture the dynamics is [ITASCA, 2004]

$$\delta t \sim \sqrt{m/k_n}, \quad (6)$$

where m is the mass of the particle. In PFC2D, grains are assumed to be disks of unit width ($w = 1$ m), so $m = 2\pi r_g^2 w \rho_s$ and, therefore, the critical time step for mechanical stability scales as follows:

$$\delta t_{\text{crit}}^m \sim r_g \sqrt{\rho_s/k_n}. \quad (7)$$

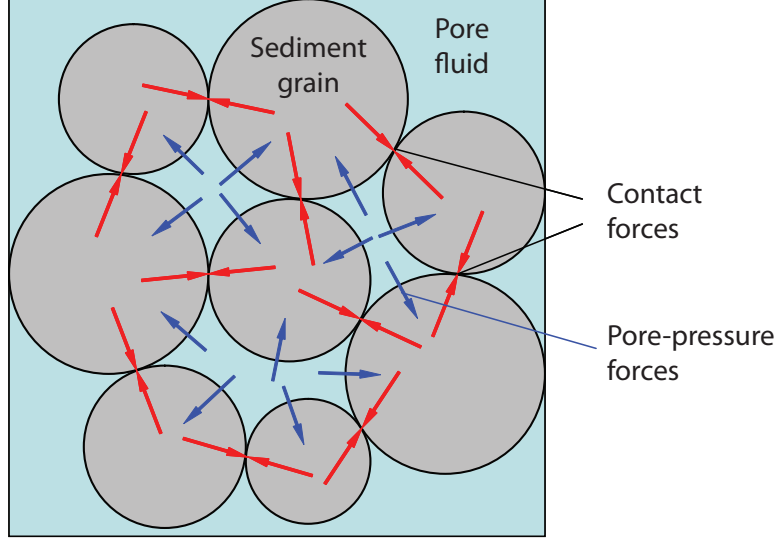


Figure 70: Conceptual picture of the fluid-solid interaction model at the pore scale when a single fluid is present.

Micro-Poromechanics of Single-Fluid Systems

From the theory of poromechanics [Biot, 1941], it is well known that pore pressure will influence mechanical behavior. Essentially, compressive stresses in granular media are transmitted both through a solid skeleton and the pore fluids. Recently, models have been developed to incorporate this effect in DEM with a single-phase pore fluid [Shimizu, 2004; Cook et al., 2004; Li and Holt, 2001, 2004].

When the pore space is filled with a single fluid phase at non-negligible pressure, the associated forces must be incorporated in the model. A conceptual view of the new set of forces is shown in Figure 70. Computationally, the model then consists of two overlapping and interacting networks: the grain network and the fluid network. A particular instance is shown in Figure 71. The force fluid in a given domain exerts on a neighboring grain is obtained by integrating the pressure along the pore–grain contact area. In our implementation, a pressure force is directed from the center of the fluid domain to the grain center. Therefore, pressure forces do not induce rotation.

Consider one particular fluid domain, as sketched in Figure 72. The micromechanical equations can be summarized as follows. The flow rate out of the fluid domain through a pore throat is

$$q_j = C_j \frac{p - p_j}{L_j}, \quad (8)$$

where C_j is the throat conductance, L_j is an effective distance between pore centers, and p , p_j represent the pressures in the fluid domain and its neighbor, respectively. The conductance is inversely proportional to the fluid viscosity μ , and proportional to the square of the effective throat area A_j :

$$C_j = \frac{\tilde{C}_j A_j^2}{\mu 2r_g} w, \quad (9)$$

where \tilde{C}_j is a dimensionless throat conductance. The derivation of this equation from the solution of a Stokes flow problem, and the expressions for \tilde{C} and A , are given in Appendix .

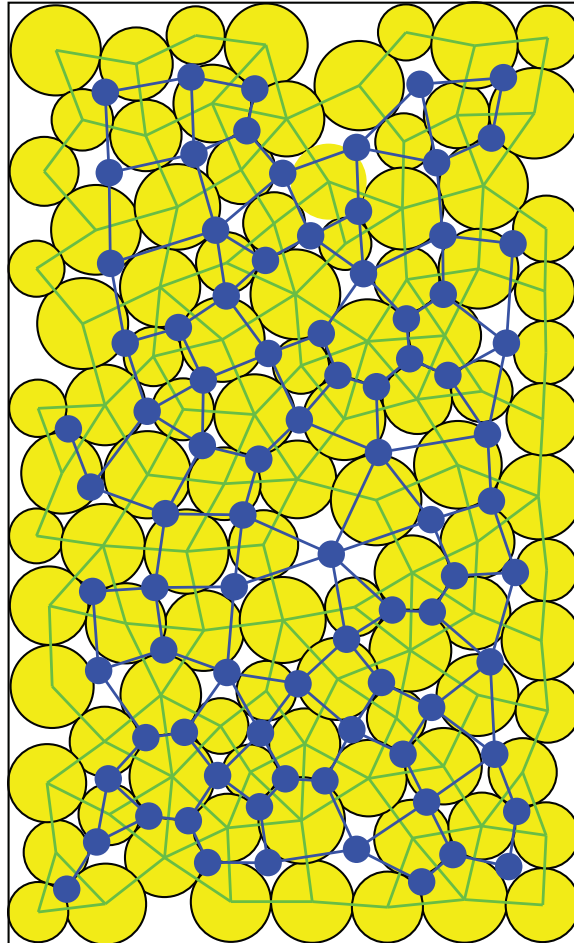


Figure 71: Representation of the grain assembly (yellow circles) and the grain network (green lines). At the center of each fluid domain is a pore body (blue dots), connected by the fluid network (blue lines).

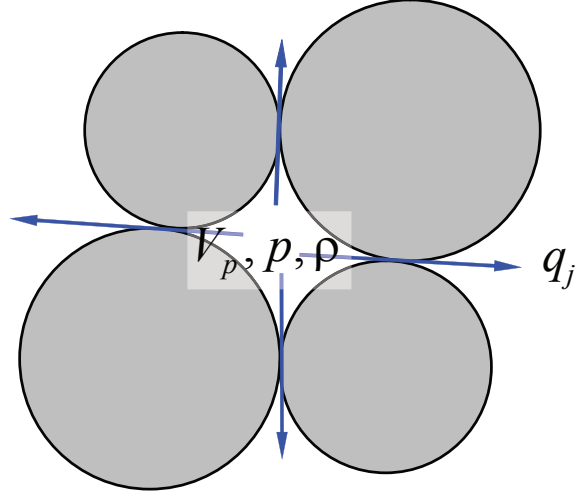


Figure 72: Schematic representation of a fluid domain. At any given time, each fluid domain is characterized by its pore volume V_p , and the pressure p and density ρ of the fluid. Fluid can go in and out of the pore domain at a rate q_j into the neighboring fluid domains.

The grains have certain compressibility, and the radius of a spherical grain varies according to

$$r_g = r_{g,0} \left(1 - \frac{p}{3K_s} \right), \quad (10)$$

where $r_{g,0}$ is the initial radius (at zero fluid pressure), K_s is the bulk modulus of the solid grain, and p is the average of the pore pressures around the grain. Finally, mass balance over a fluid domain gives the following pressure evolution equation for a pore volume V_p :

$$\delta p = \frac{K_f}{V_p} \left(-\delta V_p - \sum_j q_j \delta t \right), \quad (11)$$

where K_f is the fluid bulk modulus, and δp is the pressure variation after a time step δt . The main feature of our model is the term $-\delta V_p$, which accounts for the change in volume of each pore caused by changes in grain locations. This term has been neglected in previous investigations of pore-scale poromechanical models but is essential, for example, to reproduce pressurization of the fluid upon fast compaction. It also reflects the reverse coupling present in Biot's self-consistent theory of poroelasticity.

There is a formal analogy between the micro-poromechanical equations presented above and Biot's self-consistent theory of poroelasticity [Biot, 1941; Wang, 2000]. We expect the DEM formulation will reproduce the linear theory of poroelasticity only in the range of small deformations and small pressure changes. Under such conditions, the poroelastic parameters can then be determined from DEM simulations. When these conditions are not met, nonlinear/irreversible behavior is expected to emerge in the DEM model, driven by contact slip, bond breaking and grain rearrangement.

Time Step Selection For Fluid Flow Simulation The grain-scale fluid flow equations (11) are solved using an explicit time integration scheme. The time step must be restricted for the scheme

to be stable. The characteristic time associated with the microscopic fluid flow dynamics is

$$\delta t \sim \frac{V_p}{K_f} \frac{\delta p}{\sum_j q_j}. \quad (12)$$

Introducing Equations (8) and (9), we express the characteristic time as

$$\delta t \sim \frac{V_p}{K_f} \frac{2r_g \mu}{w} \sum_j \frac{L_j}{\tilde{C}_j A_j^2}. \quad (13)$$

Using the scaling $V_p \sim r_g^2 w$, and $A \sim r_g^2$, the critical time step for fluid flow stability scales as follows:

$$\delta t_{\text{crit}}^f \sim \frac{\mu}{\tilde{C} K_f}. \quad (14)$$

In a coupled poromechanics simulation, the time step must be smaller than the minimum of the critical values in Equations (7) and (14).

Micro-Poromechanics of Two-Fluid Systems

In the environments of interest for methane hydrates—in particular, at the base of the hydrate stability zone—two fluid phases exist: a liquid brine phase, and methane gas. One of the key differences between single-fluid and two-fluid systems is the presence of a fluid–fluid interface. Due to surface tension effects, the pressures on both sides of the interface (that is, the pressure in the brine and the pressure in the methane gas) can be very different.

The key question is: what is the preferential mode of gas invasion? Two different fundamental mechanisms are at play (Figure 73): (1) capillary-dominated invasion of a rigid solid skeleton, and (2) fracturing of the sediment. While capillarity governs invasion of gas through the porous medium, mechanical effects may lead to deformation and fracturing of the sediment skeleton, thereby triggering invasion when it would otherwise not occur. Preferential fracturing of the sediment requires differences in pressure between neighboring pores. While this is typically not a favored scenario in single-fluid systems (unless a fluid is injected at very fast flow rates and pressures, as in hydraulic fracturing operations), it is natural in two-fluid systems because the two fluids have different pressures. Before the pore is invaded, the pore-pressure forces correspond to the water pressure. Once the pore is invaded by gas, it is the gas pressure that exerts a net force onto the surrounding grains. Since the two fluids do not mix, a pressure difference does not dissipate. This pressure difference may lead to preferential fracturing of the sediment. These processes clearly couple flow and deformation, at both the grain scale and the macroscopic scale.

Capillary Invasion Consider invasion of methane free gas by capillary invasion (Figure 73(middle)). The gas/water interface will invade a throat if the capillary pressure (that is, the difference between gas pressure and water pressure) is larger than the capillary entry pressure [Richards, 1931; Leverett, 1941; Mayer and Stowe, 1965]. The capillary entry pressure is proportional to the interfacial tension γ , and inversely proportional to the throat opening. Let d be the throat gap (which, in a 2D model, may be negative if there is overlap between the grains). In Appendix , we derive the

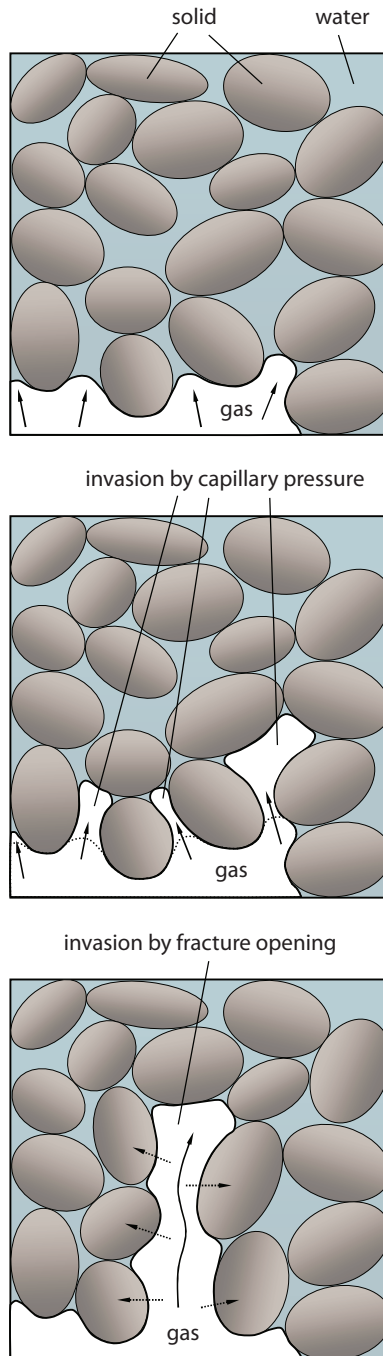


Figure 73: Schematic diagram of the two modes of methane gas invading a sediment. **Top:** before invasion, the gas–water interface of a buoyant gas plume underlies water-filled sediment. **Middle:** invasion will occur if the capillary pressure (the difference between gas pressure and water pressure) exceeds the capillary entry pressure, which is inversely proportional to the pore diameter. **Bottom:** invasion by fracture opening; if the exerted pressure is sufficient to overcome compression and friction at grain contacts, a fracture will form. In a multiphase environment, due to surface tension effects, the pressure difference between water and gas will *not* dissipate quickly through the porous medium, and water at grain contacts will increase cohesion.

following expression for the gas pressure to invade a throat:

$$p_g - p_w \geq \frac{2}{\sqrt{1 + \left(1 + \frac{d}{2r_g}\right)^2} - 1} \frac{\gamma}{r_g}. \quad (15)$$

Fracture Opening Clearly, if the grain size is large, the process of capillary invasion is favored and gas invasion can occur even if the porous medium is rigid. In this case, the gas invasion pressure into the sediment is given by Equation (15). On the other hand, for small grain size (high capillary entry pressures), gas invasion will not occur until the grains are pushed apart (Figure 73(bottom)).

For an idealized scenario of cohesionless material under undrained plane-strain conditions, a fracture will propagate when the gas pressure exceeds the minimum compressive stress (assumed horizontal):

$$p_g - \sigma_H \geq 0. \quad (16)$$

This condition of fracture opening must be extended to the case when cohesion $\bar{\sigma}_c$ exists. In porous media filled with a single fluid, the source of cohesion (tensile strength) is grain cementation and consolidation. When the pore space is occupied by two fluids of different wettability, capillary forces induce additional adhesion between particles (Figure 74) [Orr et al., 1975; Lian et al., 1993; Cho and Santamarina, 2001].

Because there is stress concentration at the fracture tip, the fracturing pressure depends not only on the earth stresses and the cohesive stress, but also the fracture's length. In the realm of linear elastic fracture mechanics (LEFM), the fracturing pressure is

$$p_g - \sigma_H \geq C_{\text{LEFM}} \frac{K_{Ic}}{\sqrt{\pi a}}, \quad (17)$$

where K_{Ic} is the fracture toughness, a is the length of the fracture, and C_{LEFM} is a coefficient that depends on the geometry, the ratio of horizontal to vertical stresses, and loading conditions [Anderson, 1991]. In the context of particle assemblies, the “measurable” fracture toughness depends on the cohesive strength (and, therefore, on the interfacial tension between fluids) and on the grain size. This last dependency emanates from the observation that the internal lengthscale in the fracture toughness is determined by the grain size [Potyondy and Cundall, 2004]. Therefore, under the assumptions of LEFM, the gas pressure for fracture opening takes the form:

$$p_g - \sigma_H \geq C_{\text{LEFM}} \frac{\gamma \sqrt{r_g}}{r_g \sqrt{\pi a}}. \quad (18)$$

Even though LEFM conditions do not apply to natural sediments, Equation (18) indicates that asymptotically, $p_g^{\text{frac}} - \sigma_H \sim r_g^{-1/2}$. Equation (15) says that the gas pressure for capillary invasion scales like $p_g^{\text{cap}} - p_w \sim r_g^{-1}$. Both invasion pressures increase as the grain size decreases, but the capillary invasion pressure increases faster. This analysis suggests that fracturing is favored over capillary invasion for fine-grained sediments.

In any case, we do *not* use LEFM. It is the nonlinear evolution of the DEM micro-poromechanical model that determines when bonds break, and when the gap between grains is large enough for

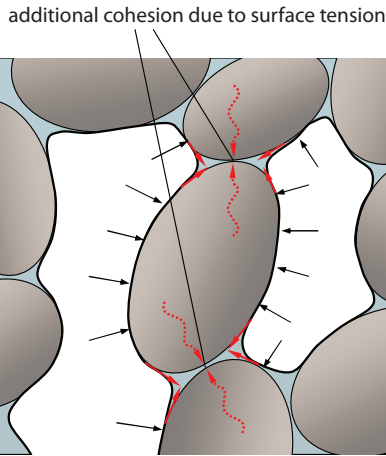


Figure 74: Meniscus pinning in the presence of two fluid phases in the sediment. During multiphase flow in porous media, the least wetting phase (gas, white) migrates through the center of the pores, while the most wetting phase (brine, blue) coats the grains (gray) and forms filaments around the crevices of the pore space. This configuration leads to gas–water menisci around the grain contacts. Due to interfacial tension (solid red arrows), these menisci are responsible for an attraction force between grains (dotted red arrows). At the macroscopic level, this can be interpreted as an increment in the cohesion of the material. This is a purely multiphase-flow effect, not present in single-phase poromechanics.

the gas interface to advance, according to Equation (15). In this fashion, the gas/water interface advances and a new pore is loaded with a higher pressure. The implementation of multi-fluid poromechanics is therefore very similar to that of single-fluid systems, except that the key hydraulic property (the conductance between pore bodies) is set to zero until condition (15) is satisfied.

Capillary invasion and fracture opening are the two end-member mechanisms for methane transport in its own gas phase, and our coupled grain-scale model allows us to investigate the competition between the two as a function of grain size, earth stresses, and sediment cohesion.

Results

Micromechanics of “Dry” Media

Sediment Model Generation and Initialization A model sediment is generated by first choosing the number of particles, and reproducing the desired grain size distribution. As we shall see below, several macroscopic properties (both mechanical and fluid-flow properties) are dependent on the grain size. Therefore, it is important that the sediment model either reproduces the desired grain size distribution, or that the assigned microproperties (e.g. bond strength) reflect the disparity in grain size [Potyondy and Cundall, 2004]. In most of the examples shown in this paper, we have chosen a relatively narrow, uniform grain radius distribution $[r_{\min}, r_{\max}]$, with $r_{\max} = (5/3)r_{\min}$.

The particles are randomly placed in a box and allowed to fall under gravity, simulating sedimentation (Figure 75). The settling process has two differentiating stages: (1) free fall under gravity, with limited grain–grain interaction, and (2) settling and grain rearrangement until static conditions are reached.

The time step is larger initially, during the “free fall” stage, and quickly converges to the value required for stability of the dynamical system dominated by grain–grain interactions. The time step is proportional to the grain radius, and inversely proportional to the square root of the grain stiffness, confirming the stability condition of Equation (7).

Uniaxial Compaction for “Dry” Media Here we show that DEM simulations of “dry” media (infinitely compressible pore fluid) are able to capture the mechanical behavior of real sediments. In Figure 76 we plot experimental stress–strain curves of sediment samples from Hydrate Ridge [Tan et al., 2006] along with curves from DEM simulations. The data come from triaxial tests that reproduce constant rate of strain (CRS) conditions, in which the lateral stress was also measured. The DEM model was created by sedimenting particles, and applying an isotropic confining stress of 20kPa, to start the uniaxial vertical compaction test at the same stress level as the experiments [Tan, 2004]. The only parameter that we varied to reproduce measured stress–strain behavior was the grain stiffness k_n . The rest of the micromechanical parameters are as follows: $k_s = k_n$, $\bar{\mu} = 0.5$, $\bar{\sigma}_c = \bar{\tau}_c = 0$.

The DEM simulations match the stress–strain behavior measured in the lab even for very high deformations (up to 16% strain), capturing the material nonlinearity. For an undisturbed ideal clay sample, the initial portion of the strain–log stress curve would be a straight line with slope equal to the unload/reload loop slope until reaching its preconsolidation stress. After this point, the slope would change to the virgin consolidation line slope. The Hydrate Ridge samples exhibit a large “rollover” at small strains (in the plot of vertical strain versus effective vertical stress on a

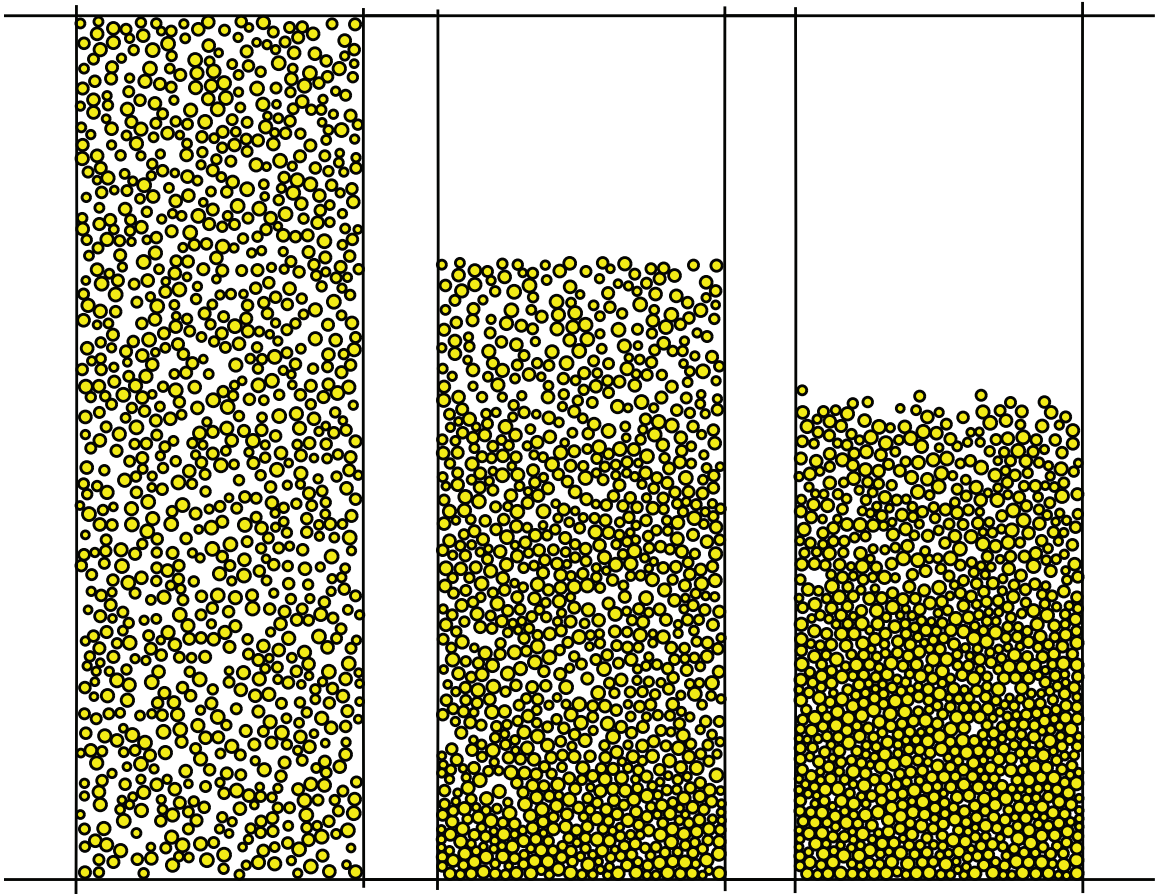


Figure 75: Snapshots of the particle settling process.

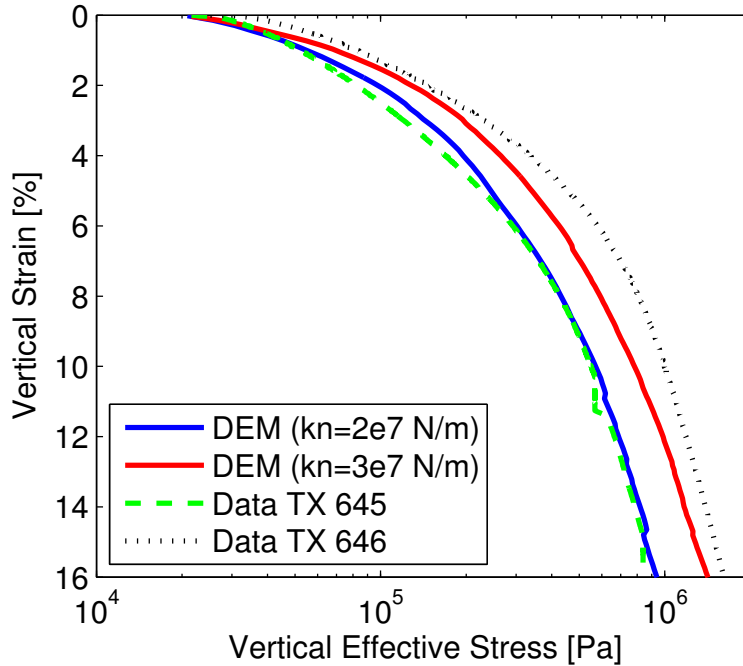


Figure 76: Experimental stress–strain curves for sediments from Hydrate Ridge [Tan et al., 2006], and comparison with DEM simulations for two different values of the grain stiffness.

logarithmic scale) because they are highly disturbed [Tan, 2004]. For the purpose of validation of the DEM model, the relevant portion of the curve is that above the pre-consolidation stress.

Although we do not show it here, the DEM model also displays irreversible behavior in that loading/unloading cycles show hysteresis. However, it is unable to reflect the dramatic increase in stiffness upon unloading that the data show [Jain and Juanes, 2008].

We also compared the lateral-to-vertical stress ratio, K_0 , predicted by the DEM model with the values measured for Hydrate Ridge sediment samples [Tan et al., 2006]. The stress ratio is measured during 1D consolidation in triaxial cells. In preparation for the test, and to make sure the sample is fully saturated, initial vertical and horizontal effective stresses were brought to about 20kPa (which is small enough that there is not significant strain) to remove any bubbles from the sample. To reproduce these conditions, we isotropically consolidated the DEM samples to 20kPa as well prior to performing the 1D consolidation. Therefore, the initial K_0 value is 1. We used the same grain stiffness parameters employed to match the lab stress–strain behavior (Figure 76), and let the DEM model predict the evolution of the K_0 ratio for those experimental conditions (Figure 77). While the agreement between model and experiments is generally good, the experimentally-measured values drop down to about 0.5, while those predicted by the DEM model drop to about 0.6.

Micro-Poromechanics of Single-Fluid Systems

Uniaxial Fluid Flow In this section, we evaluate the fluid flow capabilities of the grain-scale model. We do so by simulating a one-dimensional fluid flow problem in a cell with drained top and bottom boundaries, and impervious fixed lateral boundaries. The initial pressure is constant,

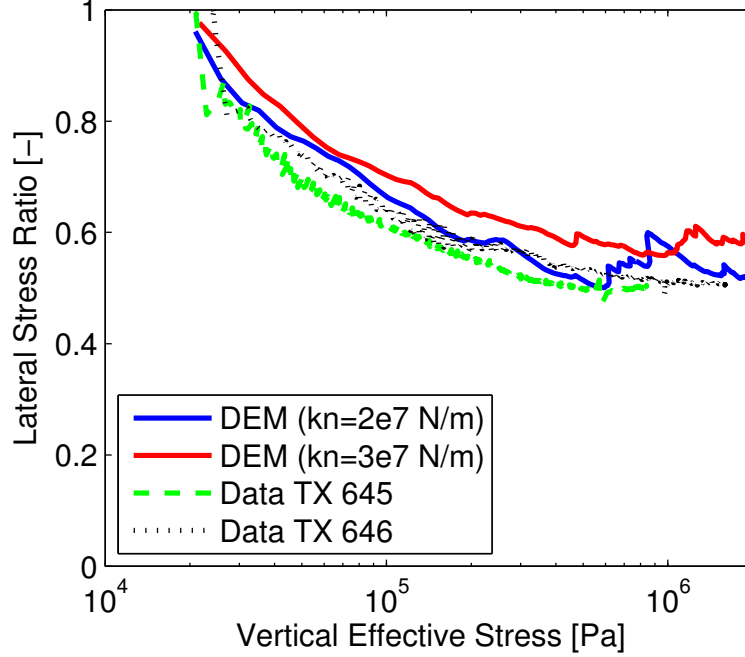


Figure 77: Experimental lateral-to-vertical stress ratio curves for sediments from Hydrate Ridge [Tan et al., 2006], and comparison with DEM simulations for the same values of grain stiffness used to match the vertical stress–strain behavior in Figure 76.

and equal to the boundary pressures. Suddenly, a pressure change is applied to the top boundary, and we simulate the evolution of the pressure and fluid inflow/outflow until a new steady state is reached. The continuum problem is described mathematically by the partial differential equation:

$$c_v \frac{\partial p}{\partial t} - \frac{k}{\mu} \frac{\partial^2 p}{\partial x^2} = 0, \quad 0 < x < H, \quad (19)$$

where x is elevation, H is the height of the cell, k is the intrinsic permeability, μ is the fluid viscosity, and c_v is the consolidation coefficient [Wang, 2000]. The initial condition is given by:

$$p(x, 0) = 0, \quad 0 \leq x \leq H, \quad (20)$$

and the boundary conditions are:

$$p(0, t) = 0, \quad p(H, t) = \Delta p, \quad t > 0. \quad (21)$$

The problem can be expressed in dimensionless form by defining the following dimensionless quantities:

$$\begin{aligned} \text{distance :} & \quad \xi = \frac{x}{H}, \\ \text{time :} & \quad \tau = \frac{t}{T_c}, \quad T_c = \frac{c_v \mu H^2}{k}, \\ \text{pressure :} & \quad p_D = \frac{p}{\Delta p}, \\ \text{flowrate :} & \quad Q_D = \frac{Q}{Q_c}, \quad Q_c = \frac{k \Delta p}{\mu H} W w, \end{aligned}$$

where W is the width and w is the thickness of the cell (that is, the dimensions of the cell in the directions perpendicular to the flow). The analytical solution to the problem can be found by the method of separation of variables [Crank, 1975]. The dimensionless pressure field is given by:

$$p_D(\xi, \tau) = \xi + \frac{2}{\pi} \sum_{n=1}^{\infty} \frac{(-1)^n}{n} \sin(n\pi\xi) \exp(-(n\pi)^2\tau). \quad (22)$$

By differentiating the expression above, we find the expression for the dimensionless flow rate in and out of the cell:

$$Q_D^{\text{in}} = 1 + 2 \sum_{n=1}^{\infty} (-1)^n \cos(n\pi) \exp(-(n\pi)^2\tau), \quad (23)$$

$$Q_D^{\text{out}} = 1 + 2 \sum_{n=1}^{\infty} (-1)^n \exp(-(n\pi)^2\tau). \quad (24)$$

The objective is to determine whether the grain-scale model reproduces the macroscopic behavior. The relevant macroscopic parameters are the intrinsic permeability k and the consolidation coefficient c_v . The intrinsic permeability is obtained by matching the flow rate at steady state. The consolidation coefficient is determined by matching the dimensionless inflow and outflow curves.

We generated an assembly with 1000 grains, and a minimum radius $r_{\min} = 1$ cm. The vertical and horizontal dimensions of the cell are, approximately, $H = 1$ m and $W = 0.7$ m. We set the pressure increment Δp to a small value, so that the effects of pore pressure on the mechanical deformation are minimal. Once the flow stabilizes, inflow and outflow rates are equal to Q_c , and the intrinsic permeability of the medium can be computed as:

$$k = \frac{\mu H Q_c}{W w \Delta p}. \quad (25)$$

The characteristic time T_c is then obtained by matching the numerical inflow and outflow curves, from which the macroscopic consolidation coefficient is computed as:

$$c_v = \frac{k T_c}{\mu H^2}. \quad (26)$$

In Figure 78 we plot the dimensionless inflow and outflow rates as a function of dimensionless time. The agreement between the DEM results and the analytical solution is excellent, indicating the flow formulation accurately captures the macroscopic behavior (Darcy flow in porous media). As a further validation of the model, we compare in Figure 79 the evolution of dimensionless pore pressure within the sample. By plotting the pressure values from the DEM simulation at individual pores, we obtain a scattered profile of the average pressure as a function of depth. We compare these results with the analytical solution at different dimensionless times. Again, the agreement is excellent.

By repeating the fluid flow simulations with different values of r_{\min} , we determine the dependence of the hydraulic and poromechanical parameters on grain size. The results are compiled in Table 1, where we confirm that the intrinsic permeability scales with the square of the grain size (as expected from Stokes theory, and the Kozeny–Carman relation for granular materials). Moreover, if the fluid is significantly more compressible than the skeleton, the DEM simulations also reflect that the effective consolidation coefficient c_v is inversely proportional to K_f , with the constant of proportionality being approximately equal to the porosity [Wang, 2000].

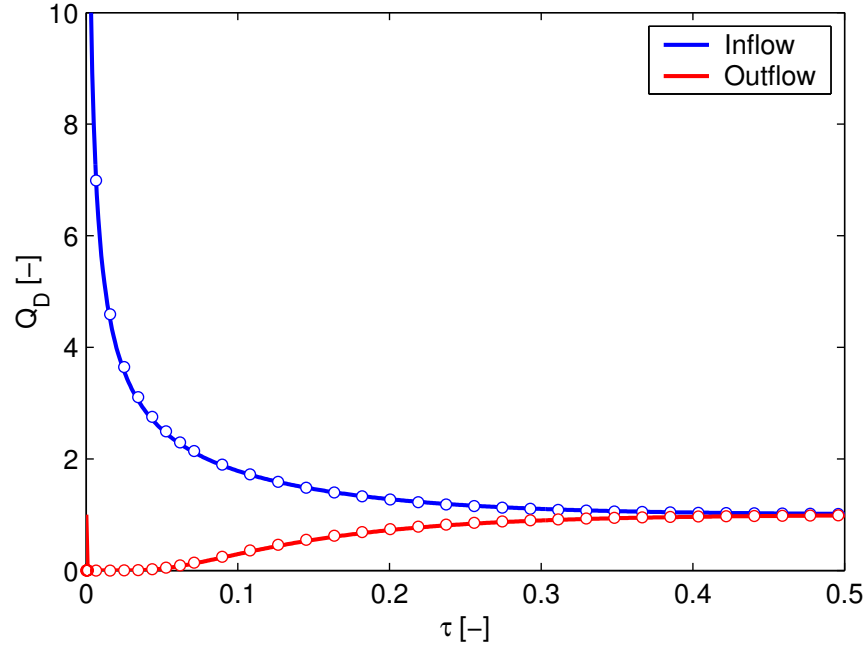


Figure 78: Inflow and outflow rates into the pressure cell. Comparison of DEM simulation (circles) and analytical solution (solid line).

Table 1: Macroscopic hydraulic and poromechanical parameters for different grain size distributions.

r_{\min} [m]	k [m ²]	c_v/K_f [-]
0.01	0.289×10^{-6}	0.161
0.001	0.289×10^{-8}	0.156

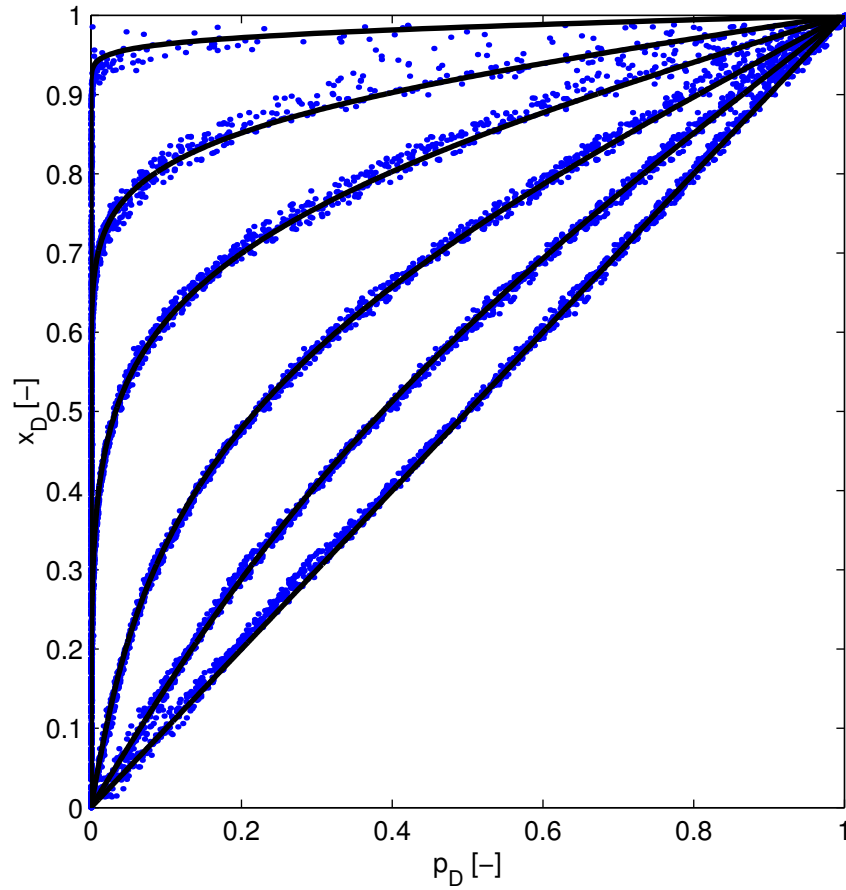


Figure 79: Evolution of pressure profiles during the uniaxial fluid flow test. Comparison of DEM simulation (dots) and analytical solution (solid line) at different dimensionless times: $\tau = 0.000242, 0.00671, 0.0275, 0.0829, 0.175, 1.404$.

Uniaxial Undrained Compaction A sensitive test of the DEM coupled model’s validity is fluid–solid behavior during undrained consolidation tests. A sediment model is initialized by gravitational settling. Then the walls are adjusted to achieve an isotropic confining stress state of 0.1MPa (above atmospheric pressure). Until that point, the fluid is allowed to drain and the pore pressure is atmospheric ($p = 0$). Thus, the initial effective stress is 0.1MPa. After that, the sample is sealed so that no fluid is allowed to drain, and it is subjected to uniaxial compaction. During the undrained compaction process, the vertical strain ε , total vertical stress σ , and average pore pressure p are recorded. In view of the effective stress concept [Terzaghi, 1943; Biot, 1941], the total stress required to achieve a given deformation in a fluid-saturated medium is larger than for a dry medium. In the realm of the linear theory of poroelasticity, the *effective stress* is given by:

$$\sigma' = \sigma - bp, \quad (27)$$

where b is the Biot coefficient. The dependence of the Biot coefficient on the solid and fluid properties of the constituents is reasonably well understood [Coussy, 1995; Wang, 2000]. The Biot coefficient approaches a value of one only in the limit of incompressible grains and point grain–grain contacts. If the grain and fluid compressibilities are comparable, the Biot coefficient is less than one.

We used an assembly with 1000 grains, $r_{\min} = 0.01$ m, $k_n = 10^7$ N/m, $k_n/k_s = 2.5$, and $K_f = 10^7$ Pa. In Figure 80 we show the stress–strain curves for a cemented/cohesive sample (bond strength $\bar{\sigma}_c = \bar{\tau}_c = 10^6$ Pa—left figure), and for an unconsolidated/cohesionless sample (bond strength $\bar{\sigma}_c = \bar{\tau}_c = 10^2$ Pa—right figure). In both cases, we plot the stress–strain curves for the fluid-saturated medium (total stress), and for a dry medium. We confirm that the dry stress curve can be interpreted as the effective stress, and recovered by subtracting the pore pressure times the Biot coefficient from the total stress. We infer the Biot coefficient in this way, and the values obtained agree well with experimental values [Wang, 2000, Table C.1].

Micro-Poromechanics of Two-Fluid Systems

Migration of a gas phase through a deformable medium may occur by two end-member mechanisms: (1) capillary invasion through a rigid medium, and (2) fracture opening. Our DEM model is capable of reproducing *both* mechanisms, and can therefore predict the conditions under which one is favored over the other, and predict gas migration as a result of their *combined* effect.

Capturing the Fracturing Phenomenon We first illustrate that our DEM model of coupled two-phase fluid flow and grain mechanics can reproduce fracture initiation and propagation upon invasion of an immiscible gas phase.

In many (passive) depositional environments, the horizontal stress is lower than the vertical stress. In such scenarios, one expects the development of vertical fractures that open up the sediment in the direction of minimum compressive stress. In Figure 81 we show that fracturing of the sediment is not necessarily restricted to anisotropic earth stresses. Even when horizontal and vertical stresses are equal, the medium tends to fracture in a set of radial, geometrically complex fractures if gas is injected into a brine-saturated sediment.

Fracturing vs. Capillary Invasion: Influence of Grain Size We find the most sensitive factor in determining the mode of methane gas transport (sediment fracturing or capillary invasion) is the

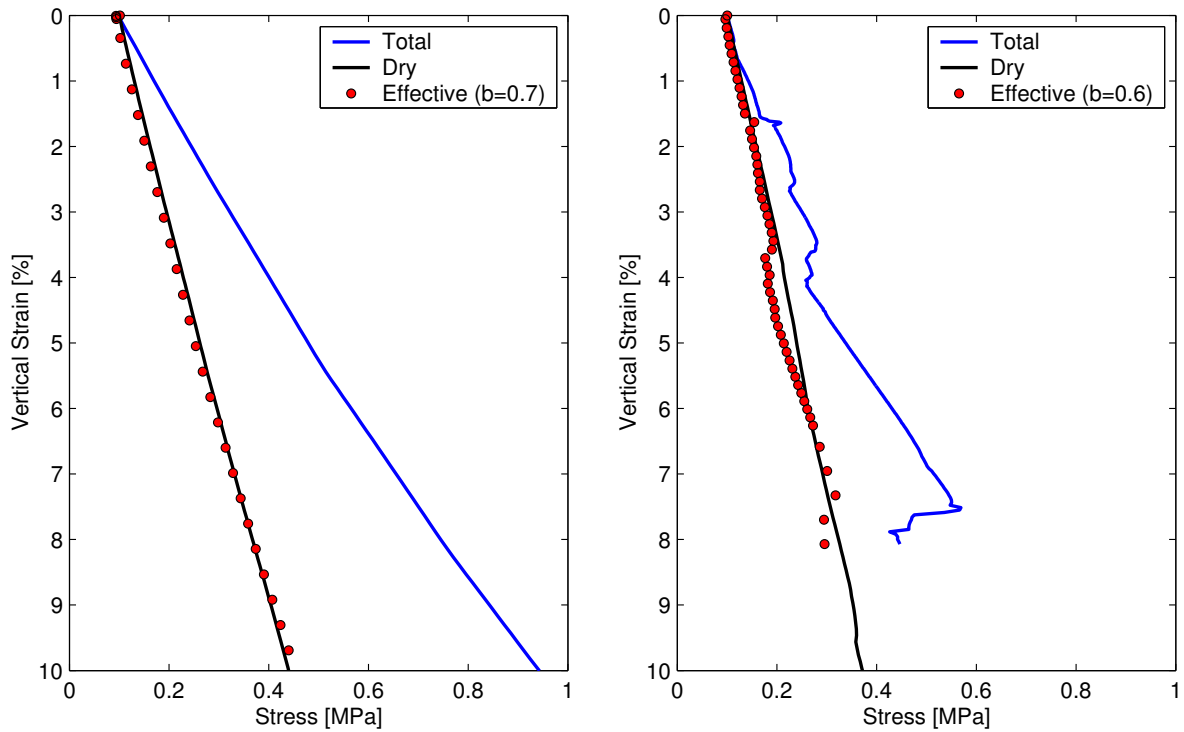


Figure 80: Stress–strain curves for uniaxial undrained compaction. The total stress in the fluid-filled sample (blue solid line) is higher than the stress in the “dry” sample (black solid line). The effective stress curve (red circles) is obtained by subtracting the pore pressure (not plotted) premultiplied by the Biot coefficient from the total stress. An appropriate value of the Biot coefficient is found by matching the effective stress curve with the “dry” stress curve. Left: cemented/cohesive sample. Right: unconsolidated/cohesionless sample.

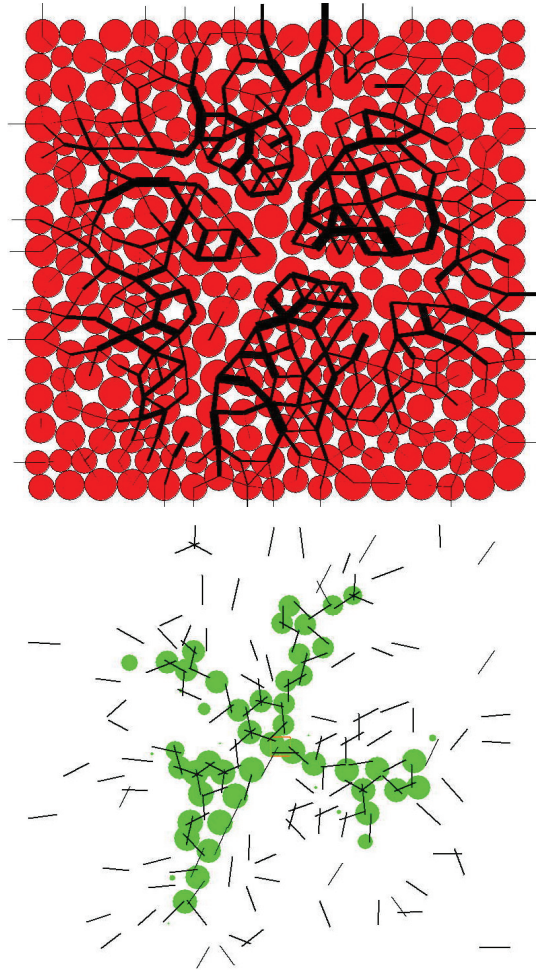


Figure 81: Illustration of the fracturing behavior of a model sediment upon injection of gas, when the vertical and horizontal stresses are equal. The sediment fractures “isotropically” into a set of radial, geometrically-complex fractures. Top: The grain assembly (red circles) after fracturing due to “injection” of gas at the center of the domain. The thick black lines denote compressive forces at the grain–grain contacts. Note that they are missing from the fractured areas. Bottom: Representation of the pores occupied by the injected gas (green circles). The thin black lines indicate grain–grain contacts that have exceeded the contact strength and have therefore “broken”. Note the complementary nature of this set of lines to that of the force network above.

grain size: fracturing is favored for fine-grained sediments, while capillary invasion is favored for coarse-grained sediments. Here we illustrate these two end-members.

The simulation is set up as follows. A sample of 300 grains of grain size $[r_{\min}, 2r_{\min}]$ is generated by gravitational settling. Since the sample size is much smaller than a representative elementary volume of sediment, we only simulate a narrow range of grain sizes at a time. The lateral boundaries are fixed. The sediment is then compacted vertically under constant pore pressure until a vertical effective stress of 3MPa is achieved. This level of vertical effective stress corresponds to a depth of about 300m below seafloor. During this vertical compaction, the horizontal effective stress increases to a value of about 1.6MPa, that is, $K_0 \approx 0.53$. Inasmuch gravity effects are negligible in a grain-scale model, the results are independent of water depth; they depend on the relative magnitudes of capillary pressure (the difference between gas pressure and water pressure) and *effective* stress (the difference between the total stress and the pore pressure).

The interfacial tension is $\gamma = 50 \times 10^{-3}$ N/m. We assume that the cohesion is inversely proportional to grain radius. This is phenomenologically adequate (fine-grained material like clays are cohesive) and is also consistent with the adhesive forces that result from the presence of a gas–water interface [Kato et al., 2004]. For simplicity, we take $\bar{\sigma}_c = 2\gamma/r_g$. The only parameter that is left free is the grain size r_{\min} .

During the simulation, we inject gas at the bottom center pore. We incrementally increase the gas pressure. Between each increment, we allow sufficient time to pass for fluid flow and granular displacements to stabilize, so mechanical equilibrium is reached.

In Figure 82 we show two snapshots of the evolution of the methane–water interface for a coarse-grain sediment of characteristic size $r_{\min} = 50 \mu\text{m}$. It is apparent that during the invasion of methane gas, there is virtually no movement of the solid grains: the sediment acts like a rigid skeleton. Indeed, the network of grain contact compressive forces remains the same during the process. Invasion of gas from pore to pore occurs when the gas pressure (minus the water pressure) exceeds the capillary entry pressure of the throat (Equation (15)). In this case, the capillary entry pressure is much lower than the fracturing pressure (the left figure corresponds to $P_c \approx 5$ kPa), and fluid transport is well described by *invasion percolation* [Wilkinson and Willemsen, 1983; Lenormand et al., 1988]. Ultimately, if the gas pressure is sufficiently high, almost all the pores have been invaded by methane gas. In this case, this occurs at a slightly higher capillary entry pressure of $P_c \approx 6$ kPa.

The behavior is completely different when a much smaller grain size is used. The evolution of the methane gas migration for $r_{\min} = 0.1 \mu\text{m}$ is shown in Figure 83. The range of capillary entry pressure for the initial configuration is now in the order of 3MPa. However, at this pressure, mechanical effects become dominant, and the solid skeleton no longer behaves like a rigid medium. At $P_c \approx 2.5$ MPa, the invading gas starts to initiate a fracture, with its characteristic stress concentration at the fracture tip captured by the DEM model [Potyondy and Cundall, 2004]. The fracture propagates vertically. The value of the capillary pressure needed to open the fracture corresponds to a gas column thickness of about 300m below the base of the HSZ. Gas column thicknesses of this magnitude have been observed in similar geologic environments [Holbrook et al., 1996; Hornbach et al., 2004], and interpreted as the cause of critical pressures for gas migration through faults [Flemings et al., 2003; Hornbach et al., 2004; Trehu et al., 2004a].

Our grain-scale model explains why focused gas flow can occur by means of fracture opening, even in the absence of pre-existing faults and fractures. It is likely, however, that our model overestimates the invasion capillary pressure required for fracturing, due to boundary effects. This can

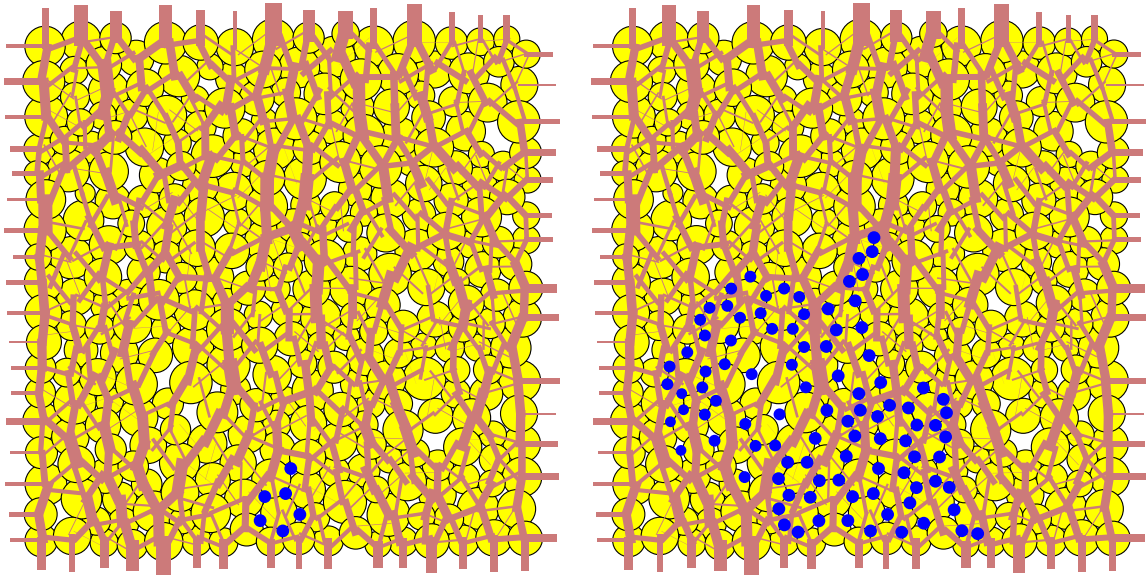


Figure 82: Snapshots of the evolution of the methane gas-water interface for the case $r_{min} = 50\mu\text{m}$. The pores occupied fully by gas are represented with blue dots at the pore centers. The maroon lines indicate compression at grain-grain contacts. The green lines represent tension, which is supported by cohesion between grains. Left: $P_c = 5\text{ kPa}$. Right: $P_c = 6\text{ kPa}$.

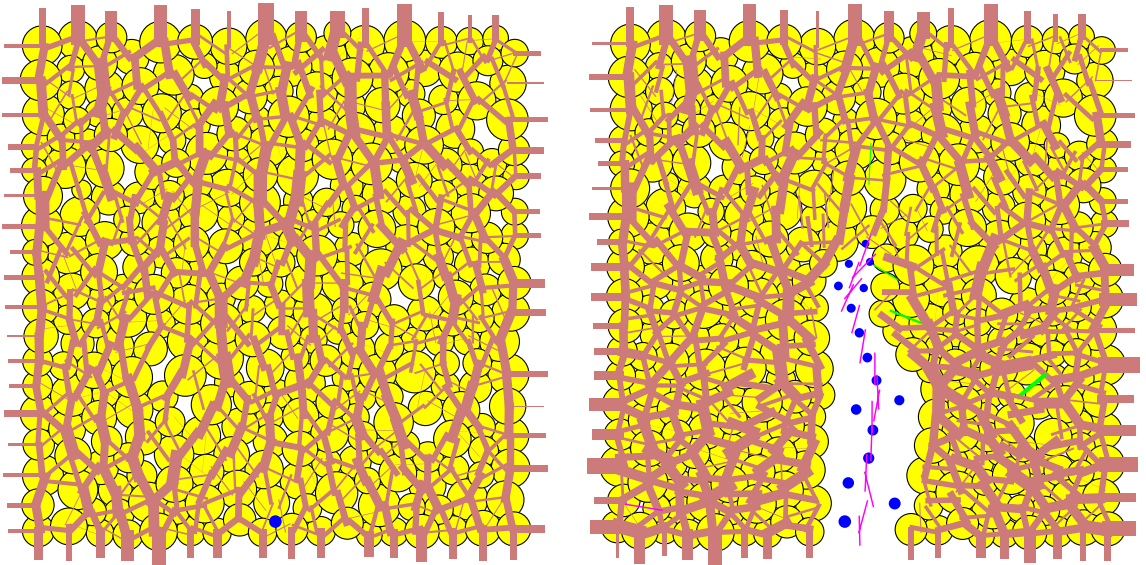


Figure 83: Snapshots of the evolution of the methane gas-water interface for an assembly with $r_{min} = 0.1\mu\text{m}$. The pores occupied fully by gas are represented with blue dots at the pore centers. The maroon lines indicate compression at grain-grain contacts. The green lines represent tension, which is supported by cohesion between grains. The pink lines show where cohesive bonds were broken. Left: $P_c = 2.5\text{ MPa}$. Right: $P_c = 2.55\text{ MPa}$.

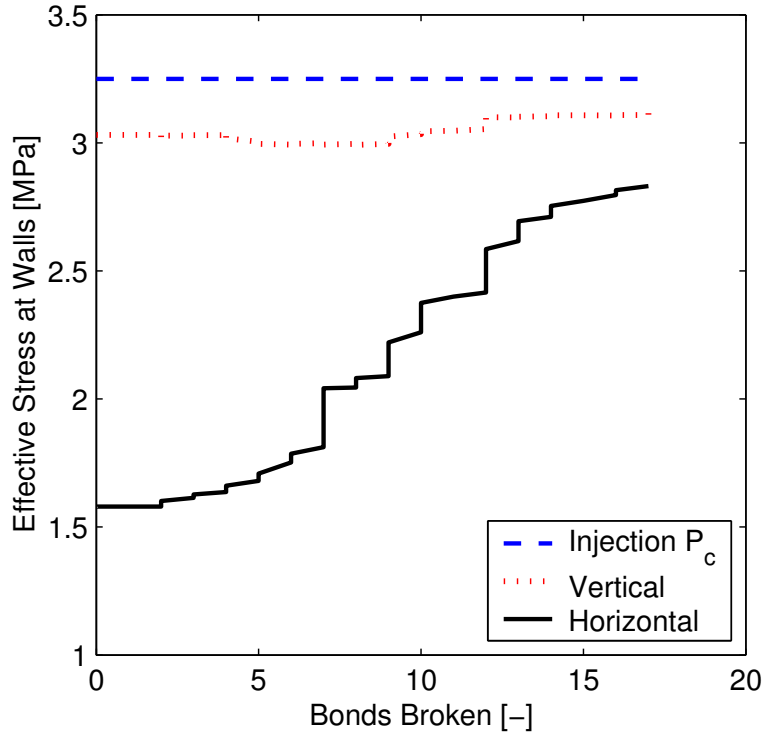


Figure 84: Evolution of the vertical and horizontal mean effective stress during fracture propagation for the simulation shown in Figure 83. The invading gas pressure remains constant throughout, but the vertical and, especially, the horizontal stress at the boundaries increase during fracture growth. The boundaries introduce an artificial stiffness in the problem that results in an overestimation of the gas invasion pressure.

be seen from the grain forces on the lateral boundaries in Figure 83, which change significantly as the fracture propagates. This is confirmed by the increase of the vertical and, especially, horizontal mean effective stress during fracture growth (Figure 84). The presence of computational boundaries near the propagating fracture introduces an artificial stiffness to the problem.

Discussion and Conclusions

We have presented a discrete element model for simulating, at the grain scale, gas migration in brine-saturated deformable media. The model has been validated for many processes, including: (1) generating sediment models by gravitational settling and compaction; (2) stress-strain behavior of ocean sediments; (3) transient single-phase flow for determining hydraulic parameters; (4) undrained compaction tests for determining poromechanical parameters.

The coupled model permits investigating an essential process that takes place at the base of the hydrate stability zone: the upward migration of methane in its own free gas phase. We elucidate the two ways in which gas migration may take place: (1) by capillary invasion in a rigid-like medium; and (2) by initiation and propagation of a fracture.

Each end member can be analyzed separately, and conditions for gas invasion can be found for the capillary-dominated and fracture-dominated regimes. We find the main factors controlling the

mode of gas transport in the sediment are the grain size and the effective confining stress. We have shown that coarse-grain sediments favor capillary invasion, whereas fracturing dominates in fine-grain media. Recent laboratory experiments of gas invasion and bubble growth in soft, fine-grained sediments provide convincing evidence that fracturing is a relevant mechanism for gas transport [Boudreau et al., 2005; Best et al., 2006]. The cornflake-shaped, subvertical fractures observed in those experiments are strikingly similar to those simulated with the mechanistic grain-scale model presented here.

The significant contribution of our coupled model is that it captures both phenomena and, as a result, allows us to study the transition between the two regimes. We synthesize the transition from capillary invasion to fracture opening in Figure 85. We plot the gas pressure required for invasion into a sediment at an effective confining stress of 3MPa (typical of a sediment-column depth of about 300m) as a function of grain size. For sufficiently coarse grain size, gas invades by capillarity. According to Equation (15), the invasion capillary pressure for this regime decreases with increasing grain size, and has the following scaling:

$$P_c^{\text{cap}} \sim r_g^{-1}. \quad (28)$$

This scaling is clearly confirmed by our DEM simulations, which collapse onto a straight line of slope -1 on the log-log plot of P_c vs. r_g .

There exists a critical grain size, in this case $r_g \approx 0.1 \mu\text{m}$, at which the transition from capillary invasion to fracturing occurs. For grain sizes below this critical value, invasion is *always* by fracture opening. The pressure required for opening a fracture, however, does depend on grain size. Under LEFM conditions, the expected scaling from Equation (18) is:

$$P_c^{\text{frac}} - \sigma'_H \sim r_g^{-1/2}, \quad (29)$$

which corresponds to a straight line of slope $-1/2$. This behavior is *not* confirmed by our grain-scale model, which accounts for the coupling between two-phase flow and *inelastic* grain-scale mechanics. This suggests that inelastic and capillary effects are essential in the fracturing process.

These emergent phenomena have important implications for understanding hydrates in natural systems (either ocean sediments and permafrost regions). Our model predicts that, in fine sediments, hydrate will likely form in veins that follow a fracture-network pattern. Since the mechanism of fracture propagation is self-reinforcing, our results indicate that it is possible, and even likely, that methane gas will penetrate deeply into the HSZ (and maybe all the way to the ground surface).

Our model supports the view that, in coarse sediments, the buoyant methane gas is likely to invade the pore space more uniformly, in a process akin to invasion percolation. While this is definitely affected by heterogeneity in grain-size distribution, the overall pore occupancy is likely to be higher than for a fracture-dominated regime, leading to larger time scales for transport. The predictions from our model are consistent with field observations of hydrates in natural systems [Suess et al., 1999; Sassen et al., 2001; Flemings et al., 2003; Trehu et al., 2004a; Hornbach et al., 2004; Trehu et al., 2006a; Riedel et al., 2006; Weinberger and Brown, 2006; Liu and Flemings, 2006, 2007; Collett et al., 2008].

We have not undertaken here an analysis on the relative importance of transport in solution versus as a separate free gas phase flowing through fractures. However, the importance of free

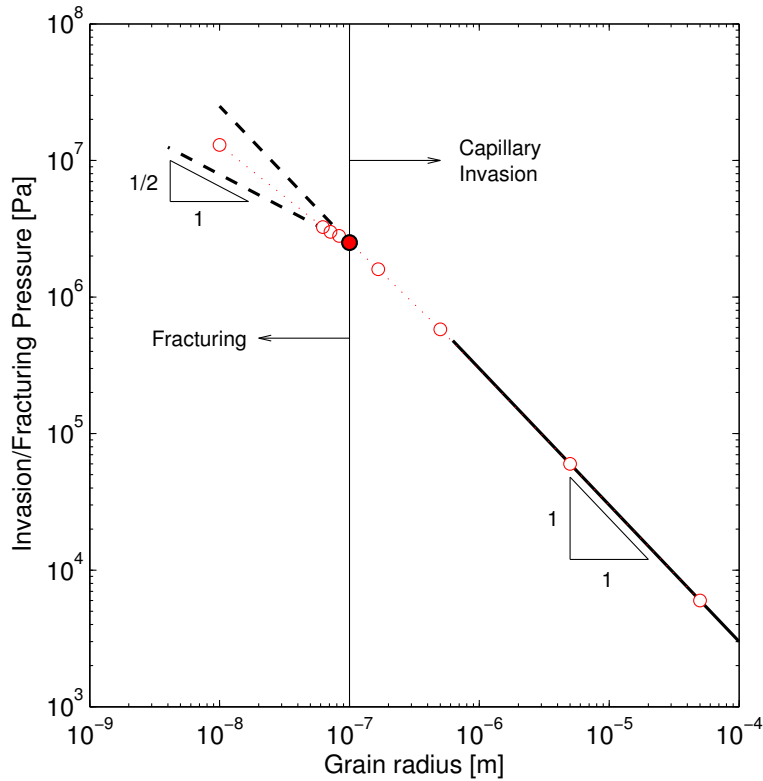


Figure 85: Plot of invasion pressure vs. grain size (red circles) for a sediment under 3MPa vertical effective stress (sediment column depth of about 300m). The red-filled circle denotes the critical grain size at which the transition in the mode of gas invasion occurs. For larger grain size, gas invades by capillarity. For smaller grain size, it invades by opening a fracture. In the capillarity-dominated regime, the invasion capillary pressure decreases with increasing grain size with a slope of -1 (black solid line), consistent with the theory (Equation (28)). In the fracture-dominated regime, the invasion capillary pressure increases with decreasing grain size, though the predictions of linear elastic fracture mechanics (black dashed line with slope $-1/2$) are not in agreement with our coupled grain-scale model. This suggests the effects of capillarity and inelastic material behavior cannot be neglected.

gas fluxes through fractures is demonstrated by the massive free methane gas venting rates observed intermittently at northern Hydrate Ridge [Torres et al., 2002]. Tryon et al. [1999, 2002] hypothesized that fracture networks rapidly transport the gas from beneath the HSZ to the vents, a distance of 70–100m. The total methane flux coming out of 10 discrete vents (~ 1 cm diameter each), clustered in a depression several meters in diameter, constitutes two-thirds of the total flux, calculated from seawater methane concentrations in the overlying water column [Heeschen et al., 2005]. Acoustic imaging shows massive bubble plumes at two other sites in the region [Heeschen et al., 2005], which likely account for the remaining one-third of the flux to the water column. Free gas ebullition through vents fed by fractures releases methane from the sea floor at rates many orders of magnitude faster than transport by advection of dissolved methane in solution through sediments [Torres et al., 2002]. In terms of velocities, the gas bubbles exit conduits episodically at about 1m/s [Torres et al., 2002], whereas pore water advection occurs at 0.5–1m/yr, calculated from dissolved calcium profiles in sediment pore water, or 0.3–1m/yr, calculated from sea floor methane seepage rates [Torres et al., 2002], so free gas exits conduits more than 10^7 times faster than the speed of fluid advection in the sediments. At less active regions, like Blake Ridge, advective fluxes are two to three orders of magnitude slower than those at Hydrate Ridge [Nimblett and Ruppel, 2003].

The results from this work also have important implications for carbon dioxide storage in the deep sub-seafloor, where sequestration is possible by hydrate formation [Koide et al., 1995, 1997b] and gravitational trapping [Koide et al., 1997a; House et al., 2006; Levine et al., 2007; Goldberg et al., 2008]. Whether the migration of supercritical CO_2 is dominated by capillary invasion or fracture opening may determine the viability of this sequestration concept in ocean sediments. In these systems, fractures will have a tendency to propagate vertically [Nunn and Meulbroek, 2002; Boudreau et al., 2005], which could provide fast pathways for the escape of injected CO_2 by pressure gradients. In order to avoid the fracturing regime, it is conceivable that one should inject in coarse-grained, high-energy sediments such as turbidites.

Appendix A. Throat Conductance

In this section we derive Equation (9) for the throat conductance. Our formulation resolves one fundamental problem of two-dimensional grain-scale models: the fact that when grains are in contact, the aperture of the throat between pores is zero. Three-dimensional models do not suffer from this problem, because the throat can be associated with the section of minimum cross-sectional area between two pore bodies.

Before discussing our formulation for 2D models, consider an individual pore throat in 3D, as shown in Figure 86. A throat can be considered a microfluidics pipe, with a certain angular cross section. For creeping flow in a small channel, the Navier–Stokes equations reduce to the elliptic Poisson equation. For a coordinate system in which one of the axes (say, the z -axis) is parallel to the channel, the equation and boundary conditions describing the flow read [Bird et al., 1960]:

$$\nabla^2 v = -\frac{\Xi}{\mu} \quad \text{in } \Omega, \quad (30)$$

$$\Xi = -\frac{\partial p}{\partial z}, \quad (31)$$

$$v(x, y) = 0 \quad \text{on } \partial\Omega, \quad (32)$$

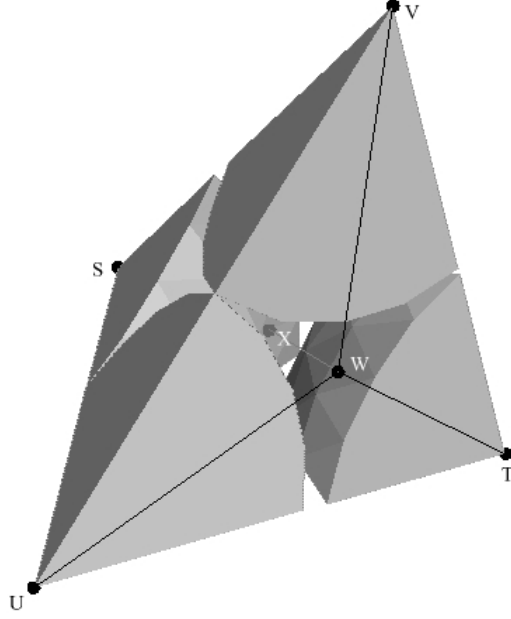


Figure 86: Representation of a pore throat in a three-dimensional grain-scale model [Prodanovic and Bryant, 2006]. The throat is the section with minimum cross-sectional area between two pore bodies. This area is positive even when the surrounding grains are in contact, or even if they overlap.

where μ is the fluid viscosity, Ξ is the (negative) pressure gradient, and $\partial\Omega$ is the boundary of the two-dimensional cross section Ω .

Many solutions to this equation exist for simplified geometries, and useful parameterizations have been developed in the context of pore-network models of fluid-flow through rocks [Øren et al., 1998; Patzek and Silin, 2001]. The total flowrate q through the throat cross section can be expressed in the following form:

$$q \equiv \int_{\Omega} v(x, y) \, d\Omega = C\Xi, \quad (33)$$

where C is the throat conductance. Dimensional analysis dictates that the conductance can, in turn, be expressed as follows:

$$C = \frac{1}{\mu} A^2 \tilde{C}, \quad (34)$$

where A is the cross-sectional area of the throat, and \tilde{C} is a dimensionless conductance. It has been shown that, for a very wide range of throat shapes, the dimensionless conductance is simply a function of the shape factor,

$$G = \frac{A}{P^2}, \quad (35)$$

where P is the perimeter of the throat. In fact, for triangular cross sections, the dimensionless conductance can be approximated by the simple expression [Patzek and Silin, 2001]:

$$\tilde{C} = \frac{3}{5} G. \quad (36)$$

With precise knowledge of the geometry of the grain assembly, one could compute the area and shape factor for each throat, and evaluate the throat conductance using the expressions above. However, since these equations themselves rely on the assumption of creeping flow in cylindrical channels, it is sufficient to consider a “master” geometry (like the one shown in Figure 86). In any case, it is important to note that the throat conductance scales with the fourth power of the grain size:

$$C \sim \frac{\tilde{C}}{\mu} r_g^4. \quad (37)$$

The question is: how do we apply this conductance formulation to *two-dimensional* grain-scale models? In 2D models, the cross section (or aperture) of a pore throat is zero if grains are in contact. This would lead to a model that does not conduct fluid. To address this issue, previous investigations typically resort to defining an artificial throat aperture using heuristic arguments [Bruno and Nelson, 1991; Li and Holt, 2001, 2004; ITASCA, 2004].

We resolve this problem by understanding a two-dimensional model as a collapsed three-dimensional model. We must make some approximations with respect to the grain arrangement in the third dimension. In particular, we assume cubic packing of the 3D assembly. Consider two grains of the same size that are in contact in the 2D model. For cubic packing in the third dimension, the geometry of the throats is well defined, and the flow rate through an individual throat can be computed with Equations (33)–(34).

Importantly, this model leads to physically-realistic throat geometries (and, therefore, throat conductances) regardless of whether the two grains defining a throat are just in contact (gap $d = 0$), whether there is a gap between them ($d > 0$), or whether there is overlap between them ($d < 0$). For each configuration, the shape factor can be computed using elementary geometry, and the dimensionless conductance evaluated therefrom. In Figure 87, we summarize the throat conductance formulation for 2D grain assemblies.

In a 2D model, we must collapse the third dimension, and compute the flow rate between pore bodies as

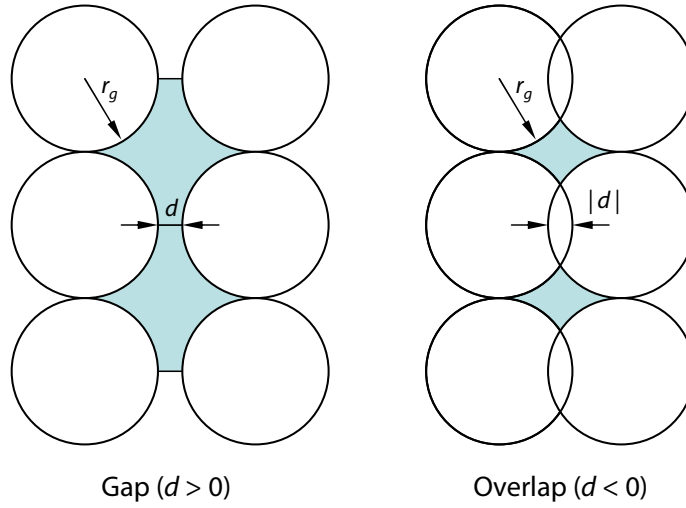
$$q_{2D} = q_{3D} \frac{w}{2r_g}, \quad (38)$$

where, if $w = 1$, Q is the flowrate per unit width. Combining Equation (38) with (33) and (34) leads to Equations (8) and (9), as desired.

Appendix B. Capillary Entry Pressure

The conceptual model presented above also provides a framework for determining capillary entry pressures in two-dimensional models, which is required to simulate two-phase flow.

Consider, first, invasion of gas through a throat in a three-dimensional setting (Figure 86). The surface tension between gas and brine is γ , and the contact angle between the gas–water interface and the solid surface is θ . Gas will penetrate through the throat cross section when the capillary pressure (the gas pressure minus the water pressure) exceeds the threshold capillary pressure. The Mayer–Stowe–Princen (MSP) [Mayer and Stowe, 1965; Princen, 1969a,b, 1970] method for calculating the threshold pressure relies on equating the curvature of the corner arc menisci to the curvature of the invading interface. Expressions for the drainage capillary entry pressure have been derived for a variety of cross sections [Mason and Morrow, 1991; Øren et al.,



If $d > 0$ (gap)

$$A = 4r_g^2 \left(1 - \frac{\pi}{4} + \frac{d}{r_g} \right)$$

$$P = 2r_g \left(\pi + \frac{2d}{r_g} \right)$$

Elseif $d \leq 0$ (overlap)

$$A = 4r_g^2 \left(1 - \sqrt{\frac{|d|}{r_g} - \left(\frac{|d|}{2r_g} \right)^2} \right) \left(1 - \frac{|d|}{r_g} \right)$$

$$\alpha = \sin^{-1} \left(1 - \frac{|d|}{2r_g} \right)$$

$$P = 2r_g \cdot 2\alpha$$

Endif

$$G = \frac{A}{P^2}$$

$$\tilde{C} = \frac{3}{5}G$$

Figure 87: Summary of the throat conductance formulation for 2D grain assemblies. The figure shows the top view of the cross-sectional area of the throat in the collapsed 3D model. (See text for the definition of the variables and a discussion of the formulation.)

1998; Patzek, 2001]. They take the form:

$$P_c^e = \frac{2\gamma}{r_{\text{th}}} F(\theta, G, D), \quad (39)$$

where r_{th} is the radius of the inscribed circle, and F is a function of the receding contact angle and the geometry of the throat—through the throat shape factor G and a function D of the throat corner angles. It turns out that, if the contact angle is small (as it normally is for gas invasion into a natural sediment), $F \approx 1$ [Lenormand et al., 1983; Patzek, 2001]. Therefore, for zero contact angle, the capillary entry pressure can be approximated by

$$P_c^e = \frac{2\gamma}{r_{\text{th}}}. \quad (40)$$

For a throat formed in the space between three spherical grains of equal radius r_g that are in contact, elementary geometry leads to the expression:

$$r_{\text{th}} = r_g \left(\frac{2}{\sqrt{3}} - 1 \right), \quad (41)$$

and, therefore, we obtain the simple and useful estimate:

$$P_c^e \approx 10 \frac{\gamma}{r_g}. \quad (42)$$

Once again, we apply this concept to two-dimensional grain-scale models, by assuming simple cubic packing in the third dimension. In this way, we can rigorously define a throat radius (and, from it, a capillary entry pressure) even when the 2D throat aperture is zero (because the 2D grains defining a pore throat are in contact). If the two grains are exactly in contact (see Figure 88), one can immediately obtain the relation:

$$r_{\text{th}} = r_g(\sqrt{2} - 1). \quad (43)$$

When the two grains of equal size are separated by a gap ($d > 0$), or when they overlap ($d < 0$), the relation above can be extended as follows:

$$r_{\text{th}} = r_g \left(\sqrt{1 + \left(1 + \frac{d}{2r_g}\right)^2} - 1 \right). \quad (44)$$

Substituting Equation (44) into (40) leads to Equation (15), as desired.

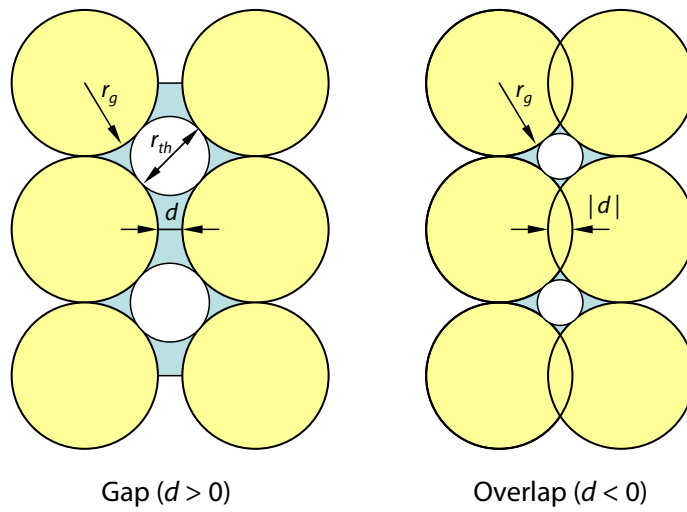


Figure 88: Geometry of the pore throat in the third dimension of a 2D grain-scale model, for the definition of the throat radius r_{th} .

Crossover from fingering to fracturing in deformable disordered media

The displacement of one fluid by another in disordered media—such as porous media, etched micromodels, nanopatterned surfaces, or biological tissues—gives rise to complex invasion patterns [Gollub and Langer, 1999]. The classical phase diagram of fluid–fluid displacement delineates three different regimes [Lenormand et al., 1988]: compact displacement, capillary fingering or invasion percolation [Wilkinson and Willemsen, 1983], and viscous fingering [Paterson, 1984; Måløy et al., 1985; Stokes et al., 1986]. This classification, which is based on micromodel experiments and modified invasion percolation models, is applicable to drainage in rigid media under negligible gravity effects. Much attention has been devoted to the characterization of each regime, as well as the transition among the different regimes [Chen and Wilkinson, 1985; Yortsos et al., 1997; Ferer et al., 2004; Toussaint et al., 2005]. It has been shown, for instance, that pore-scale disorder in rigid media impacts the regime transition from invasion-percolation to viscous fingering [Chen and Wilkinson, 1985; Toussaint et al., 2005].

Coupled fluid and granular flow also leads to a variety of patterns, including fractures [Chevalier et al., 2009], viscous fingers [Cheng et al., 2008], desiccation cracks [Meakin, 1991] and labyrinth structures [Sandnes et al., 2007]. The formation of these patterns typically involves large particle rearrangements. Interestingly, a transition from viscous fingering to fracturing has been observed for fluid displacement in viscoelastic fluids and colloidal suspensions [Lemaire et al., 1991; Lindner et al., 2000]. This crossover depends on the system deformability and on the Deborah number—a ratio of the characteristic times of a flow event and viscoelastic relaxation [Lemaire et al., 1991].

The fracturing process in a disordered medium has been studied at length [Meakin, 1991]. Block–spring network models that simulate fracture growth have emphasized the role of heterogeneity in the mechanical properties (elasticity or strength of the springs), using either annealed disorder [Meakin et al., 1989; Levermann and Procaccia, 2002] or quenched disorder [Tzschichholz and Herrmann, 1995; t. Leung and Néda, 2000]. However, the transition from fluid instability (capillary or viscous fingering) to fracturing remains poorly characterized at the pore scale. Recent modeling results suggest that the mode of gas invasion in a porous medium shifts from capillary invasion to fracture opening as the grain size decreases [Jain and Juanes, 2009], in agreement with observations of gas bubble growth in sediments [Boudreau et al., 2005], and drying in three-dimensional granular media [Xu et al., 2008].

In this paper, we investigate the crossover from fingering to fracturing patterns in deformable, disordered media, by means of a pore-scale model of the displacement of one fluid by another. Our pore-scale model captures the dynamics of pressure redistribution at the invading front, allowing us to characterize the effect of the initial disorder in hydraulic properties on the transition from capillary to viscous fingering. The model incorporates the two-way coupling between fluid displacement and mechanical deformation, providing the mechanisms for pore opening in response to pressure loading (direct coupling), and alteration of the flow properties by particle rearrangements (reverse coupling). Despite its simplicity, the model predicts the emergence of fracture opening as a dominant feature of the invasion pattern for sufficiently deformable systems.

We develop a 2-D discrete model of a random medium. Since we are interested in elucidating the general mechanisms of fluid invasion, rather than performing predictions for a particular type of

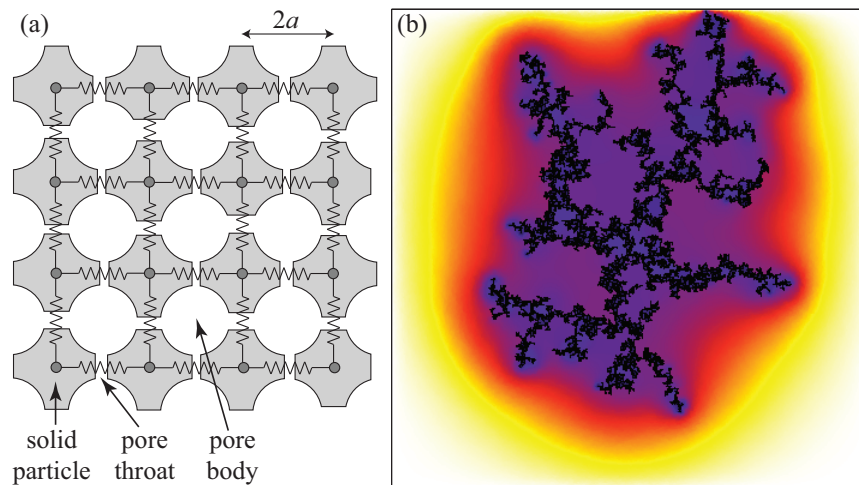


Figure 89: (a) Schematic of the model and simulation of drainage. The solid matrix is represented by a square lattice of dented blocks, connected mechanically by springs. The narrow openings between particles are the pore throats, which connect the larger openings (pore bodies). (b) An inviscid, nonwetting fluid is injected at the center of the network, displacing a viscous, wetting fluid. The pressure “halo” that surrounds the ramified invaded region reflects the finite timescale required for pressure dissipation in the defending fluid. The color scheme represents the log of pressure normalized by the invading fluid pressure. In all our simulations, we use networks of 400×400 pores ($L = 400a$), and set $a = 0.1 \mu\text{m}$, $\mu = 10^{-3} \text{ Pa} \cdot \text{s}$, $\gamma = 0.07 \text{ N m}^{-1}$, and $\epsilon_0 = 0.05$. Here, $\text{Ca} = 9 \times 10^{-4}$ and $\lambda = 0.3$.

medium, we assume a simple square-lattice arrangement of dented blocks [Fig. 89(a)]. Variation in particle shapes leads to disorder in throat apertures, which is assumed to be uncorrelated in space. Mechanical interaction among the particles is represented through a block-and-spring model. The springs are assumed to be uniformly pre-stressed under compression. Such confinement prevents large microstructural rearrangements.

We construct two interacting networks: a solid network and a fluid network, whose nodes are the solid particles and the pore bodies, respectively. We solve for particle displacements and fluid pressures at the pore bodies. The characteristic length scale is the pore size a , which here we take as half the distance between nodes in the lattice. We model pore-scale disorder by assigning different initial area A and permeability k to the throats between pore bodies. Both the throat area and permeability scale with the square of the throat aperture r , that is, $A \sim r^2$, $k \sim r^2$. We characterize the disorder in throat aperture by drawing values from a uniform distribution, $r \in [1 - \lambda, 1 + \lambda]\bar{r}$, where $\bar{r} \sim a$. The coefficient $\lambda \in (0, 1)$ is a measure of the degree of disorder [Chen and Wilkinson, 1985].

We simulate the invasion of an inviscid, nonwetting fluid into a medium initially saturated with a wetting fluid of dynamic viscosity μ . The inviscid fluid pressure is spatially uniform. A fluid-fluid interface will advance from one pore to another if the capillary pressure (the difference between nonwetting and wetting phase pressures) exceeds the capillary entry pressure $2\gamma/r$, where γ is the interfacial tension between the fluids and r is the aperture of the connecting throat [de Gennes, 1985]. If both fluids are inviscid, pressure variations in response to interface movement dissipate instantaneously; then, the process is described by the classical invasion-percolation algorithm [Wilkinson and Willemsen, 1983], and depends exclusively on the quenched disorder.

Consideration of fluid viscosity introduces spatial non-locality due to redistribution of the defending fluid along the invasion front. Slow drainage in disordered media occurs in the form of bursts, which lead to sudden changes in the defending fluid pressure (“Haines jumps” [Haines, 1930]). When one or more pores are drained during a burst, the interface menisci at neighboring pores readjust, receding along throats or even leading to a backfilling of previously drained pores [Xu et al., 2008]. The short timescales associated with pressure buildup in the defending fluid relative to that of drainage out of the system makes fluid redistribution along the front a crucial mechanism [Måløy et al., 1992; Furuberg et al., 1996; Xu et al., 2008]. This mechanism reduces the capillary pressure (the local curvature decreases as the meniscus recedes) and suppresses further invasion until the excess pressure in the defending fluid is dissipated, thus limiting the burst size.

Incorporating meniscus readjustments in a dynamic pore-network model [Aker et al., 1998; Lam, 2004] is computationally intensive. Here, we introduce the main effect of front interface dynamics: an effective compressibility of the system, even though the defending fluid is nearly incompressible.

The effective compressibility c_t can be obtained by the following argument. The capillary number is a ratio of viscous forces over capillary forces at the pore scale, $\text{Ca} = \Delta p_{\text{visc}}/\Delta p_{\text{cap}}$. Assuming Poiseuille flow, the viscous pressure drop over a pore length is $\Delta p_{\text{visc}} \sim \mu v a/k$, with $k \sim a^2$, and v the average flow velocity evaluated from the cumulative values of the drained volume, time, and cross-sectional area along the boundaries [Furuberg et al., 1996]. Together with the Young-Laplace equation, $\Delta p_{\text{cap}} \sim \gamma/a$, this leads to the classical definition $\text{Ca} = \mu v/\gamma$. An alternative definition is the ratio of time scales for pressure dissipation and pore filling [Furuberg et al., 1996], $\text{Ca}^* = \Delta t_{\text{press}}/\Delta t_{\text{fill}}$. Unlike [Furuberg et al., 1996], here we invoke pore-scale quantities only.

The time scale for pressure dissipation is $\Delta t_{\text{press}} \sim a^2/D$, where $D = (k/\mu)/c_t$ is the hydraulic diffusivity. The pore filling time scale is simply $\Delta t_{\text{fill}} \sim a/v$, leading to $\text{Ca}^* = (\mu v/\gamma)(c_t \gamma/a)$. Equating the two definitions of the capillary number provides the effective compressibility of slow drainage in a disordered medium:

$$c_t = \frac{a}{\gamma}. \quad (45)$$

In our simulations, the nonwetting fluid is injected at the center of the lattice at an approximately constant volumetric injection rate. Since the invading fluid is inviscid, we focus on the pressure evolution in the defending fluid. From mass conservation at a pore body, we write the equation of pressure evolution at an undrained pore, $p(t + \Delta t) = p(t) + \sum_j q_j \Delta t / (c_t V)$, where Δt is the time step, V is the pore volume, and the summation is over all neighboring pores. The volumetric flow rate between the pore and its neighbor j is given by Darcy's law $q_j = (Ak/\mu)(p_j - p)/\ell_j$, where ℓ_j is the length over which the pressure drop $p_j - p$ is applied. For flow between two undrained pores, $\ell = 2a$. If pore j is drained, the meniscus between the two pores starts advancing if $p_j - p > 2\gamma/r$. The consequent pressure variations in the undrained pore are governed by the ability of the medium to dissipate pressure through the effective compressibility. The length over which viscous pressure drop takes place decreases as the meniscus advances, according to the expression $\ell_j(t + \Delta t) = \ell_j(t) - (q_j/A)\Delta t$.

A typical invasion pattern from our model for conditions near the transition between capillary fingering and viscous fingering is shown in Fig. 89(b). The simulation clearly shows the presence of a pressure ‘‘halo’’ surrounding the invaded region, as a result of the non-negligible time required to dissipate pressure in the viscous defending fluid.

We are interested in the effect of heterogeneity on the flow pattern. The advancement of the interface is determined by the competition among different pores along the front, which depends on the distribution of throat apertures and pore pressures. We expect the transition from capillary to viscous fingering to occur when the characteristic macroscopic viscous pressure drop ‘‘perpendicular’’ to the interface, δp_{\perp} , exceeds the variation in capillary entry pressures along the front, δp_{\parallel} . We express $\delta p_{\perp} \sim \nabla p_{\perp} L$, where L is the macroscopic length scale, and use Darcy's law, $\nabla p_{\perp} \sim \mu v/k$, to obtain $\delta p_{\perp} \sim \mu v L/a^2$. We use a fixed value of the macroscopic length scale with $L \gg a$ for the viscous pressure drop in the defending phase, an assumption that is justified during the initial stages of the invasion but that becomes questionable at later stages, when the invasion front approaches the system's boundaries and becomes fractal [Lenormand, 1989]. The maximum capillary pressure difference along the front is $\delta p_{\parallel} = \gamma/r_{\min} - \gamma/r_{\max} \sim [\lambda/(1-\lambda^2)]\gamma/a$. Equating $\delta p_{\perp} \sim \delta p_{\parallel}$, and using the definition of the capillary number, $\text{Ca} = \mu v/\gamma$, we predict a transition from viscous fingering to capillary fingering with the scaling $\text{Ca} \sim [\lambda/(1-\lambda^2)]a/L$.

We synthesize our results on a phase diagram in $\text{Ca}-\lambda$ space (Fig. 90). The invasion patterns are classified by visual appearance, as well as by the fractal dimension D_f (see Appendix). The value of D_f by itself is insufficient to provide unequivocal classification due to expected fluctuations for finite samples. The simulations confirm our predictions on the transition from capillary to viscous fingering. For $\text{Ca}/\lambda \gg a/L$ the effect of heterogeneity is negligible relative to that of Laplacian-driven growth [Niemeyer et al., 1984], allowing the most advanced fingers to continue propagating. This results in long and thin fingers typical of viscous fingering. For $\text{Ca}/\lambda \ll a/L$, the heterogeneity in throat apertures dominates, leading to invasion that propagates at alternating locations. As a result, different parts of the front will coalesce and trap some of the defending fluid

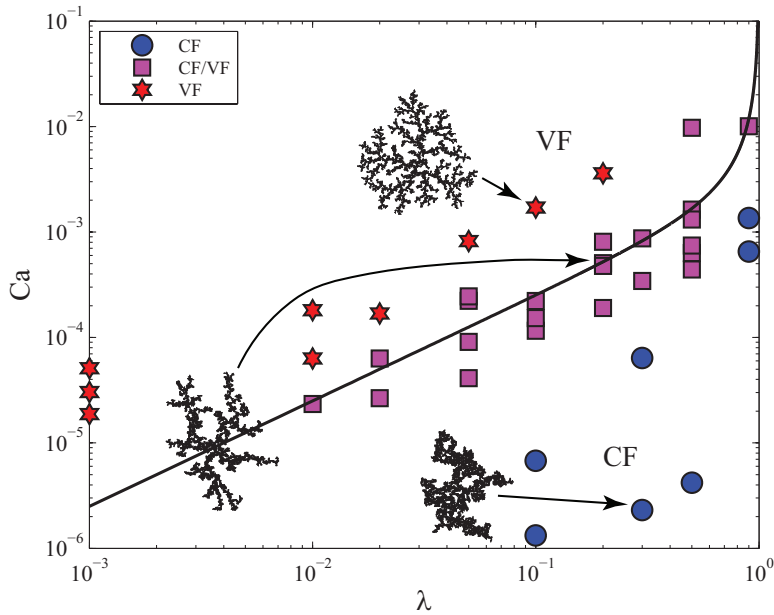


Figure 90: Phase diagram of the invasion pattern as a function of capillary number Ca and the pore-scale disorder λ , in a rigid solid matrix. The classification is based on visual appearance (see insets), as well as the mass fractal dimension D_f . Box counting [Niemeyer et al., 1984] provides estimates of $D_f \approx 1.82$ and $D_f \approx 1.64$ for capillary fingering (CF) and viscous fingering (VF), respectively, with standard deviation $\sigma_{D_f} = 0.08$ (see Appendix). The transition from capillary to viscous fingering (CF/VF) occurs at $Ca \approx [\lambda/(1 - \lambda^2)]a/L$ (black solid line), reflecting a balance between viscosity and pore-scale disorder in capillary entry pressures.

behind, creating the fat clusters with thick fingers characteristic of capillary fingering.

The two regimes are separated by an intermediate regime centered around the theoretical curve $\text{Ca} \sim [\lambda/(1 - \lambda^2)]a/L$. In the limit $\lambda \rightarrow 1$ the capillary disorder blows up. The analysis above indeed suggests that the capillary fingering regime always dominates in this limit (the crossover curve diverges in Ca - λ space). In the limit of nearly homogeneous media and high capillary number (not shown in Fig. 90), the model's anisotropy becomes dominant and dendritic growth occurs along the lattice axes, similar to the experimental results in [Chen and Wilkinson, 1985]. Our analysis suggests the existence of a crossover length scale $L_\times \sim [\lambda/(1 - \lambda^2)]\text{Ca}^{-1}a$, at which the displacement experiences a regime shift from capillary fingering (below L_\times) to viscous fingering (above L_\times). A similar conclusion was drawn from the mass fractal dimension of the pattern in drainage experiments [Toussaint et al., 2005].

A compliant solid matrix can deform in drainage, which in turn may lead to fracture opening during fluid invasion. Here, we investigate the impact of system deformability on the emergence of invasion patterns. Particle displacements cause changes in the contraction of the springs over time, $h(t)$. To highlight the effect of disorder in flow properties, we assume the system is initially pre-stressed homogeneously, such that all springs are subject to the same compression, h_0 , corresponding to a macroscopic strain $\epsilon_0 = h_0/2a$. Each particle is subject to two types of forces: pressure forces and contact forces. The force exerted on a particle by the fluid occupying an adjacent pore body is oriented at 45° and is of magnitude $f_p = pA_p$, where $A_p \sim a^2$ represents the area upon which the pressure acts. The interparticle contact forces f_c are updated by $f_c(t + \Delta t) = f_c(t) + K\Delta h$, where K is the spring stiffness and $\Delta h = h(t + \Delta t) - h(t)$ is the change in spring contraction. Particle positions are determined at the new time step by imposing force balance at every block, $\sum(\vec{f}_p + \vec{f}_c) = \vec{0}$, which leads to a linear system of equations to be solved for Δh of every spring. Particle displacements impact fluid flow because they modify the throat apertures. We evaluate changes in throat apertures and in interparticle forces from the particle displacements in analogy with cubic packing of particles with frictionless, Hertzian contacts, such that $\Delta r = -\Delta h(1 - \epsilon)/[2\sqrt{1 + (1 - \epsilon)^2}]$, where $\epsilon = h(t)/2a$, and the spring stiffness $K = 2E^*\sqrt{R^*h}$, where $R^* = a/2$, and E^* is the constrained Young modulus of the particle material [Johnson, 1987]. We simulate material behavior that cannot sustain tension and, therefore, a spring is removed when there is net elongation between blocks ($h \leq 0$). A small cohesive force is applied as a regularization parameter. This force is orders of magnitude smaller than the typical pressure force, and we have confirmed that the results are insensitive to the value of this cohesive force, as long as it is small.

Our model predicts fracturing patterns that are strikingly similar to those observed in 2-D experiments, with thin, long features which are straight over a length larger than a pore size [Chevalier et al., 2009], and fractal dimension lower than in fingering, $D_f \approx 1.43$ (see Appendix). The straight segments of the invasion pattern form as a result of localized rearrangements: increasing throat aperture by displacing particles in a direction perpendicular to that of the finger advancement promotes finger growth in that direction. This mechanism is arrested when the front reaches a bottleneck, associated with either initial disorder or compaction ahead of another propagating fracture.

Emergence of a fracturing pattern requires sufficiently large change in throat apertures. Particle rearrangements depend on the balance between the forces applied by the fluids and the interparticle forces holding the particles in place. We define a dimensionless ‘‘fracturing number’’ N_f as the ratio

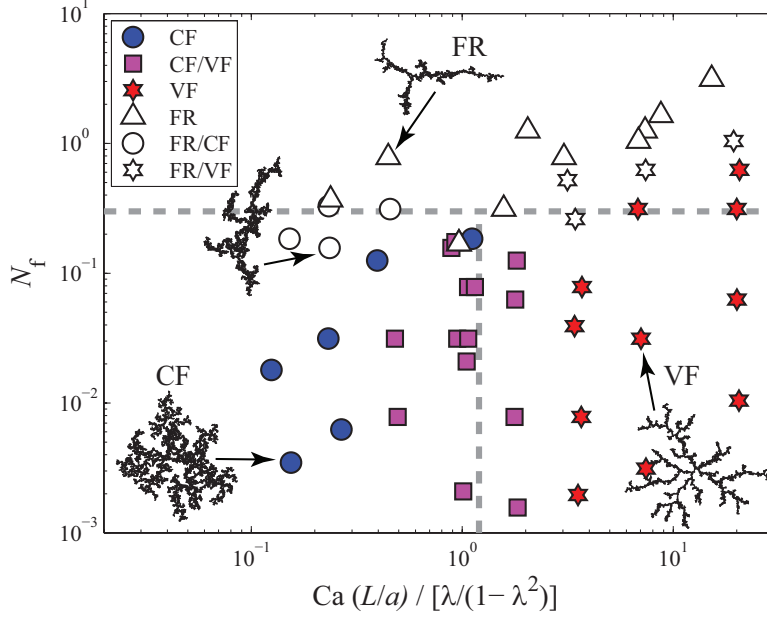


Figure 91: Phase diagram of drainage in deformable, disordered media, showing three distinct invasion patterns: viscous fingering (VF), capillary fingering (CF), and fracturing (FR). The gray dashed lines denote transitions among the different regimes. Intermediate regimes are marked by CF/VF, FR/VF and FR/CF. The deformability of the system is characterized by the “fracturing number” N_f : drainage is dominated by fracturing in systems with $N_f \gg 1$. At lower N_f values, a transition between capillary and viscous fingering occurs around $\text{Ca}(L/a)/[\lambda/(1-\lambda^2)] \approx 1$.

of the typical pressure force increment after drainage of a pore, $\Delta f_p \sim \gamma a$, and the force increment resulting from deformation, $\Delta f_c \sim \lambda E^* a^2 \epsilon_0^{1/2}$. The latter is obtained from the condition $\Delta h \sim \Delta r$, where the required change in throat aperture is $\Delta r \sim \lambda \bar{r} \sim \lambda a$, and using the initial overlap h_0 to compute the interparticle stiffness K . With that,

$$N_f = \frac{\gamma}{\lambda a E^* \epsilon_0^{1/2}}. \quad (46)$$

An alternative expression for N_f is obtained by substituting the initial confining stress $\sigma_0 \sim E^* \epsilon_0^{3/2}$ into Eq. (46).

We synthesize drainage behavior in a deformable medium in a phase diagram with two dimensionless groups, the fracturing number N_f and a modified capillary number $\text{Ca}(L/a)/[\lambda/(1-\lambda^2)]$ —see Fig. 91. For a rigid medium ($N_f \ll 1$), the transition from capillary to viscous fingering occurs at $\text{Ca}(L/a)/[\lambda/(1-\lambda^2)] \approx 1$. Fracturing is evident when $N_f \gg 1$. A crossover from fingering to fracturing occurs at $N_f \approx 1$. Equation (46) implies that fractures tend to open in fine-particle media, suggesting that below a critical particle size—which decreases with the particle stiffness and the external confinement—invasion is dominated by fracturing. This is consistent with observations of gas bubble growth in sediments [Boudreau et al., 2005; Jain and Juanes, 2009] and drying in porous media [Xu et al., 2008].

In conclusion, this study explains the crossover among the different fluid displacement patterns of drainage in a deformable medium. The invasion behavior depends on two dimensionless groups.

One is related to the influence of pore-scale disorder on the balance between viscous forces and capillary forces. The other measures the deformability of the medium as a function of capillary effects, material properties and initial confinement. Despite its simplicity, our model predicts the transition from capillary fingering to viscous fingering in rigid media, and a crossover from fingering to fracturing in deformable media, suggesting that it captures the essential aspects of the interplay between multiphase fluid flow and mechanical deformation.

Appendix

In this appendix we demonstrate the ability of our pore-scale model to capture the transition among the different invasion regimes—viscous fingering (VF), capillary fingering (CF) and fracturing (FR). Our classification of the displacement pattern is based on visual appearance, as well as the fractal dimension D_f (using box counting [Niemeyer et al., 1984]). Visual appearance is an essential consideration in the classification because the estimation of the fractal dimension from the mass vs. distance curves is subject to large fluctuations for finite-size systems [Måløy et al., 1985; Blunt and King, 1990; Løvoll et al., 2004; Praud and Swinney, 2005].

First, we illustrate the transition between VF and CF. For a given value of the disorder parameter, $\lambda = 0.1$, we investigate the displacement pattern for a range of capillary numbers. For each value of Ca , we show the displacement pattern, and the curve of mass vs. distance from which the fractal dimension is obtained (Fig. 92). It is evident that the model predicts a transition from VF (high Ca) to CF (low Ca). Moreover, the values of the fractal dimension are in excellent agreement with experimentally-determined values of 1.60–1.65 for VF in a *porous* Hele-Shaw cell [Måløy et al., 1985; Løvoll et al., 2004] to the well known value of 1.82 for invasion-percolation corresponding to CF.

Next, we show the transition between VF and FR, by studying displacements with a similar value of the modified capillary number, $Ca^* = Ca(L/a)/[\lambda/(1 - \lambda^2)] \approx 10$ and a range of values of the key dimensionless group, the fracturing number N_f . The fracturing pattern is characterized by fingers with straight segments and a lower fractal dimension (Fig. 93).

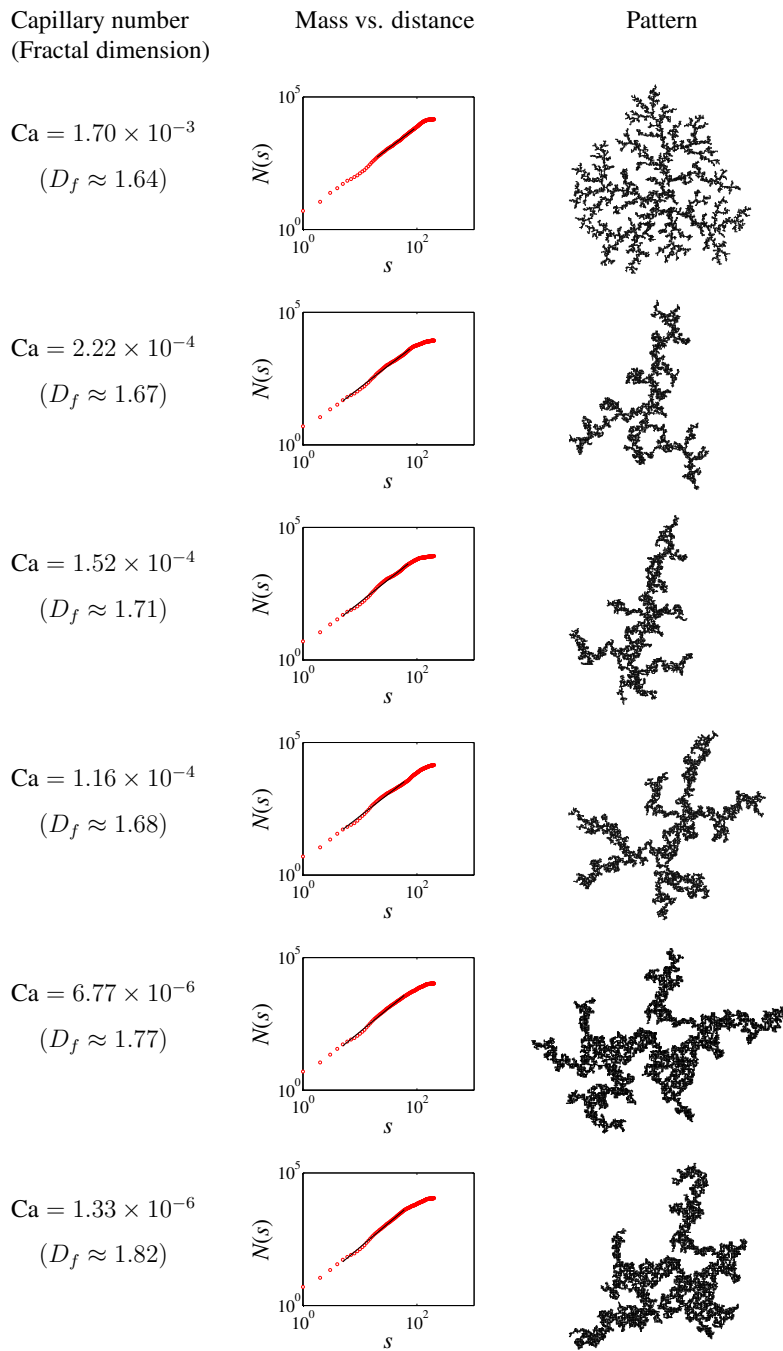


Figure 92: Fractal dimension and displacement pattern for rigid medium, with a value of $\lambda = 0.1$, showing a transition from viscous fingering to capillary fingering as the capillary number is reduced.

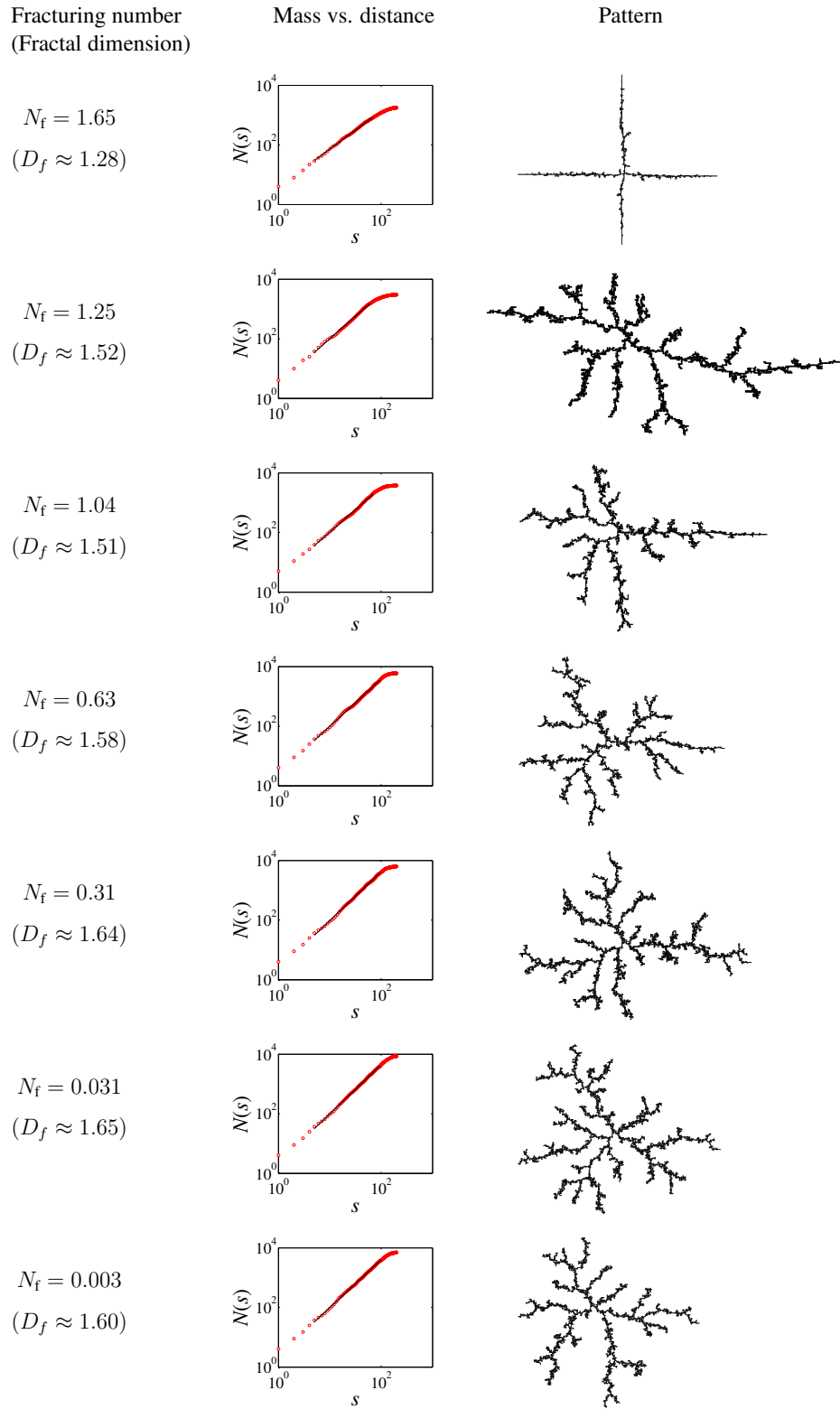


Figure 93: Fractal dimension and displacement pattern for deformable medium, with a value of $Ca^* \approx 10$, showing a transition from fracturing to fingering as the fracturing number is reduced.

Thermodynamic and hydrodynamic constraints on overpressure caused by hydrate dissociation: A porescale model

Introduction

Methane hydrate is a solid compound that forms by crystallization of water and methane upon cooling and/or pressurization. Accumulations of methane hydrate in hydrate-bearing sediments (HBS) have gained much attention for their potential as an energy resource [Boswell, 2009] and their role as a greenhouse gas in future global warming [Archer et al., 2009]. Heating or depressurization cause hydrate to dissociate into free gas and water. Dissociation of hydrate within the pore space of sediments has often been invoked as a mechanism that may lead to significant overpressures (up to tens of MPa), in view of the multiple-fold volume increase that occurs upon dissociation [Xu and Germanovich, 2006; Kwon et al., 2006; Rutqvist and Moridis, 2009]. Overpressure induced by dissociation has been suggested as a trigger for sediment failure, including submarine landslides [Sultan et al., 2004; Mienert et al., 2005; Xu and Germanovich, 2006], soft-sediment deformation [Kennett and Fackler-Adams, 2000], pingo-like features [Paull et al., 2007], mud volcanoes [Van Rensbergen et al., 2002] and wellbore damage [Rutqvist and Moridis, 2009]. Warming of ocean waters and consequent dissociation of extensive HBS layers, leading to sediment failure and massive release of methane gas, has been proposed as the cause of the Paleocene-Eocene Thermal Maximum [Dickens et al., 1995], and as a potential key player in the current carbon cycle [Dickens, 2003; Westbrook et al., 2009].

The possible implications of dissociation raise the need for understanding the relevant mechanisms, in particular the interplay between dissociation and pressure evolution. Existing models predict large overpressures in fine-grained sediments, where the low permeability would prevent rapid pressure dissipation [Xu and Germanovich, 2006; Kwon et al., 2006; Rutqvist and Moridis, 2009; Kwon et al., 2010]. Xu and Germanovich [2006] evaluate overpressures as high as 50 MPa for undrained (no-flow) conditions and 7 MPa for low permeability sediment, assuming a constant dissociation rate which is independent of the pore pressure. The end-member scenario of no flow and restricted volumetric expansion was investigated by Kwon et al. [2006], who correctly point out that since rising pressure stalls further dissociation, additional heat is required to continue the dissociation process. This self-preservation mechanism leads to pressure-temperature (p-T) conditions which follow the three-phase (hydrate-gas-brine) equilibrium curve during dissociation. Therefore, a large overpressure (hereafter defined as the gas pressure above the initial water pressure p_0 prior to dissociation) implies a large temperature increase; for example, an increase of ~ 9 MPa is accompanied by a temperature rise of over 9°C . A pressure increase of tens of MPa requires heating by tens of degrees. Simulating long-term thermal stimulation by a hot wellbore (90°C), Rutqvist and Moridis [2009] predict overpressures of ~ 15 MPa in nearby sediments. Smaller pressures (less than 3 MPa) were predicted by Kwon et al. [2010] in simulating dissociation due to a wellbore ($\sim 20^\circ\text{C}$ warmer than its surrounding) in a low-permeability clay. While the authors honor self-preservation by constraining the pressure by the equilibrium pressure, they do not account for dissociation kinetics, and assume that hydrate saturation is sufficiently low to neglect gas flow. However, we will show that gas flow and percolation can occur at hydrate saturations as low as 5%, in agreement with Tsimpanogiannis and Lichtner [2006].

A crucial mechanism which is missing from the models cited above is the coupling among

dissociation kinetics, flow of gas and water, and sediment deformation, including the formation of preferential flow paths and fractures. Consideration of this mechanism requires description of the pore-scale physics. Tsimpanogiannis and Lichtner [2006] investigated the flow patterns of methane gas produced by heating an HBS, and showed that larger pore apertures and a broader range of aperture sizes allow larger gas quantities to percolate through a sample, hence increasing the gas productivity. The authors used a pore-network model based on invasion percolation, assuming instantaneous dissociation and fixed network properties (no geomechanical effects).

In this paper we study the pressure evolution during thermally-induced dissociation. We present a mechanistic, pore-scale model that couples dissociation kinetics, multiphase flow and sediment mechanics. We explore the range of behaviors between the two end-members: (a) no-flow (undrained) conditions; and (b) instantaneous pressure dissipation (fully drained). We model the physics at the pore scale and thus perform all computations at the pore level. The collective dynamics give rise to global effects such as pressurization of the entire sample and gas-invasion patterns. While upscaling the results from our simulations with millimeter-size samples to the reservoir scale is not straightforward, our model elucidates fundamental mechanisms that control the sediment behavior at the pore scale. We demonstrate that rapid pressure buildup is not possible because of the negative feedback between dissociation rate and fluid pressure. The strict upper bound for the gas pressure is its thermodynamic limit: the equilibrium pressure. However, for typical values of the kinetic rates and medium permeability, our results show that pressure build-up by dissociation is slow compared with pressure dissipation by drainage. As a result, overpressures are controlled by the value of the gas pressure required to invade into the porous medium, and are typically much lower than the equilibrium pressure.

Model Formulation

We simulate a low-permeability sample saturated with water and dispersed hydrate crystals, subjected to a sudden temperature increase which brings hydrate out of thermodynamic equilibrium. The small inhibiting effect of the latent heat on the dissociation rate allows us to consider isothermal dissociation under fixed, uniform temperature and exclude heat transfer effects. We evaluate the temporal and spatial evolution of the mass, volume and pressure of hydrate, water and gas, and their impact on the sediment's mechanical and flow properties. At each time step we compute: (1) the dissociated hydrate mass for every crystal, given the surrounding fluid pressures; (2) pore pressure variations caused by the conversion of hydrate into water and gas; (3) flow of gas and water induced by the rising pore pressure; and (4) changes in hydraulic properties by deformation of the solid matrix (microstructural rearrangements).

We emphasize in our model the role of multiphase flow by assuming that the driving force for the flow is the generation of pressurized gas by hydrate dissociation. Once gas pressure overcomes the local capillary thresholds, gas expands by invading into nearby water-filled pores. We evaluate the pressure of gas clusters as they expand and coalesce and the local increase in water pressure due to fluid redistribution along the gas-water interface [Måløy et al., 1992; Xu et al., 2008].

We capture the interplay between pore pressure and dissociation by computing the decomposition rate of each hydrate crystal using a kinetic model. The hydrate mass dissociated during each time step Δt , $\Delta m_h = (dm_h/dt)\Delta t$, is determined according to a driving force which is proportional to the difference between the phase equilibrium fugacity f_{eq} and the methane fugacity at the hydrate crystal surface f [Kim et al., 1987],

$$\frac{dm_h}{dt} = -K_h \exp\left(\frac{-E}{RT}\right) F_A A_h (f_{eq} - f). \quad (47)$$

where K_h is the hydration reaction constant, E is the hydration activation energy, A_h is the surface area for the reaction, and $R = 8.314 \text{ J mol}^{-1} \text{ K}^{-1}$ is the universal gas constant. Negative Δm_h implies decreasing mass. The area A_h is computed from the hydrate crystal volume (which is updated in time as it shrinks), assuming spherical crystal with area adjustment factor of $F_A = 1$. We evaluate f_{eq} and f from the equilibrium pressure p_{eq} (for a given temperature T) and the pressure of gas surrounding the dissociating crystal, p_g . The reverse process, hydrate reformation, can occur locally upon reversal of the driving force ($p_{eq} > p_g$) [Waite et al., 2008]; this process is excluded from our current model.

The gas pressure in each gas cluster, p_g , is evaluated through the ideal-gas equation of state (EOS), where we compute the cluster volume V_g from mass balance. Each mole of dissociated hydrate (with volume of $\Delta V_h = M_h/\rho_h$) is converted to N_h moles of water, which occupies a volume of $\Delta V_w = N_h M_w/\rho_w$. Here, $\rho_h = 900 \text{ kg/m}^3$, $M_h = 0.119 \text{ kg/mol}$, $\rho_w = 1000 \text{ kg/m}^3$ and $M_w = 0.018 \text{ kg/mol}$ are the density and molar mass of methane hydrate and water, respectively, and $N_h = 5.75$ is the hydration number [Sloan and Koh, 2008]. To obtain the cluster volume V_g we note that $\Delta V_w/\Delta V_h \approx 0.8$, hence the remainder 20% of the dissociated hydrate volume ΔV_h is replaced with gas. For simplicity, we use here the ideal gas law, $p_g V_g = n_g R T$, where n_g is the number of gas moles in the cluster. We have confirmed that the use of a more accurate EOS does not alter our results substantially; for example, the difference between overpressures evaluated with the ideal gas law and with the EOS in Duan et al. [1992] in several representative simulations is $\sim 0.1\%$. The number of gas moles n_g is computed from the number of dissociated hydrate moles, $\Delta n_h = \Delta m_h/M_h$. Given the low solubility of methane in water [Sloan and Koh, 2008], we consider only two methane phases, hydrate and gas, neglecting the small quantities that dissolve in water.

Our model incorporates the two-way coupling between fluid displacement and mechanical deformation: pore opening in response to pressure loading (direct coupling), and alteration of the flow properties by grain rearrangements (reverse coupling) [Holtzman and Juanes, 2010]. A deformable porous material is represented by a 2-D square lattice of dented blocks (grains), connected mechanically by nonlinear springs [Fig. 94(a)]. The voids between the blocks define a pore network: the narrow openings at the contacts are the pore throats, which connect the larger openings (pore bodies). Variation in block shapes leads to variability in throat apertures, which is assumed to be uncorrelated in space. This provides two interacting networks, solid and fluid, whose nodes are the grain centers and the pore bodies, respectively. We solve for displacement of the grains and fluid pressures at the pore bodies.

Pore-scale disorder in hydraulic properties is represented by assigning a distribution of initial area A and permeability k to the pore throats. Both parameters scale with the square of the throat aperture r , that is, $A \sim r^2$, $k \sim r^2$ (assuming Stokes flow in cylindrical tubes provides $A = \pi r^2$, $k = r^2/8$). We characterize the disorder in the hydraulic properties through a scalar parameter, $\lambda \in (0, 1)$, drawing values from a uniform distribution, $r \in [1 - \lambda, 1 + \lambda]\bar{r}$, where $\bar{r} \sim a$. The characteristic length scale is the pore size a , which here we take as half the distance between nodes in the lattice [Fig. 94(a)]. Partially-drained conditions are simulated through a decrease in permeability and throat area at the boundary (each by 3 orders of magnitude, equivalent to a reduction in throat aperture by a factor of $10^{3/2}$) relative to the sample's interior. We enforce a

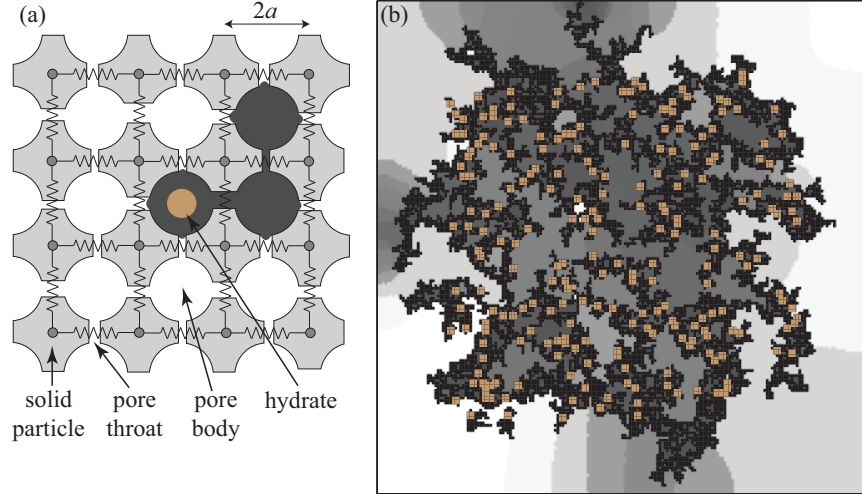


Figure 94: (a) Schematic of the pore-scale model. The solid matrix is represented by a square lattice of dented blocks (grains), connected mechanically by springs. The narrow openings between the grains are the pore throats, which connect the larger openings (pore bodies). Some pores are filled with hydrate crystals (brown), which decompose into water (white) and free gas (dark gray). (b) Pore pressure during simulation of dissociation. The grayscale intensity represents the pressure scaled to increase contrast: white corresponds to the ambient pressure p_0 , black to high pressures in gas filled pores. The location of clusters of 3×3 pores originally occupied by hydrate crystals is marked in brown. The pressure halo that develops ahead of newly invaded pores reflects the finite timescale required for pressure dissipation. We use a network of 200×200 pores with $\lambda = 0.2$, $\epsilon_0 = 0.01$, $a = 1 \mu\text{m}$, $\mu = 10^{-3} \text{Pa s}$ and $\gamma = 0.07 \text{N/m}$. A system in equilibrium at $T_0 = 0.5^\circ\text{C}$ and $p_0 = 2.58 \text{MPa}$ is subjected to $\Delta T = 10^\circ\text{C}$.

constant hydrostatic pressure p_0 at the boundary pores.

In simulating flow we assume that gas is inviscid, such that its pressure adjusts instantaneously and is uniform within each cluster. The water pressure in a water-filled pore is updated from mass conservation at a pore body: $p_w(t + \Delta t) = p_w(t) + \sum_j q^j \Delta t / (c_t V)$, where V is the pore volume, c_t is an effective compressibility of the system (see below), and the summation is over all neighboring pores. The volumetric flow rate between the pore and its neighbor j is given by Darcy's law $q^j = (Ak/\mu)(p^j - p_w)/\ell^j$, where μ is the water dynamic viscosity and ℓ^j is the length over which the pressure drop $p^j - p_w$ occurs. For flow between two water-filled pores, $\ell^j = 2a$. If pore j is gas-filled, the meniscus between the two pores starts advancing once the capillary pressure exceeds the capillary entry pressure, $p^j - p_w > 2\gamma/r$, where γ is the gas-water interfacial tension. As the meniscus advances, the length is updated by $\ell^j(t + \Delta t) = \ell^j(t) - (q^j/A)\Delta t$.

The gas generated by hydrate dissociation invades the porous medium, displacing water. Slow drainage in disordered media occurs in the form of bursts ("Haines jumps" [Haines, 1930]), which lead to sudden changes in water pressure. When one or more pores are invaded during a burst, the interface menisci at neighboring pores readjust, receding along throats or even leading to a backfilling of previously invaded pores [Måløy et al., 1992; Xu et al., 2008]. This phenomenon suppresses further invasion until the excess water pressure is dissipated, thus limiting the burst size. The aggregate behavior resulting from this phenomenon is an effective system compressibility,

$c_t = a/\gamma$ [Holtzman and Juanes, 2010]. The finite time required for pressure dissipation leads to the development of a pressure halo around the expanding gas clusters [Fig. 89(b)].

Changes in pore pressure cause grain rearrangements, which are represented in our model through contraction of the springs over time, $h(t)$. We highlight the effect of disorder in flow properties by using uniform spring stiffness K and enforcing an initially uniform contraction of all spring, h_0 , corresponding to a macroscopic strain $\epsilon_0 = h_0/2a$. This guarantees an initially uniform pre-stressed state, which becomes spatially-variable upon hydrate dissociation. The confinement ϵ_0 is sufficiently large to prevent granular flow. Each grain is subject to two types of forces: pressure and contact forces. The force exerted by the fluid occupying an adjacent pore body is oriented at 45° relative to the lattice axes and is of magnitude $f_p = pA_p$, where $A_p \sim a^2$ is the area upon which the pressure p acts. The intergranular contact forces f_c are updated by $f_c(t + \Delta t) = f_c(t) + K\Delta h$, where $\Delta h = h(t + \Delta t) - h(t)$ is the change in spring contraction. Grain positions are determined at the new time step by imposing force balance at every grain, $\sum(\vec{f}_p + \vec{f}_c) = \vec{0}$, which leads to a linear system of equations in Δh . Grain displacements impact fluid flow by modifying the throat apertures. We evaluate changes in apertures and in intergranular forces from the grain displacements in analogy with cubic packing of spherical grains with frictionless, Hertzian contacts, such that $\Delta r = -\Delta h(1 - \epsilon)/[2\sqrt{1 + (1 - \epsilon)^2}]$, where $\epsilon = h(t)/2a$ [Jain and Juanes, 2009], and $K = 2E^*\sqrt{R^*h}$, where $R^* = a/2$, and E^* is the constrained Young modulus of the grain material [Johnson, 1987; Holtzman and Juanes, 2010]. We model an unconsolidated sediment with negligible tensile strength. Therefore, a spring is removed when there is net elongation between blocks ($h < 0$). A small cohesive force is applied as a regularization parameter.

Results

Our simulations demonstrate that the pressure always remains below the equilibrium value, $p_{eq}(T)$. Self-preservation, where increasing gas pressure diminishes the driving force for further dissociation [Eq. (47)], is evident from the decreasing rate of pressure buildup by dissociation between gas invasion (pore filling) events. Furthermore, comparison of the gas and water pressure evolution indicates that the timescale for pressure buildup by dissociation, t_d , is much larger than that of pressure dissipation following gas invasion of one or more pores and water flow ahead of the moving meniscus, t_p (Fig. 95). The contrast in timescales can be deduced by scaling: $t_p \sim L_p^2/D$, where $D = (k/\mu)/c_t$ is the hydraulic diffusivity, and L_p is the characteristic distance over which pressure dissipation takes place. With $k \sim a^2$ and $c_t \sim a/\gamma$ we obtain $t_p \sim \mu L_p^2/(\gamma a)$. The dissociation timescale can be obtained from Eq. (47), by using the EOS to relate the change in the number of gas moles ($-\Delta m_h/M_h$) to the change in gas pressure, Δp_g , and assuming that the latter scales as the fugacity driving force, $\Delta p_g \sim f_{eq} - f$. This provides $t_d \sim M_h a/[RTK_h \exp(-E/RT)]$. Using published values of $E = 8.1 \times 10^4 \text{ J mol}^{-1}$ and $K_h = 3.6 \times 10^4 \text{ kg m}^{-2} \text{ Pa}^{-1} \text{ s}^{-1}$ [Clark and Bishnoi, 2001] suggests that t_p is smaller than t_d by 4 to 8 orders of magnitude, depending on the value of L_p ; $L_p \sim a$ provides an upper bound of 10^8 , whereas the contrast becomes smaller as L_p approaches the system size. Since L_p reflects the spacing between gas clusters, the timescale ratio will be between the two values.

The rapid dissipation of pressure by drainage relative to its buildup by dissociation implies that the pressure evolution is governed by capillary effects: once the gas pressure exceeds the sum of the water pressure p_w and entry pressure p_c^e in an adjacent water-filled pore, gas expands by invasion

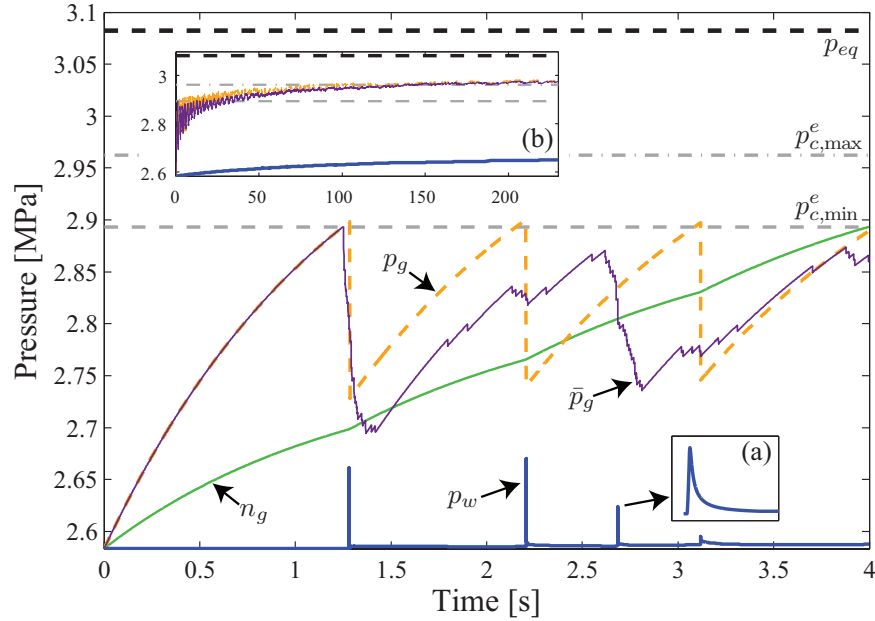


Figure 95: Pressure evolution during thermally-induced hydrate dissociation. The pressures p_g and p_w shown in the plot are measured in a specific gas cluster and in an adjacent pore, respectively. The effect of expansion and coalescence of different gas clusters is captured by the mean gas pressure, $\bar{p}_g = \sum_j (p^j V^j) / \sum_j V^j$ (summation over all gas-filled pores). The concave shape of both the gas pressure p_g and the (normalized) number of moles within a cluster n_g demonstrates the self-preservation mechanism: reduction in dissociation rate as p_g increases. The sharp drop in p_g marks gas expansion during an invasion event: once p_g exceeds the sum of the capillary entry pressure p_c^e and the water pressure in an adjacent water-filled pore p_w , gas invades that pore. The timescale for pressure buildup by dissociation, $t_d \sim 1$ s, is 5 orders of magnitude larger than that of pressure dissipation following an invasion event, $t_p \sim 10^{-5}$ s [between the peak and the plateau in inset (a)]. During the entire simulation [inset (b)], the gas pressure is constrained by both thermodynamics ($p_g < p_{eq}$) and hydrodynamics ($p_g < p_c^e + p_w$). We use a network of 100×100 pores and $\lambda = 0.1$. Here, we simulated a relative low temperature increase, $\Delta T = 1.5^\circ\text{C}$, to emphasize the effect of self-preservation.

and its pressure drops. For the scale of interest here, we can understand gas invasion driven by hydrate dissociation as a quasi-static process, where the water pressure relaxes quickly to a value close to p_0 (Fig. 95). Thus, gas overpressure is controlled by the capillary entry thresholds for gas invasion.

To demonstrate the role of capillarity we compare the maximum pressure that develops during the simulations (until complete dissociation) in systems of different permeability. We vary the permeability by scaling a given aperture distribution (r_0 , similar in all samples) by a pore-to-throat parameter $\beta = r_0/r$, keeping the pore size a fixed. The resulting gas overpressures in most simulations are bounded between the minimum and maximum capillary entry pressures, $p_{c,\min}^e = 2\gamma/[(1 + \lambda)\bar{r}]$ and $p_{c,\max}^e = 2\gamma/[(1 - \lambda)\bar{r}]$, with values closer to $p_{c,\max}^e$ as the permeability increases and to $p_{c,\min}^e$ as it gets smaller (Fig. 96). This behavior is caused by two mechanisms: heterogeneity and matrix deformation. The higher capillary pressures that develop in low-permeability systems result in smaller number of invaded pores (higher-density gas compressed into a smaller volume), where the invasion of only the widest throats (lowest p_c^e) implies that a smaller portion of the aperture distribution is sampled. In addition, higher capillary entry pressures cause more pore opening through grain rearrangements, creating fractures [Jain and Juanes, 2009; Holtzman and Juanes, 2010]. Fracturing allows gas invasion at a capillary pressure lower than the original threshold p_c^e in the undeformed system. Fractures as conduits for gas migration have been observed in experiments [Boudreau et al., 2005] and inferred in the field [Scandella et al., 2011]. In our model, for a given aperture distribution, the mode of invasion is determined by the grain stiffness (E^*) and the external confinement (ϵ): fracturing tends to occur in softer sediments under lower confinement [Holtzman and Juanes, 2010]. In addition, fracturing is more pronounced in sediments with lower heterogeneity in hydraulic properties, corresponding to smaller values of λ (Fig. 97).

Finally, the scaling of the characteristic time for dissociation t_d suggests that it can become comparable to that of pressure dissipation t_p if the kinetics were much faster, that is, for much larger reaction constant K_h or characteristic distance L_p values. We investigate this theoretical limit by simulating dissociation with K_h values up to 10^4 higher than published values [Clark and Bishnoi, 2001]. While the resulting overpressures are higher than those of a quasi-static process controlled by the capillary entry pressures, they always remain well below the thermodynamic equilibrium value p_{eq} .

Conclusions

In conclusion, we have shown that the overpressure from hydrate dissociation in sediments is governed by the competition between kinetic dissociation rate and pressure dissipation. Due to self-preservation, the overpressures cannot exceed the phase equilibrium pressure, regardless of the heat supply and sediment permeability. If the intrinsic kinetic rate was many orders of magnitude faster than its published value, the dissociation rate could be controlled by the ability of the medium to dissipate the pressure. Our results suggest, however, that the timescale for pressure buildup by dissociation is much larger than that of pressure dissipation by drainage, even for low-permeability sediments. We can thus view gas invasion driven by dissociation as a quasi-static process, where the water pressure relaxes quickly and the gas pressure is limited by the characteristic capillary thresholds. Hence, the pressure evolution is dominated by hydrodynamics, where the maximum pressure depends on the mode of gas invasion. In systems with large pore apertures,

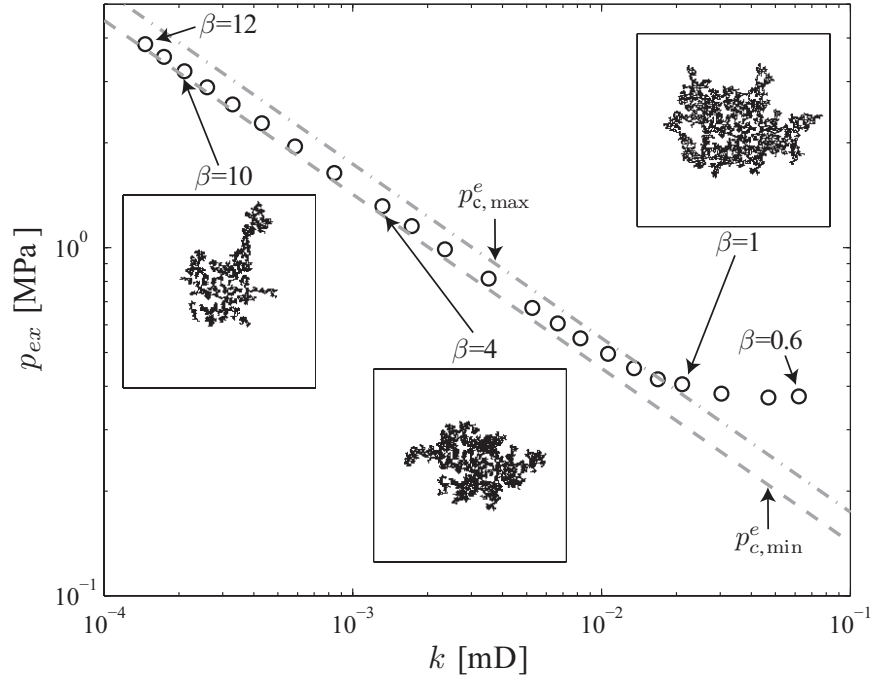


Figure 96: Mean overpressure $p_{ex} = \bar{p}_g - p_0$ and typical invasion pattern (insets) in systems of different permeability $k \sim \bar{r}^2$ (varied by scaling the aperture distribution by β). Because dissipation of pressure by drainage is much faster than its buildup by dissociation, the overpressure is governed by the capillary entry thresholds. In most simulations, $p_{c,\min}^e < p_{ex} < p_{c,\max}^e$. As the permeability becomes smaller, p_{ex} approaches the lower bound $p_{c,\min}^e$, due to the combined effect of heterogeneity and deformation. In low-permeability systems, the highly-pressurized gas occupies a smaller volume and hence samples a smaller portion of the aperture distribution, with only the widest throats (lowest p_c^e) invaded. In addition, the high capillary pressures can lead to fracture opening, which is the preferred mode of gas invasion in soft, fine-grained sediments (see Fig. 97). In the coarsest samples ($k > 0.02$ mD), the overpressures slightly exceed $p_{c,\max}^e$ (by ~ 0.1 MPa) due to a similar increase in water pressure (Fig. 95) which elevates the gas pressure required for invasion. Such pressure increment is negligible relative to the high gas pressure that develops in lower-permeability systems. We use networks of 100×100 and 200×200 pores for the main plot and the insets, respectively, with $\lambda = 0.1$ and $E^* = 2$ GPa.

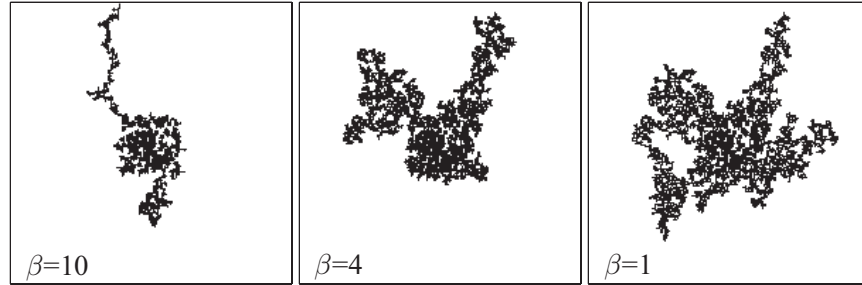


Figure 97: Modes of gas invasion following hydrate dissociation in systems of different permeability, showing a transition from capillary fingering for more permeable media ($\beta = 1$) to fracture opening for less permeable media ($\beta = 10$). In these simulations, we used parameters reflecting slightly lower pore-scale heterogeneity ($\lambda = 0.05$), slightly softer grains ($E^* = 1.85$ GPa) and more concentrated hydrate distribution at the center of the sample than in Fig. 96. Hydrate dissociation in the low-permeability medium (left, $\beta = 10$) leads to the creation and propagation of a fracture.

gas invades with negligible amount of matrix deformation, and the overpressures are constrained by the capillary thresholds. The overpressure may be further limited by geomechanical effects, especially in soft, low-permeability sediments where fracturing is the preferred gas invasion mechanism. Gas invasion by way of fracturing is a mechanism that offers a plausible explanation for massive sediment failure and methane venting by hydrate dissociation.

Capillary fracturing in granular media

The invasion of one fluid into a porous medium filled with another fluid occurs in many natural and industrial processes. These processes include gas venting, hydrocarbon recovery, geologic CO₂ sequestration, and soil wetting and drying. Pore-scale disorder, hydrodynamic instabilities, and mechanical deformation of the pore geometry result in complex displacement patterns. Understanding the emergent patterns is both scientifically fascinating and technologically important [Gollub and Langer, 1999].

Fluid-fluid displacements in rigid porous media have been studied in depth. While many fundamental questions remain, a basic understanding of the different displacement regimes, including compact displacement, capillary fingering, and viscous fingering, has been obtained through laboratory experiments and computer simulations [Lenormand et al., 1988; Wilkinson and Willemsen, 1983; Paterson, 1984; Måløy et al., 1985; Stokes et al., 1986; Chen and Wilkinson, 1985; Yortsos et al., 1997; Ferer et al., 2004; Toussaint et al., 2005]. These regimes depend on the flow velocity, the degree of pore-scale disorder, and the interfacial tension and viscosity contrast between the fluids.

In a deformable medium such as a granular bed, fluid flow can displace the particles and affect the pore geometry, which in turn can affect the flow. This interplay between the displacements of the fluids and the particles leads to a variety of patterns, including desiccation cracks [Meakin, 1991], granular fingers [Cheng et al., 2008], labyrinth structures [Sandnes et al., 2007], stick-slip bubbles [Sandnes et al., 2011], open channels [Kong et al., 2010; Varas et al., 2011] and fractures [Chevalier et al., 2009; Boudreau et al., 2005; Xu et al., 2008; Shin and Santamarina, 2010; Choi et al., 2011; Sandnes et al., 2011].

While fracturing during gas invasion in liquid-saturated media has been observed in several experiments [Chevalier et al., 2009; Boudreau et al., 2005; Xu et al., 2008; Shin and Santamarina, 2010; Choi et al., 2011; Sandnes et al., 2011] and simulations [Jain and Juanes, 2009], the underlying mechanisms and controlling parameters behind the morphodynamics of gas invasion in liquid-filled deformable granular media remain poorly understood. Holtzman and Juanes [Holtzman and Juanes, 2010] developed a model that predicts the transitions among capillary fingering, viscous fingering, and fracturing. The authors used pore-scale simulations and scaling analysis to show that fracturing caused by elastic deformation of particles is the dominant mode of invasion for fine, soft particles under low confining stress. In this Letter, we study fracturing in a system of rigid particles. We show that frictional sliding, rather than elastic deformation, is the key mechanism controlling fracturing. We provide experimental evidence for three displacement regimes—capillary fingering, viscous fingering, and capillary fracturing—and derive two dimensionless groups that govern the transitions among these regimes [Holtzman et al., 2012].

We inject air into a thin bed of water-saturated glass beads packed in a cylindrical cell. We prepare each granular bed by pouring beads into the cell and then vibrating it to increase the packing homogeneity (see Appendix). There are three control parameters: the mean particle diameter, d , the air injection rate, q , and the confining weight, w . The confinement is applied by weights placed on a rigid disk that rests on top of the beads. To allow fluids (but not the particles) to leave the cell, the disk is made slightly smaller than the interior of the cell (inner diameter L), leading to a thin gap along the edge of the cell. We inject the fluids with a syringe pump at a fixed rate to the center of the cell, and image the invasion pattern during the experiment with a digital camera (Fig. 98). To analyze the images, we subtract the initial image prior to injection. For most experimental

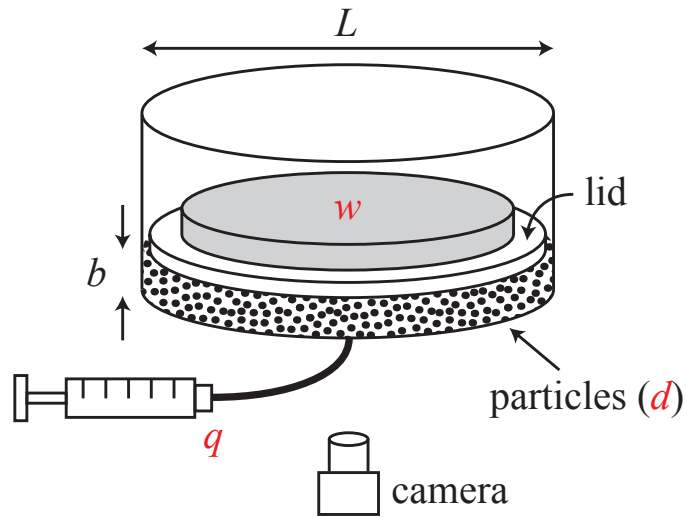


Figure 98: Experimental setup: a thin bed (thickness b) of water-saturated glass beads (mean diameter d) is confined in a cylindrical acrylic cell (internal diameter L). Vertical confinement is supplied by a weight, w , placed on a disk (“lid”) that rests on top of the beads. The disk is slightly smaller than the cell to allow fluids (but not particles) to leave the cell. Air is injected into the center of the cell at a fixed flow rate q . Time-lapse images are captured by a camera placed underneath the cell.

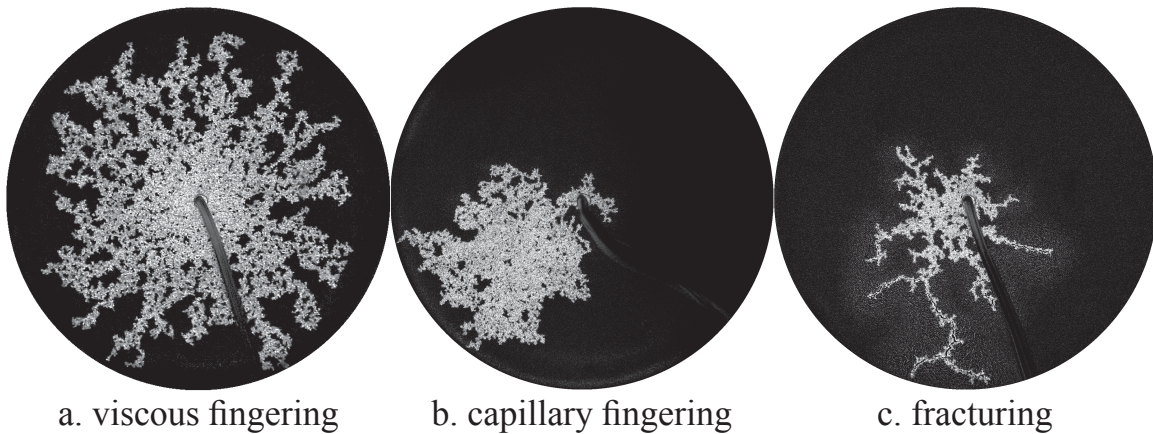


Figure 99: Examples of experimentally-observed patterns. We classify these patterns into three regimes: viscous fingering, capillary fingering, and fracturing. In these difference images, obtained by subtracting the initial image prior to air invasion, air shows as clear white, water and beads as black, and deformed regions as a sparkly halo (bead displacements changes the reflected light). Experimental conditions: $d=360 \mu\text{m}$; $w=181 \text{ N}$ (a, b) and 3 N (c); and $q=100$ (a), 0.1 (b), and 1 mL/min (c).

conditions, we perform repeatability experiments.

The experiments exhibit three displacement regimes: viscous fingering, capillary fingering, and capillary fracturing. We identify the regimes based on the qualitative characteristics of the invasion pattern, as has been done previously [Paterson, 1984; Chen and Wilkinson, 1985; Lenormand et al., 1988; Chevalier et al., 2009; Holtzman and Juanes, 2010]. In viscous fingering, the air-water interface grows continuously and at several locations simultaneously. The resulting pattern is radial and exhibits thin fingers and few trapped water clusters. The pattern appears more space-filling than in 2-D experiments (e.g. in a monolayer of beads [Måløy et al., 1985]) because in 3-D water clusters that appear to be trapped actually remain connected vertically across layers (Fig. 99a). In capillary fingering, the air-water interface propagates intermittently at alternating locations, leading to a pattern that is non-radial, irregular, and patchy, with multiple trapped water clusters (Fig. 99b). In capillary fracturing, the air-water interface advances continuously in thin fingers with long, straight segments. The resulting pattern is asymmetric and occupies a much smaller portion of the cell compared with capillary fingering and viscous fingering. While capillary fracturing exhibits a distinct morphology, we identify it exclusively from visual observation of bead displacements. These displacements appear as “halos” in the subtracted images, caused by changes to light reflection by bead displacements (Fig. 99c). The three regimes display transition zones, in which the invasion patterns exhibit mixed characteristics of the end-member patterns.

The mode of displacement depends on the competition between forces. The transition between capillary fingering and viscous fingering depends on the competition between viscous forces and capillary forces, whereas the transition between fingering and fracturing depends on the competition between hydrodynamic forces that promote pore opening, and mechanical forces that resist it. Since these forces depend on a combination of the control parameters, the same transition between the regimes can be achieved by changing different parameters: the displacement can transition from capillary fingering to viscous fingering by increasing the injection rate, q , or reducing the bead size, d ; and from fingering to fracturing by reducing the confining weight, w , or the bead size, d (Fig. 100). The wide transition zone between capillary and viscous fingering has been observed previously [Lenormand et al., 1988], and is due to gradual changes in the governing forces with the experimental conditions. The capillary fracturing patterns transition from few, small fractures to many, large fractures as the confinement is reduced, though this trend is not conveyed in the plots since our identification of fracturing does not account for the frequency or magnitude of bead displacements. Repetition of experiments with similar conditions yield the same invasion regime, even if the details of the invasion pattern differ.

We rationalize these transitions by computing the ratio between the driving forces that promote the development of a particular pattern. For a rigid medium, the transition between capillary fingering and viscous fingering occurs when the characteristic macroscopic viscous pressure drop in the direction parallel to flow, δp_v , exceeds the variation in capillary entry pressures along the interface, δp_c . We compute δp_v as $\nabla p_v L$, and use Darcy’s law, $\nabla p_v \sim \eta v/k$ with $k \sim d^2$, to obtain $\delta p_v \sim \eta v L/d^2$. Here, η is the dynamic viscosity of water, and $v \sim q/(bd)$ is the flow velocity. We use a fixed value of the macroscopic length scale with $L \gg d$ for the viscous pressure drop in the defending phase, an assumption that is justified during the initial stages of the invasion but that becomes questionable at later stages, when the invasion front approaches the system’s boundaries and becomes fractal [Lenormand, 1989]. The maximum difference in capillary pressures along the interface is $\delta p_c = \gamma/r_{\min} - \gamma/r_{\max} \sim \gamma\chi(\lambda)/\bar{r}$, where γ is the air-water interfacial tension, $\bar{r} \sim d$ is the mean throat aperture, and $\chi(\lambda)$ describes the distribution of throat apertures, a function of the

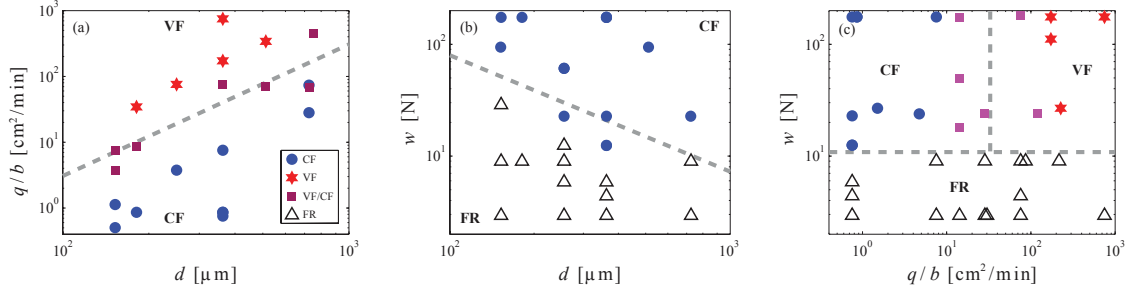


Figure 100: Phase diagrams of fluid-fluid displacement patterns in the experiments. The diagrams demonstrate how changing the control parameters affects the patterns. Diagram (a) shows that the transition from viscous fingering (VF) to capillary fingering (CF) occurs at $q/b \sim d^2$ (fixing $w=181$ N). Intermediate patterns are marked as VF/CF. Diagram (b) shows that the transition from capillary fingering to fracturing (FR) occurs at $w \sim d^{-1}$ ($q=0.1$ mL/min). Diagram (c) shows that the transition from fingering to fracturing is independent of q/b ($d=360$ μm).

degree of pore-scale disorder $\lambda \in (0, 1)$ [Holtzman and Juanes, 2010]. For instance, for a uniform aperture distribution, $r \in [1 - \lambda, 1 + \lambda]\bar{r}$, we get $\chi(\lambda) = \lambda/(1 - \lambda^2)$.

The transition from viscous to capillary fingering occurs when $\delta p_v \sim \delta p_c$, and is therefore controlled by the following “modified capillary number”, $\text{Ca}^* = \delta p_v / \delta p_c$:

$$\text{Ca}^* = \text{Ca} \frac{L}{d} \chi^{-1}(\lambda) = \frac{\eta q L}{\gamma b d^2} \chi^{-1}(\lambda), \quad (48)$$

where $\text{Ca} = \eta v / \gamma$ is the classical capillary number. For a given pair of fluids, the viscosity and interfacial tension are fixed. Assuming similar disorder across experiments, this scaling suggests that the phase boundary between viscous fingering and capillary fingering is $q/b \sim d^2$, in agreement with our experimental data (Fig. 100a).

In a granular medium, fractures open when forces exerted by the fluids exceed the mechanical forces that resist particle rearrangements. In cohesionless granular material, these forces include elastic compression and friction. For systems with densely packed, highly compliant particles, pore opening occurs by means of particle deformation [Holtzman and Juanes, 2010]. However, for many types of particles including most mineral grains and manufactured beads, the high particle stiffness limits interparticle compression, making frictional sliding the dominant deformation mechanism that alters the pore geometry.

To demonstrate this quantitatively, we compare the two characteristic resisting forces. The increment in elastic compressive force associated with a relative particle displacement (interparticle deformation) Δh is $\Delta f_e \sim K \Delta h$, where K is the interparticle contact stiffness. The stiffness $K \sim E \sqrt{d h}$ is computed by assuming Hertzian interparticle forces, $f_e \sim E \sqrt{d h}^{3/2}$, where E is the Young’s modulus of the particle material and h is the total interparticle deformation [Johnson, 1987]. We evaluate K at $h = h_0$, where h_0 is the initial (prior to fracturing) interparticle deformation. We obtain h_0 from the expression for the initial interparticle force, $f_{e,0} \sim E \sqrt{d h_0}^{3/2}$, which, assuming homogenous force distribution, can also be evaluated from the vertical confinement, $f_{e,0} \sim w / (L/d)^2$. Fracturing requires a sufficiently large change in the throat apertures, $\lambda \bar{r} \sim \lambda d$, implying interparticle displacement of $\Delta h \sim \lambda d$. The elastic resisting force is therefore $\Delta f_e = \lambda E^{2/3} L^{-2/3} w^{1/3} d^2$. We compare this force with the frictional resistance force, evaluated

from the limiting value at sliding, $\Delta f_f \sim \mu f_{e,0} \sim \mu w / (L/d)^2$, where μ is the coefficient of friction. The resulting force ratio is then:

$$\frac{\Delta f_e}{\Delta f_f} = \frac{\lambda E^{2/3} L^{4/3}}{\mu w^{2/3}}. \quad (49)$$

For our experimental system, with $E=70$ GPa, $\mu = 0.3$ [Li et al., 2005], $L=0.2$ m, $\lambda=0.75$ and $w=3-181$ N, the elastic resistance is 5–6 orders of magnitude higher than frictional resistance, suggesting that pore opening occurs by overcoming friction. Elasticity would play an important role in fracturing only for much softer beads and much larger confining stresses.

We predict the emergence of fracturing through a dimensionless parameter we call the “fracturing number”, N_f , that measures the system deformability as the ratio of the pressure forces that drives fracturing, Δf_p , and the resisting force, Δf_f . The driving force is the product of the local pressure difference at the front tip, Δp , and the area over which it acts, $A_p \sim d^2$. The pressure difference is the sum of the capillary pressure, γ/d , and the local viscous pressure drop, $\nabla p_v \sim \eta v/d$. Thus, $\Delta f_p = \gamma d + \eta v d = \gamma d(1 + \text{Ca})$, and

$$N_f = \frac{\gamma L^2}{\mu w d} (1 + \text{Ca}). \quad (50)$$

This scaling suggests that, for a given fluid pair, particle material, and system size, the transition from fingering to fracturing occurs at $w \sim d^{-1}$. This is consistent with our observations (Fig. 100b). While the scaling accounts for the effects of both the capillary pressure and the local viscous pressure drop, the capillary pressure is the dominant cause of fracturing in our experiments (with $\eta \approx 10^{-3}$ Pa s, $\gamma \approx 0.07$ N/m, $q \leq 100$ mL/min, and therefore $\text{Ca} \ll 1$). As a result, the observed transition does not depend on the flow rate (Fig. 100c).

The scaling analyses allow us to collapse our data from a three-parameter dimensional phase space (q, w, d) into a two-parameter dimensionless space (Ca^*, N_f). For $N_f \gg 1$, fracturing is the dominant mode of invasion. For $N_f \ll 1$, the medium is essentially rigid (negligible particle rearrangements), and the transition from capillary to viscous fingering occurs at $\text{Ca}^* \approx 1$ (Fig. 101).

These results demonstrate and rationalize the crossover among three regimes of drainage in granular media: capillary fingering, viscous fingering, and capillary fracturing. They show that the crossover between capillary fingering and viscous fingering can be characterized by a modified capillary number, Ca^* . Our results demonstrate the emergence of capillary fracturing, in which capillary forces dilate pore throats by exceeding the internal frictional resistance of the medium. The scaling of the fracturing number [Eq. (50)] suggests that, in granular systems with rigid solid particles, capillary fracturing tends to occur when the particle size falls below a critical value, $d_c \sim \gamma L^2 / \mu w$. This provides a rationale to observations of capillary-induced fracturing in a variety of natural systems, such as drying in granular media [Meakin, 1991; Xu et al., 2008], gas venting in lake sediments [Boudreau et al., 2005; Scandella et al., 2011], and hydrate veins in the ocean floor [Hester and Brewer, 2009]. In all of these settings, the formation of fractures provides open conduits that allow fast exchange of elements, which are likely critical to the water, carbon and energy budgets in the biosphere.

Appendix. Experimental procedure

We begin the experiments by pouring a known volume V of glass beads with mean diameter d into a cylindrical acrylic cell of internal diameter L . To distribute the beads uniformly across the

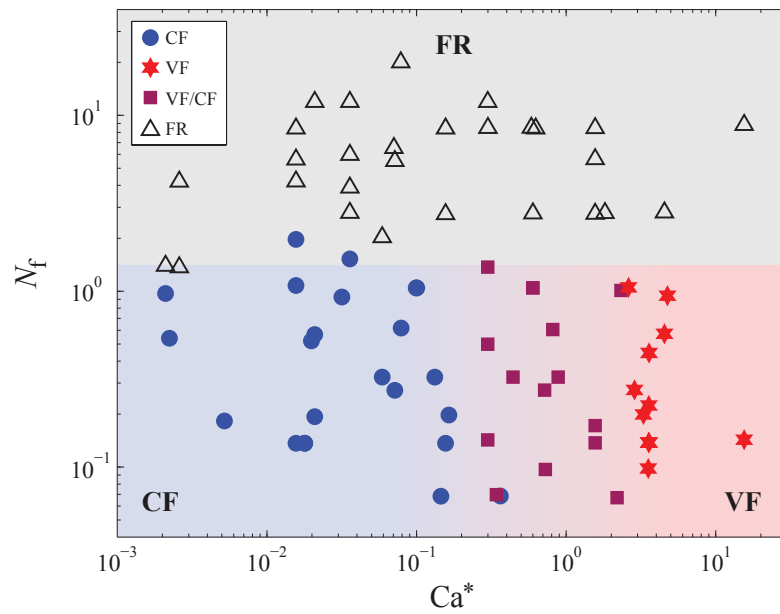


Figure 101: Phase diagram of drainage in granular media, showing three invasion regimes: viscous fingering (VF), capillary fingering (CF), and fracturing (FR). The dashed lines denote the approximate locations of the transitions among regimes. The tendency to fracture is characterized by the “fracturing number” N_f : drainage is dominated by fracturing in systems with $N_f \gg 1$. At lower N_f values, the type of fingering depends on the modified capillary number, Ca^* .

cell and homogenize the packing, we vibrate the cell by tapping on it in the horizontal direction in two rounds: first with no confinement, and then after placing an acrylic disk (the “lid” in Fig. 1, weighing 0.3 kg) on top of the beads. After tapping, the bed is a few layers thick with approximate thickness $b = V/(\pi L^2/4)$. To saturate the bed, we place weights (18.5 kg total mass including the lid) on top of the lid and then inject water at a constant rate into the center of the cell with a syringe pump. We inject at a sufficiently high rate to avoid trapping of air, but at a sufficiently low rate to avoid displacing the beads. After the bed is saturated, we load the desired weight w onto the lid and inject air at a constant rate q . To observe the invasion pattern, we illuminate the bottom of the cell with reflected light from LED panels and take images with a digital camera.

Creating a mechanically and hydraulically homogeneous packing—with uniform distribution of interparticle forces and pore apertures—is an extremely difficult task. We evaluate the hydraulic homogeneity by observing the invasion front of the water during the initial saturation step: a radially symmetric, circular invasion front indicates that the permeability field is homogeneous in the cross-radial (θ) direction. We infer that a symmetric, circular front also indicates permeability homogeneity in the radial direction. We further infer that a bed that is hydraulically homogeneous is also mechanically homogeneous. We reject experiments for which the invasion pattern during water injection is not circular.

To investigate the reproducibility of our results, we perform repeatability experiments for most of the experimental conditions. For a given condition, the invasion patterns in the experiments differ in the details—since our packing procedure does not create a perfectly homogeneous or reproducible bed—but always fall in the same regime.

A conduit dilation model of methane venting from lake sediments

Introduction

Atmospheric methane (CH_4) concentrations have risen steadily over the past two centuries, following an anthropogenically-driven trend that is similar to that for carbon dioxide [IPCC, 2007]. Global warming is in turn affecting natural methane emissions, particularly in the largely land-covered Northern latitudes where newly-produced methane is often emitted directly to the atmosphere through an intervening (oxidizing) biofilter [Rudd et al., 1974], accessing carbon long sequestered from the global carbon cycle [Walter et al., 2006; Archer et al., 2009]. Ebullition of methane from sediments in lakes, the deep ocean, wetlands, and estuaries is a primary means for emitting methane to the ocean-atmosphere system [Walter et al., 2006; Solomon et al., 2009; Shakhova et al., 2010; Greinert et al., 2010; Bastviken et al., 2011].

Past studies have made fundamental contributions to understanding the life cycle of methane in sediments including microbial methane production, bubble growth and migration within sediments, emission at the sediment-water interface, and bubble rise, dissolution and oxidation in the water column [Martens and Klump, 1980; Valentine et al., 2001; Judd et al., 2002; Rehder et al., 2002; Heeschen et al., 2003; Boudreau et al., 2005; Leifer and Boles, 2005; McGinnis et al., 2006; Greinert et al., 2010]. The importance of methane gas in limnetic environments has also been long recognized [Fechner-Levy and Hemond, 1996], and evidence is mounting that transport of methane in the gaseous phase dominates dissolved transport both within lake sediments and once methane reaches the water column [Crill et al., 1988; Keller and Stallard, 1994; Walter et al., 2006; Delontro et al., 2010; Bastviken et al., 2011]. The magnitude of the atmospheric release—the portion of bubbles not dissolved during rise through the water column—depends on the mode and spatiotemporal character of venting from sediments [Leifer et al., 2006; Gong et al., 2009], so models of methane transport in the sediment column must reproduce the spatiotemporal signatures of free-gas release from the underlying sediments to correctly predict the fraction that by-passes dissolution and reaches the atmosphere.

Here, we introduce a quantitative model of methane production, migration and release from fine-grained sediments. We constrain and test the model against a record of variations in hydrostatic load and methane ebullition from fine-grained sediments in Upper Mystic Lake (UML), a dimictic kettle lake outside Boston, Massachusetts [Varadharajan et al., 2010] (Figure 102a). Our model is motivated by two key observations: ebullition is triggered by variations in hydrostatic load [Martens and Klump, 1980; Mattson and Likens, 1990; Fechner-Levy and Hemond, 1996; Leifer and Boles, 2005; Varadharajan et al., 2010], and gas migration in fine sediments is controlled by the opening of fractures or conduits [Boudreau et al., 2005; Jain and Juanes, 2009; Algar and Boudreau, 2010; Holtzman and Juanes, 2010]. The high degree of synchronicity in ebullitive fluxes among distant venting sites located at different depths (Figure 102) suggests that the release mechanism is governed by the effective stress, which is the average stress between solid grains [Terzaghi, 1943]. We propose that gas bubbles escape by dilating conduits upward to the sediment surface as falling hydrostatic pressure reduces the compressive effective stress below the effective tensile strength of the sediments. This model of “breathing” conduits for gas release couples continuum-scale poromechanics theory with multiphase flow in porous media to capture the

episodicity and variable rates of ebullition. The ability of the model to match the flux record from UML, as well as the direct observation of episodic gas venting (Figure 102c), suggests that this mechanism indeed controls ebullition from lake sediments.

Model Formulation

Methane is generated in anoxic lake sediments by microbial decomposition of organic matter, and the generation rate depends on organic carbon availability, reduction-oxidation potential, and temperature. Once the total pressure of all the dissolved gases exceeds the hydrostatic pressure, any additional gas exsolves into a bubble. Gas bubbles—often mostly comprised of methane—grow, coalesce, and are transported vertically through the sediment until they are released into the water column. Gas is buoyant with respect to the surrounding water filling the pore space, but mobilization of gas bubbles in a rigid, fine-grained porous medium requires connected gas bubbles of very large vertical dimension [Hunt et al., 1988], $L_v \approx \frac{2\gamma}{(\rho_w - \rho_g)gr_t}$, where γ is the interfacial tension, ρ_w and ρ_g are the water and gas densities, respectively, g is the gravitational acceleration, and r_t is the pore throat radius, which is of the order of one-tenth of the particle radius. For a typical value of $\gamma \sim 0.070$ N/m, and a conservative value of the particle diameter at UML, $d_g \sim 10$ μm , we estimate that a connected bubble height $L_v \sim 30$ m would be required to overcome capillary effects. This is three orders of magnitude larger than observed bubble sizes [Martens and Klump, 1980; Sills et al., 1991; Boudreau et al., 2005], clearly indicating that capillary invasion in a rigid medium cannot explain methane venting, and that methane release must involve sediment deformation. A drop in hydrostatic load on the sediments lowers the compressive sediment stress and provides an opportunity for buoyant bubbles to overcome their confinement and expand by deforming the sediments. However, theoretical analysis shows that spherical bubbles of realistic size would be mobilized in sediments with reasonable shear strength only under unrealistically large vertical stress variations on the order 10 m of water head [Wheeler, 1990]. The ebullition record from UML [Varadharajan et al., 2010], however, shows gas venting in response to head drops of less than 0.5 m (5 kPa, Figure 102b), which implies that some other mechanism must mobilize bubbles for vertical transport.

The observation that bubbles in clayey sediments grow in a highly-eccentric, cornflake-shaped fracture pattern [Boudreau et al., 2005; Algar and Boudreau, 2010], rather than as spherical bubbles, suggests that this mode of growth may also allow for vertical mobility. The relevance of this transport mechanism in fine-grained sediments is supported by micromechanical models of gas invasion in water-filled porous media [Jain and Juanes, 2009; Holtzman and Juanes, 2010]. Following these observations, we hypothesize that the dilation of near-vertical conduits is the primary mechanism controlling free-gas flow and release from lake sediments. Instead of modelling the rise of individual bubbles through sediment, we propose that gas cavity expansion dilates a vertical conduit for free gas flow to the sediment surface (Figure 103). Since the flow conductance of these conduits is several orders of magnitude larger than that of undisturbed sediments, we assume that bubble release is much faster than the daily timescale resolved here, and in the model implementation we evacuate gas instantaneously from the entire depth range of the open conduit. We have confirmed that the flux records using this simplification are nearly identical to those from more detailed simulations that assume Darcy flow of gas through the conduits [Scandella, 2010].

Flow conduits dilate in response to changes in effective stress, σ' , which is the average stress carried by the solid skeleton and is the primary determinant of deformation [Terzaghi, 1943]. When

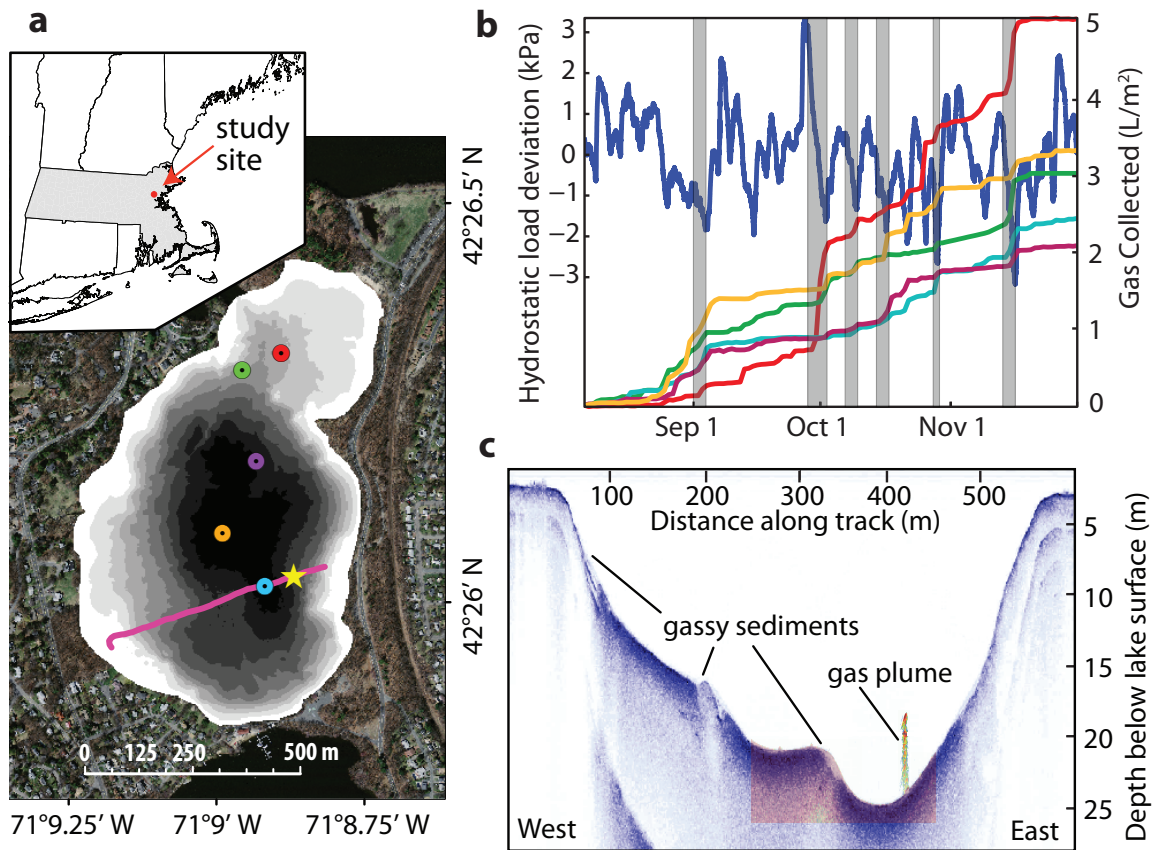


Figure 102: Spatially- and temporally-concentrated ebullition from lake sediments in response to hydrostatic pressure drops. (a) Location of Upper Mystic Lake (inset, Massachusetts shaded) and bathymetry at 2.5-m shaded intervals superposed on an aerial photomosaic. Colored circles mark bubble trap locations that produced the data shown in (b), and the profile shown in (c) was collected along the pink transect, with the star marking the gas plume location. (b) Record of hydrostatic load variations (left axis, blue curve) and cumulative gas collected (right axis) from early August through November 2008. The flux records from individual traps are highly synchronous, especially during periods of pronounced drop in hydrostatic head, denoted by grey bars. (c) Acoustic sub-bottom profile across UML (blue), where lighter shading indicates reduced reflectivity associated with gassy areas near the sediment surface. Overlain is a sonar image showing a bubble plume rising ~ 5 m from the sediments, following a drop in hydrostatic pressure in December 2009.

two fluid phases are present, the effective stress is a function of both fluid pressures [Coussy, 1995], but a series of experiments on fine, gassy sediments suggests that the overall deformation depends primarily on the total (vertical) stress and gas pressure alone [Sills et al., 1991]. This is consistent with the view that sediment and water form a coherent “mud” phase, where gas bubbles have a characteristic size much larger than the pore size [Sills et al., 1991; Boudreau et al., 2005]. Thus, we approximate the effective stress in gassy sediments as:

$$\sigma' = \sigma - P_g, \quad (51)$$

where σ is the total vertical stress—the sum of integrated bulk sediment weight and hydrostatic load—and P_g is the gas pressure. In soft, cohesive sediments, the ratio of lateral to vertical effective stress is often around one, so vertical and horizontal stresses are roughly equal. Conduits dilate when the effective stress at a particular depth becomes negative and matches the magnitude of the effective tensile strength, T .

A drop in hydrostatic load may reduce σ' to this cohesive yield limit and initiate bubble transport to the sediment surface. While the total stress is forced by changes in hydrostatic load, the gas pressure evolves in response to compression and dilation of gas cavities within a plastic, incompressible matrix of sediment and water. Therefore, two separate mechanisms are at play: cavity deformation and conduit opening. Cavity deformation changes the gas pressure and volume whenever the effective stress reaches tensile or cohesive limits. The conduits, however, open only at the tensile limit. The gas generation rate is assumed to be constant and to increase the bubble volume only. Thus, changes in gas pressure occur only in response to changes in hydrostatic load. Specifically, the gas cavities maintain their pressure until the effective stress in the surrounding matrix reaches a plastic yield limit [Coussy, 1995] under compression (C) during hydrostatic loading, or tension (T) during hydrostatic unloading,

$$-T(z) \leq \sigma'(z, t) \leq C(z), \quad (52)$$

where both $T(z)$ and $C(z)$ are assumed to increase linearly with depth from a zero value at the sediment surface, reflecting that sediment strength increases with the degree of compaction (Figure 103). Experiments confirm that the compression of gas cavities is a plastic process, in which compressed cavities do not expand upon subsequent unloading [Sills et al., 1991] (see Figure S1 of the auxiliary material). When the effective stress reaches either yield limit, the gas pressure changes during dilation or contraction to keep the effective stress within these bounds, and gas volume variations are calculated using the ideal gas law. Because gas conduits dilate at the tensile yield limit, these changes in gas pressure and volume impact the timing and magnitude of gas release from each depth interval.

The model of plastic cavity evolution and release through dynamic conduits is designed to capture the average gas venting behavior from a representative area (such as an entire lake), rather than to simulate the detailed dynamics of a single venting site. The model was run for a period of four months from an initial gas-free state, and the simulated lake-surface fluxes were compared against data from UML, which were collected near the lake surface using bubble traps (Figure 102a). Each surface-buoyed bubble trap—an inverted funnel connected to a PVC pipe that collects a column of free gas—continuously records the buoyant force from the gas as a proxy for the column height, which allows estimation of the rate at which gas enters the funnel [Varadharajan et al., 2010]. The dynamics of bubble dissolution during rise through the water column are complex [Rehder et al.,

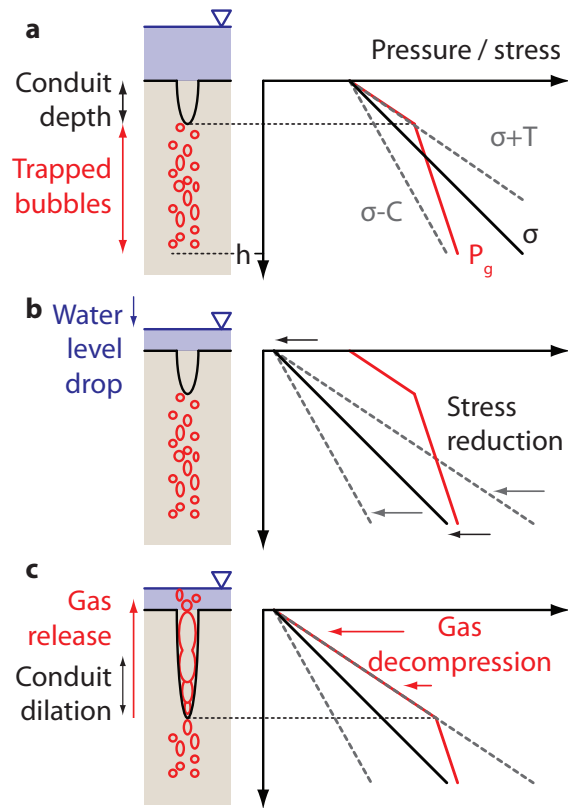


Figure 103: Model response to water level drop. (a) Initial condition: the cartoon at left shows the lake level (blue) above a sediment column with gas bubbles trapped below the open conduit depth and down to the active bubble generation depth, h (not to scale). The conduit opens to the surface from the greatest depth where the effective stress, $\sigma' = \sigma - P_g$, falls to its tensile limit, $-T$. The stress and pressure profiles at right show that this occurs when P_g (red solid line) equals $\sigma + T$ (gray dashed line). (b) A drop in hydrostatic load reduces σ throughout the sediment column. (c) Plastic cavity dilation allows shallow gas bubbles to decompress to $\sigma + T$. The conduit opens from the deepest location where $\sigma' = -T$ and releases the formerly trapped bubbles. In the case of a hydrostatic load increase (not shown), the stress rises, and the cavity compression mechanism pressurizes gas bubbles to enforce $\sigma' \leq C$, or equivalently $P_g \geq \sigma - C$. The effective stress would nowhere equal its tensile limit, and the conduit would close completely.

2002; McGinnis et al., 2006; Gong et al., 2009], and beyond the scope of this sediment-centric study. Here, we assume that volume fluxes at the sediment and lake surfaces are proportional, and the season-averaged release from the model is scaled to the season-averaged flux from the lake-surface trap data, averaged over all traps. Although the assumption of proportional fluxes at the lake bottom and lake surface is clearly an approximation (water depths at the bubble traps vary between 9 and 25 m), it is justified given the uncertainty in sensing the spatially heterogeneous surface flux using only five, randomly placed bubble traps. The assumption of constant methane generation rate is also a simplification, but it is well justified for our four-month venting record given the anoxic conditions through the measurement period and the near-sediment water temperature of $\sim 4^\circ\text{C}$ in all measurements [Varadharajan, 2009].

Results

We applied our model to study the dynamics of methane venting at UML during a period of ~ 120 days over which gas flux was recorded (Figure 104). Because the seasonally-integrated model flux is scaled to match the cumulative gas collected by the five traps, the overall magnitude of the model flux has little significance. The timing and *relative* magnitudes of the venting events, however, are characteristics that our model predicts given the input hydrostatic pressure variations and a single, dimensionless parameter. These characteristics of the data are clearly well-reproduced, suggesting that the model captures the essential dynamics of methane ebullition.

The distribution of ebullition in time is controlled by three physical quantities: the generation zone depth, h , and the vertical gradients in tensile and compressive strength, dT/dz and dC/dz , respectively. These variables, however, do not act independently. The amount of gas released following a given drop in hydrostatic load depends on the depth to which the flow conduit dilates, and the drop required at a given depth depends on the total sediment strength, the sum of T and C . The appropriate dimensionless parameter characterizing the balance of total sediment strength and hydrostatic load variations is the *ebullition number*,

$$N_e = \frac{h(dT/dz + dC/dz)}{\Delta P_h}, \quad (53)$$

which defines the drop in hydrostatic load, normalized by an arbitrary characteristic variation ΔP_h , required to evacuate the entire active generation zone. Alternatively, N_e^{-1} defines the fraction of the active zone evacuated by a characteristic drop in hydrostatic load, ΔP_h . The value of the ebullition number, N_e , must be obtained by calibration of the model response to flux data. Taking ΔP_h as the standard deviation of nearly normally-distributed hydrostatic pressure inputs, ~ 1 kPa, the best model fit for UML is obtained with $N_e = 5$. Smaller values of N_e in the model result in methane being released in response to smaller hydrostatic variations, and predictions that are less sensitive to extreme pressure drops—the model flux signal is composed of more frequent, smaller peaks. Larger values of N_e in the model cause gas stored deep in the sediment column to remain trapped during the smallest hydrostatic drops; this trapped gas is released more vigorously but less frequently during the largest pressure drops (see Figure S2 of the auxiliary material).

Discussion and Conclusion

We have shown that the timing and distribution of flux magnitudes predicted by our single-parameter model match the flux data, averaged over 5 traps (Figure 104). However, the methane venting signals from individual traps are composed of fewer, more vigorous events because not all venting sites activate strictly simultaneously (Figure 102b). The single parameter, called the ebullition number, controls the venting episodicity and reflects the balance between hydrostatic pressure forcing and sediment strength. The model calibration of the ebullition number ($N_e = 5$) is more representative for the average flux of the system, and larger values of N_e are required to capture the dynamics of individual venting sites.

Our mechanistic model of methane transport captures the dynamics of ebullition by coupling the plastic evolution of trapped gas bubbles with their release through dynamic flow conduits. Reproducing these dynamics is important not only to understand how gas escapes the sediments into the water column, but also to understand the subsequent dissolution and atmospheric release [Leifer et al., 2006; McGinnis et al., 2006; Gong et al., 2009; Greinert et al., 2010]. The same mechanisms likely control gas release from fine, methane-bearing sediments under other surface water bodies, including marine sediments controlled by tides [Martens and Klump, 1980] or swell [Leifer and Boles, 2005], and the model could be extended to systems where the methane source pressurizes gas sufficiently to drive the episodic releases [Tryon et al., 2002]. Our model lays the groundwork for integrated modelling of methane transport in the sediment and water column, linking estimates of methane generation [Price and Sowers, 2004] with models of water column dissolution [Leifer et al., 2006; McGinnis et al., 2006] to constrain the global methane release from lakes, wetlands, estuaries and shallow continental margins.

Appendix A. Methods Summary

Ebullition measurements.

The ebullition data were collected using surface-buoyed bubble traps, which funnel rising methane bubbles into a column and measure the gas volume collected with a temperature-corrected pressure sensor at the top. A pressure sensor fixed relative to the lake bottom measured the total hydrostatic load. Both gas flux and hydrostatic load data were recorded at 5-minute resolution and smoothed using a 1-hour moving average filter to remove noise from surface waves [Varadharajan et al., 2010].

Geophysical surveys.

Acoustic imagery was acquired in December 2009 using an Edgetech 424 Chirp fish towed ~30 cm below the lake's surface and operating at 4 to 24 kHz with 4 ms sampling. Acoustic data and GPS navigation were recorded in real-time in SEG Y files, and two-way travel time to depth conversion was accomplished using freshwater sound velocity of 1472 m/s. The superposed water column image of a methane plume was simultaneously captured using the 83 kHz mode of a Humminbird 798ci fishfinder with built-in GPS. The bathymetric data shown in Figure 102a were gridded in ESRI ArcMap software using lake bottom depths picked from Chirp data acquired during 3 surveys in 2009 and 2010, as well as depths independently recorded by the fishfinder in October 2010.

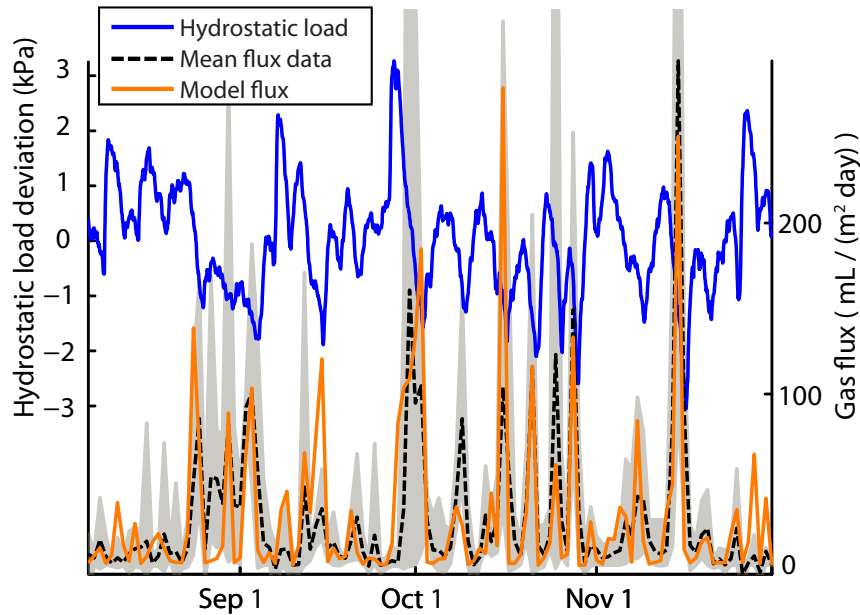


Figure 104: Best fit of model gas ebullition fluxes to data from Upper Mystic Lake. The left axis and solid blue line show a time series of the hydrostatic load forcing, and the right axis shows the methane fluxes from the mean bubble trap data (black, dashed) and model (orange, solid). The gray shaded area indicates the range of flux values from the five traps; note that in four instances the range extends above the limit of the vertical axis up to a value of ~ 700 mL/m²/day. The fluxes are binned daily, and the cumulative model release is constrained to match the data. The calibrated value of the ebullition number, $N_e = 5$, reflects that a hydrostatic pressure drop of about 5 standard deviations (5 kPa in this case) is required to evacuate the methane from the entire active generation depth, h (equation (3)). The single-parameter model accurately predicts the timing of large flux events and usually their magnitude, as well.

Numerical methods.

We solved the model equations numerically to evolve the gas pressure and gas saturation (fraction of the pore volume occupied by gas), in each depth interval in response to variations in the hydrostatic load at the surface. We discretized the equations in space using a second-order finite volume scheme with linear reconstruction and a central limiter to ensure monotonicity. Time integration was performed using second-order Runge-Kutta method, following the poromechanical evolutions in a staggered manner. The numerical grid was the same for poromechanics and flow, with 64 control volumes in the vertical direction. Both the cm-scale vertical resolution and hourly time-step were fine enough that the results are insensitive to further refinement [Scandella, 2010].

Numerical modeling of hydrate formation and methane gas transport through dynamic conduits

Introduction

The dissociation of methane hydrates in shallow ocean sediments has long been suggested as a potential feedback to climate change [Dickens et al., 1995; Judd et al., 2002; Archer et al., 2009]. One of the primary modes of methane export from submerged sediments is free-gas ebullition, but gas bubbles dissolve during rise, exposing the methane to oxidation to the less potent greenhouse gas CO₂ [Valentine et al., 2001]. The ability of rising bubbles to transport methane to the atmosphere depends on the release depth, bubble density and size distribution [Leitch and Baines, 1989; Greinert and Nutz, 2004; Leifer et al., 2006; McGinnis et al., 2006; Gong et al., 2009]. Thus, the atmospheric release depends not only on how much hydrate dissociates but how it is released from the sediments.

Focused ebullition has been observed at Hydrate Ridge, especially in a periodic pattern during low tides [Torres et al., 2002]. The gas is likely supplied from a deep geologic reservoir, but the mechanism that allows it to travel through the Hydrate Stability Zone (HSZ) from near the base of the HSZ (BHSZ) and to escape only during low tides has yet to be determined. Multiple mechanisms have been proposed for coexistence of free gas and hydrates in the HSZ [Milkov and Xu, 2005; Torres et al., 2005; Ruppel et al., 2005]: (1) regional geotherms, (2) reduction in hydrate stability by salt accumulation, (3) kinetics of hydrate formation, and (4) fast, focused flow of free gas through high-permeability conduits. Evidence of fractures and flow through them at Hydrate Ridge has been inferred from field observations [Torres et al., 2002; Flemings et al., 2003; Trehu et al., 2004a; Weinberger and Brown, 2006] and modeling studies [Liu and Flemings, 2007; Daigle and Dugan, 2010].

The combined observations of tidally-controlled ebullition with evidence of gas flow through conduits gives us an opportunity to investigate the mechanisms controlling gas migration through the hydrate stability zone. Previous modeling work has sought to estimate the distribution of hydrates by considering methane transport in the dissolved phase only [Xu and Ruppel, 1999; Buffett and Archer, 2004; Daigle and Dugan, 2010] or as gas flowing by capillary invasion [Liu and Flemings, 2007; Garg et al., 2008; Reagan and Moridis, 2009; Daigle and Dugan, 2010]. These models capture slow processes of pore water flow, heat and salt transport to capture important impacts on hydrate stability and the equilibrium distribution of hydrates [Kowalsky and Moridis, 2007]. Other models have been used to estimate the hydrate response to slow sea level change [Liu and Flemings, 2009] and the onset time for fracturing [Liu and Flemings, 2007; Daigle and Dugan, 2010].

In contrast, we model fast processes of free-gas flow through fractures, tidal variations, and kinetic hydrate formation. Previous modeling of gas release from hydrate-free lake sediments has shown that conduit flow can reproduce the observed, hydrostatically-forced episodicity of gas venting [Scandella et al., 2011], and we hypothesize that a similar mechanism controls tidally-forced venting from hydrate-bearing sediments. Here, we develop a numerical model of this mechanism and show that it can indeed reproduce the tidally-dependent ebullition record observed at Hydrate Ridge. In addition, we find that within a tidal low the ebullition will manifest as distinct bursts that arise from a geyser-like instability. The ability of gas to traverse the HSZ depends on the vertical

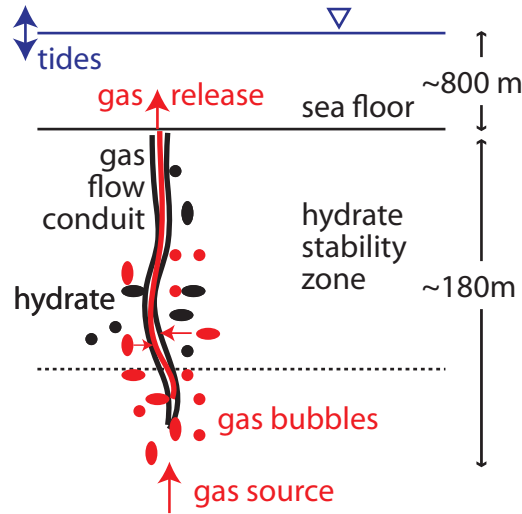


Figure 105: Conceptual model of gas flowing through the hydrate stability zone by dilating near-vertical conduits. These conduits access gas in a small domain of surrounding porous media, especially through conductive horizontal strata [Weinberger and Brown, 2006], and transport the gas vertically. Vertical dimensions reflect the south summit of Hydrate Ridge, where tidally-forced ebullition has been observed [Torres et al., 2002].

gas conductivity and kinetic hydrate formation rate.

Theory, Formulation and Methods

Model domain

We investigate the dynamics of gas flow through the hydrate stability zone with a one-dimensional, continuum-scale numerical model. The model attempts to capture the aggregate behavior of sediments fractured periodically in space. Because the model is 1D, the transport and accumulation reflect the vertical flow through the fractures as well as the fluid exchange between the fracture and the sediment matrix.

The model is intended to resolve the release of methane at sub-tidal timescales (minutes to hours). At this timescale, fast transport mechanisms such as gas-phase flow are expected to dominate pore-fluid solute advection and diffusion. Thus, we neglect the accumulation and transport of dissolved methane, salt, and heat, with hydrate formation and aqueous flow. These mechanisms control the hydrate distribution by changing the local hydrate stability conditions [Bhatnagar et al., 2007; Liu and Flemings, 2007; Garg et al., 2008; Liu and Flemings, 2009; Daigle and Dugan, 2010] and thus the long-term hydrate distribution. In turn, hydrate formation can influence the transport regime by cementing the grains [Waite et al., 2009; Klar et al., 2010] or clogging the pores [Nimblett and Ruppel, 2003; Liu and Flemings, 2007; Daigle and Dugan, 2010]. We neglect these slow feedback mechanism to develop a simple continuum model of fast gas flow through conduits that respond to both internal pressurization and a tidal forcing.

Poromechanics

Gas behaves differently in fine-grained sediments, such as the clay-dominated sediments found in the HSZ at Hydrate Ridge [Trehu et al., 2004a], compared with coarse-grained sediments. Gas invades large-grained porous media when the capillary pressure ($P_g - P_w$) becomes large enough for the curved interface to squeeze through a pore throat. In fine-grained sediments, gas invades by deforming the grains because the capillary pressure required to squeeze through the throats is prohibitively large [Jain and Juanes, 2009]. Instead of small interstitial bubbles characteristic of a capillary-controlled system, gas bubbles in fine sediments take the form relatively large gas cavities surrounded by a matrix of water and sediment grains [Sills et al., 1991]. Because these bubbles grow in a highly-eccentric, cornflake-shaped fracture pattern [Boudreau et al., 2005; Algar and Boudreau, 2010], rather than as spherical bubbles, this mode of growth may also allow for vertical mobility.

The effective stress, σ' , controlling the deformation of this continuum around the gas cavities may then be approximated as,

$$\sigma' = \sigma_h - P_g, \quad (54)$$

where σ_h is the horizontal stress and P_g is the gas pressure [Scandella et al., 2011]. This contrasts with the typical form of the effective stress, in which the fluid pressure of concern is the water pressure [Terzaghi, 1943; Daigle and Dugan, 2010] or when both fluid pressures are considered [Bishop, 1959; Klar et al., 2010]. Equation 54 is consistent with the view that sediment and water form a coherent “mud” phase against which large gas bubbles must push to expand.

The deformation of this matrix-water continuum may be treated as a plastic process that occurs at yield limits in tension (σ_T) and compression (σ_C):

$$-\sigma_T \leq \sigma' \leq \sigma_C. \quad (55)$$

Cavities dilate in tension ($\sigma' = -\sigma_T$), reducing the gas pressure sufficiently to maintain the plastic equilibrium defined in Equation 55. In compression ($\sigma' = \sigma_C$), the cavities shrink and the gas pressure rises in step with the horizontal stress. This mechanism of cavity deformation is used to attribute accumulation of gas mass to changes in pressure and volume, in the following order as necessary:

1. Generate maximum gas pressure change at current volume, up to a plastic yield limit

$$\Delta P_g^{max} = \frac{\Delta M_g RT}{S_g \phi m_{CH_4}}. \quad (56)$$

2. If a yield limit is reached, deform cavities to change volume. Vary saturation at the new fixed gas pressure, according to the ideal gas law, up to a maximum that satisfies the volume constraints $S_g + S_h \leq 1$ and $S_g \geq S_g^{min}$.
3. If a volume constraint is reached, allow pressure to rise or fall outside the plastic limits ($\sigma_h - \sigma_C \leq P_g \leq \sigma_h + \sigma_T$) at the new fixed saturation according to the ideal gas law.

Thus, gas accumulation first forces the gas pressure to a yield limit before changing the gas saturation. This allows for compressible gas flow but requires a small time step to resolve frequent pressure changes.

In all simulations here we assume $\sigma_C = 0$ and $\sigma_T = 0.3$ MPa, consistent with estimates from combined modeling and field observations at South Hydrate Ridge [Weinberger and Brown, 2006]. The gas pressure may exceed the plastic yield limits, especially when hydrate formation depletes the gas to a minimum saturation (for stability) $S_g^{min} = 0.005$. However, this does not occur in any of the simulations shown here.

Gas flow through conduits

The core of our model is free-gas flow through dynamic, vertical conduits. These conduits dilate at the tensile plastic yield limit and close at the compressive limit (Figure 106). In addition to the dependence on effective stress, we impose a minimum gas saturation, $S_g^{conduit} = 0.1$, which is required for the conduits to connect across depth intervals [Weinberger and Brown, 2006]. Similar model behavior is obtained when $S_g^{conduit} = 0$, except the low gas saturations exacerbate the gas pressure fluctuations during cavity deformation (Equation 56), and resolving these larger pressure swings requires a smaller time step.

The model captures gas flow through fractured porous media without distinguishing the pools of gas in the conduit and porous medium separately. Instead, the effect of dilation is captured by increasing the vertical intrinsic permeability, k , from 0 to a parameterized permeability of the conduit-matrix continuum, $k_{conduit}$, which accounts for both the dimensions and lateral spacing of conduits. The gas mass conservation equation uses a multiphase extended form of Darcy's law for the gas flux [Muskat, 1949]:

$$\partial_t(\phi\rho_g S_g) = -\partial_z F_g + Q_g^h \quad (57)$$

$$F_g = -\rho_g \frac{k k_{rg}}{\mu_g} (\partial_z P_g - \rho_g g) \quad (58)$$

$$k_{rg} = S_g \quad (59)$$

where Q_g^h is the rate of gas mass generation from hydrate per unit volume and constitutes all the gas loss from hydrate dissociation, Q_h :

$$Q_g^h = -\chi_h^{CH_4} Q_h \quad (60)$$

The model is initially free of hydrate but includes gas saturations equal to the minimum for conduit opening, $S_g^{conduit}$, in order to eliminate the initial time necessary to accumulate this minimum saturation. The gas pressure, however, is assumed to begin at the compressive yield limit so that the conduit is initially closed everywhere. At the top boundary the gas pressure equals the tidally-forced hydrostatic pressure, with $S_g = 0$, and the gas flux in the bottom is set by the parameter F_g^{source} , which represents the source supplied through Horizon A at the BHSZ [Trehu et al., 2004a; Weinberger and Brown, 2006].

Hydrate formation and dissociation

Given the high temporal resolution of the model (seconds to minutes), a kinetic model of hydrate formation was adopted following [Kim et al., 1987]. The model for microscale hydrate formation is driven by the departure from equilibrium fugacity, and we simplify this by considering the nearly-equivalent departure from equilibrium pressure [Duan et al., 1992]. We also adopt the same

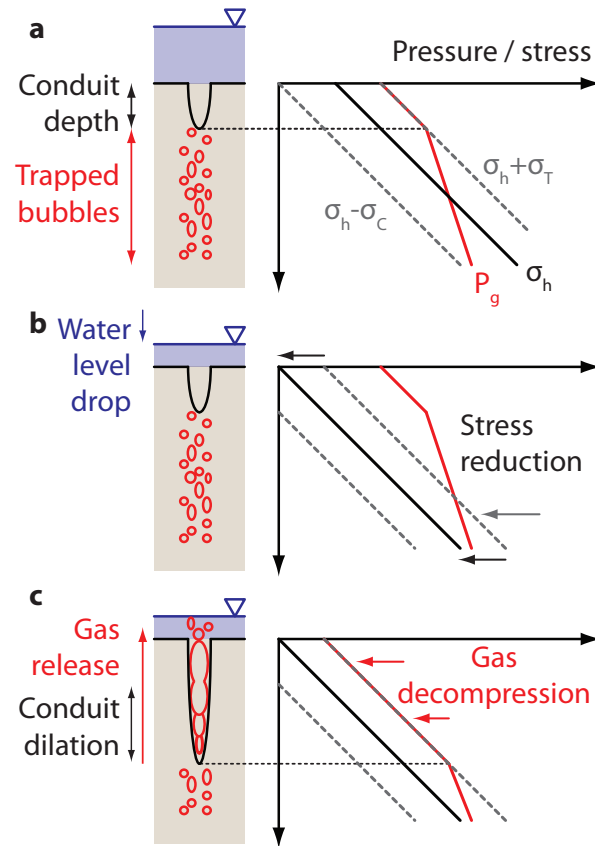


Figure 106: Model response to water level drop. (a) Initial condition: the cartoon at left shows the water level (blue) above a sediment column with gas bubbles trapped below the open conduit (not to scale in vertical). The conduit opens when the effective stress, $\sigma' = \sigma_h - P_g$, falls to its tensile yield limit, $-\sigma_T$. The stress and pressure profiles at right show that this occurs when P_g (red solid line) equals $\sigma_h + \sigma_T$ (gray dashed line). (b) A drop in hydrostatic load reduces σ_h throughout the sediment column. (c) Plastic cavity dilation allows shallow gas bubbles to decompress to $\sigma + \sigma_T$. The conduit opens from the deepest location where $\sigma' = -\sigma_T$ and releases the formerly trapped bubbles. In the case of a hydrostatic load increase (not shown), the stress rises, and the cavity compression mechanism pressurizes gas bubbles to enforce $\sigma' \leq \sigma_C$, or equivalently $P_g \geq \sigma_h - \sigma_C$. On open conduit remains open until this compressive limit is reached. Modified from [Scandella et al., 2011].

temperature dependence but neglect the dependence on surface area of hydrate [Kim et al., 1987]. The rate of hydrate mass generation per bulk volume is:

$$Q_h = K_h(P_g - P_{eq}) \exp\left(-\frac{E}{RT}\right), \quad (61)$$

where K_h is a rate constant with units of $\text{kg/m}^3/\text{Pa/s}$, $E = 8.1 \times 10^4 \text{ J/mol}$ is the activation energy of the reaction, $R = 8.314 \text{ J/mol/K}$ is the gas constant. This model transfers mass of CH_4 from the gas to hydrate phases when $P_g > P_{eq}$, in the hydrate stability zone, and it transfers mass in the other direction when $P_g < P_{eq}$, generally below the hydrate stability zone. The equilibrium pressure is evaluated as the hydrate-gas phase boundary, $P_{eq}[\text{kPa}] = \exp(40.234 - 8860/T[\text{K}])$ [Kwon et al., 2006], for a temperature profile from a seafloor temperature of 277 K and constant geothermal gradient of 0.053 K/m at Hydrate Ridge [Daigle and Dugan, 2010]. This causes hydrate to form slightly below the traditional BHSZ, defined as $P_w = P_{eq}$, because $P_g \geq P_w$ when free gas is present. Whenever either phase is depleted or when the sum of gas and hydrate saturations exceeds 1, the rate of transfer is reduced to avoid unphysical mass transfer.

Tidal forcing

Impact on vertical stress. A central goal of our model is to capture the observed relationship between tides and ebullition from hydrate-bearing sediments [Torres et al., 2002], and the link is made through the impact of hydrostatic pressure on total and effective stresses. The total vertical (lithostatic) stress, σ_v , is the sum of the hydrostatic pressure at the sea floor and the integrated bulk density:

$$\sigma_v(z, t) = P_h(t) + \int_0^z \rho_b(z') g dz' \quad (62)$$

$$P_h(t) = \rho_w g \left(D + z_{tide} * \sin\left(\frac{2\pi t}{t_{tide}}\right) \right), \quad (63)$$

where ρ_b is the bulk density, P_h is the hydrostatic pressure at the seafloor, z_{tide} and t_{tide} are the tidal amplitude and period, respectively. These equations simply show that tidal variations reflect the total vertical stress throughout the HSZ.

Lateral and vertical stresses. The total vertical stress varies with tides as shown above, but near-vertical conduits should in the direction where the gas opposes the minimum stress, which is generally horizontal near the crest of south Hydrate Ridge [Weinberger and Brown, 2006]. We calculate the horizontal stress that would be imposed on the model domain by the surrounding, water-saturated sediments. The vertical and lateral stresses are connected through the water-saturated effective stresses by the lateral stress coefficient, K_0 . In water-saturated rock and soil, K_0 may be expressed as

$$K_0 = \frac{\sigma'_{hw}}{\sigma'_{vw}} = \frac{\nu}{1 - \nu}, \quad (64)$$

where $\sigma'_{hw} = \sigma_h - P_w$ and $\sigma'_{vw} = \sigma_v - P_w$ are the water-saturated effective stresses, and ν is Poisson's ratio [Wang, 2000]. We adopt $\nu = 3/7 \rightarrow K_0 = 0.75$ and for our system [Thomas,

1987]. Estimating the horizontal stress from the vertical stress requires both the lateral stress coefficient and water pressure:

$$\sigma_h = \sigma'_{hw} + P_w = K_0\sigma_v + (1 - K_0)P_w \quad (65)$$

The water pressure response on short timescales and deep in sediments is undrained, where the fluid pressurization with laterally-uniform variations in vertical stress is determined by the loading efficiency, $\lambda = \partial P_w / \partial \sigma_v$ [Wang, 2000]. For the water-saturated sediments surrounding the model domain, we assume $\lambda = 1$ [Liu and Flemings, 2009], and therefore that the water pressure changes synchronously and in the same amount as vertical stress.

Combined model

During each time step, the mechanisms are applied in a staggered manner:

1. Impose hydrostatic forcing.
2. Determine where conduits open and close to impose permeability profile.
3. Flow gas through the open conduits.
4. Exchange mass between gas and hydrate phases.
5. Deform cavities, altering P_g and S_g , to plastic equilibrium in response to the hydrostatic forcing and the mass accumulation combined from flow and phase transfer.

Results

Episodicity of gas release at the seafloor

We perform a base-case scenario designed to reproduce the general pattern of ebullition during tidal lows for conditions observed at the southern summit of Hydrate Ridge [Torres et al., 2002]. The parameter values used for this base scenario are $D = 800$ m, $H = 180$ m, $z_{tide} = 1$ m, $t_{tide} = 12$ hours, $k_{conduit} = 2 \times 10^{-14}$ m², $K_h = 100$ kg/m³/Pa/s, $F_g^{source} = 10^{-4}$ kg/m²/s, $\sigma_T = 0.3 \times 10^6$ Pa, and $S_g^{conduit} = 0.1$. Under these conditions gas indeed traverses the HSZ and escapes during falling tides (Figure 107).

The time for gas to traverse the HSZ may be estimated using the multiphase Darcy flux (Equation 58):

$$t_{flow} \sim \frac{z_{BHSZ} \mu_g \phi}{k_{conduit} \rho_b g}, \quad (66)$$

where the characteristic gas pressure gradient has been approximated by a characteristic value relative to the lithostatic gradient, $\rho_b g$. The model predicts that gas typically accumulates beneath the sediment surface until the hydrostatic pressure falls with tides (Figure 108) and the tensile plastic deformation at the surface allows gas to escape into the water column. After an initial peak in gas flux, the ebullition continues at a moderate rate until the near-surface gas is depleted or the tides begin to rise again and cause the conduits to close (Figure 107).

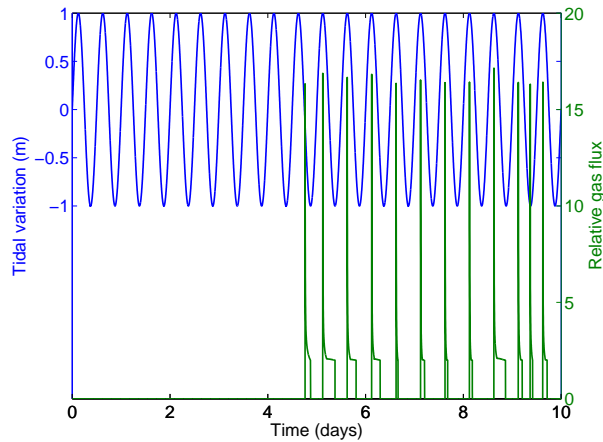


Figure 107: Periodic venting of gas (green, right scale) at the seafloor in response to 1 m tidal signal (blue, left scale). Gas flux is normalized by the input flux at the bottom of the model, F_g^{source} . The delay before the initial release reflects the timescale for gas to build up pressure and traverse the HSZ. The strong peak leading each release reflects a buildup of pressure just below the seafloor that is released during plastic tensile opening of the gas flow conduit at the surface, after which the gas pressure drive is reduced. Gas vents only during falling tides.

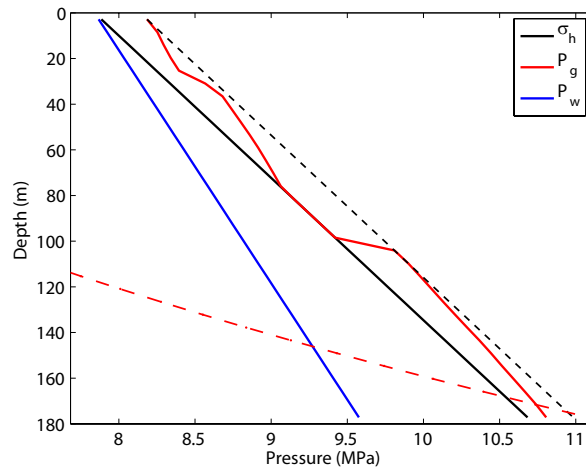


Figure 108: Profile of pressures and stresses at the end of the base simulation. The horizontal stress, gas and water pressures appear as solid lines of black, red and blue, respectively. The tensile limit on gas pressure, $\sigma_h + \sigma_T$, is shown as a dotted black line, and the equilibrium gas pressure, P_{eq} is a red dashed curve. The region from 0 – 80 mbsf is a connected gas plume where the conduit remains open because $P_g > \sigma_h - \sigma_C$. This plume is separated from the other rising plume, from 100 – 180 mbsf, by a region where the gas pressure has fallen to the compressive yield limit and the conduit has closed.

Timescales of flow through dynamic conduits. Even without a tidal forcing or hydrate formation, compressible gas flow through a system of dynamic conduits displays two primary time scales at steady state: the release time for a connected gas plume, and the duration of an individual ebullition event. Each rising gas plume, displayed as a region of gas pressure elevated above the horizontal stress and the conduit remains open (Figure 108), may reach the sediment surface and escape over a time period on the order of 1 day (Figure 109, top). This release time scales as

$$t_{plume} \sim t_{flow} \frac{h_{plume}}{z_{BHSZ}}, \quad (67)$$

where h_{plume} is the height of a rising gas plume. This height depends on the ratio of gas influx from below (F_g^{source}) and the vertical conductivity and may be estimated as

$$h_{plume} \sim t_{flow} \frac{F_g^{source}}{M_g^0}, \quad (68)$$

where M_g^0 is the initial mass of gas per unit bulk volume. This equation yields an estimate of ~ 130 m for the base simulation and agrees well with the observed heights of ~ 100 m in Figure 108.

However, a plume is not necessarily released in a continuous event. The release of methane gas from the top of the sediment column locally reduces the gas pressure and can close the conduit before the underlying gas plume is depleted. This geyser-like instability releases a rising gas plume as multiple separate ebullition events (Figure 109, bottom).

Interaction of flow with tides and hydrates. The inherent episodicity of gas release through conduits is complicated by the influence of tides and hydrate formation. The relatively slow release of a connected plume may be broken up into individual releases as falling tides facilitate conduit opening by reducing the hydrostatic load and total stress (Equation 62 and Figure 110, top). The release during a single cycle may then be further divided by the geyser instability (Figure 110, bottom).

Hydrate formation simultaneously reduces the gas pressure and closes the conduits more quickly, which delays the arrival at the surface, reduces the total output of gas, and changes the fine-scale episodicity of gas release (Figure 111).

Gas survival through the HSZ

The amount of methane that traverses the HSZ depends on the relative rates of gas flow and conversion to hydrate. The time required for gas to traverse the HSZ is estimated from Equation 66, although the flow timescale itself depends on the rate of hydrate formation because hydrate formation tends to close the conduits or prevent their opening by reducing the gas pressure. The flow timescale should be compared with the timescale for hydrate formation, which may be estimated from Equation 61 as the time required to consume the initial gas at its initial pressure:

$$t_{hydrate} \approx \frac{M_g^0 / \chi_{CH_4}^h}{K_h (P_g - P_{eq}) \exp(-E/(RT))}, \quad (69)$$

where $\chi_{CH_4}^h$ is the mass fraction of methane in hydrates. Because the initial pressure and temperature profiles are not spatially uniform, $t_{hydrate}$ is estimated as the average over all depth intervals.

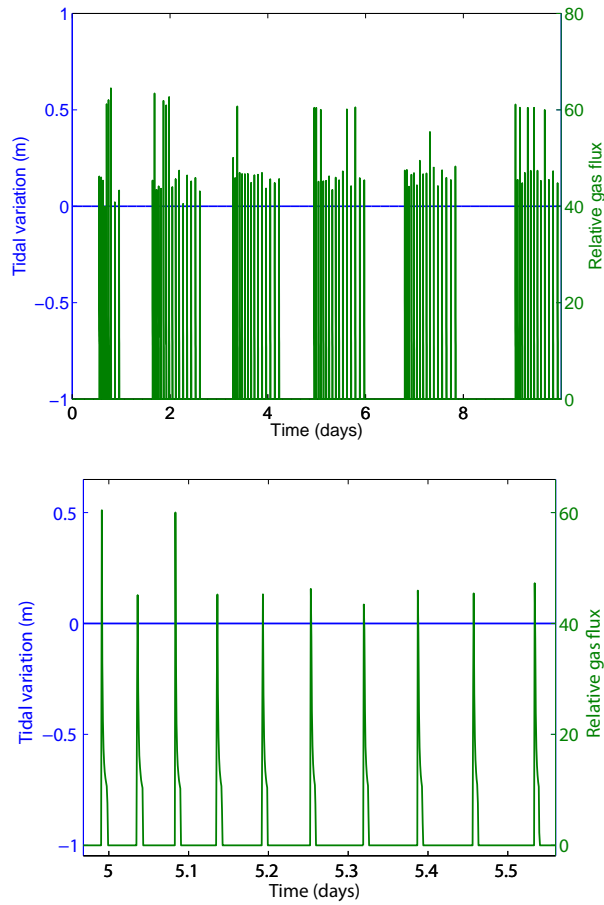


Figure 109: Time series showing an internally-driven run with no tidal forcing. The top figure shows two timescales relevant to the release: a longer timescale created by the rise of connected gas plumes, which vent for and are separated by about a day, and a shorter timescale of discrete ebullition events. The zoomed bottom figure shows that these releases are separated by about 1/20 day.

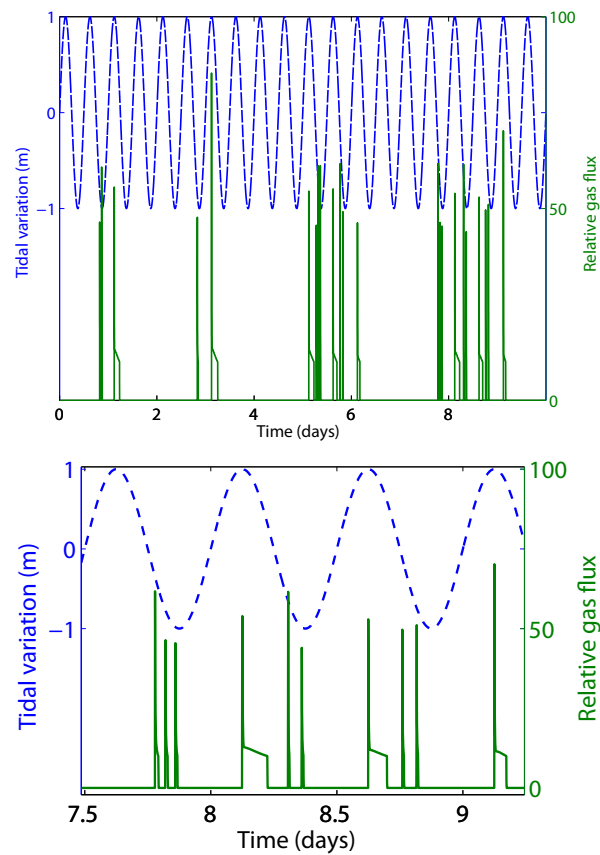


Figure 110: Impact of combined internal and external forcings on gas flow without hydrate formation. Top: time series showing the long timescale of plume release of ~ 2 days (days 1,3, 5, and 8) along with other effects within each plume release. Bottom: zoom of the top figure shows that, within a given plume release, the individual ebullition events occur only during falling tides and display different geyser-driven episodicity depending on the pressure and saturation conditions in the near-surface sediments.

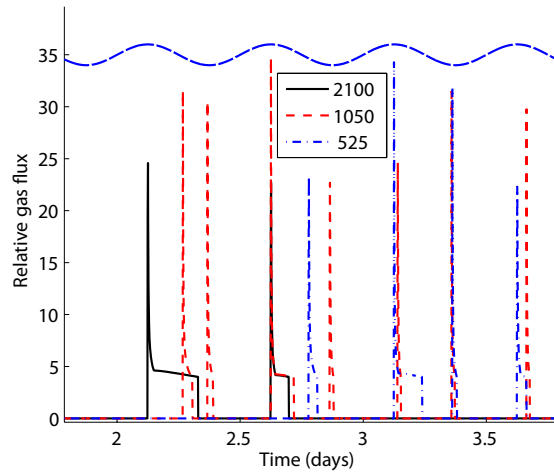


Figure 111: Sensitivity of venting timeseries to rate of hydrate formation. In all cases, $k_{conduit} = 5 \times 10^{-14} \text{ m}^2$, $z_{tide} = 1 \text{ m}$ (blue dashed sinusoid centered on 35 on the vertical axis), and K_h is varied to control the ratio $t_{hydrate}/t_{flow}$, shown in the legend. Smaller values of $t_{hydrate}/t_{flow}$ relate to faster hydrate conversion and both delay the first ebullition event and reduce the total gas vented to the ocean and (see Figure 112).

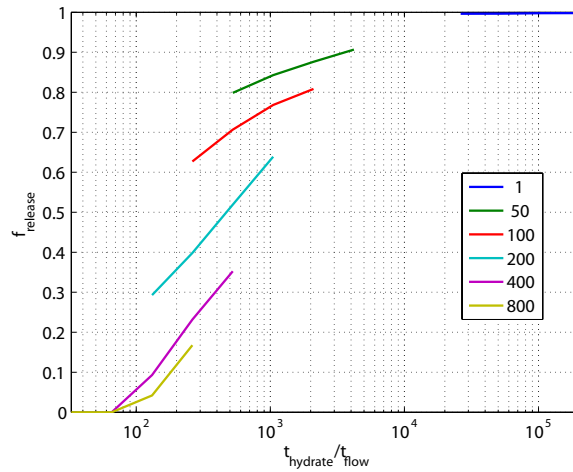


Figure 112: Sensitivity of gas release to rates of gas flow and hydrate formation. The fraction of gas that escapes without conversion to hydrate, $f_{release}$, increases as the timescale of hydrate formation increases relative to the timescale of flow. The timescale ratio $t_{hydrate}/t_{flow}$ was varied using both $k_{conduit}$ and K_h . The legend shows particular values of K_h , and the discontinuities show that the release fraction is somewhat dependent on $t_{hydrate}$ independently of $t_{hydrate}/t_{flow}$.

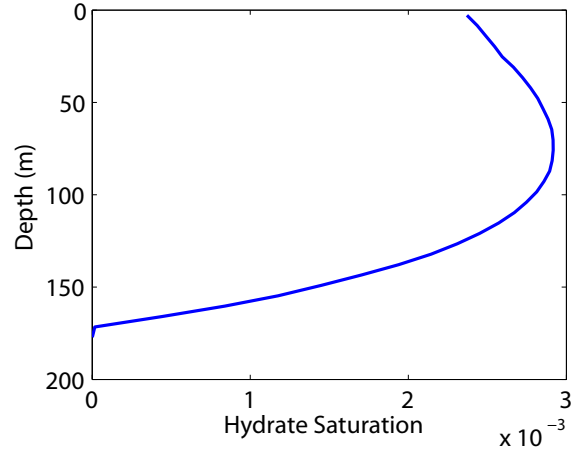


Figure 113: Final hydrate saturation profile for the same conditions as in Figure 107 after 10 days.

We quantify the fraction of methane flowing through the model that reaches the ocean by tracking these fluxes over the course of a given simulation. If the time period is long enough to reach pseudo-steady state conditions, changes in the methane storage become small relative to the cumulative fluxes into and out of the system. In this case, the ability of methane to escape to the sediment surface may be estimated as the ratio of time-integrated fluxes across the top and bottom of the model. However, the poorly-constrained initial gas content of the system motivates us to account for the change in *gas* storage over the time period:

$$\Delta M_g = \int_0^H (M_g(z, t_f) - M_g(z, t = 0)) dz \quad (70)$$

$$f_{\text{release}} \approx \frac{\int_0^{t_f} F(z = 0, t) dt}{\int_0^{t_f} F(z = H, t) dt - \Delta M_g}, \quad (71)$$

where $M_g = \rho_g S_g \phi$ is the mass of accumulated gas per volume. This release fraction is highly sensitive to the ratio of flow and hydrate timescales, and it also depends on the hydrate generation rate (Figure 112).

Vertical hydrate distribution

Hydrate formation increases the saturation of hydrate, but the assumed formation rates are slow and cause little to appear during the course of simulations here. A profile of hydrate saturation shows this growth throughout the HSZ (Figure 113). The distribution reflects the balance of the driving force, $P_g - P_{eq}$, which increases upwards (Figure 108), against the temperature-dependent term, which increases about threefold downward from the water column to the BHSZ. Hydrate may form or dissociate based on Equation 61, but because the HSZ is always populated with gas for these simulations, $P_g \geq P_{eq}$ in this region and hydrate only forms and never dissociates.

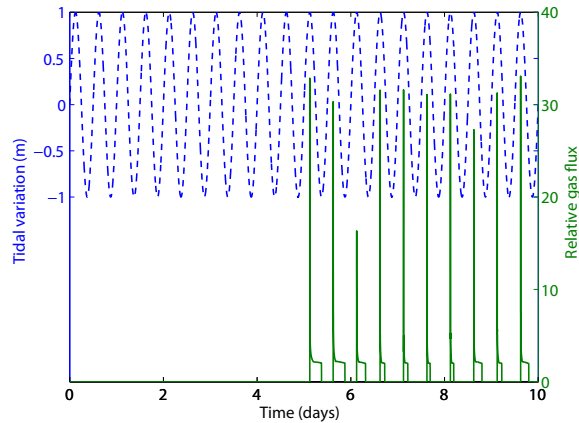


Figure 114: Spatial discretization sensitivity with $n_z = 64$ and $dz = 2.8$ m, compared with $n_z = 32$ and $dz = 5.6$ m in Figure 107. Increasing the spatial discretization causes the initial peaks in gas release to be larger due to the stronger gas pressure gradient between the top cell and seafloor. In both these cases, the finite volume interface permeabilities were estimated from the cell values using a moving average filter with enough cells to cover a width of 10 m.

Numerical techniques

The flow Equations (57–59) are discretized in space using a finite volume method with first-order upwinding and integrated in time using a forward Euler scheme. The model is sensitive to the spatial discretization because of the nonlinear relationship between permeability and effective stress through conduit dilation. This means that the gas pressure gradients which build up at the top of the sediment column are larger for finer discretization, and hence the driving force for gas flow is stronger and the initial peak in ebullition is larger (compare Figures 107 and 114).

The model timestep is chosen dynamically to keep the magnitude of gas pressure changes from flow and hydrate formation small compared with the sediment strength. This condition is strict enough that the results do not change when a smaller timestep is imposed.

Discussion and Conclusions

The model developed here shows that free gas flow through dynamic conduits is a potential mechanism by which tides trigger ebullition from hydrate-bearing sediments at South Hydrate Ridge [Torres et al., 2002] (Figure 107). Although the model neglects spatial heterogeneity and processes that control the long-term dynamics of hydrate-bearing sediments, its ability to balance free-gas flow through dynamic conduits against conversion to hydrates allows us to identify emergent behavior and the relevant temporal and spatial scales that may control venting at the seafloor. For example, the tidal forcing imposes gas-flux periodicity on the release of connected gas plumes that rise through the HSZ, and within a tidal ebb the release may break into multiple bursts as the flow conduit opens and closes near the surface, in a mechanism reminiscent of fluid expulsion from a geyser.

This fraction of injected gas that escapes conversion to hydrate is sensitive to the timescales of fluid flow and hydrate formation. More gas escapes conversion to hydrate when the ratio

$t_{hydrate}/t_{flow}$ is larger, but even at a given value of this ratio, faster hydrate formation causes less gas to survive the rise (Figure 112). We suggest the explanation that gas rises more slowly as the hydrate formation rate increases because hydrate formation reduces the gas pressure and delays conduit opening. As the time for gas to rise increases, a corrected ratio $t_{hydrate}/t_{flow}$ would be smaller, and the lines might coincide better in Figure 112.

A number of neglected mechanisms impact the efficiency of gas transport and hydrate formation assumed by our model. The transport and accumulation of heat and dissolved methane and salt all tend to inhibit gas flow and hydrate formation and dissociation. Gas and hydrate are only stable when surrounded by methane-saturated pore water, and background aqueous flow flushes away concentrated methane, dissolving gas and hydrates. Our model overestimates the efficiencies of both vertical gas transport and mass transfer from gas to hydrate phases. Meanwhile, salt expulsion from pore water and heat generation during hydrate formation reduce hydrate stability, providing negative feedbacks on hydrate generation.

Given that neither gas flow nor hydrate formation in our model depends on the presence of hydrates, the current model is not an ideal tool for speculating on the impact of gas flow on the vertical hydrate distribution. Future models may be made sensitive to hydrates by considering increased tensile strength [Waite et al., 2009; Klar et al., 2010] or pore clogging [Nimblett and Ruppel, 2003; Liu and Flemings, 2007; Daigle and Dugan, 2010] with hydrate formation, as well as a dependence of the hydrate formation rate on the available hydrate surface area [Kim et al., 1987]. Such models may test the stability of hydrate distributions suggested by models that capture long-timescale effects in the presence gas flow through fractures.

References for Fracturing Dominated Behavior

- E. Aker, K. J. Måløy, and A. Hansen. Simulating temporal evolution of pressure in two-phase flow in porous media. *Phys. Rev. E*, 58(2):2217–2226, 1998.
- C. K. Algar and B. P. Boudreau. Stability of bubbles in a linear elastic medium: Implications for bubble growth in marine sediments. *J. Geophys. Res.*, 115:F03012, 2010.
- A. L. Anderson, F. Abegg, J. A. Hawkins, M. E. Duncan, and A. P. Lyons. Bubble populations and acoustic interaction with the gassy floor of Eckernförde Bay. *Cont. Shelf Res.*, 18:1807–1838, 1998.
- A. L. Anderson and L. D. Hampton. Acoustics of gas-bearing sediments. 1. Background. *J. Acoust. Soc. Am.*, 67(6):1865–1889, 1980.
- T. L. Anderson. *Fracture Mechanics: Fundamentals and Applications*. CRC Press, Boca Raton, Florida, 1991.
- D. Archer, B. Buffett, and V. Brovkin. Ocean methane hydrates as a slow tipping point in the global carbon cycle. *Proc. Natl. Acad. Sci. U.S.A.*, 106(49):20596–20601, 2009.
- D. Bastviken, L. J. Tranvik, J. A. Downing, P. M. Crill, and A. Enrich-Prast. Freshwater methane emissions offset the continental carbon sink. *Science*, 331(6013):50, 2011.
- J. Behseresht, Y. Peng, M. Prodanovic, S. L. Bryant, A. K. Jain, and R. Juanes. Mechanisms by which methane gas and methane hydrate coexist in ocean sediments. In *Offshore Technology Conference*, Houston, TX, May 5–8, 2008. (OTC 19332).
- A. I. Best, M. D. Richardson, B. P. Boudreau, A. G. Judd, I. Leifer, A. P. Lyons, C. S. Martens, D. L. Orange, and S. J. Wheeler. Shallow seabed methane gas could pose coastal hazard. *Eos Trans. AGU*, 87(22):213,217, May 2006.
- G. Bhatnagar, W. G. Chapman., G. R. Dickens, B. Dugan, and G. J. Hirasaki. Generalization of gas hydrate distribution and saturation in marine sediments by scaling of thermodynamic and transport processes. *Am. J. Sci.*, 307(6):861–900, 2007.
- M. A. Biot. General theory of three-dimensional consolidation. *J. Appl. Phys.*, 12(155–164), 1941.
- R. B. Bird, W. E. Stewart, and E. N. Lightfoot. *Transport Phenomena*. John Wiley and Sons, New York, 1960.
- A. W. Bishop. The principle of effective stress. *Teknisk Ukeblad*, 39:859–863, 1959.
- M. Blunt and P. King. Macroscopic parameters from simulations of pore scale flow. *Phys. Rev. A*, 42(8):4780–4787, 1990.
- R. Boswell. Is gas hydrate energy within reach? *Science*, 325(5943):957–958, 2009.

- B. P. Boudreau, C. Algar, B. D. Johnson, I. Croudace, A. Reed, Y. Furukawa, K. M. Dorgan, P. A. Jumars, and A. S. Grader. Bubble growth and rise in soft sediments. *Geology*, 33(6):517–520, doi:10.1130/G21259.1, 2005.
- M. S. Bruno. Micromechanics of stress-induced permeability anisotropy and damage in sedimentary rocks. *Mech. Mater.*, 18:31–48, 1994.
- M. S. Bruno and R. B. Nelson. Microstructural analysis of the inelastic behavior of sedimentary rock. *Mech. Mater.*, 12(2):95–118, 1991.
- B. Buffett and D. Archer. Global inventory of methane clathrate: sensitivity to changes in the deep ocean. *Earth Planet. Sci. Lett.*, 227:185–199, 2004.
- J.-D. Chen and D. Wilkinson. Pore-scale viscous fingering in porous media. *Phys. Rev. Lett.*, 55(18):1892–1895, 1985.
- X. Cheng, L. Xu, A. Patterson, H. M. Jaeger, and S. R. Nagel. Towards the zero-surface-tension limit in granular fingering instability. *Nature Phys.*, 4(3):234–237, 2008.
- C. Chevalier, A. Lindner, M. Leroux, and E. Clement. The instability of slow, immiscible, viscous liquid-liquid displacements in permeable media. *J. Non-Newton. Fluid.*, 158:63–72, 2009.
- G. C. Cho and J. C. Santamarina. Unsaturated particulate materials—Particle-level studies. *J. Geotech. Geoenviron. Eng.*, 127(1):84–96, 2001.
- J.-H. Choi, Y. Seol, R. Boswell, and R. Juanes. X-ray computed-tomography imaging of gas migration in water-saturated sediments: from capillary invasion to conduit opening. *Geophys. Res. Lett.*, 38:L17310, doi:10.1029/2011GL048513, 2011.
- M. Clark and P. R. Bishnoi. Determination of activation energy and intrinsic rate constant of methane gas hydrate decomposition. *Can. J. Chem. Eng.*, 79(1):143–147, doi=10.1002/cjce.5450790122, 2001.
- T. Collett, M. Riedel, J. Cochran, R. Boswell, J. Presley, P. Kumar, A. Sathe, A. Sethi, M. Lall, V. Sibal, and the NGHP Expedition 01 Scientists, editors. *Indian National Gas Hydrate Program Expedition 01 Initial Reports*, New Delhi, India, 2008. Indian Directorate General of Hydrocarbons.
- B. K. Cook, D. R. Noble, and J. R. Williams. A direct simulation method for particle-fluid systems. *Eng. Comput.*, 21(2–4):151–168, 2004.
- O. Coussy. *Mechanics of Porous Media*. John Wiley & Sons, Chichester, England, 1995. Originally published in French as *Mécanique des Milieux Poreux*, Editions Technip, 1991.
- J. Crank. *Mathematics of Diffusion*. Oxford University Press, second edition, 1975. (First edition, 1956).
- P. M. Crill, K. B. Bartlett, J. O. Wilson, D. I. Sebacher, R. C. Harriss, J. M. Melack, S. Macintyre, L. Lesack, and L. Smithmorrill. Tropospheric methane from an Amazonian floodplane lake. *J. Geophys. Res.*, 93(D2):1564–1570, 1988.

- P. A. Cundall and O. D. L. Strack. Discrete numerical model for granular assemblies. *Geotechnique*, 29:47–65, 1979.
- H. Daigle and B. Dugan. Origin and evolution of fracture-hosted methane hydrate deposits. *J. Geophys. Res.*, 115:B11103, doi:10.1029/2010JB007492, 2010.
- P. G. de Gennes. Wetting: statics and dynamics. *Rev. Mod. Phys.*, 57:827–863, 1985.
- T. Delsontro, D. F. McGinnis, S. Sobek, I. Ostrovsky, and B. Wehrli. Extreme methane emissions from a Swiss hydropower reservoir: Contribution from bubbling sediments. *Environ. Sci. Technol.*, 44(7):2419–2425, 2010.
- G. R. Dickens. Rethinking the global carbon cycle with a large, dynamic and microbially mediated gas hydrate capacitor. *Earth Planet. Sci. Lett.*, 213:169–183, 2003.
- G. R. Dickens, J. R. O’Neil, D. K. Rea, and R. M. Owen. Dissociation of oceanic methane hydrate as a cause of the carbon isotope excursion at the end of the Paleocene. *Paleoceanography*, 10(6):965–971, 1995.
- G. R. Dickens, C. K. Paull, and P. Wallace. Direct measurement of in situ methane quantities in a large gas-hydrate reservoir. *Nature*, 385:426–428, 1997.
- Z. H. Duan, N. Møller, and J. H. Weare. An equation of state for the CH₄-CO₂-H₂O system: I. Pure systems from 0 to 1000°C and 0 to 8000 bar. *Geochim. Cosmochim. Acta*, 56(7):2605–2617, 1992.
- E. J. Fechner-Levy and H. F. Hemond. Trapped methane volume and potential effects on methane ebullition in a northern peatland. *Limnol. Oceanogr.*, 41(7):1375–1383, 1996.
- M. Ferer, C. Ji, G. S. Bromhal, J. Cook, G. Ahmadi, and D. H. Smith. Crossover from capillary fingering to viscous fingering for immiscible unstable flow: Experiment and modeling. *Phys. Rev. E*, 70:016303, 2004.
- P. B. Flemings, X. Liu, and W. J. Winters. Critical pressure and multiphase flow in Blake Ridge gas hydrates. *Geology*, 31(12):1057–1060, 2003.
- L. Furuberg, K. J. Måløy, and J. Feder. Intermittent behavior in slow drainage. *Phys. Rev. E*, 53(1):966–977, 1996.
- S. K. Garg, J. W. Pritchett, A. Katoh, K. Baba, and T. Fujii. A mathematical model for the formation and dissociation of methane hydrates in the marine environment. *J. Geophys. Res.*, 113(B1):10.1029/2006JB004768, 2008.
- G. D. Ginsburg and V. A. Soloviev. Methane migration within the submarine gas-hydrate stability zone under deep-water conditions. *Mar. Geol.*, 137:49–57, 1997.
- D. Goldberg, T. Takahashi, and A. L. Slagle. Carbon dioxide sequestration in deep-sea basalt. *Proc. Natl. Acad. Sci. U.S.A.*, 105:9920–9925, 2008.

- J. P. Gollub and J. S. Langer. Pattern formation in nonequilibrium physics. *Rev. Mod. Phys.*, 71: S396–S403, 1999.
- X. Gong, S. Takagi, and Y. Matsumoto. The effect of bubble-induced liquid flow on mass transfer in bubble plumes. *Int. J. Multiphase Flow*, 35:155–162, 2009.
- A. R. Gorman, W. S. Holbrook, M. J. Hornbach, K. L. Hackwith, D. Lizarralde, and I. Pecher. Migration of methane gas through the hydrate stability zone in a low-flux hydrate province. *Geology*, 30(4):327–330, 2002.
- J. Greinert, D. F. McGinnis, L. Naudts, P. Linke, and M. De Batist. Atmospheric methane flux from bubbling seeps: Spatially extrapolated quantification from a Black Sea shelf area. *J. Geophys. Res.*, 115:C01002, 2010.
- J. Greinert and B. Nutz. Hydroacoustic experiments to establish a method for the determination of methane bubble fluxes at cold seeps. *Geo-Mar. Lett.*, 24(2):75–85, 2004.
- W. B. Haines. Studies in the physical properties of soils. V. The hysteresis effect in capillary properties, and the modes of moisture redistribution associated therewith. *J. Agr. Sci.*, 20:97–116, 1930.
- K. U. Heeschen, R. W. Collier, M. A. de Angelis, E. Suess, G. Rehder, P. Linke, and G. P. Klinkhammer. Methane sources, distributions, and fluxes from cold vent sites at Hydrate Ridge, Cascadia Margin. *Glob. Biogeochem. Cycle*, 19(2):GB2016, 2005.
- K. U. Heeschen, H. J. Hohnberg, M. Haeckel, F. Abegg, M. Drews, and G. Bohrmann. In situ hydrocarbon concentrations from pressurized cores in surface sediments, Northern Gulf of Mexico. *Mar. Chem.*, 107:498–515, 2007.
- K. U. Heeschen, A. M. Trehu, R. W. Collier, E. Suess, and G. Rehder. Distribution and height of methane bubble plumes on the Cascadia Margin characterized by acoustic imaging. *Geophys. Res. Lett.*, 30(12):1643, doi:10.1029/2003GL016974, 2003.
- K. C. Hester and P. G. Brewer. Clathrate hydrates in nature. *Annu. Rev. Mar. Sci.*, 1(1):303–327, 2009.
- W. S. Holbrook, H. Hoskins, W. T. Wood, R. A. Stephen, and D. Lizarralde. Methane hydrate and free gas on the Blake Ridge from vertical seismic profiling. *Science*, 273:1840–1842, September 27, 1996.
- R. Holtzman and R. Juanes. Crossover from fingering to fracturing in deformable disordered media. *Phys. Rev. E*, 82:046305, doi:10.1103/PhysRevE.82.046305, 2010.
- R. Holtzman, M. L. Szulczewski, and R. Juanes. Capillary fracturing in granular media. *Phys. Rev. Lett.*, page in press, 2012.
- M. J. Hornbach, C. Ruppel, and C. L. Van Dover. Three-dimensional structure of fluid conduits sustaining an active deep marine cold seep. *Geophys. Res. Lett.*, 34:L05601, doi:10.1029/2006GL028859, 2007.

- M. J. Hornbach, D. M. Saffer, and W. S. Holbrook. Critically pressured free-gas reservoirs below gas-hydrate provinces. *Nature*, 427(6970):142–144, 2004.
- K. Z. House, D. P. Schrag, C. F. Harvey, and K. S. Lackner. Permanent carbon dioxide storage in deep-sea sediments. *Proc. Natl. Acad. Sci. U.S.A.*, 103:12291–12295, 2006.
- M. Hovland, J. V. Gardner, and A. G. Judd. The significance of pockmarks to understanding fluid flow processes and geohazards. *Geofluids*, 2:127–136, 2002.
- J. R. Hunt, N. Sitar, and K. S. Udell. Nonaqueous phase liquid transport and cleanup, 1. Analysis of mechanisms. *Water Resour. Res.*, 24(8):1247–1258, 1988.
- IPCC. *Climate Change 2007: The Physical Science Basis*. Cambridge University Press, Cambridge, UK, 2007.
- ITASCA. *PFC2D, v3.1 – Theory and Background*. Itasca Consulting Group, Inc., Minneapolis, MN, 2004.
- A. K. Jain and R. Juanes. Pore-scale mechanistic study of the preferential mode of hydrate formation in sediments: Coupling of multiphase fluid flow and sediment mechanics. In *Proc. 6th Intl. Conf. Gas Hydrates (ICGH 2008)*, Vancouver, Canada, July 6–10, 2008.
- A. K. Jain and R. Juanes. Preferential mode of gas invasion in sediments: grain-scale mechanistic model of coupled multiphase fluid flow and sediment mechanics. *J. Geophys. Res.*, 114:B08101, doi:10.1029/2008JB006002, 2009.
- K. L. Johnson. *Contact Mechanics*. Cambridge University Press, 1987.
- A. G. Judd, M. Hovland, L. I. Dimitrov, S. Garcia Gil, and V. Jukes. The geological methane budget at Continental Margins and its influence on climate change. *Geofluids*, 2:109–126, 2002.
- S. Kato, T. Sakakibara, and H. Yoshimori. Effects of intergranular adhesive force on behavior of granular material. In Y. Shimizu, R. D. Hart, and P. Cundall, editors, *Numerical Modeling in Micromechanics Via Particle Methods. Proc. of the 2nd International PFC Symposium, Kyoto, Japan*, pages 347–354, Balkema, Leiden, October 2004.
- M. Keller and R. F. Stallard. Methane emission by bubbling from Gatun Lake, Panama. *J. Geophys. Res.*, 99(D4):8307–8319, 1994.
- J. P. Kennett and B. N. Fackler-Adams. Relationship of clathrate instability to sediment deformation in the upper Neogene of California. *Geology*, 28(3):215–218, 2000.
- H. C. Kim, P. R. Bishnoi, R. A. Heideman, and S. S. H. Rizvi. Kinetics of methane hydrate decomposition. *Chem. Eng. Sci.*, 42(7):1645–1653, doi=10.1016/0009–2509(87)80169–0, 1987.
- A. Klar, K. Soga, and M. Y. A. Ng. Coupled deformation-flow analysis for methane hydrate extraction. *Geotechnique*, 60(10):765–776, 2010.
- H. Koide, Y. Shindo, Y. Tazaki, M. Iijima, K. Ito, N. Kimura, and K. Omata. Deep sub-seabed disposal of CO₂ – The most protective storage. *Energy Conv. Manag.*, 38:S253–S258, 1997a.

- H. Koide, M. Takahashi, Y. Shindo, Y. Tazaki, M. Iijima, K. Ito, N. Kimura, and K. Omata. Hydrate formation in sediments in the sub-seabed disposal of CO₂. *Energy*, 22:279–283, 1997b.
- H. Koide, M. Takahashi, and H. Tsukamoto. Self-trapping mechanisms of carbon dioxide in the aquifer disposal. *Energy Conv. Manag.*, 36:505–508, 1995.
- X.-Z. Kong, W. Kinzelbach, and F. Stauffer. Morphodynamics during air injection into water-saturated movable spherical granulates. *Chem. Eng. Sci.*, 65:4652–4660, 2010.
- M. B. Kowalsky and G. J. Moridis. Comparison of kinetic and equilibrium reaction models in simulating gas hydrate behavior in porous media. *Energy Conv. Manag.*, 48(6):1850–1863, 10.1016/j.enconman.2007.01.017, 2007.
- K. A. Kvenvolden. Methane hydrate – a major reservoir of carbon in the shallow geosphere? *Chem. Geol.*, 71:41–51, 1988.
- T. H. Kwon, G.-C. Cho, and J. C. Santamarina. Gas hydrate dissociation in sediments: Pressure-temperature evolution. *Geochem. Geophys. Geosyst.*, 9(3):Q03019, doi=10.1029/2007GC001920, 2006.
- T. H. Kwon, K.-I. Song, and G.-C. Cho. Destabilization of marine gas hydrate-bearing sediments induced by a hot wellbore: A numerical approach. *Energ. Fuel.*, 24(10):5493–5507, 2010.
- C.-H. Lam. Fluid invasion in porous media: viscous gradient percolation. *Phys. Rev. Lett.*, 92(25):254503, 2004.
- I. Leifer and J. Boles. Turbine tent measurements of marine hydrocarbon seeps on subhourly timescales. *J. Geophys. Res.*, 110(C1):C01006, 2005.
- I. Leifer, B. P. Luyendyk, J. Boles, and J. F. Clark. Natural marine seepage blowout: Contribution to atmospheric methane. *Glob. Biogeochem. Cycle*, 20(3):GB3008, 2006.
- A. M. Leitch and W. D. Baines. Liquid volume flux in a weak bubble plume. *J. Fluid Mech.*, 205:77–98, 1989.
- E. Lemaire, P. Levitz, G. Daccord, and H. Van Damme. From viscous fingering to viscoelastic fracturing in colloidal fluids. *Phys. Rev. Lett.*, 67(15):2009–2012, 1991.
- R. Lenormand. Flow through porous media: limits of fractal patterns. *Proc. R. Soc. Lond. A*, 423:159–168, 1989.
- R. Lenormand, E. Touboul, and C. Zarcone. Numerical models and experiments on immiscible displacements in porous media. *J. Fluid Mech.*, 189:165–187, 1988.
- R. Lenormand, C. Zarcone, and A. Sarr. Mechanisms of the displacement of one fluid by another in a network of capillary ducts. *J. Fluid Mech.*, 135:123–132, 1983.
- M. C. Leverett. Capillary behavior of porous solids. *Petrol. Trans. AIME*, 142:152–169, 1941.

- A. Levermann and I. Procaccia. Bi-Laplacian growth patterns in disordered media. *Phys. Rev. Lett.*, 89(23):234501, 2002.
- J. S. Levine, J. M. Matter, D. Goldberg, A. Cook, and K. S. Lackner. Gravitational trapping of carbon dioxide in deep sea sediments: Permeability, buoyancy, and geomechanical analysis. *Geophys. Res. Lett.*, 34:L24703, doi:10.1029/2007GL031560, 2007.
- L. Li and R. M. Holt. Simulation of flow in sandstone with fluid coupled particle model. In *Rock Mechanics in the National Interest. Proceedings of the 38th U.S. Rock Mechanics Symposium, Washington, D.C.*, volume 1, pages 165–172, Balkema, Rotterdam, July 2001.
- L. Li and R. M. Holt. A study on the calculation of particle volumetric deformation in a fluid coupled PFC model. In Y. Shimizu, R. D. Hart, and P. Cundall, editors, *Numerical Modeling in Micromechanics Via Particle Methods. Proc. of the 2nd International PFC Symposium, Kyoto, Japan*, pages 273–279, Balkema, Leiden, October 2004.
- Y. Li, Y. Xu, and C. Thornton. A comparison of discrete element simulations and experiments for “sandpiles” composed of spherical particles. *Powder Technol.*, 160(3):219–228, 2005.
- G. Lian, C. Thornton, and M. J. Adams. A theoretical study of the liquid bridge forces between two rigid spherical bodies. *J. Colloid Interface Sci.*, 161:138–147, 1993.
- A. Lindner, P. Coussot, and D. Bonn. Viscous fingering in a yield stress fluid. *Phys. Rev. Lett.*, 85: 314–317, 2000.
- X. Liu and P. B. Flemings. Passing gas through the hydrate stability zone at southern Hydrate Ridge, offshore Oregon. *Earth Planet. Sci. Lett.*, 241:211–216, 2006.
- X. Liu and P. B. Flemings. Dynamic multiphase flow model of hydrate formation in marine sediments. *J. Geophys. Res.*, 112:B03101, doi:10.1029/2005JB004227, 2007.
- X. Liu and P. B. Flemings. Dynamic response of oceanic hydrates to sea level drop. *Geophys. Res. Lett.*, 36:L17308, doi:10.1029/2009GL039821, 2009.
- G. Løvoll, Y. Méheust, R. Toussaint, J. Schmittbuhl, and K. J. Måløy. Growth activity during fingering in a porous Hele-Shaw cell. *Phys. Rev. E*, 70:026301, 2004.
- K. J. Måløy, J. Feder, and T. Jøssang. Viscous fingering fractals in porous media. *Phys. Rev. Lett.*, 55(24):2688–2691, 1985.
- K. J. Måløy, L. Furuberg, J. Feder, and T. Jøssang. Dynamics of slow drainage in porous media. *Phys. Rev. Lett.*, 68(14):2161–2164, 1992.
- C. S. Martens and J. Val Klump. Biogeochemical cycling in an organic-rich coastal marine basin. 1. Methane sediment-water exchange processes. *Geochim. Cosmochim. Acta*, 44(3):471–490, 1980.
- G. Mason and N. R. Morrow. Capillary behavior of a perfectly wetting liquid in irregular triangular tubes. *J. Colloid Interface Sci.*, 141:262, 1991.

- M. D. Mattson and G. E. Likens. Air pressure and methane fluxes. *Nature*, 347:718–719, 1990.
- R. P. Mayer and R. A. Stowe. Mercury-porosimetry breakthrough pressure for penetration between packed spheres. *J. Colloid Interface Sci.*, 20:893, 1965.
- D. F. McGinnis, J. Greinert, Y. Artemov, S. E. Beaubien, and A. Wuest. Fate of rising methane bubbles in stratified waters: How much methane reaches the atmosphere? *J. Geophys. Res.*, 111 (C9):C09007, 2006.
- P. Meakin. Models for material failure and deformation. *Science*, 252:226–234, 1991.
- P. Meakin, G. Li, L. M. Sander, E. Louis, and F. Guinea. A simple two-dimensional model for crack propagation. *J. Phys. A: Math. Gen.*, 22:1393–1403, 1989.
- J. Mienert, M. Vanneste, S. Bünz, K. Andreassen, H. Haflidason, and H. P. Sejrup. Ocean warming and gas hydrate stability on the mid-Norwegian margin at the Storegga slide. *Mar. Pet. Geol.*, 22:233–244, 2005.
- A. V. Milkov, G. R. Dickens, G. E. Claypool, Y.-J. Lee, W. S. Borowski, M. E. Torres, W. Xu, H. Tomaru, A. M. Trehu, and P. Schultheiss. Co-existence of gas hydrate, free gas, and brine within the regional gas hydrate stability zone at Hydrate Ridge (Oregon margin): evidence from prolonged degassing of a pressurized core. *Earth Planet. Sci. Lett.*, 222:829–843, 2004.
- A. V. Milkov and W. Xu. Comment on “Gas hydrate growth, methane transport, and chloride enrichment at the southern summit of Hydrate Ridge, Cascadia margin off Oregon” by Torres et al. [Earth Planet. Sci. Lett. 226:225–241 (2004)]. *Earth Planet. Sci. Lett.*, 239:162–167, 2005.
- M. Muskat. *Physical Principles of Oil Production*. McGraw-Hill, New York, 1949.
- G. L. Netzeband, C. P. Hübscher, D. Gajewski, J. W. G. Grobys, and J. Bialas. Seismic velocities from the Yaquina forearc basin off Peru: evidence for free gas within the gas hydrate stability zone. *Int. J. Earth Sci.*, 94:420–432, 2005.
- L. Niemeyer, L. Pietronero, and H. J. Wiesmann. Fractal dimension of dielectric breakdown. *Phys. Rev. Lett.*, 52(12):1033–1036, 1984.
- J. Nimblett and C. Ruppel. Permeability evolution during the formation of gas hydrates in marine sediments. *J. Geophys. Res.*, 108(B9):2420, doi:10.1029/2001JB001650, 2003.
- J. A. Nunn and P. Meulbroek. Kilometer-scale upward migration of hydrocarbons in geopressed sediments by buoyancy-driven propagation of methane-filled fractures. *AAPG Bull.*, 86(5):907–918, 2002.
- A. Obzhirov, R. Shakirov, A. Salyuk, E. Suess, N. Biebow, and A. Salomatin. Relations between methane venting, geological structure and seismo-tectonics in the Okhotsk Sea. *Geo-Mar. Lett.*, 24:135–139, 2004.
- P. E. Øren, S. Bakke, and O. J. Arntzen. Extending predictive capabilities to network models. *Soc. Pet. Eng. J.*, 3(4):324–336, December 1998.

- F. M. Orr, L. E. Scriven, and A. P. Rivas. Pendular rings between solids: meniscus properties and capillary force. *J. Fluid Mech.*, 67:723–742, 1975.
- L. Paterson. Diffusion-limited aggregation and two-fluid displacements in porous media. *Phys. Rev. Lett.*, 52(18):1621–1624, 1984.
- T. W. Patzek. Verification of a complete pore network simulator of drainage and imbibition. *Soc. Pet. Eng. J.*, 6(2):144–156, June 2001.
- T. W. Patzek and D. B. Silin. Shape factor and hydraulic conductance in noncircular capillaries: I. One-phase creeping flow. *J. Colloid Interface Sci.*, 296:295–304, 2001.
- C. K. Paull, P. G. Brewer, W. Ussler, E. T. Peltzer, G. Rehder, and D. Clague. An experiment demonstrating that marine slumping is a mechanism to transfer methane from seafloor gas-hydrate deposits into the upper ocean and atmosphere. *Geo-Mar. Lett.*, 22:198–203, 2003.
- C. K. Paull, W. Ussler, S. R. Dallimore, S. M. Blasco, T. D. Lorensen, H. Mellling, B. E. Medioli, F. M. Nixon, and F. A. McLaughlin. Origin of pingo-like features on the Beaufort Sea shelf and their possible relationship to decomposing methane gas hydrates. *Geophys. Res. Lett.*, 34:L01603, 2007.
- D. O. Potyondy and P. A. Cundall. A bonded-particle model for rock. *Int. J. Rock Mech. Min. Sci.*, 41:1329–1364, 2004.
- O. Praud and H. L. Swinney. Fractal dimension and unscreened angles measured for radial viscous fingering. *Phys. Rev. E*, 72:011406, 2005.
- P. B. Price and T. Sowers. Temperature dependence of metabolic rates for microbial growth, maintenance, and survival. *Proc. Natl. Acad. Sci. U.S.A.*, 101(13):4631–4636, 2004.
- H. M. Princen. Capillary phenomena in assemblies of parallel cylinders. I. Capillary rise between two cylinders. *J. Colloid Interface Sci.*, 30:60, 1969a.
- H. M. Princen. Capillary phenomena in assemblies of parallel cylinders. II. Capillary rise in systems with more than two cylinders. *J. Colloid Interface Sci.*, 30:359, 1969b.
- H. M. Princen. Capillary phenomena in assemblies of parallel cylinders. III. Liquid columns between horizontal parallel cylinders. *J. Colloid Interface Sci.*, 34:171, 1970.
- M. Prodanovic and S. Bryant. A level set method for determining critical curvatures for drainage and imbibition. *J. Colloid Interface Sci.*, 304:442–458, 2006.
- M. T. Reagan and G. J. Moridis. Large-scale simulation of methane hydrate dissociation along the West Spitsbergen Margin. *Geophys. Res. Lett.*, 36:L23612, 2009.
- G. Rehder, P. W. Brewer, E. T. Peltzer, and G. Friederich. Enhanced lifetime of methane bubble streams within the deep ocean. *Geophys. Res. Lett.*, 29(15):1731, 2002.
- L. A. Richards. Capillary conduction of liquids through porous mediums. *Physics*, 1:318–333, 1931.

- M. Riedel, T. S. Collett, M. J. Malone, and the Expedition 311 Scientists, editors. *Cascadia Margin Gas Hydrates*, volume 311 of *Proc. IODP, Expedition Reports*, College Station, TX, 2006. Integrated Ocean Drilling Program.
- J. W. M. Rudd, R. D. Hamilton, and N. E. Campbell. Measurement of microbial oxidation of methane in lake water. *Limnol. Oceanogr.*, 19(3):519–524, 1974.
- C. Ruppel, G. R. Dickens, D. G. Castellini, W. Gilhooly, and D. Lizarralde. Heat and salt inhibition of gas hydrate formation in the northern Gulf of Mexico. *Geophys. Res. Lett.*, 32:L04605, doi:10.1029/2004GL021909, 2005.
- J. Rutqvist and G. J. Moridis. Numerical studies on the geomechanical stability of hydrate-bearing sediments. *Soc. Pet. Eng. J.*, 14(2):267–282, 2009.
- H. Sahling, G. Bohrmann, V. Spiess, J. Bialas, M. Breitzke, M. Ivanov, S. Kasten, S. Krastel, and R. Schneider. Pockmarks in the Northern Congo Fan area, SW Africa: Complex seafloor features shaped by fluid flow. *Mar. Geol.*, 249:206–225, 2008.
- B. Sandnes, E.G. Flekkøy, H.A. Knudsen, K. J. Måløy, and H. See. Patterns and flow in frictional fluid dynamics. *Nat. Commun.*, 2:288, 2011.
- B. Sandnes, H. A. Knudsen, K. J. Måløy, and E. G. Flekkøy. Labyrinth patterns in confined granular-fluid systems. *Phys. Rev. Lett.*, 99(3):038001, 2007.
- R. Sassen, S. L. Losh, L. Cathles III, H. H. Roberts, J. K. Whelan, A. V. Milkov, S. T. Sweet, and D. A. DeFreitas. Massive vein-filling gas hydrate: relation to ongoing gas migration from the deep subsurface in the Gulf of Mexico. *Mar. Pet. Geol.*, 18:551–560, 2001.
- B. P. Scandella. Numerical modeling of methane venting from lake sediments. Master’s thesis, Massachusetts Institute of Technology, Cambridge, Massachusetts, 2010.
- B. P. Scandella, C. Varadharajan, H. Hemond, C. Ruppel, and R. Juanes. A conduit dilation model of methane venting from lake sediments. *Geophys. Res. Lett.*, 38:L06408, doi:10.1029/2011GL046768, 2011.
- N. Shakhova, I. Semiletov, A. Salyuk, V. Yusupov, D. Kosmach, and Ö. Gustafsson. Extensive methane venting to the atmosphere from sediments of the East Siberian Arctic shelf. *Science*, 327:1246–1250, 2010.
- Y. Shimizu. Fluid coupling in PFC2D and PFC3D. In Y. Shimizu, R. D. Hart, and P. Cundall, editors, *Numerical Modeling in Micromechanics Via Particle Methods. Proc. of the 2nd International PFC Symposium, Kyoto, Japan*, pages 281–287, Balkema, Leiden, October 2004.
- Hosung Shin and J. Carlos Santamarina. Fluid-driven fractures in uncemented sediments: Underlying particle-level processes. *Earth Planet. Sci. Lett.*, 299(1–2):180–189, 2010.
- G. C. Sills, S. J. Wheeler, S. D. Thomas, and T. N. Gardner. Behavior of offshore soils containing gas bubbles. *Geotechnique*, 41(2):227–241, 1991.

- E. D. Sloan. *Clathrate Hydrates of Natural Gases*. Marcel Dekker, New York, second edition, 1998.
- E. D. Sloan. Fundamental principles and applications of natural gas hydrates. *Nature*, 426:353–359, November 23, 2003.
- E. D. Sloan and C. A. Koh. *Clathrate Hydrates of Natural Gases*. CRC Press, New York, third edition, 2008.
- E. A. Solomon, M. Kastner, I. R. MacDonald, and I. Leifer. Considerable methane fluxes to the atmosphere from hydrocarbon seeps in the Gulf of Mexico. *Nat. Geosci.*, 2(8):561–565, 2009.
- V. A. Soloviev and G. D. Ginsburg. Water segregation in the course of gas hydrate formation and accumulation in submarine gas-seepage fields. *Mar. Geol.*, 137:59–68, 1997.
- J. P. Stokes, D. A. Weitz, J. P. Gollub, A. Dougherty, M. O. Robbins, P. M. Chaikin, and H. M. Lindsay. Interfacial stability of immiscible displacement in a porous medium. *Phys. Rev. Lett.*, 57:1718–1721, 1986.
- E. Suess, M. E. Torres, G. Bohrmann, R. W. Collier, J. Greinert, P. Linke, G. Rehder, A. Trehu, K. Wallmann, G. Winckler, and E. Zuleger. Gas hydrate destabilization: enhanced dewatering, benthic material turnover and large methane plumes at the Cascadia convergent margin. *Earth Planet. Sci. Lett.*, 170:1–15, 1999.
- N. Sultan, P. Cochonat, J.-P. Foucher, and J. Mienert. Effect of gas hydrates melting on seafloor slope instability. *Mar. Geol.*, 213:379–401, 2004.
- K. t. Leung and Z. Néda. Pattern formation and selection in quasistatic fracture. *Phys. Rev. Lett.*, 85(3):662–665, 2000.
- B. B. Tan. Geotechnical characterization of sediments from Hydrate Ridge, Cascadia continental margin. M.Sc. Thesis, MIT, Cambridge, MA, 2004.
- B. B. Tan, J. T. Germaine, and P. B. Flemings. Data report: Consolidation and strength characteristics of sediments from ODP Site 1244, Hydrate Ridge, Cascadia continental margin. In *Proc. Ocean Drilling Program, Sci. Results*, volume 204, 2006.
- K. Terzaghi. *Theoretical Soil Mechanics*. John Wiley, New York, 1943.
- S. D. Thomas. *The consolidation behaviour of gassy soil*. PhD thesis, University of Oxford, 1987.
- M. E. Torres, J. McManus, D. E. Hammond, M. A. de Angelis, K. U. Heeschen, S. L. Colbert, M. D. Tryon, K. M. Brown, and E. Suess. Fluid and chemical fluxes in and out of sediments hosting methane hydrate deposits on Hydrate Ridge, OR, I: Hydrological provinces. *Earth Planet. Sci. Lett.*, 201:525–540, 2002.
- M. E. Torres, K. Wallmann, A. M. Trehu, G. Bohrmann, W. S. Borowski, and H. Tomaru. Gas hydrate growth, methane transport, and chloride enrichment at the southern summit of Hydrate Ridge, Cascadia margin off Oregon. *Earth Planet. Sci. Lett.*, 226:225–241, 2004.

- M. E. Torres, K. Wallmann, A. M. Trehu, G. Bohrmann, W. S. Borowski, and H. Tomaru. Reply to comment on: “Gas hydrate growth, methane transport, and chloride enrichment at the southern summit of Hydrate Ridge, Cascadia margin off Oregon”. *Earth Planet. Sci. Lett.*, 239:168–175, 2005.
- R. Toussaint, G. Løvoll, Y. Méheust, K. J. Måløy, and J. Schmittbuhl. Influence of pore-scale disorder on viscous fingering during drainage. *Europhys. Lett.*, 71(4):583–589, 2005.
- A. M. Trehu, G. Bohrmann, M. E. Torres, and F. S. Colwell, editors. *Drilling Gas Hydrates on Hydrate Ridge, Cascadia Continental Margin*, volume 204 of *Proc. ODP, Sci. Results*, College Station, TX, 2006a. Ocean Drilling Program. doi:10.2973/odp.proc.sr.204.2006.
- A. M. Trehu, P. B. Flemings, N. L. Bangs, J. Chevalier, E. Gracia, J. E. Johnson, C.-S. Liu, X. Liu, M. Riedel, and M. E. Torres. Feeding methane vents and gas hydrate deposits at south Hydrate Ridge. *Geophys. Res. Lett.*, 31:L23310, doi:10.1029/2004GL021286, 2004a.
- A. M. Trehu, P. E. Long, M. E. Torres, G. Bohrmann, F. R. Rack, T. S. Collett, D. S. Goldberg, A. V. Milkov, M. Riedel, P. Schultheiss, N. L. Bangs, S. R. Barr, W. S. Borowski, G. E. Claypool, M. E. Delwiche, G. R. Dickens, E. Gracia, G. Guerin, M. Holland, J. E. Johnson, Y. J. Lee, C. S. Liu, X. Su, B. Teichert, H. Tomaru, M. Vanneste, M. Watanabe, and J. L. Weinberger. Three-dimensional distribution of gas hydrate beneath southern Hydrate Ridge: constraints from ODP Leg 204. *Earth Planet. Sci. Lett.*, 222:845–862, 2004b.
- A. M. Trehu, C. Ruppel, M. Holland, G. R. Dickens, M. E. Torres, T. S. Collett, D. Goldberg, R. Riedel, and P. Schultheiss. Gas hydrates in marine sediments: lessons from scientific drilling. *Oceanography*, 19(4):124–143, 2006b.
- M. D. Tryon, K. M. Brown, and M. E. Torres. Fluid and chemical flux in and out of sediments hosting methane hydrate deposits on Hydrate Ridge, OR, II: Hydrological processes. *Earth Planet. Sci. Lett.*, 201:541–557, 2002.
- M. D. Tryon, K. M. Brown, M. E. Torres, A. M. Trehu, J. McManus, and R. W. Collier. Measurements of transience and downward fluid flow near episodic methane gas vents, Hydrate Ridge, Cascadia. *Geology*, 27(12):1075–1078, 1999.
- I. N. Tsimpanogiannis and P. C. Lichtner. Pore-network study of methane hydrate dissociation. *Phys. Rev. E*, 74(5):056303, 2006.
- F. Tzschichholz and H. J. Herrmann. Simulations of pressure fluctuations and acoustic emission in hydraulic fracturing. *Phys. Rev. E*, 51(3):1961–1970, 1995.
- D. L. Valentine, D. C. Blanton, W. S. Reeburgh, and M. Kastner. Water column methane oxidation adjacent to an area of active hydrate dissociation, Eel River Basin. *Geochim. Cosmochim. Acta*, 65(16):2633–2640, 2001.
- P. Van Rensbergen, M. De Batist, J. Klerkx, R. Hus, J. Poort, M. Vanneste, N. Granin, O. Khlystov, and P. Krinitsky. Sublacustrine mud volcanoes and methane seeps caused by dissociation of gas hydrates in Lake Baikal. *Geology*, 30(7):631–634, 2002.

- C. Varadharajan. *Magnitude and Spatio-Temporal Variability of Methane Emissions from a Eutrophic Freshwater Lake*. PhD Dissertation, November 2009.
- C. Varadharajan, R. Hermosillo, and H. F. Hemond. A low-cost automated trap to measure bubbling gas fluxes. *Limnol. Oceanogr. Methods*, 8:363–375, 2010.
- G. Varas, V. Vidal, and J.-C. Géminard. Morphology of air invasion in an immersed granular layer. *Phys. Rev. E*, 83:061302, 2011.
- W. F. Waite, T. J. Kneafsey, W. J. Winters, and D. H. Mason. Physical property changes in hydrate-bearing sediment due to depressurization and subsequent repressurization. *J. Geophys. Res.*, 113:B07102, 2008.
- W. F. Waite, J. C. Santamarina, D. D. Cortes, B. Dugan, D. N. Espinoza, J. Germaine, J. Jang, J. W. Jung, T. J. Kneafsey, H. Shin, K. Soga, W. J. Winters, and T-S. Yun. Physical properties of hydrate-bearing sediments. *Rev. Geophys.*, 47:10.1029/2008RG000279, 2009.
- K. M. Walter, S. A. Zimov, J. P. Chanton, D. Verbyla, and F. S. Chapin III. Methane bubbling from Siberian thaw lakes as a positive feedback to climate warming. *Nature*, 443:71–75, 2006.
- H. F. Wang. *Theory of Linear Poroelasticity*. Princeton University Press, 2000.
- J. L. Weinberger and K. M. Brown. Fracture networks and hydrate distribution at Hydrate Ridge, Oregon. *Earth Planet. Sci. Lett.*, 245:123–136, 2006.
- J. L. Weinberger, K. M. Brown, and P. E. Long. Painting a picture of gas hydrate distribution with thermal images. *Geophys. Res. Lett.*, 32:L04609, doi:10.1029/2004GL021437, 2005.
- G. K. Westbrook, K. E. Thatcher, et al. Escape of methane gas from the seabed along the West Spitsbergen continental margin. *Geophys. Res. Lett.*, 36:L15608, doi:10.1029/2009GL039191, 2009.
- S. J. Wheeler. Movement of large gas bubbles in unsaturated fine-grained sediments. *Mar. Geotechnol.*, 9(2):113–129, 1990.
- D. Wilkinson and J. Willemsen. Invasion percolation: a new form of percolation theory. *J. Phys. A*, 16:3365–3376, 1983.
- W. T. Wood, J. F. Gettrust, N. R. Chapman, G. D. Spence, and R. D. Hyndman. Decreased stability of methane hydrates in marine sediments owing to phase-boundary roughness. *Nature*, 420:656–660, 2002.
- L. Xu, S. Davies, A. B. Schofield, and D. A. Weitz. Dynamics of drying in 3D porous media. *Phys. Rev. Lett.*, 101:094502, 2008.
- W. Xu and L. N. Germanovich. Excess pore pressure resulting from methane hydrate dissociation in marine sediments: A theoretical approach. *J. Geophys. Res.*, 111:B01104, doi:10.1029/2004JB003600, 2006.

- W. Xu and C. Ruppel. Predicting the occurrence, distribution, and evolution of methane gas hydrate in porous marine sediments. *J. Geophys. Res.*, 104(B3):5081–5095, 1999.
- Y. C. Yortsos, B. Xu, and D. Salin. Phase diagram of fully-developed drainage in porous media. *Phys. Rev. Lett.*, 79(23):4581–4584, 1997.
- L. Zühlsdorff and V. Spiess. Three-dimensional seismic characterization of a venting site reveals compelling indications of natural hydraulic fracturing. *Geology*, 32(2):101–104, 2004.

Appendix – Description of Underlying Models

A significant portion of this research involved the development of new models of grain-scale phenomena, especially the motion of gas/water interfaces in granular materials. Novel aspects included the development of physically representative network models that eliminate the artificial boundary conditions that have been applied to all network models in the past; models and methods that simultaneously account for capillarity-driven gas invasion and grain displacement by gas pressure forces; a method to approximate the fundamental physics of imbibition (which requires explicit representation of the geometry of grains in the porous medium) in a network model which has no representation of the grain geometry; a method to validate the basic premise of network modeling (viz. that individual pore-filling events can be correctly captured by a set of rules).

These models underlie much of the analysis described in the body of this report. However many of them do not have immediate application to the behavior of hydrate-bearing sediments, which is the main focus of this report. We therefore describe these models by reference, that is, we cite the series of quarterly progress reports prepared over the course of this project for DOE NETL, and we refer to publications that have appeared on the same topics. All reports and publications are publicly available. We group these citations under three broad categories: model sediments, drainage/imbibition simulations, and capillarity/mechanics coupling.

Model Sediments

We developed algorithms to produce model sediments (dense, disordered packings of spheres) with a range of grain size distributions. The set of model sediments provided a test bed for drainage and imbibition simulations. The models are described in

Juanes R., and Bryant, S. L., 2007. “Mechanisms Leading to Co-Existence of Gas and Hydrate in Ocean Sediments,” *Creation of Sediment Models – Task 3 Technical Report*, University of Texas, DOE Award No.: DE-FC26-06NT43067. April 2007. (<http://1.usa.gov/HvIJHF>)

Advanced Methods for Simulating Drainage and Imbibition

We extended the Level Set Method for capillarity-controlled displacements (Prodanović and Bryant, *J. Colloid. Interfac. Sci.*, 2006) to account for the geometry in rough-walled fractures (relevant to the problem of when and where hydrates could grow following gas invasion by fracturing a sediment). We also developed the concept of infinite-acting network models. These enabled the first fundamentally correct prediction of residual saturations resulting from drainage/imbibition displacements in nature, where no explicit boundaries for the sediment/rock exist.

Prodanović, M., Bryant, S.L., and Karpyn, Z.T., “Investigating Matrix/Fracture Transfer via a Level Set Method for Drainage and Imbibition,” *Society of Petroleum Engineers Journal*, Volume 15, Number 1, pp. 125-136, March 2010. DOI: 10.2118/116110-PA, published online 12 November 2009.

Prodanović, M. and Bryant, S., “Physics-Driven Interface Modeling for Drainage and Imbibition in Fractures,” *Society of Petroleum Engineers Journal*, Volume 14, Number 3, pp. 532-542, September 2009. DOI: 10.2118/110448-PA, published online 27 July 2009.

- Behseresht, J., Bryant, S. and Seperhnoori, K., “Infinite-Acting Physically Representative Networks for Capillarity-Controlled Displacements,” *Society of Petroleum Engineers Journal*, Volume 14, Number 4, pp. 568-578, December 2009. DOI: 10.2118/110581-PA, published online 16 July 2009.
- Peng, Y., Prodanović, M., and Bryant, S., “Improving Fidelity of Network Models for Drainage and Imbibition,” SPE 124440 prepared for presentation at the 2009 SPE Annual Technical Conference and Exhibition held in New Orleans, Louisiana, USA, 4–7 October 2009.
- Behseresht, J., Peng, Y., Prodanovic, M., and Bryant, S. L., 2008. “Grain Scale Study of Hydrate Formation in Sediments from Methane Gas: Role of Capillarity,” *Proceedings of the 6th International Conference on Gas Hydrates (ICGH 2008)*, Vancouver, British Columbia, CANADA, July 6-10, 2008. (<http://1.usa.gov/H85rUn>)
- Prodanović, M. and Bryant, S., “Physics-Driven Interface Modeling for Drainage and Imbibition in Fractures,” SPE110448, *Proceedings of the 2007 SPE Annual Technical Conference and Exhibition*, Anaheim, California, USA, 11–14 November 2007.

Coupled Capillarity-Controlled Fluid Displacement with Mechanics

The competition between fracturing and drainage as modes of gas invasion is fundamental to oceanic hydrate-bearing sediments. Thus we carried out extensive development of methods that account for both processes simultaneously.

- Prodanović, M., Holder, J. and Bryant, S. “Pore Scale Coupling of Fluid Displacement and Unconsolidated Sediment Mechanics,” accepted for publication in the *International Journal of Oil, Gas and Coal Technology*, 21 Oct 2011.
- Holtzman, R. and R. Juanes. Mechanisms of gas transport in sediments: crossover from fingering to fracturing. In CD Proc., 7th International Conference on Gas Hydrates (ICGH 2011), Edinburgh, Scotland, UK, July 17-21, 2011.
- Holtzman, R. and R. Juanes. Crossover from fingering to fracturing in deformable disordered media. *Physical Review E*, 82(4):046305 (2010), doi:10.1103/PhysRevE.82.046305.
- Prodanović, M., Holder, J. and Bryant, S., “Coupling Capillarity-Controlled Fluid Displacement With Unconsolidated Sediment Mechanics: Grain Scale Fracture Opening,” SPE 124717 prepared for presentation at the 2009 SPE Annual Technical Conference and Exhibition held in New Orleans, Louisiana, USA, 4–7 October 2009.
- Jain, A. K. and R. Juanes. Preferential mode of gas invasion in sediments: grain-scale mechanistic model of coupled multiphase fluid flow and sediment mechanics. *Journal of Geophysical Research*, 114, B08101 (2009), doi:10.1029/2008JB006002.
- Jain, A. K., and Juanes, R., 2008. “Pore-scale Mechanistic Study of the Preferential Mode of Hydrate Formation in Sediments: Coupling of Multiphase Fluid Flow and Sediment Mechanics,” *Proceedings of the 6th International Conference on Gas Hydrates (ICGH 2008)*, Vancouver, British Columbia, CANADA, July 6-10, 2008.
- Prodanović, M. and Bryant, S., “Capillarity Controlled Displacements in Sediments With Movable Grains: Implications for Growth of Methane Hydrates,” SPE 116663, *Proceedings of the 2008 SPE Annual Technical Conference and Exhibition*, Denver, Colorado, USA, 21–24 September 2008.

Experiments of Multiphase Fluid Displacement with Mechanics

- R. Holtzman, M. L. Szulczewski, and R. Juanes. Capillary fracturing in granular media. *Physical Review Letters*, in press (2012).
- Choi, J.-H., Y. Seol, R. Boswell and R. Juanes. X-ray computed-tomography imaging of gas migration in water-saturated sediments: from capillary invasion to conduit opening. *Geophysical Research Letters*, 38, L17310 (2011), doi:10.1029/2011GL048513.

Publications on Field-scale Modeling and Hydrate-Bearing Sediments

For completeness we list other publications based on the research described in this report that deal with hydrate-bearing sediments; these topics are covered in the main body of the report.

- Scandella, B. P. and R. Juanes. Numerical modeling of hydrate formation from methane gas transport through dynamic conduits. In CD Proc., 7th International Conference on Gas Hydrates (ICGH 2011), Edinburgh, Scotland, UK, July 17-21, 2011.
- Scandella, B. P., C. Varadharajan, H. F. Hemond, C. Ruppel and R. Juanes. A conduit dilation model of methane venting from lake sediments. *Geophysical Research Letters*, 38, L06408 (2011), doi:10.1029/2011GL046768.
- Holtzman, R. and R. Juanes. Pore-scale modeling of overpressure caused by hydrate dissociation. In CD Proc., 7th International Conference on Gas Hydrates (ICGH 2011), Edinburgh, Scotland, UK, July 17-21, 2011.
- Holtzman, R. and R. Juanes. Thermodynamic and hydrodynamic constraints on overpressure caused by hydrate dissociation: a pore-scale model. *Geophysical Research Letters*, 38, L14308 (2011), doi:10.1029/2011GL047937.
- Behseresht, J. and Bryant, S., 2011. "Sedimentological Control on Saturation Distribution in Arctic Gas-Hydrate-Bearing Sands," *U.S. DOE-NETL Fire in the Ice Newsletter*, Vol. 11, Issue 1.
- Behseresht, J. and Bryant, S., "Effect of Relative Permeability Characteristics and Gas/Water Flow on Gas-Hydrate Saturation Distribution," SPE 147221 prepared for presentation at the SPE Annual Technical Conference and Exhibition to be held in Denver, Colorado, USA, 30 October–2 November 2011.
- Behseresht, J. and Bryant, S., "Sedimentological Control On Hydrate Saturation Distribution In Arctic Gas-Hydrate-Bearing Deposits," Proceedings of the 7th International Conference on Gas Hydrates (ICGH 2011), Edinburgh, Scotland, United Kingdom, July 17-21, 2011.
- Behseresht, J., Peng, Y., Bryant, S. and Winters, W. "Sedimentological Control on Arctic Gas-Hydrate-Bearing Deposits," poster GC51A-0707, American Geophysical Union Fall Meeting, San Francisco, 14-18 Dec. 2009.
- Juanes, R., and Bryant, S. L., 2009. "Models provide clues to how methane gas and hydrate coexist in nature," *U.S. DOE-NETL Fire in the Ice Newsletter*, Vol. 9, Issue 4, pgs. 7-11. (<http://1.usa.gov/HBY7gM>)
- Behseresht, J., Peng, Y., Prodanovic, M., and Bryant, S. L., 2008. "Mechanisms by Which Methane Gas and Methane Hydrate Coexist in Ocean Sediments," *Offshore Technology Conference*, Houston, Texas, May 5-8, 2008. (<http://1.usa.gov/H46RP8>)
- Holtzman, R., and Juanes, R., 2009. "Hydrate Formation in Gas-Rich Marine Sediments: A Grain-Scale Model," *Eos Trans. AGU* 90(52), Fall Meet. Suppl. OS41A-08.

Material in Preparation or in Review

At the time of submission of this report, several scholarly works are in progress. We include them here for reference.

- Behseresht, J. Dec 2012. “Sedimentological and Transport Control of Conversion of Gas Reservoirs to Hydrate during Global Cooling”. Ph.D. Dissertation – The University of Texas at Austin.
- Behseresht, J. and Bryant, S. Sedimentological Control on Saturation Distribution in Arctic Gas-Hydrate-Bearing Sands, in review, *Earth Plan. Sci. Lett.*

Theses and Dissertations

- Behseresht, J. 2008. “Infinite-Acting Physically Representative Networks for Capillarity-Controlled Displacements”. M.S. Thesis – The University of Texas at Austin.
- Jain, A. K., 2009. “Preferential Mode of Gas Invasion in Sediments: Grain-Scale Model of Coupled Multiphase Fluid Flow and Sediment Mechanics,” M. S. Thesis - Massachusetts Institute of Technology.
- Peng, Y. 2011. “Study of Methane Hydrate Formation and Distribution in Arctic Regions: From Pore Scale to Field Scale” Ph.D. Dissertation – The University of Texas at Austin.
- Scandella, B. P. 2010. “Numerical modeling of methane venting from lake sediments.” M.S. Thesis, Massachusetts Institute of Technology.

Progress Reports

Quarterly progress reports in chronological order include

- 2006 Q4
- 2007 Q1
- 2007 Q2
- 2007 Q3
- 2007 Q4
- 2008 Q1
- 2008 Q2
- 2008 Q4
- 2009 Q1
- 2009 Q2
- 2009 Q3
- 2009 Q4
- 2010 Q1
- 2010 Q2
- 2010 Q3
- 2010 Q4
- 2011 Q1
- 2011 Q2
- 2011 Q3

In addition to the quarterly reports, the deliverables on several specific tasks or subtasks included a technical report. The quarterly report for 2008 Q3 was subsumed by the report

deliverable for Task 5.3. A full listing of these reports follows. Reports prepared as deliverables are denoted by “*”.

- Juanes R., and Bryant, S. L., 2007. “Mechanisms Leading to Co-Existence of Gas and Hydrate in Ocean Sediments,” *Quarterly Progress Report, October - December 2006*, University of Texas, DOE Award No.: DE-FC26-06NT43067. March 2007. (<http://1.usa.gov/Hpzqtx>)
- Juanes R., and Bryant, S. L., 2007. “Mechanisms Leading to Co-Existence of Gas and Hydrate in Ocean Sediments,” *Quarterly Progress Report, January – March 2007*, University of Texas, DOE Award No.: DE-FC26-06NT43067. April 2007. (<http://1.usa.gov/HvPfxY>)
- * Juanes R., and Bryant, S. L., 2007. “Mechanisms Leading to Co-Existence of Gas and Hydrate in Ocean Sediments,” *Creation of Sediment Models – Task 3 Technical Report*, University of Texas, DOE Award No.: DE-FC26-06NT43067. April 2007. (<http://1.usa.gov/HvIJHF>)
- Juanes R., and Bryant, S. L., 2007. “Mechanisms Leading to Co-Existence of Gas and Hydrate in Ocean Sediments,” *Quarterly Progress Report, April – June 2007*, University of Texas, DOE Award No.: DE-FC26-06NT43067. July 2007. (<http://1.usa.gov/Hv4QeR>)
- Juanes R., and Bryant, S. L., 2007. “Mechanisms Leading to Co-Existence of Gas and Hydrate in Ocean Sediments,” *Quarterly Progress Report, July –September 2007*, University of Texas, DOE Award No.: DE-FC26-06NT43067. October 2007. (<http://1.usa.gov/HA4Hr4>)
- Juanes R., and Bryant, S. L., 2008. “Mechanisms Leading to Co-Existence of Gas and Hydrate in Ocean Sediments,” *Quarterly Progress Report, October – December 2007*, University of Texas, DOE Award No.: DE-FC26-06NT43067. January 2008. (<http://1.usa.gov/H42Qgu>)
- Juanes R., and Bryant, S. L., 2007. “Mechanisms Leading to Co-Existence of Gas and Hydrate in Ocean Sediments,” *Quarterly Progress Report, January – March 2008*, University of Texas, DOE Award No.: DE-FC26-06NT43067. May 2008. (<http://1.usa.gov/HA4OTu>)
- * Juanes R., and Bryant, S. L., 2008. “Mechanisms Leading to Co-Existence of Gas and Hydrate in Ocean Sediments,” *Fracture Initiation and Propagation – Task 4 Technical Report*, University of Texas, DOE Award No.: DE-FC26-06NT43067. May 2008. (<http://1.usa.gov/HvPFVe>)
- * Juanes R., and Bryant, S. L., 2008. “Mechanisms Leading to Co-Existence of Gas and Hydrate in Ocean Sediments,” *Compute Critical Curvatures for Pore-level Events – Task 5.1 Technical Report*, University of Texas, DOE Award No.: DE-FC26-06NT43067. June 2008. (<http://1.usa.gov/HvPKbx>)
- Juanes R., and Bryant, S. L., 2008. “Mechanisms Leading to Co-Existence of Gas and Hydrate in Ocean Sediments,” *Quarterly Progress Report, April – June 2008*, University of Texas, DOE Award No.: DE-FC26-06NT43067. August 2008. (<http://1.usa.gov/HBfvnj>)
- Juanes R., and Bryant, S. L., 2008. “Mechanisms Leading to Co-Existence of Gas and Hydrate in Ocean Sediments,” *Quarterly Progress Report, July – September 2008*, University of Texas, DOE Award No.: DE-FC26-06NT43067. October 2008. (<http://1.usa.gov/H2IoLy>)

- * Juanes R., and Bryant, S. L., 2008. “Mechanisms Leading to Co-Existence of Gas and Hydrate in Ocean Sediments,” *Compute gas/water interface geometry during drainage and imbibition in model sediments – Task 5.2 Technical Report*, University of Texas, DOE Award No.: DE-FC26-06NT43067. October 2008. (<http://1.usa.gov/HpAyxn>)
- * Juanes R., and Bryant, S. L., 2008. “Mechanisms Leading to Co-Existence of Gas and Hydrate in Ocean Sediments,” *Compute gas/water interface geometry within fracture – Task 5.3 Technical Report*, University of Texas, DOE Award No.: DE-FC26-06NT43067. October 2008. (<http://1.usa.gov/H8jIMU>)
- Juanes R., and Bryant, S. L., 2009. “Mechanisms Leading to Co-Existence of Gas and Hydrate in Ocean Sediments,” *Quarterly Progress Report, October – December 2008*, University of Texas, DOE Award No.: DE-FC26-06NT43067. February 2009. (<http://1.usa.gov/H226rM>)
- * Juanes R., and Bryant, S. L., 2009. “Mechanisms Leading to Co-Existence of Gas and Hydrate in Ocean Sediments,” *Couple gas/water interface dynamics with fracture propagation – Task 6 Technical Report*, University of Texas, DOE Award No.: DE-FC26-06NT43067. February 2009. (<http://1.usa.gov/H225nM>)
- Juanes R., and Bryant, S. L., 2009. “Mechanisms Leading to Co-Existence of Gas and Hydrate in Ocean Sediments,” *Quarterly Progress Report, January – March 2009*, University of Texas, DOE Award No.: DE-FC26-06NT43067. May 2009. (<http://1.usa.gov/H2Ixyz>)
- Juanes R., and Bryant, S. L., 2009. “Mechanisms Leading to Co-Existence of Gas and Hydrate in Ocean Sediments,” *Quarterly Progress Report, April – June 2009*, University of Texas, DOE Award No.: DE-FC26-06NT43067. July 2009. (<http://1.usa.gov/H8jRjf>)
- * Juanes R., and Bryant, S. L., 2009. “Mechanisms Leading to Co-Existence of Gas and Hydrate in Ocean Sediments,” *Coupled gas/water/sediment dynamics with rigid hydrate films – Task 7.1 Technical Report*, University of Texas, DOE Award No.: DE-FC26-06NT43067. October 2009. (<http://1.usa.gov/HC4EIB>)
- Juanes R., and Bryant, S. L., 2010. “Mechanisms Leading to Co-Existence of Gas and Hydrate in Ocean Sediments,” *Quarterly Progress Report, October - December 2009*, University of Texas, DOE Award No.: DE-FC26-06NT43067. January 2010. (<http://1.usa.gov/H2IAdV>)
- Juanes R., and Bryant, S. L., 2010. “Mechanisms Leading to Co-Existence of Gas and Hydrate in Ocean Sediments,” *Quarterly Progress Report, January - March 2010*, Massachusetts Institute of Technology, DOE Award No.: DE-FC26-06NT43067. March 2010. (<http://1.usa.gov/H51Fyn>)
- Juanes R., and Bryant, S. L., 2010. “Mechanisms Leading to Co-Existence of Gas and Hydrate in Ocean Sediments,” *Quarterly Progress Report, April - June 2010*, University of Texas, DOE Award No.: DE-FC26-06NT43067. August 2010. (<http://1.usa.gov/H8k71M>)
- Juanes R., and Bryant, S. L., 2010. “Mechanisms Leading to Co-Existence of Gas and Hydrate in Ocean Sediments,” *Quarterly Progress Report, July - September 2010*, University of Texas, DOE Award No.: DE-FC26-06NT43067. November 2010. (<http://1.usa.gov/HrJSQd>)
- Juanes R., and Bryant, S. L., 2011. “Mechanisms Leading to Co-Existence of Gas and Hydrate in Ocean Sediments,” *Quarterly Progress Report, October - December 2010*,

- University of Texas, DOE Award No.: DE-FC26-06NT43067. February 2011. (<http://1.usa.gov/HpBmlZ>)
- Juanes R., and Bryant, S. L., 2011. "Mechanisms Leading to Co-Existence of Gas and Hydrate in Ocean Sediments," *Quarterly Progress Report, January – March 2011*, University of Texas, DOE Award No.: DE-FC26-06NT43067. April 2011. (<http://1.usa.gov/H5kYmM>)
- Juanes R., and Bryant, S. L., 2011. "Mechanisms Leading to Co-Existence of Gas and Hydrate in Ocean Sediments," *Quarterly Progress Report, April –June 2011*, University of Texas, DOE Award No.: DE-FC26-06NT43067. July 2011. (<http://1.usa.gov/H38NoV>)
- Juanes R., and Bryant, S. L., 2011. "Mechanisms Leading to Co-Existence of Gas and Hydrate in Ocean Sediments," *Quarterly Progress Report, July –September 2011*, University of Texas, DOE Award No.: DE-FC26-06NT43067. October 2011. (<http://1.usa.gov/H5l39S>)

National Energy Technology Laboratory

626 Cochran Mill Road
P.O. Box 10940
Pittsburgh, PA 15236-0940

3610 Collins Ferry Road
P.O. Box 880
Morgantown, WV 26507-0880

13131 Dairy Ashford, Suite 225
Sugarland, TX 77478

1450 Queen Avenue SW
Albany, OR 97321-2198

2175 University Ave. South
Suite 201
Fairbanks, AK 99709

Visit the NETL website at:
www.netl.doe.gov

Customer Service:
1-800-553-7681

